UNIVERSITA' DEGLI STUDI DELL'INSUBRIA
Dipartimento di Scienza ed Alta Tecnologia

QUASAR PHYSICAL PAIRS

A Thesis submitted for the degree of Doctor of Philosophy

Angela Sandrinelli

supervisor: A. Treves
co-supervisors: S. Covino and R. Falomo

November 2014

Contents

1. Preface **1**

I. Quasar pairs environment **3**

2. Quasar Pairs **5**
2.1. Why it is important to study quasar pairs and their environment 5
2.2. Environment and clustering of the QSO pairs: previous works 7
2.3. This work 10

3. Search for quasar pairs **13**
3.1. Large-survey spectroscopic archival selection 13
3.2. Our search 14
3.2.1. Selection 15
3.2.2. Random Test 17
3.3. Other ways to find QSO pairs 18
3.3.1. Photometrical selections 18
3.3.2. Lens selection 19

4. The environment of low-redshift QSO pairs **33**
4.1. Summary 33
4.2. Low-redshift QSO pair sample 34
4.2.1. Selection of QSO candidates from SDSS catalogues 34
4.2.2. Selection on the basis of $\Delta V_{\|}$ from [OIII]λ5007 35
4.3. Host galaxies 41
4.3.1. Modeling the nuclear source 41
4.3.2. Modeling the galaxy luminosity 42
4.3.3. Luminosity of the quasar pair host galaxies 42
4.3.4. Host masses of QSO pairs 46
4.4. Nuclei of QSO pairs 48
4.4.1. Black Holes luminosities 48
4.4.2. The mass of quasar black holes: the single-epoch spectrum approach 48
4.4.3. Masses of black holes of QSO in pairs 50
4.5. Galaxy environment of the QSO pairs 52
4.5.1. Catalogues of galaxies 52
4.5.2. Galaxy count 54
4.5.3. Galaxy overdensity around QSOs in pairs 54
4.5.4. Comparison with isolated quasars and galaxies. 61
4.5.5. Galaxy overdensity dependence on QSO projected separation . . . 61

4.6. Discussion . . . 63
4.6.1. Virial mass of the quasar pairs . . . 67
4.7. Supplemental material . . . 71

5. Ongoing programs **79**
5.1. Summary . . . 79
5.2. Close QSO pairs . . . 80
5.2.1. Sample . . . 80
5.2.2. Spectroscopy . . . 80
5.2.3. The environment: preliminary analysis . . . 81
5.3. NOT observations. . . . 88
5.3.1. Sample selection . . . 88
5.3.2. Observations . . . 88
5.4. Future programs . . . 92
5.5. Supplemental material . . . 93

II. Blazar photometry **97**

6. Blazar photometry **99**
6.1. Summary . . . 99
6.2. TeV Blazar Photometry . . . 101
6.3. 3C 279 variability . . . 101
6.4. Quasi-periodicities of BL Lacs: the case of 3C 279. . . . 104
6.5. Supplemental material . . . 107
6.5.1. Methods of period estimation . . . 107
6.5.2. Check test for significance and alias. . . . 113

III. Publications **115**

7. List of publications and full papers **117**

1. Preface

The path to my PhD is rather unconventional but not unique. In fact, after the Laurea in Physics back in the 80s, for years I have worked as Math and Physics teacher in an Italian State high school. A teacher in Italy is a public service employee. Under a special agreement with the Italian Ministry of Education, University and Research, I was awarded to enter in a PhD program maintaining the teacher status but free of the teacher duties for the whole duration of the doctoral program. In Italy, the lack of links and synergies between high schools and universities are pushing more and more teachers in considering the opportunity offered by the Italian State to allow public employees to attend courses for the attainment of the PhD. This is one of the best resources for a real update for their own knowledge as well as a real opportunity of being able to contribute to the development of new knowledge.

As result of this, I choose to work within the observational programs of the Astrophysics group at the University of Insubria. My first task was to take care of a long series of CCD optical and IR photometric data regarding several Blazars taken at the Rapid Eye Mount (REM) located in the La Silla premises of the ESO Chilean Observatory. This required on my side to learn the basics of Active Galactic Nuclei (AGN) astrophysics and the hard practice to dominate the abilities of photometry using the PYTHON language. This led to the publication of a paper (**Sandrinelli et al., 2014, A&A, 562, A79**).

The next step was to deal with spectroscopy of optically selected BL Lac objects taken with FORS2 mounted on the Antu Very Large Telescope (VLT) of the ESO in Paranal. Spectra analysis had been performed using The Image Reduction and Analysis Facility (IRAF) for astronomical data reduction and analysis, Supermongo (SM) and a custom library of special applications mostly developed by INAF - Astronomical Observatory of Padova for all other analysis. Also this activity led to a publication (**Sandrinelli et al., 2013 AJ, 146, 163**).

At this stage I started with the subject that became the focus of my research activity. It is the spectral and environmental study of quasar (QSO) physical pairs. This is part of a program which is developed in collaboration with the Astronomical Observatory of Padova (Italy) and the Finnish Centre for Astronomy at University of Turku (Finland).

My contribution started with the identification of physical pairs both using the Sloan Digital Sky Survey (SDSS) as well as other public surveys. From several hundred thousands Quasars we were able to select 14 low redshift pairs which on statistically basis are consistent with physical bound systems. For each pair objects the SDSS spectra were carefully measured in order to derive the relative velocity between the two components. The host galaxies of the QSOs are measured, the environment is examined and the two objects of quasar pairs are compared with those of isolated quasar. This material is published in **Sandrinelli et al., 2014, MNRAS, 444, 1835**.

A second phase of this research line regards observations taken at Nordic Optical Tele-

scope (NOT) in the near Infrared which allow us to explore objects at higher redshifts. A preliminary account of our results is given in this thesis.

In spring of 2014 a significant progress took place in the research line dealing with BL Lac photometry. We reconsidered our study on PKS2155-304 and confirmed the quasi-periodicity of $\sim$ 315 days proposed by Zhang et al. (2014). Moreover we have shown that such periodicity is present in γ-rays from the examination of the *Fermi* archives. The results are published in **Sandrinelli et al., 2014, ApJL, 793**. Since I consider of some importance the result on PKS2155, they are presented in the second part of this thesis.

Part I.

Quasar pairs environment

2. Quasar Pairs

2.1. Why it is important to study quasar pairs and their environment

It is widely accepted that all massive galaxies contain in their centers a supermassive black hole (SMBH, Kormendy & Richstone 1995; Kormendy & Gebhardt 2001) of up to $\sim$ 1 billion of solar masses . However, only a small fraction of them is active.

Powered by some form of accretion of matter onto central super-massive black holes, as it was early suggested (Salpeter 1964; Zel'dovich 1964; Lynden-Bell 1969), quasars (QSOs) are believed to reside in massive bulge-dominated galaxies (e.g. Kormendy & Richstone 1995; Magorrian et al. 1998; Yu & Tremaine 2002; Dunlop et al. 2003) and are now explained as an extraordinary stage of the evolutionary processes of galaxies. However, about 50 years after their discovery (Schmidt 1963) the mechanism that activates and fuels the nuclei of galaxies is still not well understood.

Studies of the central black holes in nearby galaxies have been revealed SMBHs are closely related to the large-scale properties of their host galaxy spheroid. These correlations take various forms, relating the black hole mass to the mass or the luminosity (e.g. Kormendy & Richstone 1995; Magorrian et al. 1998; Kormendy & Gebhardt 2001)the velocity dispersion (Ferrarese & Merritt 2000; Gebhardt et al. 2000) and the concentration or Sersic index (Graham et al. 2001) of the host bulge component.

Those correlations result in a connection or feedback between SMBH and its host galaxy formation and growth and indicate that the evolution of the galaxies and their nuclear activity are linked. Moreover, the SMBH are related with the masses of the underling dark matter (DM) halos (Ferrarese 2002). This relation implies that the formation of SMBHs is controlled, perhaps indirectly, by the properties of the DM halos in which they reside.

It is also well known that formation and evolution of galaxies are influenced by the environment, with galaxies in clusters tending to exhibit elliptical morphology (e.g. Dressler 1980; Poggianti et al. 1999; Hashimoto, Henry, & Boehringer 2014) and deprived of most of their gaseous content (e.g. Silk & Wyse 1993; Vollmer & Huchtmeier 2007; Kormendy et al. 2009). In a number of cases the galaxies in clusters bear the signatures of interactions and mergers by nearby companions (e.g. Moore, Lake, & Katz 1998; Canalizo & Stockton 2001; Bennert et al. 2008; McIntosh et al. 2008). There are, moreover, observations of QSO host galaxies in interacting systems or apparent merger products (e.g. Canalizo & Stockton 2001; Green et al. 2011). Nevertheless, despite its importance, the role which may be attributed to the environment in the QSO ignition and fueling is still now an open subject.

In the current hierarchical scenario of galaxy formation and evolution (e.g. White &

Rees 1978), the most accredited causes believed to be responsible for transforming a dormant massive black hole into a luminous QSO are dissipative tidal interactions and gas-rich galaxy mergers (e.g. Di Matteo, Springel, & Hernquist 2005; Hopkins et al. 2008; Callegari et al. 2011, and references therein).

QSOs are rare objects in the Universe. However, in last decades a small fraction of QSOs were shown to have a companion at separation $\lesssim$ 0.5 -1 Mpc. Observational results associated these pairs of QSOs to groups or clusters of galaxies and, for this, they are supposed to be tracers of large structures. These works relate in general to a small number of pairs (e.g. Djorgovski et al. 2003; Boris et al. 2007). Moreover, these QSO pairs have been seen exhibiting a remarkable excess of clustering at small scale than the expectation from the correlation function at larger distances. This excess of QSO pairs (also termed binary QSOs, i.e. two QSOs with very close redshifts and gravitationally bound together or in a larger structure) strengthened the long argued idea of tidal forces in gas-driver mergers (e.g. Barnes & Hernquist 1996) leading to the mutual activation of both QSOs (e.g. Djorgovski 1991; Myers et al. 2007b, see next Section for details and references) and multiple QSO systems (Djorgovski et al. 2007). Mutual triggering, however, may not be the only actor in the activation of luminous QSOs and QSO pairs. The measured excess at small scale could be a statistically predictable result of a local overdensity of galaxies, due to the enhanced bias of the dark matter environments, in which mergers are more likely to occur (Di Matteo, Springel, & Hernquist 2005; Hopkins et al. 2008; Green et al. 2011). The concentration of QSOs (i.e. the presence of a QSO pair) in a small space may represent a natural consequence of the presence of clusters (Boris et al. 2007). For their huge luminosity QSO are excellent tracers of massive galaxies at every epoch of the Universe. If the QSO activity is associated to the galaxy mergers, the observation and the study of QSO pairs at the scale of galaxy interactions may provide useful constraints on that picture.

Alternatively, different models could be advocated to explain the QSO activations in the absence of external phenomena such as galaxy merging. An interesting prospective is that the recycled gas from dying stars is an important source of fuel for the central SMBH, even in the absence of external phenomena such as galaxy merging. The recycled gas, arising from stars in the inner several kiloparsecs of the galaxy (assumed a giant elliptical), will drive a radiative instability and a collapse toward the center of metal-rich gas. As a consequence, a starburst must occur and also the central SMBH can be fed (e.g. Ciotti & Ostriker 2007).

In both scenarios, merging or intrinsic activation, clustering of QSOs and of galaxies around QSOs, in comparison with that of normal galaxies, needs to be studied in great detail on various scales (from few kpc to Mpc) and at different cosmic epochs, to investigate if it reflects a true tendency to reside in regions of small-scale overdensity. This is a way to unravel the QSO phenomenon, its activation and the link between nuclear activity and immediate environment, and to locate it in the history of the Universe.

2.2. Environment and clustering of the QSO pairs: previous works

Dating back to Stockton (1978), early studies of galaxy clustering around QSOs (Yee & Green 1984, 1987) and other active galaxies (e.g. Wake et al. 2004) aim to characterize the properties of the environment and to compare them with the environment of non-active galaxies. The emerging picture is not clear. Most of the papers conclude that QSOs reside in regions more strongly clustered than galaxies, (e.g. Shanks, Boyle, & Peterson 1988; Chu & Zhu 1988; Ellingson et al. 1991) on Mpc scales, albeit with significant difference among various objects. Only in rare cases QSOs are found in a particularly rich environments (Stockton 1978; Yee & Green 1984) with core volume density similar to Abell clusters, while the typical environment is a modest group or a poor cluster of galaxies at the same redshift (Bahcall & Chokshi 1991; Fisher et al. 1996; McLure & Dunlop 2001).

Contrasting results emerge when the QSO environments are compared with those of non-active galaxies depending on the properties of the sample (nuclear luminosity, redshift, radio loudness, etc.). Some differentiation emerges from the comparison of radio loud and radio quiet QSOs. Ellingson et al. (1991) studied a sample of radio loud QSOs (RLQs) and radio quiet QSOs (RQQs) at $0.3 < z < 0.6$ and found that the environments around RLQs are significantly denser than those around RQQs. However, Fisher et al. (1996) and McLure & Dunlop (2001) find no difference between the environments of RLQs and RQQs.

From the search for clustered protogalaxies around QSOs, Djorgovski et al. (1999) indicated that QSOs at large redshifts (z>4) could provide a powerful probe of structure formation in the early universe and be signposts of future rich clusters.

Later studies based on large surveys, such as the Two Degree Field (2dF Croom et al. 2004) and the Sloan Digital Sky Survey (SDSS, York et al. 2000), as well as on more complete samples have found the environmental galaxy densities of QSOs and galaxies to be comparable on 1 - 10 Mpc scale (e.g. Croom et al. 2004, 2005; Smith, Boyle, & Maddox 2000; Wake et al. 2004; Coil et al. 2007; Padmanabhan et al. 2009), with QSOs systematically avoiding high-density regions (Roberts, Odell, & Burbidge 1977; Yee & Green 1984; Coldwell & Lambas 2006). This suggests that QSOs and L* inactive galaxies inhabit similar environments.

From the analysis of a large data set of $\sim$ 2000 QSOs from SDSS Data Release 3 (DR3) at $z < 4$ Serber et al. (2006) found a significant local excess of neighbor galaxies when QSOs are compared with L* galaxies, but only at $\lesssim 0.2$ scale, and that most luminous QSOs harbor in denser small-scale regions than typical L* galaxies. Similar density results were obtained by Strand, Brunner, & Myers (2008) on $\sim$ 6000 QSOs at $z < 0.6$ from SDSS DR5, with a marginal evidence of overdensity with the redshift, but without the comparison with an inactive-galaxy control sample.

Considering more recent results, a significant redshift-dependent clustering amplitude around QSOs with more massive black holes or bluer colors was reported by Zhang et al. (2013a) around $\sim$ 2300 QSOs in the SDSS Stripe 82. They found blue galaxies more strongly clustered around QSOs than red galaxies, while no luminosity dependence was reported. They suggested that, at the investigated redshift ($0.6 < z < 1.2$), QSOs in

general do not reside in massive clusters, but rather in less massive groups of galaxies, since blue-galaxy clustering is enhanced in the centers of low mass halos, while more luminous red galaxies reside in more massive halos (Zehavi et al. 2005). In this picture minor mergers could assume a not negligible role in triggering the QSO activity. However, a more complete comparison of QSOs and inactive galaxy environments was carried out, by Karhunen et al. (2014) in the SDSS Stripe 82, where they considered $\sim$ 400 QSOs and $\sim$ 300 giant elliptical galaxies matching in redshift and galaxy luminosity with the resolved QSO host galaxies. They found that a galaxy overdensity is apparent within 400 kpc around the QSOs and that, on average, it is comparable to that of the inactive galaxies, i.e. QSOs don't live in richer environments than galaxies. No significant dependence of the overdensity on QSO luminosity or redshift was observed.

Since its first detections, the QSO clustering was considered as possible tracer of high density fields (Shaver 1984; Andreani & Cristiani 1992; Mo & Fang 1993; Croom & Shanks 1996). In the merger scenario, an obvious outcome of galaxy assembly on a small scale and a first clear sign of QSO clustering is the finding of QSO associations, consisting typically of pairs, see e.g. the pioneering work of Djorgovski (1991) and the analysis on the Veron-Cetty & Veron (2000) by Zhdanov & Surdej (2001).

Progress on wide-area dedicated surveys has made it possible to carry out more accurate QSO clustering measurements by the two point correlation function (2pcf, Peebles 1980) on wide ranges of z (e.g. Porciani, Magliocchetti, & Norberg 2004; Croom et al. 2005; Myers et al. 2006, 2007a,b, 2008; Shen et al. 2009; da Ângela et al. 2008; Hennawi et al. 2006, 2010; Shen et al. 2013b; Croom et al. 2004; Coil et al. 2007; Padmanabhan et al. 2009; Strand, Brunner, & Myers 2008). The 2pcf is a conventional approach to probe the entire distribution of a class of objects (e.g. autocorrelation of galaxies, or AGNs, or QSOs), from void to large-scale structures. The 2pcf is determined comparing the observational sample with a randomly generated sample subjected to the same positional and redshift selection effects. It indicates the probability of an excess of objects in relation to the random at a given separation. For QSOs this function is found with an overall agreement to have a power-law shape and the QSO clustering scale length, where the correlation function is unity, is $r_0 = 5 - 6\ h^{-1}$ Mpc at a mean redshift (e.g. z=1.5, Porciani, Magliocchetti, & Norberg 2004). This amplitude is comparable to that found for luminous local galaxies and is consistent with the idea that powerful AGNs are found in luminous galaxies and thus share their clustering properties. At high redshift the clustering of QSOs is more difficult to measure. Croom et al. (2004) gave results compatible with a constant behavior from z=0.5 to z=2.2, consistent with quasars inhabiting halos of similar mass at every redshift but there are also indications that the clustering strength would be higher in the past than in the present epoch (e.g. Porciani, Magliocchetti, & Norberg 2004).

Clustering measurements were also extended to small scales ($\lesssim$1 Mpc, e.g. Hennawi et al. 2006; Myers et al. 2008; Kayo & Oguri 2012). However, clustering measurements at small separation scales ($\lesssim$ 100 kpc), which represent a nodal point for testing the suggested merger-driven activation, are made difficult by the inability to observe simultaneously (i.e. through the same multi-object spectroscopic plate) two objects with angular separations $\lesssim$ 1 arcmin, due to the finite sizes of the optical fibers carrying the

optical signal of each individual object (see Section 3.1). In absence of multiple observations of the same sky region, techniques other than spectroscopic surveys are to be followed (see Section 3.3) in the search of QSO associations (typically pairs), requiring spectroscopic follow-ups.

A number of close QSO pairs were discovered in the search for gravitational lensed quasars and subsequently identified as being physical QSO pairs (e.g. Kochanek, Falco, & Muñoz 1999; Oguri et al. 2006; Hennawi et al. 2006). Some of them were recovered in an intriguing heterogeneous collection of more than 200 QSO pair candidates with $<$ 1 Mpc separations by Hennawi et al. (2006), also containing a color selection (see Richards et al. 2001, 2004) and numerous pairs from large survey datasets. Despite the expectation that these rare pairs could trace rich overdensities, a detailed study of the environment was not carried out. Most of those QSO pairs ($\sim$ 80 %) are at z $>$ 1 (z_{ave}=1.8) hindering observations of their environment. The main result from these pairs is that QSOs appear to be more clustered ($\sim$ 10 times) on small scales ($\lesssim$ 50 kpc) compared to the power-law extrapolation of clustering measurement the larger scale (Mpc) by Porciani, Magliocchetti, & Norberg (2004). Other searches in the SDSS footprint (Myers et al. 2007a,b, 2008; Kayo & Oguri 2012) revealed similar systems. In particular, Myers et al. (2008), on the basis of a more complete and homogeneous sample of SDSS color-selected (see Richards et al. 2004) binary QSOs at limited angular separations, independently corroborated the evidence of the QSO clustering excess on small scales. ($\sim$ 25 h^{-1} kpc), but with smoother results than Hennawi et al. (2006). Similar outputs were found by Kayo & Oguri (2012). A number of high redshift QSO pairs have also been discovered (e.g. Hennawi et al. 2010).

The excess of QSO pairs at tens kpc scale has been interpreted as a signature of galaxy interactions triggering gas inflows toward the nuclear region, responsible for the intense accretion activity in both the nuclei of the interacting components (Djorgovski 1991; Kochanek, Falco, & Muñoz 1999; Myers et al. 2008). It was also suggested that close pairs are tracers of regions with small-scale galaxy overdensities excess, where mergers will be more likely to occur (Hopkins et al. 2008). One might expect different redshift evolution in small-scale quasar clustering if it is due to a gas-driven effect rather than being due to the enhanced bias of the dark matter environments. Further, some merger-driven models predict stronger small-scale clustering for quasars than for lower luminosity AGNs due to their different fueling mechanisms (e.g. Hopkins et al. 2008).

The fraction of QSO pairs (or binary QSOs) at separations of tens to hundreds kpc is $\lesssim$ 0.1 % at $1 \lesssim z \lesssim 5$ (Hennawi et al. 2006; Myers et al. 2008), while the evidence of cases in kpc scale in which both binary QSOs are detected is much smaller. The efficiency of mergers may be greater at higher redshifts, where the observation of close QSOs is more difficult, while at low-redshift mergers should be less likely to occur (Hopkins et al. 2008).

The environment of QSO pairs has been probed in detail only for a few systems. Circumstantial study has been reported by Boris et al. (2007) who investigated the environment of 4 QSO pairs at z $\sim$ 1 with separations $\gtrsim$ 1 Mpc. They found one pair in a particularly high-density region, some evidences for galaxy cluster in the proximity

of another two, while one pair appears isolated. On this basis and following Djorgovski et al. (1999), QSO pairs has been claimed as a method for tracing clusters. A first systematic study of the QSO environment was presented by Farina, Falomo, & Treves (2011) on six low redshift physical QSO pairs extracted from the SDSS DR7 dataset. They reported one case of pair in a moderately rich group of galaxies together with dynamical evidence of additional mass around some pairs to make them bound systems. Green et al. (2011) search for X-ray signatures of galaxy clusters and hot inter cluster medium associated with a host group or cluster for 7 close ($R_{\perp} < 25\ h^{-1}$ kpc) QSO pairs. From their near-IR images they are unable to detect the emission from the host galaxies, or signature of mergers and/or disturbed morphology and set stringent limits to the galaxy environments. Within these limits, they found no evidence that these pairs inhabit significant galaxy overdensities.

At high redshift (z $\sim$ 4) a QSO pair was found by Fukugita et al. (2004) in no enhanced galaxy density. Rare examples of QSO association with more than two objects have been observed (Djorgovski et al. 2007; Farina et al. 2013) but the limited number makes a statistical analysis impossible.

2.3. This work

To explore the QSO phenomenon and systematically investigate the environment of close QSO pairs, an observing program was planned, starting in 2012 and still ongoing. This is a part of a more comprehensive program developed in collaboration with the Astronomical Observatory of Padova (Italy) and the Finnish Centre for Astronomy at University of Turku (Finland), aiming to explore the QSO properties and environment.

As regards this work on the QSO pairs, we searched for observation QSO pairs drawn from the whole database of known QSOs and selected from those having readily examinable spectra from SDSS,the 2dF QSO Redshift Survey (2QZ Croom et al. 2004b), and 2-degree Field (2dF) SDSS Luminous Red Galaxies and QSO survey (2dF-SDSS LRG and QSO, 2SLAQ, Croom et al. 2009). public releases (Chapter 3).

As the first step, a spectroscopic and imaging study of a representative sample of 14 low redshift (z < 0.85) QSO pairs derived from SDSS datasets was performed. We have aimed to investigate nucleus and host properties and study the neighborhood galaxies in a field of 1 Mpc around the QSOs. We are able to compare these features to those of isolated QSOs with similar redshift and luminosity (Chapter 4). We want to probe if these objects share any characteristics among them with respect the QSOs which are not in pairs and to investigate whether the QSO pairs need to inhabit a large structure or if they are isolated systems. The spectra allow us to accurately evaluate the velocity difference ΔV_r and to obtain a probe of the relative velocity of the two galaxies through careful measures of the forbidden [OIII]λ5007 transition, since it is not affected by the peculiar dynamics of the broad line region. Assuming that the QSO pairs are bound systems, we can derive the minimum total mass of the dynamical system to which each pair belongs, and we can compare it with the masses of the pair host galaxies. The analysis of the distribution of galaxies in the field of the QSO pair is compared with that in the background in the same frames to study the galaxy environment, its richness and

distribution. In addition, the image observations could also allow us to derive a direct estimate of the masses of the host galaxies of the QSOs.

The ongoing programs are described in Chapter 5

Finally, Chapter 6 summarises the progress in the program of my work related to the photometry of blazars and their variability. In the Part III I attach my published papers.

3. Search for quasar pairs

In this chapter we present our search for QSO pairs. We describe the procedure adopted and how we select high significance physical pairs.

In this Thesis we assume a concordant cosmology with $H_0 = 70\ km\ s^{-1}\ Mpc^{-1}$, $\Omega_m = 0.30$ and $\Omega_\Lambda = 0.70$.

3.1. Large-survey spectroscopic archival selection

Different methods can be used to search for QSO pairs, which are described below and in Chapter 5. We perform a selection based on large-survey datasets.

Great help in compiling QSO pair catalogues is provided by from the SDSS archives, which since 2000 have been using a dedicated 2.5 m telescope at the Apache Point Observatory site in New Mexico. Subsequent to two founding phases termed SDSS-I and II, SDSS-III phase has now been operating since 2008, engaged in 4 different surveys. Several data releases have been distributed over the years. They are cumulative, so all previously-released images, spectra, and measurements are still available. The Baryon Oscillation Spectroscopic Survey (BOSS),which was begun with SDSS-III, is complementing previous programs in mapping the Universe on the largest scales, in order to create a three-dimensional map of galaxies and quasars.

Over the years SDSS has carried out deep multi-color images for objects in a large part of the sky ($\sim$ 15,000 square degrees), obtained in 5 broad photometric bands[1] u, g, r, i, and z, peaking at wavelengths 3551, 4686, 6166, 7480, and 8932 Å, respectively (Fukugita et al. 1996). The automated pipeline leads to astrometric accuracy better than about 0.1. The spectroscopic targets are chosen on the basis of the imaging data, including candidate quasars selected based on colors (Richards et al. 2002). Spectroscopy, performed through multi-object fiber spectrographs, covers a spectral range between 3800-9200 Å (SDSS-I and II) and 3600-10400 Å (BOSS), with a resolution R from $\sim$ 1400 up to 2600. All the SDSS images, spectra and data are publicly available.

The latest Data Release 10 (DR10, Ahn et al. 2014) contains more that 300,000 optical quasar spectra. Spectroscopically confirmed QSOs are collected in Schneider et al. (2010) and Pâris et al. (2014) catalogues ($\sim$ 105,000 and $\sim$170,000 [2], respectively).

Note that the spectroscopic surveys can efficiently cover a large sky area and simultaneously obtain redshifts for a large set of targeted galaxies. In multi-object spectroscopy, telescopes are equipped with fiber-fed spectrographs. A fiber-plug aluminum plate, individually drilled for each field, is mounted at the telescope focus when it is changed from

[1] https://www.sdss3.org/dr9/imaging/imaging_basics.php

[2] We note that Pâris et al. (2014) catalogue also includes previously known quasars (mostly from SDSS-I and II) that were re-observed by BOSS

imaging to spectroscopic mode. The finite size of the fiber plugs prevents two fibers from being placed too close to one another. Consequently, only one quasar (or any other object from a photometric catalogue) in a close pair with separation $< \alpha_{fiber}$ can be be assigned to a fiber and be spectroscopically observed in a given plate. A significant fraction of targeted objects cannot obtain measured spectroscopic redshifts, unless that portion of sky is re-observed with a new plate. This well-known problem is termed as fiber collision.

One way to obtain QSO pairs is to autocorrelate the same survey information and cross-correlate data coming from a number ofsurveys, when they overlap in some regions of the sky, to increase the number of detections in spite of the fiber collision. This is the case of SDSS, 2dF QSO Redshift Survey (2QZ, Croom et al. 2004b, with included bright 6dF QSO Redshift Survey, 6QZ), and 2-degree Field (2dF) SDSS Luminous Red Galaxies and QSO survey (2dF-SDSS LRG and QSO, 2SLAQ, Croom et al. 2009). More than 25,000 QSO have been observed during the 2QZ survey with the Anglo-Australian Telescope using the 2-degree Field multi-object spectrographic system. The 2SLAQ catalogue contains $\sim$ 11,000 QSOs selected from SDSS photometry and spectroscopically confirmed with the 2dF spectrograph. For the 2dF Quasar Redshift Survey (2QZ Croom et al. 2004) $\alpha_{fiber} = 30$", while for the SDSS spectroscopic survey $\alpha_{fiber} = 55$".

Our selection procedure starts from the coordinates of the objects acquired from one or more quasar catalogues. Redshifts are drawn from spectroscopic catalogues or directly measured using narrow emissions when they appear in the spectral window and lines are scarcely affected by noise. We correlate these information to find the QSO projected separations $R_\perp$ and the differences in radial velocities $\Delta V_\parallel$ between each pair coupled from QSO catalogues and to compile a catalogue of QSO pairs, as fully described in Section 3.2. We also evaluate the excess of QSO pairs with respect the random distribution of the redshifts in each bin of $R_\perp$ and $\Delta V_\parallel$. This allows us to estimate the fraction of observed pairs with respect to the chance superpositions (see Section 3.2.2) and trace in the $R_\perp - \Delta V_\parallel$ plane the locus where physical pairs, i.e. bound systems belonging to the same cosmological structure, are more likely to be found.

This method is adopted in the works illustrated in this thesis for searching and selecting QSO pairs suitable to be gravitationally bound candidates. It is also effective in the search for projected pairs, in which QSOs are at small angular distance but at different redshifts.

3.2. Our search

A QSO pair is selected on the basis of two physical quantities, the projected separation $R_\perp$ between the members and the difference of their radial velocities $\Delta V_\parallel$, which are calculated from the coordinates of the objects and the redshifts.

As numerical examples, we report in brackets the results obtained after each selection step in building up two catalogues:

1. starting from the SDSS QSO dataset of spectroscopic confirmed QSOs and searching for pairs at z$<$ 0.85;

2. using the overlapping SDSS, 2QZ, 6QZ and SLAQ surveys together and to search for QSO pairs at all the redshifts.

3.2.1. Selection

We start from the total number N_{tot} of spectroscopic QSOs from all the available quasar catalogues. We draw them from the The Million Quasars (MILLIQUAS[3]) Catalogue, Version 3.8, by Flesch, E., updated to 16 February 2014. The Million Quasars is a collection of all type I QSOs, AGNe, and BL Lacs in the literature, where completeness is full or nearly so. Each object is shown as one entry with the sky coordinates, its name, red and blue optical magnitudes, PSF class, redshift, and the source catalogue for its name and redshift, plus a radio and/or X−ray identifier where applicable. The N_{tot} recovered in the MILLIQUAS catalogue , Version 3.8, is 304,931.

First of all, to make a better choice in terms of $\Delta V_{\parallel}$, we replace the redshifts in the Million Quasars, that are rounded to the third decimal, with those reported in the catalogues of spectroscopically confirmed QSOs, where they are given by the spectroscopic pipeline with a higher accuracy when possible. To better determine the radial velocities and differences see Section 4.2.2.

We fix the redshift upper limit z_{up} within which we want to search for QSO pairs (e.g. 53,271 are the spectroscopic QSOs found in the MILLLIQUAS catalogue up to z_{up}=0.85 out of the total number of 304,931). We select the source catalogues to obtain QSOs and redshifts from one or more public releases with web-available spectra , if we are interested in immediately examining the overall spectral features. In this way we find the number N_{obs} of spectroscopic objects with examinable spectra (e.g. at z<0.85 we retrieve 45,687 out of the total 53,271 spectroscopic QSOs in all the SDSS catalogues ; the full number of spectroscopic quasars observed by the SDSS at all the redshifts is 262,888 out of the total number of 304,931 spectroscopic QSOs in MILLIQUAS catalogue; 288,440 out of 304,931 are the spectroscopic QSOs with available spectra at every z found from the SDSS+2SLAQ+2QZ surveys).

1. We assign a sequential number to each object among the N_{obs} spectroscopic quasars. This number is associated with the corresponding row in the starting catalogue.

2. We fix the maximum angular separation $\Delta\theta_{max}$ from two QSOs in a pair, corresponding to the maximum QSO projected separation (e.g. 2000 kpc) at the lower z at which we want to look for pairs.

3. For each object, the angular distance $\Delta\theta$ from each other is computed as if both were at the redshift of the foreground quasar. When the pair angular distance is $\Delta\theta < \Delta\theta_{max}$, we select the two objects and record the associated indices and their $\Delta\theta$.

4. We remove the repetitions.

5. We create a file with each row containing the information about each pair and the angular separation between its members.

[3] `http://quasars.org/milliquas.htm`

6. The projected separations $R_\perp$ are evaluated at the minimum z between the two quasars. Note that $R_\perp$ differs significantly from the real projected distance for two objects away from each other along the line of sight (i.e. with high Δz between the two QSOs). The smaller Δz better $R_\perp$ approaches the real QSO separation.

7. We compute the difference inradial velocities $\Delta V_\parallel$ relative to the foreground QSO in the pair. The redshift $z_{A,B}$ of an object, that we observe at redshift z_B, relative to an observer located redshift $z_A < z_B$ for us, is given [4] by

$$1 + z_{A,B} = \frac{1 + z_B}{1 + z_A} \tag{3.7}$$

Consequently, $\Delta V_\parallel$ is evaluated as

$$\Delta V_\parallel = \frac{c\ \Delta z}{(1 + z_A)} \tag{3.8}$$

where $\Delta z = z_B - z_A$. We compute $\Delta V_\parallel$ for all the pairs previously selected or for a subset of pairs under a fixed separation, imposing one or more $R_\perp$ upper limits $R_{\perp,limit}$ (e.g. $R_{\perp,limit} = 600$, 1000, 1500, 2000 km/s) especially if we are interested in obtaining information about physically bound pairs. We can select the pairs to be observed in terms of $\Delta V_\parallel$, fixing a difference of radial velocities upper limit

[4] The low-redshift we measure for a distant source is directly related to the scale factor of the Universe at the time the photons were emitted from the source. Starting from the Robertson-Walker metric

$$ds^2 = (cdt)^2 - a^2(t)\left[\frac{dr^2}{1 - kr^2} + r^2\left(d\theta^2 + sin^2\theta d\phi^2\right)\right] \tag{3.1}$$

and exploiting that the light propagates along the null geodetic ($ds = 0$), for an observer on the Earth ($r = 0$) we can chose a null-radial geodetic ($d\theta = 0$ and $d\phi = 0$) The eq. 3.1 results

$$\frac{cdt}{a(t)} = \pm\frac{dr}{(1 - kr^2)^{\frac{1}{2}}} \tag{3.2}$$

If a light wave crest is emitted at the time t_e and $t_e + \Delta t_e$ is the emission time of the next and we observe them at t_o and $t_o + \Delta t_o$, these times satisfy the equations (in an expanding Universe)

$$\int_{t_e}^{t_o} \frac{dt}{a(t)} = -\frac{1}{c}\int_{r_e}^{0} \frac{dr}{(1 - kr^2)^{\frac{1}{2}}} \tag{3.3}$$

$$\int_{t_e+\Delta t_e}^{t_o+\Delta t_o} \frac{dt}{a(t)} = -\frac{1}{c}\int_{r_e}^{0} \frac{dr}{(1 - kr^2)^{\frac{1}{2}}} \tag{3.4}$$

Any change in $a(t)$ during the time intervals Δt_e and Δt_o between successive wave crests can be safely ignored, so eqs. 3.3 and 3.4 reduce to

$$\frac{\Delta t_o}{\Delta t_e} = \frac{a(t_o)}{a(t_e)} \tag{3.5}$$

The emitted and received wave periods Δt_e and Δt_o are inversely proportional to λ_e/c and λ_o/c, so that

$$\frac{\lambda_o}{\lambda_e} = 1 + z = \frac{a(t_o)}{a(t_e)} \tag{3.6}$$

from which we immediately derive the eq. 3.7, stated that $\Delta v = c\Delta z$.

$\Delta V_{\parallel,limit}$ (e.g. in this way we find 27 QSO spectroscopic pairs with $R_\perp < 600$ kpc and $\Delta V_\parallel < 600$ $km\ s^{-1}$ in the SDSS datasets, and 174 from SDSS+2SLAQ+2QZ surveys at all redshifts)

8. The indices associated with the coupled quasar allow us to draw up a catalogue with the list of pairs and information about the pair and the single objects.

3.2.2. Random Test

The Random Test evaluates the fraction $\xi = N_{obs}/N_{exp}$ of observed pairs out of those due to chance superpositions, as a function of the projected QSO separation $R_\perp$. To do that we create a random catalogue of as many points as the objects at z< z_{up} in the spectroscopic catalogue(s) and determine the number of expected random pairs by Monte Carlo sampling.

In detail, we evaluate $\xi_j = N_{obs(j)}/N_{exp(j)}$ in the j^{th} projected separation bin $(R_{\perp(j)} - \Delta R_\perp/2, R_{\perp(j)} + \Delta R_{\perp(j)}/2)$ by applying the redshift permutation method (e.g. Zhdanov & Surdej 2001). It consists of keeping the positions of the N_{obs} quasars fixed, while randomly permuting the redshifts.

9. A vector of random numbers in [0,1] with the same dimension of the number of the objects at z< z_{up} is created and associated to each object redshift (to each object index). When we sort the random numbers, the z are permuted. We applied a sequence of N_i (e.g. N_i= 10,000) permutations.

10. We construct N_i catalogues, each of which contains the numbers of quasar associations $N_{random(i,j)}$ coupled after each permutation i following the recipes 1-7 and falling in the j^{th} projected separation bin under the $\Delta V_\parallel, limit$.

11. The number of the expected chance superpositions $N_{exp(j)}$ for the QSO population in the j^{th} projected separation bin is evaluated by averaging $N_{random(i,j)}$ over the N_i catalogues.

12. The distribution of ξ_j vs $R_{\perp(j)}$ is plotted,where possible after its evaluation at different $\Delta V_{\parallel,limit}$.

For example, we plot in Figure 3.1 the ξ-distributions for QSO pairs at z<1.5 from all the public releases. It is apparent that ξ rapidly increases toward small $R_\perp$ and small $\Delta V_\parallel$, defining the region in $R_\perp - \Delta V_\parallel$ plane where pairs are more likely to be physical. We start choosing pairs for which at least is ξ= 6 (i.e. every 6 pairs less than one is false) under each $\Delta V_{\parallel,limit}$.

Then we evaluated the probability of a pair to be physical in each bin of $R_\perp$ and $\Delta V_\parallel$ conditioned to the increasing probability to be physical if it belong to the bins closer to the plane axes (up to only 1 chance superposition every 23 pair observed if $\Delta V_\parallel \lesssim$ 300 km/s and $R_\perp \lesssim$ 120 kpc, corresponding to the probability of 96 % to be a physical candidate). In order to ensure a reliable population of bound pairs, the final sample has been selected so that at least $\sim$ 80 % of selected pairs are physical candidates.

Our criterion on $\Delta V_{\parallel}$ more stringent then that adopted by Hennawi et al. (2006) and Kayo & Oguri (2012) for defining binary quasars (they use $\Delta V_{\parallel} < 2000$) km/s, and we discharges many pairs in comparison.

In Figure 3.2 the selected QSO pairs from all the SDSS released, 2QZ and 2SLQ catalogues and at all the redshifts are represented in the $R_{\perp}$ - $\Delta V_{\parallel}$ plane. Table 3.2 lists our 249 physical QSO pairs candidates located at $0.236 < z < 3.874$. Redshift distribution is shown in Figure 3.5 and in Table 3.1. We are going to draw from this list for the QSO pairs candidates suitable for investigation in the following chapters.

We complemented the Table 3.2 with 8 close QSO pairs selected by color selection and lensing search (see Hennawi et al. 2006; Myers et al. 2008, and Section 3.3) and confirmed to be binary QSOs (see also Inada et al. 2012). These are at redshift $\lesssim 1$ and represent very interesting sources for both investigating morphology and mutual interactions and probing the galaxy environments. They will be object of a preliminary study in Chapter 5.

3.3. Other ways to find QSO pairs

Good confidence QSO pairs have been found in some previous works using the color selection and recovering as binary QSOs a number of pairs found in the lensed quasar search. We summarize these methods in this Section.

3.3.1. Photometrical selections

Richards et al. (2001) showed that quasars follow a relatively tight color-redshift relation in the SDSS filter system. This property has been exploited to calculate photometric redshifts of quasars (e.g. Budavári et al. 2001) based on an empirical method of the nearest known-redshift neighbor search in the color space. Based on this principle, it is possible to efficiently select pairs of QSOs at the same redshift by searching for pairs of objects with similar, quasar-like colors. Hennawi et al. (2006) described such an algorithm based on the maximum likelihood that two astronomical objects, within a certain angular projected distance annulus in the sky, have the same color in the SDSS quasar-color locus.

Using SDSS photometry QSOs can be photometrically found with high efficiency and completeness by targeting the four dimensional SDSS color space regions dominated by quasars (or with low levels of contamination). A probability density function of being a QSO (kernel density estimation, KDE) was constructed up by Richards et al. (2004), using as a training set the spectroscopically classified QSOs in the Schneider et al. (2003) catalogue. Aiming to select the largest number of QSO pairs taking into account the scatters in the QSO color-redshift relation (similarity may be optimal in detecting lenses), Myers et al. (2008) successfully selected a number of close QSO pairs among the luminous, ultraviolet excess and close-separation ($3" < \theta < 6"$) photometrically selected QSOs, but applying relaxed relative colors criteria between the QSO components

In both such approaches, the QSO pair candidates without available spectra are to be considered for follow-up spectroscopic observations.

3.3.2. Lens selection

For small-separation pairs, characteristic of the majority of gravitational lenses, a number of binary quasars were discovered in the SDSS Quasar Lens Search (SQLS, Inada et al. 2012; Oguri et al. 2012, and references therein) for gravitationally lensed quasars. SQLS is based on two selection algorithms running on the spectroscopically confirmed SDSS quasars. For $\Delta\theta < 3$", the photometric pipeline cannot deblend the two components. The two objects are classified as a single extended one, but poorly fitted by the local point spread function (PSF). The morphological selection is aimed to detect such close QSOs and exclude objects which have large flux differences. The color selection algorithm is applied to deblended components (1"$< \Delta\theta <$ 20") by comparing the colors between spectroscopically confirmed quasars and candidate companions and with similar i-optical flux. Candidates with $\Delta\theta$ larger than the Faint Images of the Radio Sky at Twenty centimeters survey (FIRST, Becker et al. 1995) resolution (6") are rejected if they show an inconsistent optical/radio flux ratio between the two components (Kochanek, Falco, & Muñoz 1999). The lens candidates are then observed in optical and near-infrared imaging and optical spectroscopy to check whether they are true gravitational lens systems or not.

Table 3.1.: Physical QSO pairs number and absolute magnitude distributions on redshift

z	No.	M_{ave}(r) [mag]	$M_{ave}(i)$ [mag]
(a)	(b)	(c)	(d)
$0< z \leqslant 0.5$	5	-22.07 ± 0.22	-22.24 ± 0.22
$0< z \leqslant 0.85$	34	-22.67 ± 0.11	-22.84 ± 0.11
$0< z \leqslant 1$	51	-22.96 ± 0.11	-23.14 ± 0.11
$1< z \leqslant 2$	65	-23.72 ± 0.61	-23.90 ± 0.61
$2< z \leqslant 3$	124	-24.43 ± 0.32	-24.62 ± 0.32
$3< z \leqslant 4$	10	-25.61 ± 0.27	-24.78 ± 0.27
$0 < z \leqslant 4$	249	-24.02 ± 0.23	-24.19 ± 0.23

Notes: (a) Redshift range. (b) Number of selected physical QSO pair candidates from our selection. (c) and (d) Mean absolute r and i magnitudes.

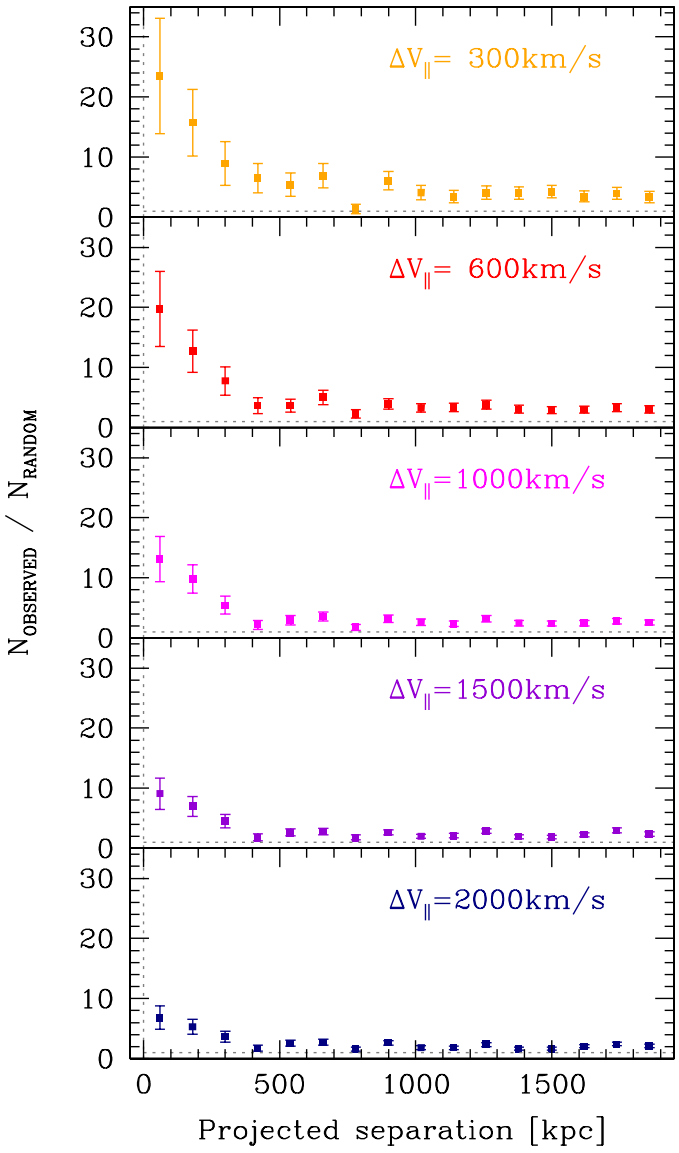

Figure 3.1.: Ratio between number of observed QSO pairs at z< 1.5 and that of chance superpositions, obtained randomly permuting the redshifts, as a function of the projected separation between the QSOs. Different difference of radial velocities thresholds have been considered.

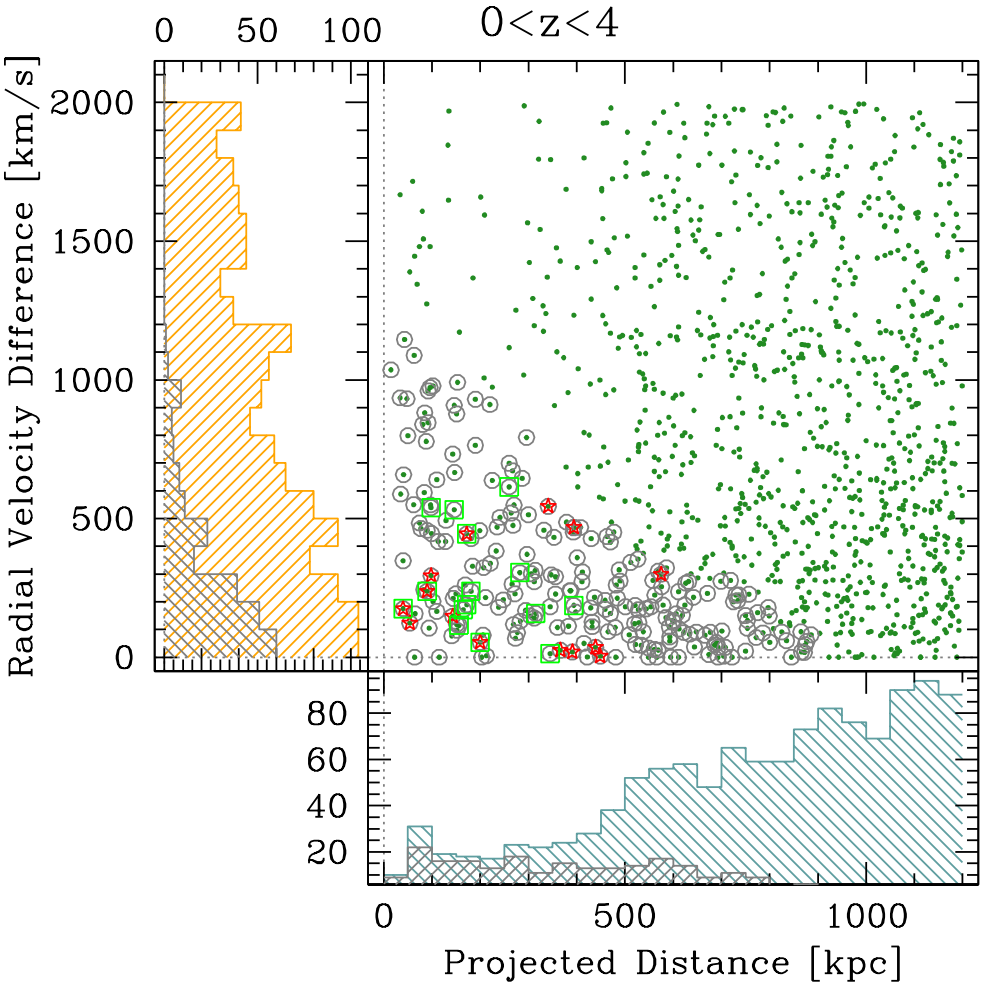

Figure 3.2.: QSO pairs from SDSS DR 3-10, 2QZ and 2SLQ catalogues in the $R_\perp - \Delta V_\parallel$ plane (green points). QSO pairs span to 0.236 to 3.874. The fiber collision effect is apparent for the pairs with $R_\perp$ <500 kpc. Note that for $R_\perp \lesssim 500$ kpc and $\Delta V_\parallel \gtrsim 600$ km/s the QSO pair density is particularly low. Physical pairs candidates in our selection are marked by grey circles and their $\Delta V_\parallel$ and $R_\perp$ distributions are represented by the grey histograms. Yellow and light blue histograms illustrate the distribution of QSO pairs with $\Delta V_\parallel <$ 2000 km/s and $R_\perp < 1200$ kpc. Red stars are the QSO pairs studied in Chapter 4 and the green squares those observed by NOT (see Chapter 5).

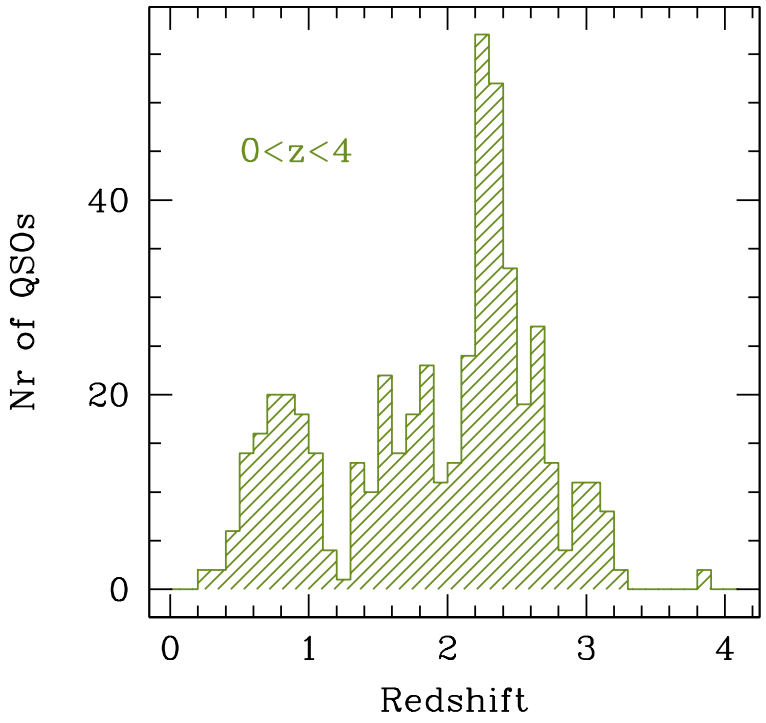

Figure 3.3.: Redshifts distribution of physical QSO pairs listed in Table 3.2.

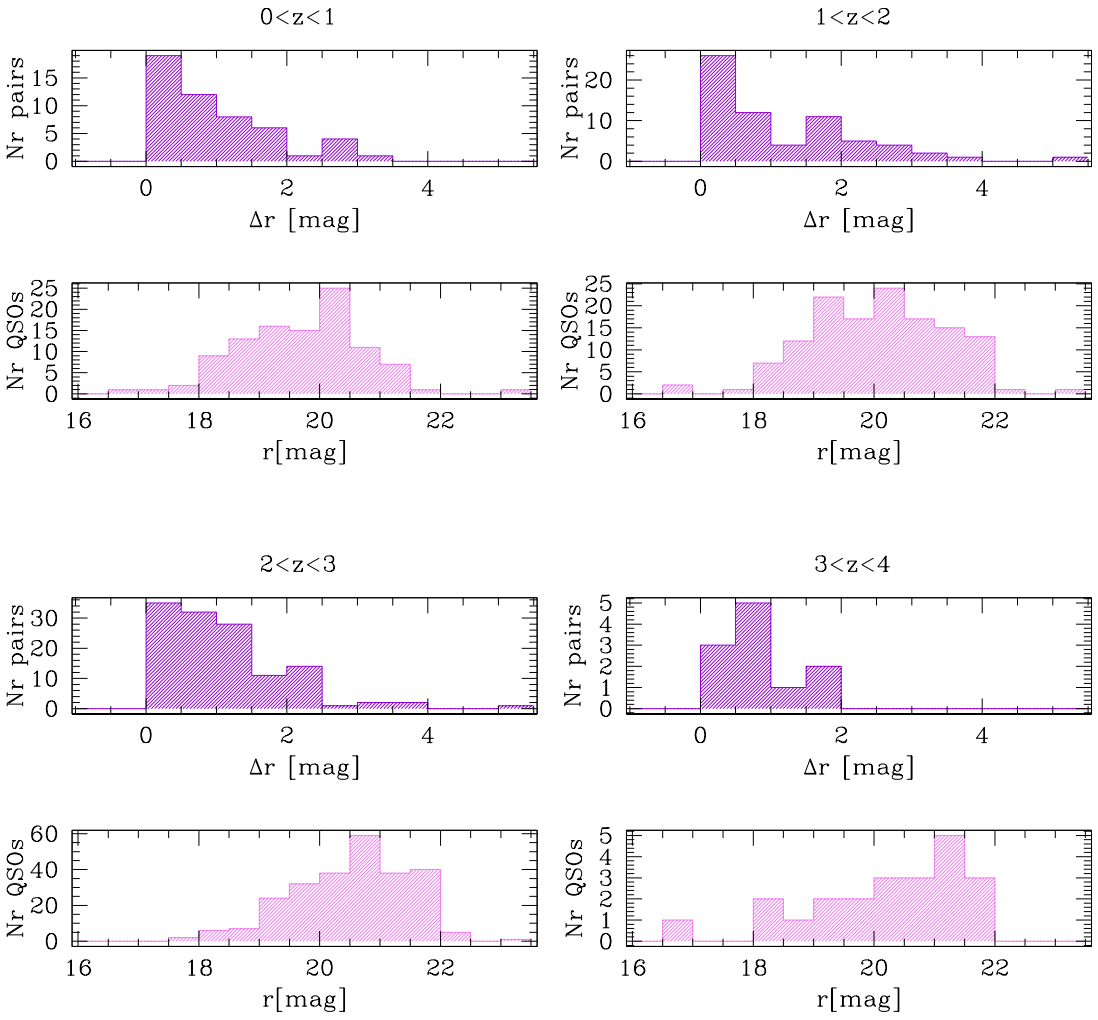

Figure 3.4.: SDSS r apparent magnitude distributions of selected physical QSO pair candidates in different ranges of redshift (pink histograms) and difference of r magnitude between the two companion QSOs (violet histograms).

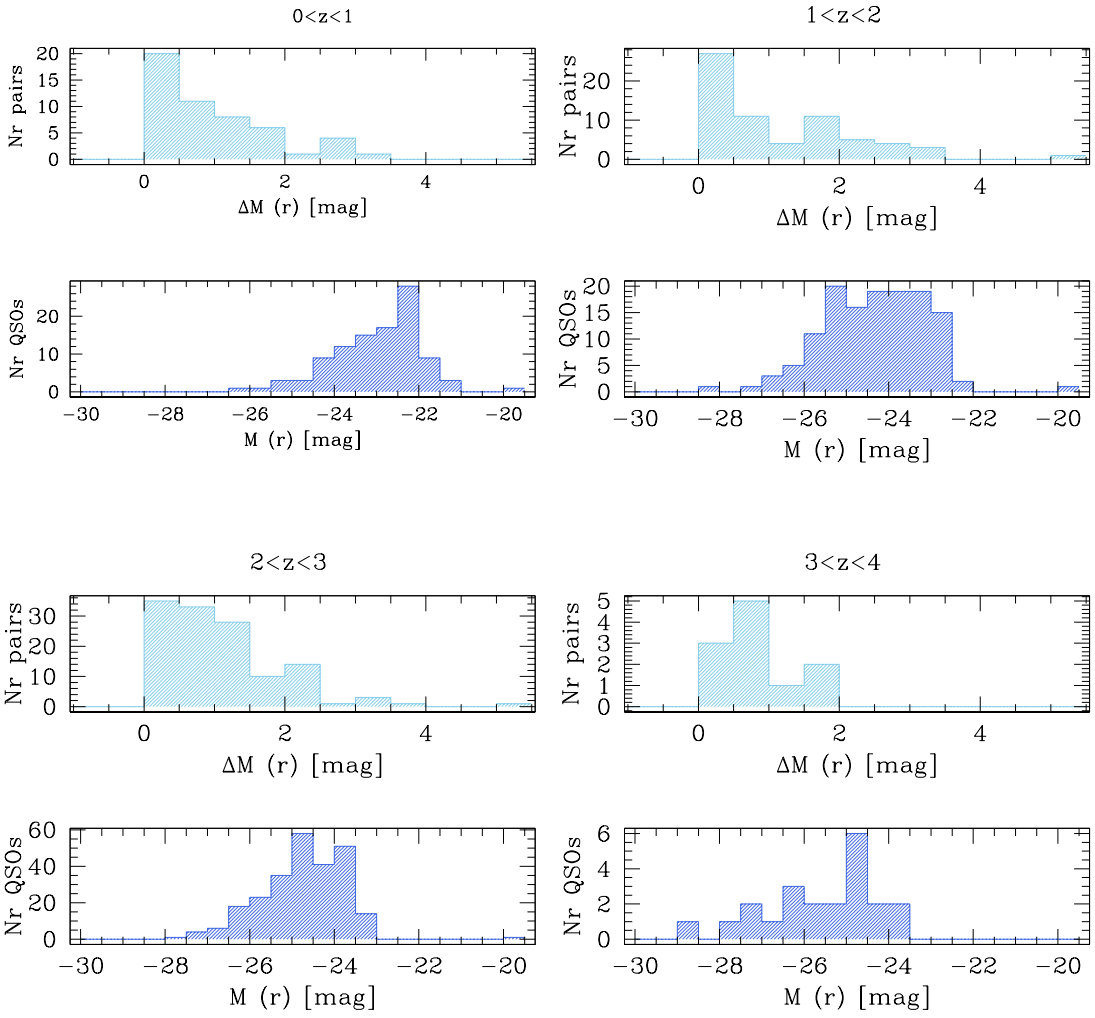

Figure 3.5.: SDSS r absolute magnitude distributions of selected physical QSO pair candidates in different ranges of redshift (blue histograms) and difference of r magnitude between the two companion QSOs (light blue histograms)

Table 3.2.: Physical QSO pairs candidates extracted from SDSS, 2QZ (6QZ), 2SLAQ surveys.

Notes: The eight physical close QSO pairs at $z < 1$ found in the search of lensed QSOs (see Chapter 5 for selection) are also included. (a) and (d) QSO names. (b) and (e) Redshifts from catalogues except for the objects studied in Chapter 4 for which redshift comes from [OIII] line positions. (c) and (f) SDSS r-band apparent magnitude of the QSO A and B, respectively. (g) Angular separation of the pair. (h) Proper traverse separation. (i) Radial velocity difference. (j) (A) (B) : QSO A (QSO B) is not present in the SDSS footprint and the listed magnitudes ($\sim$ 6500 Å) are drawn from The Million Quasar catalogue, see there for references. (L): QSO pair studied in Chapter 4; their redshift, and quantities derived, are evaluated from the [OIII] forbidden emission line, see Section 4.2.2. (R:) QSOs of NOT sample, see Chapter 5, (C): close physical QSO pairs from lensing search, redshifts are derived from [OIII] for sources with SDSS spectra, otherwise see notes to Table 5.2 for references.

QSO A	z_A	r(A) [mag]	QSO B	z_B	r (B) [mag]	$\Delta\theta$ [arcsec]	$R_\perp$ [kpc]	$\Delta V_\parallel$ [$km\ s^{-1}$]	Comm.
(a)	(b)	(c)	(d)	(e)	(f)	(g)	(h)	(i)	(j)
SDSS J001103.18+005927.2	0.4859	20.02	SDSS J001103.48+010032.6	0.4860	20.91	65.2	391	20 ± 57.	L
SDSS J001743.07+050327.3	2.7735	20.26	SDSS J001744.13+050334.8	2.7725	21.18	17.9	141	77 ± 50.	
SDSS J002038.81−030756.8	2.2218	20.81	SDSS J002039.59−030722.6	2.2200	20.69	35.6	294	169 ± 99.	
SDSS J002329.90+080655.2	2.3430	19.400	SDSS J002334.52+080708.5	2.3395	17.50	69.5	569	310 ± 99	
SDSS J002529.53+001321.0	2.0860	20.63	SDSS J002529.79+001339.6	2.0850	20.49	18.2	152	97 ± 72.	
2QZ J002829.6−321045	1.8080	20.30	2QZ J002832.8−321031	1.8070	21.90	42.7	360	107 ± 30.	AB
SDSS J003100.80+002331.6	2.5500	21.16	SDSS J003101.50+002331.3	2.5430	20.12	10.5	84	594 ± 71.	
2SLAQJ003743.89−001820.6	1.7860	21.67	2SLAQJ003745.42−001825.6	1.7830	20.95	24.5	207	323 ± 30.	
2SLAQJ003843.97−000129.9	0.8610	20.29	2SLAQJ003848.41−000014.5	0.8600	21.05	100.9	775	161 ± 45.	
2SLAQJ 06.39−001728.3	1.3080	20.29	SDSS J004307.24−001759.1	1.3090	20.59	33.8	283	130 ± 36.	
SDSS J004352.71+042426.4	2.4450	21.82	SDSS J004352.88+042427.5	2.4569	21.82	1.8	15	1036 ± 54.	
SDSS J005124.78−003848.3	2.1910	20.59	SDSS J005125.10−003823.7	2.1910	21.99	25.7	213	5 ± 120	
2SLAQJ005304.00+000531.6	1.7370	21.88	SDSS J005304.81+000537.2	1.7332	20.46	13.4	113	417 ± 31.	
SDSS J005636.92+011454.1	2.2510	21.21	SDSS J005642.68+011512.6	2.2480	21.45	87.3	719	277 ± 89.	
SDSS J010021.03+195325.3	2.5711	21.66	SDSS J010023.10+195426.7	2.5690	21.28	67.8	544	174 ± 192	
SDSS J010157.55+235903.4	2.2176	19.86	SDSS J010202.46+235902.3	2.2156	20.98	67.2	554	182 ± 67.	
SDSS J010312.19+032635.0	2.2680	20.28	SDSS J010315.30+032705.2	2.2690	19.87	56.5	465	92 ± 23.	
SDSS J010350.72−000117.3	1.9519	19.71	2SLAQJ010351.33−000214.0	1.9540	21.89	57.7	484	213 ± 28.	

– *Continued on next page*

– *Continued*

QSO A	z_A	r(A) [mag]	QSO B	z_B	r (B) [mag]	$\Delta\theta$ [arcsec]	$R_\perp$ [kpc]	$\Delta V_\parallel$ [$km\ s^{-1}$]	Comm.
(a)	(b)	(c)	(d)	(e)	(f)	(g)	(h)	(i)	(j)
SDSS J010856.36−002741.1	2.6998	21.53	SDSS J010859.56−002718.3	2.6998	20.93	53.2	422	1 ± 53.	
2QZ J011140.4−275820	1.3420	19.60	2QZ J011142.3−275928	1.3410	21.30	71.6	601	128 ± 36.	AB
SDSS J011445.89+201220.3	2.2788	20.69	SDSS J011448.79+201210.6	2.2768	21.29	42.0	345	182 ± 76.	
SDSS J011757.99+002104.1	0.6122	20.17	SDSS J011758.83+002021.4	0.6130	18.34	45.1	304	149 ± 52.	
SDSS J012109.83+153507.4	2.5070	19.11	SDSS J012112.73+153540.0	2.5020	19.80	53.3	430	428 ± 54.	
SDSS J012230.94+052655.6	1.8760	20.81	SDSS J012236.64+052706.3	1.8760	18.15	85.8	722	0 ± 110	
SDSS J012523.04+151007.3	3.1793	21.01	SDSS J012527.82+151052.0	3.1830	20.94	82.8	626	267 ± 56.	
2QZ J013531.0−302217	1.6840	20.40	2QZ J013531.4−302131	1.6830	20.20	45.3	383	112 ± 31.	AB
SDSS J013654.33−003415.4	2.7243	19.00	SDSS J013655.29−003438.1	2.7270	20.12	26.7	211	215 ± 44.	
SDSS J014400.04−001210.6	1.0282	20.90	SDSS J014400.76−001203.6	1.0348	20.43	12.6	102	978 ± 103	
SDSS J015040.22+091657.0	2.4270	21.66	SDSS J015040.56+091639.9	2.4170	18.85	18.5	151	877 ± 168	
SDSS J015342.79+205453.2	2.3388	20.62	SDSS J015343.06+205454.8	2.3453	21.62	4.3	35	588 ± 142	
SDSS J02017+0032B	2.2970	20.38	SDSS J020143.48+003222.7	2.2983	19.65	18.4	151	118 ± 25.	
SDSS J020646.31+010505.5	2.2750	19.70	SDSS J020646.36+010519.4	2.2750	21.63	14.0	115	0 ± 63.	
SDSS J022025.52+002135.1	2.6905	21.60	SDSS J022027.67+002123.2	2.6847	21.86	33.7	268	475 ± 146	
2SLAQJ022453.00−002404.3	1.6950	21.02	SDSS J022456.97−002336.2	1.6953	20.51	64.8	549	33 ± 31.	
SDSS J022610.98+003504.0	0.4230	19.98	SDSS J022612.41+003402.2	0.4234	19.34	66.0	366	84 ± 59.	L
2SLAQJ023206.77−002854.9	2.0050	20.93	SDSS J023208.68−002944.1	2.0050	20.94	57.5	481	0 ±61.	
SDSS J023921.31+000049.6	2.2901	19.95	SDSS J023921.54+000037.1	2.2879	21.25	12.4	102	201 ± 39.	
SDSS J024314.19−010322.5	1.7720	21.21	SDSS J024315.98−010433.7	1.7740	21.60	76.0	642	216 ± 30.	
SDSS J024511.93−011317.5	2.4622	20.20	SDSS J024512.12−011314.0	2.4730	19.51	4.2	34	935 ±23.	
SDSS J024647.08+043324.9	2.1970	20.78	SDSS J024651.46+043401.2	2.1950	21.70	75.5	624	188 ± 64.	
SDSS J025813.65−000326.4	1.3184	20.00	US 3437	1.3200	18.89	29.6	248	207 ± 36.	
SDSS J035053.04−003200.1	1.9926	19.88	SDSS J035053.29−003114.7	1.9950	19.71	46.1	386	240 ± 28.	
SDSS J073948.77+365414.2	2.3020	21.53	SDSS J073954.14+365531.7	2.3030	20.58	100.6	825	91 ± 93.	
SDSS J074013.42+292645.7	0.978	19.47	J074013.44+292648.3	0.9803	18.27	2.6	20.8	349 ± 155	C
SDSS J074049.10+424036.3	1.6154	18.86	SDSS J074052.52+423935.5	1.6140	18.08	71.6	606	157 ± 26.	
SDSS J074336.85+205512.0	1.5698	20.15	SDSS J074337.28+205437.1	1.5654	19.89	35.4	300	514 ± 33.	
SDSS J074759.02+431805.3	0.5010	19.20	SDSS J074759.65+431811.4	0.5012	19.39	8.9	54	40 ± 56.	L
SDSS J074843.02+361258.7	0.6533	20.25	SDSS J074843.12+361219.4	0.6503	20.28	39.0	270	549 ± 37.	
SDSS J075106.68+334308.9	2.2680	20.69	SDSS J075110.47+334344.3	2.2650	21.46	59.5	490	275 ± 25.	
SDSS J075359.87+360015.7	1.5930	20.81	SDSS J075401.18+355957.9	1.5930	20.89	23.9	203	0 ± 63.	

– *Continued on next page*

– *Continued*

QSO A	z_A	r(A) [mag]	QSO B	z_B	r (B) [mag]	$\Delta\theta$ [arcsec]	$R_\perp$ [kpc]	$\Delta V_\parallel$ [$km\ s^{-1}$]	Comm.
(a)	(b)	(c)	(d)	(e)	(f)	(g)	(h)	(i)	(j)
SDSS J075448.90+533152.5	2.3060	21.16	SDSS J075453.70+533126.2	2.3030	19.14	50.1	411	272 ± 52.	
SDSS J075531.42+284253.8	2.2450	20.83	SDSS J075535.06+284206.6	2.2450	22.11	66.7	549	0 ± 58.	
SDSS J075729.86+154956.3	2.5369	20.99	SDSS J075733.23+155009.8	2.5314	21.01	50.8	408	468 ± 71.	
SDSS J080158.93+460345.2	0.7300	19.88	SDSS J080203.08+460445.9	0.7297	20.36	73.6	534	43 ± 45.	
SDSS J080520.55+121954.8	2.3430	18.55	SDSS J080527.06+122015.7	2.3450	20.96	97.5	797	179 ± 48.	
SDSS J080949.20+312727.3	1.2975	19.40	SDSS J080949.95+312721.2	1.3010	21.01	10.8	90	457 ± 36.	
SDSS J081312.63+541649.8	0.7814	20.08	J081313.10+541646.9	0.7795	17.18	5.0	37.4	327 ± 40	C
SDSS J081345.75+534805.1	0.9390	18.18	SDSS J081347.53+534754.2	0.9454	18.20	19.4	153	991 ± 32.	
SDSS J081411.75+495543.5	2.7066	21.45	SDSS J081411.87+495609.7	2.7056	19.00	26.0	206	80 ± 45.	
SDSS J081607.82+401810.4	2.1950	21.71	SDSS J081613.88+401756.9	2.1970	21.52	70.0	579	188 ± 39.	
SDSS J081801.47+205009.9	0.2350	17.91	SDSS J081808.77+204910.1	0.2350	19.27	118.1	439	0 ± 30	L
SDSS J081812.94+511923.3	2.0983	19.35	SDSS J081816.29+511912.2	2.0990	20.49	32.8	273	68 ± 50.	
SDSS J082002.66+215127.7	2.6050	20.73	SDSS J082005.73+215216.7	2.6056	19.80	65.3	522	46 ± 29.	
SDSS J082252.50+485825.5	2.4230	20.48	SDSS J082255.40+485809.5	2.4200	20.03	32.7	266	263 ± 32.	
SDSS J082439.83+235720.3	0.5356	18.90	SDSS J082440.61+235709.9	0.5365	18.73	15.5	98	176 ± 55.	L
SDSS J082723.97+364202.5	2.3250	21.26	SDSS J082723.92+364250.6	2.3300	20.57	48.0	393	451 ± 29.	
SDSS J082934.10+045649.4	2.1420	19.31	SDSS J082937.42+045750.5	2.1450	20.41	78.4	651	286 ± 68.	
SDSS J083028.06+491909.1	2.6760	21.88	SDSS J083031.59+491907.1	2.6732	20.52	34.3	272	229 ± 80.	
SDSS J083302.42+353626.2	2.3340	21.16	SDSS J083303.32+353559.9	2.3360	19.05	29.2	238	180 ± 54.	
SDSS J084031.21+104706.0	2.9633	20.24	SDSS J084031.24+104858.6	2.9630	19.42	112.0	866	19 ± 47.	
SDSS J084044.55+030810.7	2.4550	20.58	SDSS J084049.25+030927.8	2.4550	18.27	104.3	845	0 ± 56.	
SDSS J084048.97+463137.8	1.3631	19.65	SDSS J084051.77+463126.8	1.3576	19.78	30.9	260	699 ± 89.	
SDSS J084115.30+250025.3	2.2960	19.98	SDSS J084119.87+245935.1	2.2950	20.35	79.0	648	91 ± 25.	
SDSS J084419.91+124528.2	2.5070	19.35	H 0841+1256	2.5050	17.92	65.4	528	171 ± 22.	
SDSS J084541.18+071050.3	0.5373	19.01	SDSS J084541.52+071152.3	0.5363	18.75	62.3	394	195 ± 55.	L
SDSS J084621.72+003950.7	3.0155	18.42	SDSS J084621.71+004025.2	3.0171	16.91	35.0	269	118 ± 32.	
SDSS J085509.28+465733.8	2.1700	21.60	SDSS J085513.34+465843.9	2.1730	19.65	81.6	676	284 ± 80.	
SDSS J085625.63+511137.0	0.5434	18.60	SDSS J085626.71+511117.8	0.5425	19.42	22.5	143	175 ± 54.	L
SDSS J090515.89+164722.8	0.8581	18.43	SDSS J090519.27+164816.4	0.8564	20.18	72.8	558	277 ± 67.	
SDSS J090518.66+522052.8	2.2576	19.84	SDSS J090519.94+522003.0	2.2581	20.24	50.4	415	50 ± 66.	
SDSS J090735.31+520352.5	0.9538	19.07	SDSS J090743.97+520322.6	0.9553	18.85	84.8	671	230 ± 43.	
SDSS J090923.12+000204.0	1.8820	20.18	SDSS J090924.01+000211.0	1.8780	16.67	15.2	128	417 ± 23.	

– *Continued on next page*

– *Continued*

QSO A	z_A	r(A) [mag]	QSO B	z_B	r (B) [mag]	$\Delta\theta$ [arcsec]	$R_\perp$ [kpc]	$\Delta V_\parallel$ [$km\ s^{-1}$]	Comm.
(a)	(b)	(c)	(d)	(e)	(f)	(g)	(h)	(i)	(j)
SDSS J091221.18+051608.7	2.1750	20.54	SDSS J091227.77+051530.9	2.1755	20.26	105.6	874	45 ± 51.	
SDSS J091656.06+022137.6	1.4947	19.86	SDSS J091657.71+022014.8	1.4930	18.97	86.8	734	204 ± 34.	
SDSS J092100.95+184439.1	2.5490	19.37	SDSS J092105.35+184514.5	2.5460	20.55	71.6	576	254 ± 23.	
SDSS J092830.97+052432.3	2.4140	18.48	SDSS J092833.51+052330.5	2.4140	20.12	73.1	595	0 ± 39.	
SDSS J093419.91+331743.9	1.6340	20.10	SDSS J093421.47+331729.3	1.6300	19.24	23.4	199	456 ± 32.	
SDSS J093942.03+391002.4	3.1360	21.17	SDSS J093942.90+390952.6	3.1383	20.84	14.5	110	165 ± 52.	
SDSS J094118.89+422238.3	2.2800	22.04	SDSS J094119.81+422234.8	2.2860	20.96	11.8	97	549 ± 143	
SDSS J094907.04+271142.8	0.9085	20.14	SDSS J094912.84+271218.1	0.9090	20.32	85.3	666	79 ± 44.	
SDSS J095032.10+600505.9	0.5230	20.06	SDSS J095033.27+600348.8	0.5230	19.97	77.4	483	0 ± 55.	
SDSS J095137.01−004752.9	0.6340	20.48	SDSS J095139.39−004828.7	0.6365	20.21	49.9	341	453 ± 45.	L
SDSS J095419.33+322621.3	1.7380	18.53	SDSS J095423.78+322720.1	1.7384	21.31	81.1	686	44 ± 30.	
SDSS J095543.66−012351.5	2.8441	21.38	SDSS J095544.28−012357.5	2.8329	20.90	10.8	85	881 ± 180	
SDSS J095854.71+134726.8	2.3640	18.88	SDSS J095855.22+134728.1	2.3702	19.83	7.5	62	550 ± 49.	
SDSS J095907.65+020820.6	0.3542	19.43	COS− J09591+0207	0.3530	18.97	62.8	312	272 ± 45.	
SDSS J100025.95+442108.5	2.9823	21.07	SDSS J100026.72+442103.6	2.9885	20.58	9.9	77	464 ± 48.	
2QZ J101909.9+004225	0.9810	19.74	SDSS J101915.07+004211.1	0.9820	21.27	77.8	619	151 ± 42.	
SDSS J102442.69+094326.3	1.0138	18.93	SDSS J102443.40+094340.2	1.0093	19.34	18.3	147	666 ± 30.	
2SLAQJ103437.21−000639.9	1.8750	20.21	2SLAQJ103439.32−000659.6	1.8780	21.95	37.3	314	313 ± 29.	
SDSS J103455.52+641745.1	1.1575	19.27	SDSS J103505.53+641805.1	1.1573	19.83	68.1	561	28 ± 39.	
2QZ J104044.4−003847	1.5690	19.69	2SLAQJ104047.60−003847.7	1.5730	20.64	46.5	394	467 ± 33.	
SDSS J104155.74+355206.9	2.2634	19.32	SDSS J104156.99+355036.8	2.2650	20.72	91.2	750	150 ± 32.	
SDSS J104414.02+635246.8	1.5375	20.16	SDSS J104414.90+635358.7	1.5355	20.28	72.2	611	236 ± 33.	
2SLAQJ104734.86−000537.9	1.8100	21.34	2SLAQJ104738.13−000605.2	1.8090	21.56	56.9	480	107 ±30.	
SDSS J105541.44+275801.2	1.4391	19.11	SDSS J105546.30+275721.6	1.4388	18.64	76.3	644	37 ±34.	
2SLAQJ110046.29−004621.3	1.8810	22.21	2QZ J110047.0−004553	1.8860	20.12	31.4	264	520 ±29.	
SDSS J110928.99+054106.1	2.3187	19.66	SDSS J110932.21+054017.5	2.3190	21.10	69.5	569	26 ±124	
SDSS J111010.56+145038.5	2.2040	20.39	SDSS J111011.35+145012.2	2.1990	21.70	28.5	235	469 ±164	
SDSS J111610.68+411814.4	3.0035	19.16	SDSS J111611.73+411821.5	2.9950	18.15	14.2	110	640 ±25.	
SDSS J111756.75+p062847.3	2.2450	19.700	SDSS J111757.07+062736.3	2.2415	19.70	71.1	586	322 ±25.	
SDSS J112902.06+612749.7	0.8756	19.93	SDSS J112912.13+612757.4	0.8742	18.45	72.8	562	224 ±45.	
SDSS J113457.73+084935.2	1.5333	19.05	SDSS J113459.37+084923.2	1.5251	19.38	26.6	225	974 ±33.	
SDSS J113502.03−022110.9	3.0210	21.35	SDSS J113502.51−022120.1	3.0080	21.98	12.5	96	972 ±21.	

– *Continued on next page*

– *Continued*

QSO A	z_A	r(A) [mag]	QSO B	z_B	r (B) [mag]	$\Delta\theta$ [arcsec]	$R_\perp$ [kpc]	$\Delta V_\parallel$ [$km\ s^{-1}$]	Comm.
(a)	(b)	(c)	(d)	(e)	(f)	(g)	(h)	(i)	(j)
SDSS J113509.20+034417.6	0.7557	19.81	SDSS J113510.24+034404.3	0.7610	21.11	19.8	146	908 ±40.	
SDSS J113725.69+141101.3	0.7353	19.99	SDSS J113726.12+141111.4	0.7370	20.55	12.4	90	293 ±36.	LN
SDSS J113808.87+680736.6	—	19.87	SDSS J113809.20+680738.6	0.7703	17.86	2.7	20.1	840 ± —	C
SDSS J114409.00+074945.6	2.0880	20.68	SDSS J114409.54+074909.6	2.0849	19.32	36.8	306	301 ± 53.	
SDSS J114603.49+334614.3	0.7638	20.32	SDSS J114603.76+334551.9	0.7610	19.42	23.3	172	477 ± 36.	LN
2QZ J114651.1−012457	1.9720	20.47	2QZ J114652.9−012447	1.9770	20.43	28.8	241	504 ± 28.	
SDSS J114654.25+123942.2	2.9750	20.69	SDSS J114658.60+124024.4	2.9759	21.34	76.9	593	73 ± 62.	
2QZ J115134.5+003511	2.2520	20.61	SDSS J115136.55+003531.0	2.2590	21.61	34.8	287	645 ± 108	
2QZ J115240.0−003033	0.5540	20.18	SDSS J115240.52−003004.3	0.5523	18.78	28.6	184	328 ± 54.	
2QZ J115814.7−003404	0.7930	19.09	SDSS J115817.24−003430.7	0.7931	20.90	46.2	345	13 ± 45.	N
SDSS J115822.77+123518.5	0.5996	19.85	SDSS J115822.98+123520.3	0.5957	20.12	3.6	23.7	733 ± 50	C
SDSS J120001.33+091941.5	2.6970	21.53	SDSS J120008.49+091903.9	2.6980	21.41	111.8	886	81 ± 85.	
2QZ J120700.9+011539	0.9660	18.98	2QZ J120701.3+011504	0.9640	20.34	35.5	282	305 ± 43.	N
SDSS J121414.57+163154.7	2.4404	20.51	SDSS J121418.90+163049.0	2.4378	21.63	90.7	736	224 ± 101	
SDSS J121418.85+085525.1	2.7090	20.84	SDSS J121419.94+085524.1	2.7151	21.73	16.3	129	493 ± 81.	
SDSS J121614.28+370338.9	2.6430	21.93	SDSS J121616.15+370255.9	2.6401	21.00	48.6	388	240 ± 38.	
2QZ J121734.9+000607	1.7820	19.39	2QZ J121736.1+000656	1.7840	20.18	51.7	437	216 ± 30.	
2QZ J121734.1+005521	0.9010	19.83	2QZ J121736.9+005521	0.9020	20.14	40.5	315	158 ± 44.	N
HS 1216+5032B	1.4570	18.46	HS 1216+5032A	1.4550	16.88	9.9	83	244 ± 34.	
SDSS J122448.23+021909.1	2.6915	21.19	SDSS J122453.36+021819.5	2.6890	19.24	91.3	725	200 ± 58.	
SDSS J122624.08−011234.5	0.9212	17.27	2QZ J122625.5−011321	0.9200	19.73	50.3	394	187 ± 44.	N
SDSS J122652.42−005316.0	2.6120	21.55	SDSS J122654.39−005430.6	2.6110	18.36	79.3	634	83 ± 140	
ChaM+ J122849.8+015541	2.3200	19.94	SDSS J122853.46+015648.8	2.3200	20.79	86.0	705	4 ± 53.	
SDSS J123145.16+000319.1	0.9080	21.55	2SLAQJ123145.44+000326.6	0.9070	21.48	8.3	65	157 ±44.	
SDSS J124031.42+111848.9	0.5844	20.13	SDSS J124032.67+111959.2	0.5830	20.18	73.2	482	260 ±41.	
SDSS J124037.52+094033.1	2.3443	19.87	SDSS J124042.68+094142.4	2.3450	20.52	102.2	835	60 ± 48.	
SDSS J124042.68+094142.4	2.3450	20.52	SDSS J124044.19+094142.4	2.3402	21.38	22.2	181	428 ± 60.	
KP 1244.1+34.6	2.3020	21.25	KP 1244.2+34.6	2.3020	19.85	74.5	611	0 ± 25.	
SDSS J124702.52+402410.1	0.7236	19.84	SDSS J124703.60+402415.0	0.7205	18.80	13.5	98	539 ± 40.	N
SDSS J124842.24+195639.9	3.8706	20.24	SDSS J124846.01+195716.8	3.8734	19.52	65.1	459	173 ±18.	
SDSS J124856.55+471827.7	0.4382	18.91	SDSS J124903.33+471906.0	0.4375	18.60	79.4	449	146 ± 59.	L
SDSS J125410.45+354947.7	0.6634	20.41	SDSS J125411.49+355056.1	0.6617	20.56	70.1	488	315 ±37.	

– *Continued on next page*

– *Continued*

QSO A	z_A	r(A) [mag]	QSO B	z_B	r (B) [mag]	$\Delta\theta$ [arcsec]	$R_\perp$ [kpc]	$\Delta V_\parallel$ [$km\ s^{-1}$]	Comm.
(a)	(b)	(c)	(d)	(e)	(f)	(g)	(h)	(i)	(j)
SDSS J125454.86+084652.1	0.4404	19.43	SDSS J125455.09+084653.9	0.4375	17.08	3.9	21.8	601 ± 20	C
SDSS J125716.88+103733.7	0.7992	19.00	SDSS J125719.18+103859.8	0.7994	20.69	92.4	693	36 ± 41.	
SDSS J130103.39+244918.4	1.0360	20.32	SDSS J130104.92+244859.0	1.0334	18.44	28.9	233	383 ± 129	
SDSS J130558.68+371920.6	3.1562	21.26	SDSS J130606.94+371911.5	3.1580	21.52	99.4	754	133 ± 51.	
SDSS J131112.83+070604.0	2.3000	20.22	SDSS J131113.23+070507.5	2.2983	20.15	57.3	470	158 ± 67.	
SDSS J131157.58+255648.6	1.0062	20.05	SDSS J131159.93+255650.4	1.0103	19.54	32.4	260	614 ± 49.	N
SDSS J131846.91+221029.3	3.0517	19.70	SDSS J131847.82+221130.7	3.0456	18.4	62.3	477	451 ± 49.	
SDSS J132716.41+071950.4	2.3400	18.90	SDSS J132717.72+072035.9	2.3360	20.42	49.0	401	359 ± 65.	
2QZ J132758.8−023025	2.3600	19.01	2QZ J132759.8−023140	2.3590	19.77	76.2	622	89 ± 25.	
SDSS J132821.74+351738.5	0.6857	18.49	SDSS J132823.66+351739.0	0.6847	19.86	23.3	165	171 ± 41.	N
2QZ J132830.1−015732	2.3710	19.61	2QZ J132833.6−015727	2.3730	19.87	52.6	429	178 ± 25.	
SDSS J132828.74+340859.2	2.2430	19.31	SDSS J132836.77+340825.9	2.2440	21.69	105.0	865	92 ± 77.	
SDSS J132855.14+133808.2	2.3895	21.66	SDSS J132857.89+133827.6	2.3928	21.31	43.7	356	290 ± 68.	
SDSS J133046.35+373142.8	0.8136	19.26	SDSS J133048.58+373146.6	0.8134	19.86	26.5	200	26 ± 36.	LN
SDSS J133143.62+094634.0	2.2720	21.26	SDSS J133147.35+094710.7	2.2730	21.81	65.5	538	92 ± 84.	
SDSS J133522.98+081326.1	2.4913	20.20	SDSS J133526.14+081254.8	2.4862	17.30	57.3	463	435 ± 84.	
2SLAQJ133802.31−001617.5	1.4790	20.87	2SLAQJ133806.16−001640.1	1.4780	21.24	61.5	520	121 ± 34.	
SDSS J134731.01+264310.5	2.4410	19.96	SDSS J134733.98+264336.0	2.4466	20.02	46.8	379	487 ± 72.	
2QZ J135048.9+001521	1.8340	19.30	2SLAQJ135049.10+001505.9	1.8360	20.90	17.1	144	212 ± 29.	
2SLAQJ135438.71+003150.8	1.6320	21.88	2QZ J135440.2+003203	1.6400	19.41	26.0	220	911 ± 32.	
SDSS J140542.67+102207.7	2.1730	20.88	SDSS J140544.80+102049.2	2.1759	18.77	84.5	699	274 ± 39.	
SDSS J141740.94+390920.5	2.2750	20.85	SDSS J141741.85+390841.2	2.2800	21.21	40.4	332	458 ± 51.	
SDSS J141855.41+244108.9	0.5736	19.21	SDSS J141855.53+244104.7	0.5751	20.13	4.5	29.4	287 ± 40	C
SDSS J142022.11+230624.3	2.4874	20.49	SDSS J142024.14+230458.3	2.4900	20.65	90.3	730	224 ± 39.	
SDSS J142148.79+163017.5	2.4750	20.35	SDSS J142149.00+163027.1	2.4660	20.55	10.9	88	778 ± 76.	
SDSS J142359.11+420902.9	2.2330	20.53	SDSS J142401.10+420908.7	2.2230	21.52	23.0	190	930 ± 60.	
SDSS J142500.31+243412.6	0.8591	21.08	SDSS J142507.07+243425.8	0.8589	20.62	92.3	708	36 ± 94.	
SDSS J142511.77+095538.3	2.6759	21.15	SDSS J142515.84+095651.5	2.6747	19.12	94.9	754	104 ± 39.	
SDSS J142634.54+074722.7	2.8230	21.38	SDSS J142635.57+074645.4	2.8248	20.04	39.9	312	141 ± 54.	
SDSS J142815.67+023243.5	3.0120	19.43	SDSS J142816.51+023229.2	3.0151	20.42	19.4	150	229 ± 41.	
2QZ J143506.4+000901	2.3720	19.83	2QZ J143508.3+000844	2.3730	20.55	34.0	277	89 ± 25.	
2SLAQJ144340.17−005242.1	1.0830	20.75	2SLAQJ144341.96−005208.6	1.0860	20.27	43.4	353	432 ± 40.	

– *Continued on next page*

– *Continued*

QSO A	z_A	r(A) [mag]	QSO B	z_B	r (B) [mag]	$\Delta\theta$ [arcsec]	$R_\perp$ [kpc]	$\Delta V_\parallel$ [$km\ s^{-1}$]	Comm.
(a)	(b)	(c)	(d)	(e)	(f)	(g)	(h)	(i)	(j)
SDSS J144414.99+344830.3	2.2740	19.35	SDSS J144415.35+344829.8	2.2812	21.51	5.0	41	658 ± 40.	
SDSS J144629.25+213827.2	2.3333	21.72	SDSS J144629.82+213653.0	2.3325	21.44	94.4	772	71 ± 241	
SDSS J144844.81+494834.9	2.0790	20.15	SDSS J144853.02+494818.1	2.0789	20.24	81.0	674	10 ± 27.	
SDSS J145407.11+302423.7	1.9260	21.03	SDSS J145411.01+302444.3	1.9240	18.69	54.6	459	205 ± 169	
SDSS J145553.92+181912.1	1.0714	18.33	SDSS J145555.06+181901.6	1.0722	21.36	19.1	156	115 ± 132	N
SDSS J150147.52+051955.5	2.0900	21.66	SDSS J150147.51+052006.2	2.0813	18.28	11.0	92	846 ± 27.	
SDSS J150842.19+332802.6	0.8773	17.80	SDSS J150842.21+332805.5	0.878	20.19	2.9	22.5	112 ± 160	C
SDSS J150909.07+212551.3	2.3227	21.71	SDSS J150913.95+212521.5	2.3215	21.49	74.7	612	102 ± 68.	
SDSS J151733.52+121609.5	2.4103	21.62	SDSS J151737.18+121446.4	2.4097	19.40	98.4	800	54 ± 42.	
SDSS J152356.08+081526.1	2.1910	21.35	SDSS J152400.11+081427.2	2.1900	20.20	84.8	701	94 ± 76.	
SDSS J152950.14+174621.3	1.5865	18.84	SDSS J152954.86+174641.2	1.5870	21.90	70.0	593	58 ± 48.	
SDSS J153333.52+081950.9	2.2763	21.51	SDSS J153335.36+081844.7	2.2778	21.48	71.2	585	143 ± 95.	
SDSS J153433.39+185457.2	0.9280	18.82	SDSS J153437.97+185509.7	0.9268	18.20	66.4	521	187 ± 44.	
SDSS J153708.94+381905.6	0.7450	21.48	SDSS J153710.51+381851.7	0.7461	18.78	23.5	172	189 ± 48.	N
SDSS J154320.59+025251.4	2.2162	19.65	SDSS J154327.37+025319.1	2.2160	21.21	105.6	872	17 ± 29.	
SDSS J154631.39+472752.9	1.8828	19.16	SDSS J154634.34+472847.9	1.8840	19.17	62.8	529	125 ± 29.	
SDSS J154636.34+262839.6	2.5152	19.07	SDSS J154640.01+262859.9	2.5137	21.23	53.5	432	127 ± 66.	
SDSS J155217.93+045646.7	1.5628	19.01	SDSS J155218.08+045635.2	1.5637	18.66	11.1	94	105 ± 33.	
SDSS J155330.22+223010.2	0.6405	18.30	SDSS J155330.55+223014.3	0.6419	20.82	5.8	40	249 ± 40.	LN
SDSS J155648.72+061919.6	2.4866	20.69	SDSS J155649.62+061837.3	2.4840	20.41	44.1	356	228 ± 26.	
SDSS J160406.95+431445.6	0.8066	20.94	SDSS J160408.90+431455.7	0.8080	20.66	24.0	181	238 ± 49.	N
SDSS J160602.80+290048.8	0.7711	18.35	SDSS J160603.01+290050.8	0.7692	18.25	3.5	25.6	317 ± 40	C
SDSS J161124.94+050113.7	2.2950	21.61	SDSS J161125.11+050012.6	2.2970	19.73	61.1	501	182 ± 110	
SDSS J161144.41+263555.1	2.6640	20.17	SDSS J161146.36+263606.6	2.6599	19.73	27.8	221	338 ± 38.	
SDSS J161301.69+080806.0	2.3815	19.53	SDSS J161302.03+080814.2	2.3910	18.83	10.0	81	839 ± 25.	
SDSS J162119.20+422645.2	2.7667	21.86	SDSS J162122.73+422624.5	2.7630	19.76	44.1	347	297 ± 126	
SDSS J164732.53+350524.9	0.8640	20.44	SDSS J164733.23+350541.6	0.8607	19.93	19.1	146	532 ± 45.	N
SDSS J165047.94+343033.4	1.8250	18.38	SDSS J165049.91+343043.4	1.8310	21.28	26.7	225	637 ± 100	
SDSS J165404.20+200230.5	2.3960	20.96	SDSS J165409.21+200336.2	2.3970	22.00	96.5	786	88 ± 85.	
SDSS J170008.54+393144.6	1.7600	20.96	SDSS J170012.51+393153.2	1.7585	19.07	47.1	398	163 ± 84.	
SDSS J171326.00+294924.4	0.5720	20.20	SDSS J171336.34+294915.3	0.5723	19.62	134.3	877	57 ± 53.	
SDSS J211427.02−000027.0	2.4800	19.67	SDSS J211427.36−000025.1	2.4840	20.77	4.9	40	348 ± 23.	

– *Continued on next page*

– *Continued*

QSO A	z_A	r(A) [mag]	QSO B	z_B	r (B) [mag]	$\Delta\theta$ [arcsec]	$R_\perp$ [kpc]	$\Delta V_\parallel$ [$km\ s^{-1}$]	Comm.
(a)	(b)	(c)	(d)	(e)	(f)	(g)	(h)	(i)	(j)
SDSS J211718.03+010242.0	2.9499	20.59	SDSS J211718.17+010248.9	2.9377	19.12	6.2	48	932 ± 29.	
SDSS J213043.82+044455.1	2.2730	22.15	SDSS J213044.32+044453.3	2.2730	22.05	7.7	64	0 ± 50.	
SDSS J214144.49−022946.7	2.7050	20.79	SDSS J214144.94−022936.2	2.6995	20.95	12.5	99	446 ± 74.	
2SLAQJ214328.36+000057.3	2.1520	21.24	2SLAQJ214328.43+000052.5	2.1400	21.91	5.2	43	1146 ± 27.	
SDSS J215727.26+001558.4	2.5496	20.50	SDSS J215728.35+001545.5	2.5527	19.54	21.0	169	260 ± 41.	
2QZ J220213.3−303641	1.7450	19.80	2QZ J220217.7−303722	1.7460	19.00	70.0	592	109 ± 30.	AB
2QZ J220307.0−313316	1.6440	21.90	2QZ J220311.8−313421	1.6420	19.20	89.4	757	227 ± 32.	AB
SDSS J222446.92−010245.5	1.6012	19.26	SDSS J222449.72−010328.7	1.6005	19.05	60.1	509	81 ± 32.	
SDSS J223253.57−001119.4	3.1337	20.16	Q223256.67−001246.4	3.1340	21.84	98.6	750	22 ± 20.	
SDSS J224249.76−004043.8	2.4645	21.62	SDSS J224250.27−004041.9	2.4520	20.89	7.8	63	1088 ±44.	
2QZ J224637.9−292947	0.8600	19.40	2QZ J224638.5−292944	0.8630	20.40	9.6	74	484 ± 45.	AB
2QZ J224732.5−281201	2.2990	20.20	2QZ J224738.5−281210	2.3020	99.99	77.1	632	273 ± 25.	AB
SDSS J224856.82+030700.2	2.3860	20.74	SDSS J224857.22+030659.5	2.3770	20.49	6.1	50	799 ± 300	
2QZ J225354.6−283142	1.7360	21.60	2QZ J225357.1−283220	1.7370	19.20	51.0	432	110 ± 30.	AB
SDSS J230011.16+003145.5	2.1760	21.43	SDSS J230015.69+003119.3	2.1774	19.17	72.3	599	132 ± 169	
2QZ J230911.8−273227	1.9300	18.60	2QZ J230915.3−273245	1.9270	20.50	49.0	412	307 ± 28.	AB
SDSS J230946.3−005911.2	0.6980	19.60	2SLAQJ230951.18−005928.0	0.6960	19.00	74.0	527	354 ± 28	
SDSS J230959.53+005537.3	2.4220	18.32	SDSS J230959.80+005600.9	2.4133	19.88	23.4	190	764 ± 40.	
2SLAQJ231541.12+002928.1	1.3500	20.68	SDSS J231541.66+002936.5	1.3425	21.09	11.0	92	960 ± 36.	
SDSS J231648.67+004952.7	3.2240	19.69	SDSS J231652.04+005125.9	3.2261	18.85	106.1	799	149 ± 254	
SDSS J231835.88−000627.9	1.4250	21.13	2SLAQJ231836.46−000553.5	1.4280	20.94	35.2	297	371 ± 78.	
SDSS J232034.78+000339.0	1.7637	20.14	2SLAQJ232036.16+000407.2	1.7710	21.04	35.0	296	792 ± 30.	
SDSS J232631.75−015343.1	0.7325	21.13	SDSS J232635.20−015500.4	0.7320	19.41	93.2	677	90 ± 37.	
2QZ J232906.8−295731	1.8410	19.30	2QZ J232908.6−295628	1.8410	99.99	67.2	566	0 ± 29.	AB
SDSS J234145.18−003759.6	0.7200	23.60	SDSS J234145.81−003934.6	0.7203	20.32	95.6	690	52 ± 49.	
SDSS J234326.32+001337.8	1.1090	20.50	SDSS J234326.90+001352.6	1.1039	20.03	17.5	143	732 ± 100	
2QZ J234947.1−320254	1.0510	19.60	2QZ J234953.7−320237	1.0510	19.70	85.6	693	0 ± 41.	AB

4. The environment of low-redshift QSO pairs

4.1. Summary

In this Chapter we explore the galaxy environments and the dynamical properties of a homogeneous sample of 14 low-redshift ($0.2 < z < 0.85$) QSO physical-pairs extracted from SDSS Data Release 10 (DR10, Ahn et al. 2014) data sets. The pairs have a systemic radial velocity difference $\Delta V_{\parallel} \leqslant 600\ km\ s^{-1}$ (based on [OIII]λ5007 Å line) and projected distance $R_{\perp} \leqslant 600$ kpc. The physical association of the pairs is statistically assessed at a level of $\sim 90\%$.

We recall that two QSO are considered physically associated if they are gravitationally bound each other or to a larger structure. The Random Test give us an estimation of the probability for a QSO pair to be physical rather than a chance superposition. For these QSO pairs we perform a detailed analysis of their host galaxies and of the clustering of galaxies around the pairs with the aim to probe if peculiar properties characterized the QSO pair condition and whether QSO pairs need to reside in groups of galaxies to formed or if they prefer isolated systems.

For most of the images of these QSOs we resolve their host galaxies and deconvolve the host and nucleus magnitudes. We are then able to compare the properties of the QSOs and their environments with those of a homogeneous sample of QSOs not in pairs at low redshift, spanning the same range of luminosities. On the basis of the simple dynamics of the pair, finally we set constraints on the total minimum mass of the systems to which the pair belongs and investigate whether QSO pairs are isolated systems or their differences of velocity are dominated by a larger mass.

We found that host galaxies turn out to be on average similar to those of QSOs not in pairs. Moreover, the QSOs in a pair are on average in regions of modest galaxy overdensity extending up 0.5 Mpc from the QSO. This galaxy overdensity is indistinguishable from that of a homogeneous sample of isolated QSOs at the same redshift and with the similar host galaxy luminosity. These results, albeit derived from a small, but homogeneous sample of objects, suggest that the rare activation of two QSOs with small physical separation does not require any extraordinary environment.

Part of the material contained in this Chapter is published in Sandrinelli et al. 2014, MNRAS, 444, 1835.

4.2. Low-redshift QSO pair sample

4.2.1. Selection of QSO candidates from SDSS catalogues

We searched for QSO pair candidates from a data set of $\sim$ 260,000 QSO spectra drawn from the SDSS QSO spectroscopic catalogues of Schneider et al. (2010) and of Pâris et al. (2014). We restricted the search to the $\sim$ 40,000 QSOs with z<0.85, in order to derive the redshifts from [OIII]λ5007 narrow emission line, which is a much better indicator of the systemic velocity of the QSO host galaxy (e.g. Hewett & Wild 2010; Liu et al. 2014, and see 4.2.2).

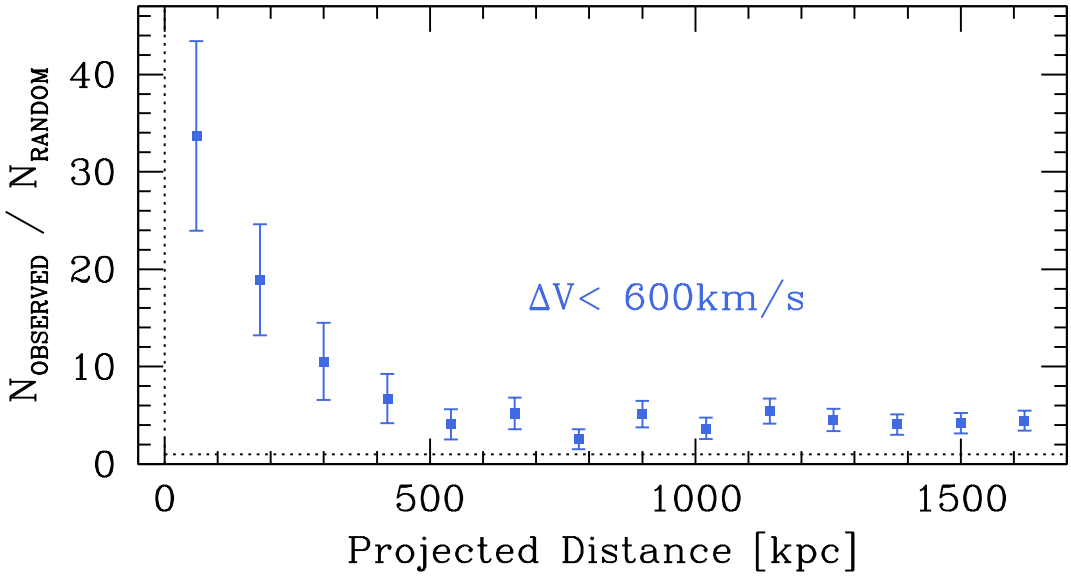

Figure 4.1.: Number of observed spectroscopically-confirmed SDSS QSO pairs at z<0.85 out of the number of the expected chance superpositions obtained with the redshift permutation method (e.g. Zhdanov & Surdej 2001) under the difference of radial velocity of 600 km/s.

As extensively described in Chapter 3, to search for QSO pair candidates we computed the number N_{obs} of QSOs in the catalogues that have $\Delta V_{\parallel} < \Delta V_{\parallel,limit}$ and $R_{\perp} < R_{\perp,limit}$, where $\Delta V_{\parallel,limit}$ and $R_{\perp,limit}$ are fixed values, and compare it with the number N_{ran} of expected random association using the redshift permutation method (e.g. Zhdanov & Surdej 2001). We repeated the search with various values of $\Delta V_{\parallel,limit}$ and $R_{\perp,limit}$ in order to optimize the number of candidates with respect to the number of chance associations. The N_{obs}/N_{ran} ratio is plotted as a function of $R_{\perp}$ under different $\Delta V_{\parallel,limit}$ in Figure 4.1. At smaller $R_{\perp}$ and lower $\Delta V_{\parallel,limit}$ it steeply increases as an evidence of enhanced physical clustering of QSOs in pair associations. It turns out that the best choice is $R_{\perp} < 600$ kpc and $\Delta V_{\parallel} < 600$ km s^{-1}. For this combination we find 26 QSO starting pair candidates as shown in the $R_{\perp} - \Delta V_{\parallel}$ plane reported in Figure 4.3. Of

these pairs only 3-4 (∼14%) are expected to be false pairs, i.e. random associations.

4.2.2. Selection on the basis of $\Delta V_{\parallel}$ from [OIII]λ5007

At this stage of the selection $\Delta V_{\parallel}$ was determined from SDSS redshifts. Uncertainties may be associated with the SDSS fit procedure applied on the overall spectrum in the redshift determination, that may prevent us from obtaining accurate $\Delta V_{\parallel}$ measurements.

In the QSO spectra, lines may exhibit a variety of shapes and asymmetric profiles (e.g. Shen & Loeb 2010). Displacements of the broad line peaks relative to the narrow ones or velocity offsets between the narrow emission [OIII] lines have also been observed (Shen & Loeb 2010; Liu et al. 2010). Moreover, the well known velocity systematic shifts up few hundred km/s between different emission lines [1] (Bonning, Shields, & Salviander 2007; Tytler & Fan 1992; Hewett & Wild 2010; Decarli et al. 2013) may blur the exact line positions (see also e.g. Smith et al. 2010; Zamfir et al. 2010). For these reasons, the most reliable estimate of the systemic velocity is that obtained from stellar absorption features of the host galaxies and/or from forbidden emission lines such as [O III]λ4949 and [O III]λ5007, arising from the narrow line region (Hewett & Wild 2010; Liu et al. 2014), where the gas is predominantly orbiting in the host galaxy potential.
We checked the spectra of all candidates to confirm the object classification and to ensure that the systemic $\Delta V_{\parallel}$ could be reliably derived from [O III]λ5007 lines. For two dubious classifications we removed 2 QSO pairs candidates and another one for the lack of the [O III]λ5007 wavelength region in one spectrum. Because of poor S/N, 8 pair candidates have the [OIII] line position barely measurable for at least one QSO. For the remaining pairs the [O III]λ5007 line position was measured with the procedure described in Farina, Falomo, & Treves (2011), where the centroid was evaluated as the median of the barycenters of the line above different flux thresholds between the level of the continuous and its peak and the interquartile range is taken as uncertainty. An example is represented in detail in Figure 4.2. In one case $\Delta V_{\parallel}$ from [O III]λ5007 did not satisfy the condition < 600 km/s, which was however fulfilled by the SDSS redshifts, and the pair candidate was removed.

We compared the $\Delta V_{\parallel}$ from SDSS catalogues and from [O III]λ5007 derivation and note that the RMS of the differences of the two data set shows on average uncertainties of ~ 100 km/s, i.e. redshift determinations based on [O III]λ5007 reduce the uncertainty on $\Delta V_{\parallel}$ of about a factor 3-4.

In our residual sample of 14 QSO pairs we expect that 1-2 pairs could be chance superpositions. We can assume that the selected sample consists for the largest part of physically associated objects, where the QSO velocities are due to gravitational binding. The final list of the QSO pairs candidates and properties are reported in Table 4.2. Details on [O III]λ5007 lines are shown in Table 4.3. The redshifts of the selected QSO pairs is $0.236 < z < 0.82$, with $z_{ave} = 0.58 \pm 0.03$. There is no evidence of lensing systems: none of these QSO pairs are present in catalogues of lensed QSOs (CfA-Arizona

[1] An improvement related to the redshift shifts due to different emission lines is applied in the compilation of Pâris et al. (2012) QSO catalogue starting from SDSS data release 8. A reference sample with reliable redshift, correct for the empirical shifts from different emission lines (Hewett & Wild 2010), and supposed representative of the whole population of QSOs was used to construct a principal-component template.

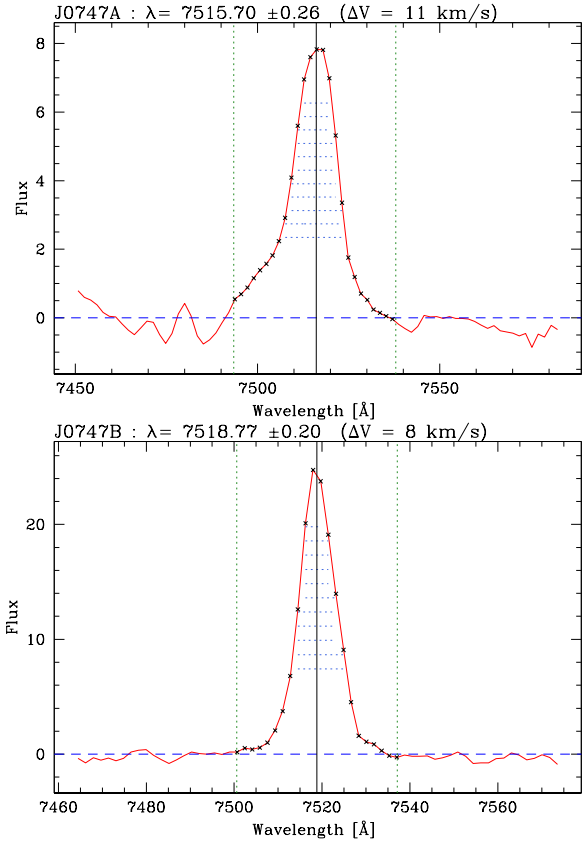

Figure 4.2.
Normalized spectra of the pair no. 3 (see Table 4.2) around the [O III]λ5007 emission line. Line position (vertical solid line) is the median of the barycenters computed above different flux thresholds (in these cases from 30% to 80% in steps of 5%, horizontal dotted lines). Vertical green dotted lines mark the limits of the line position computation. Blue dashed line is the continuum level of the spectrum. The flux is continuum-subtracted and expressed in arbitrary units.

Space Telescope LEns Survey of gravitational lenses, CASTLE[2]; SDSS QSO Lens Search, SQLS[3]). Moreover detailed comparison between the spectra of each pair exhibits clear differences that exclude the possibility of gravitational lensing. In Table 4.2 we recover 5 of the 6 pairs considered by Farina, Falomo, & Treves (2011). An example of the SDSS selected pair spectra is given in Figure 4.4, while all the spectra are collected in Section 5.5, Figure 5.17.

[2]http://www.cfa.harvard.edu/castles/
[3]http://www-utap.phys.s.u-tokyo.ac.jp/~sdss/sqls/index.html

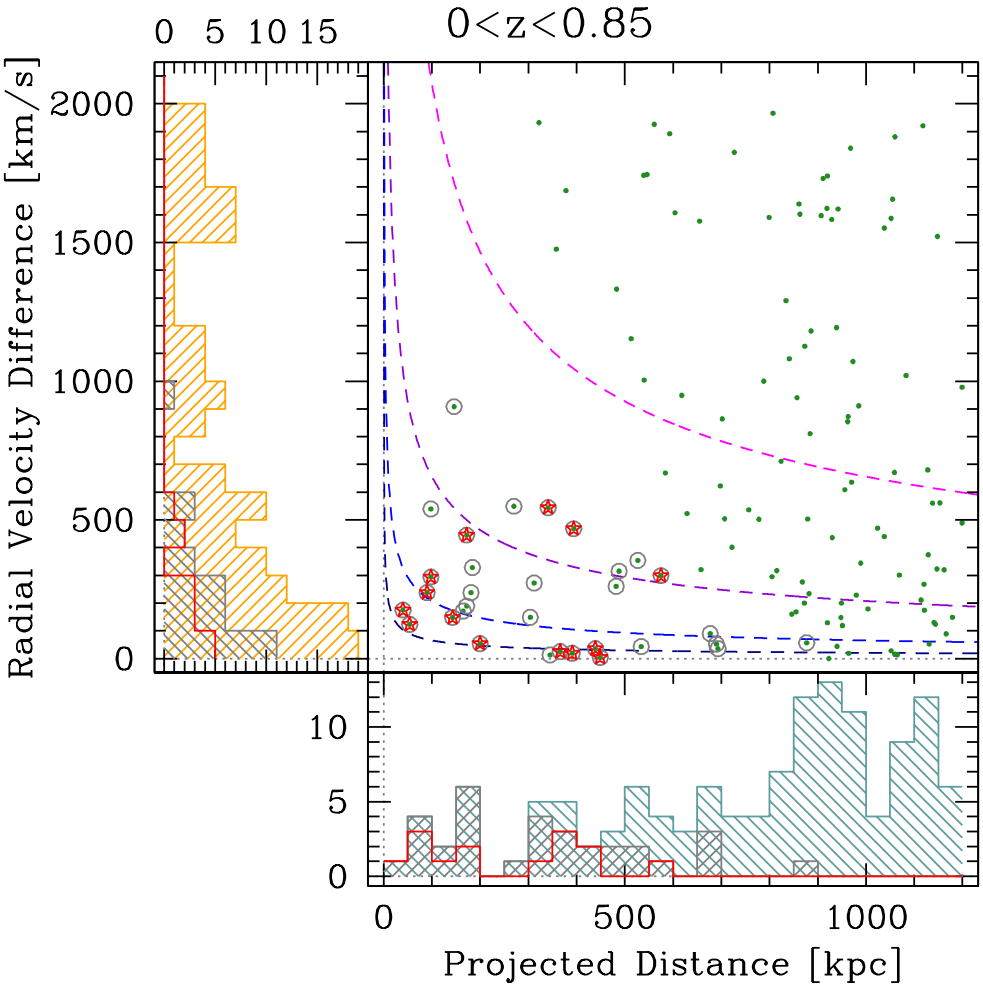

Figure 4.3.: Low-redshift (z<0.85) QSO physical pairs candidates distribution in the $R_\perp - \Delta V_\parallel$ plane(grey circles, from Table 3.2), and $R_\perp$ and $\Delta V_\parallel$ distributions (grey histograms). Light blue and orange histograms are the same for the pairs with $R_\perp <$ 1200 kpc and $\Delta V_\parallel <$ 2000 km/s (green dots). Pairs derived from the SDSS and selected for the study described in this chapter are marked with a red star; distribution are illustrate in red histograms. Iso-minimun-virial-masses from Eq. 3 , see Section 4.6, are drawn by dashed lines. From top to bottom iso-minimun-virial-mass values are $M_{vir,min} = 10^{14} M_\odot$, $10^{13} M_\odot$, $10^{12} M_\odot$, and $10^{11} M_\odot$ (from magenta line to blue line). Note that in the region with $R_\perp <$ 600 kpc and $\Delta V_\parallel >$ 600 km/s a sub density of QSO pair candidates is apparent.

Table 4.1.: Properties of low-redshift QSO pair sample.

Pair	obj	QSO	z	i [mag]	M_i [mag]	$\Delta\theta$ ["]	$R_\perp$ [kpc]	$\Delta V_\parallel$ [$km\ s^{-1}$]
	(a)	(b)	(c)	(d)	(e)	(f)	(g)	(h)
J0011	1A	J001103.18+005927.2	0.4865	19.75	-22.14	65.2	390	19 ± 28
	B	J001103.48+010032.6	0.4864	20.62	-21.28			
J0226	2A	J022610.98+003504.0	0.4240	19.54	-22.06	66.0	360	25 ± 24
	B	J022612.41+003402.2	0.4239	19.09	-22.51			
J0747	3A	J074759.02+431805.3	0.5011	18.84	-23.12	8.9	60	123 ± 18
	B	J074759.65+431811.4	0.5017	19.09	-22.87			
J0818	4A	J081801.47+205009.9	0.2357	17.45	-22.66	118	440	36 ± 16
	B	J081808.77+204910.1	0.2356	18.81	-21.31			
J0824	5A	J082439.83+235720.3	0.5353	18.71	-23.41	15.5	90	294 ± 19
	B	J082440.61+235709.9	0.5368	18.61	-23.05			
J0845	6A	J084541.18+071050.3	0.5376	18.73	-23.40	62.3	390	468 ± 51
	B	J084541.52+071152.3	0.5352	18.60	-23.52			
J0856	7A	J085625.63+511137.0	0.5420	18.38	-23.77	22.5	140	148 ± 21
	B	J085626.71+511117.8	0.5432	19.18	-22.97			
J0951	8A	J095137.01−004752.9	0.6340	20.23	-22.29	49.8	350	544 ± 23
	B	J095139.39−004828.7	0.6369	20.02	-22.51			
J1137	9A	J113725.69+141101.3	0.7358	20.03	-22.91	12.4	90	238 ± 28
	B	J113726.12+141111.4	0.7372	20.53	-22.42			
J1146	10A	J114603.49+334614.3	0.7642	20.11	-22.92	23.3	170	445 ± 38
	B	J114603.76+334551.9	0.7615	19.23	-23.79			
J1248	11A	J124856.55+471827.7	0.4386	18.62	-23.04	79.4	450	4 ± 15
	B	J124903.33+471906.0	0.4386	18.30	-23.37			
J1330	12A	J133046.35+373142.8	0.8141	19.32	-23.85	26.4	200	54 ± 43
	B	J133048.58+373146.6	0.8144	19.82	-23.35			
J1553	13A	J155330.22+223010.2	0.6413	18.22	-24.32	5.9	40	175 ± 12
	B	J155330.55+223014.3	0.6422	20.65	-21.91			
J2229	14A	J222901.08+031139.8	0.8069	21.69	-21.47	76.5	570	299 ± 19
	B	J222902.03+031024.7	0.8087	19.88	-23.28			

Notes: (a) Pair short name and QSO ID. (b) SDSS QSO name. (c) Redshifts derived from [OIII] line positions. (d) i-band apparent magnitude. (e) i-band rest-frame absolute magnitude. (f) Angular separation of the pair. (g) Proper traverse separation. (h) Radial velocity difference.

Table 4.2.: Properties of low-redshift QSO pair sample.

Pair Nr (a)	QSO A (b)	z_A (c)	i_A [mag] (d)	M_i (A) [mag] (e)	QSO B (f)	z_B (g)	i_B [mag] (h)	M_i (B) [mag] (i)	$\Delta\theta$ [arcsec] (j)	$R_\perp$ [kpc] (k)	$\Delta V_\parallel$ [$km\ s^{-1}$] (l)
1 J0011	J001103.18+005927.2	0.4865	19.75	-22.14	J001103.48+010032.6	0.4864	20.62	-21.28	65.2	390	19 ± 28
2 J0226	J022610.98+003504.0	0.4240	19.54	-22.06	J022612.41+003402.2	0.4239	19.09	-22.51	66.0	360	25 ± 24
3 J0747	J074759.02+431805.3	0.5011	18.84	-23.12	J074759.65+431811.4	0.5017	19.09	-22.87	8.9	60	123 ± 18
4 J0818	J081801.47+205009.9	0.2357	17.45	-22.66	J081808.77+204910.1	0.2356	18.81	-21.31	118.1	440	36 ± 16
5 J0824	J082439.83+235720.3	0.5353	18.71	-23.41	J082440.61+235709.9	0.5368	18.61	-23.05	15.5	90	294 ± 19
6 J0845	J084541.18+071050.3	0.5376	18.73	-23.40	J084541.52+071152.3	0.5352	18.60	-23.52	62.3	390	468 ± 51
7 J0856	J085625.63+511137.0	0.5420	18.38	-23.77	J085626.71+511117.8	0.5432	19.18	-22.97	22.5	140	148 ± 21
8 J0951	J095137.01−004752.9	0.6340	20.23	-22.29	J095139.39−004828.7	0.6369	20.02	-22.51	49.8	350	544 ± 23
9 J1137	J113725.69+141101.3	0.7358	20.03	-22.91	J113726.12+141111.4	0.7372	20.53	-22.42	12.4	90	238 ± 28
10 J1146	J114603.49+334614.3	0.7642	20.11	-22.92	J114603.76+334551.9	0.7615	19.23	-23.79	23.3	170	445 ± 38
11 J1248	J124856.55+471827.7	0.4386	18.62	-23.04	J124903.33+471906.0	0.4386	18.30	-23.37	79.4	450	4 ± 15
12 J1330	J133046.35+373142.8	0.8141	19.32	-23.85	J133048.58+373146.6	0.8144	19.82	-23.35	26.4	200	54 ± 43
13 J1553	J155330.22+223010.2	0.6413	18.22	-24.32	J155330.55+223014.3	0.6422	20.65	-21.91	5.9	40	175 ± 12
14 J2229	J222901.08+031139.8	0.8069	21.69	-21.47	J222902.03+031024.7	0.8087	19.88	-23.28	76.5	570	299 ± 19

Notes: (a) Pair identification number and short name. (b) and (f) SDSS QSO name. (c) and (g) QSO redshifts derived from [OIII] line positions. (d) and (h) i-band apparent magnitude of the QSO A and B, respectively. (e) and (i) i-band as solute magnitude of the QSO A and B, respectively. (j) Angular separation of the pair. (k) Proper traverse separation . (l) Radial velocity difference.

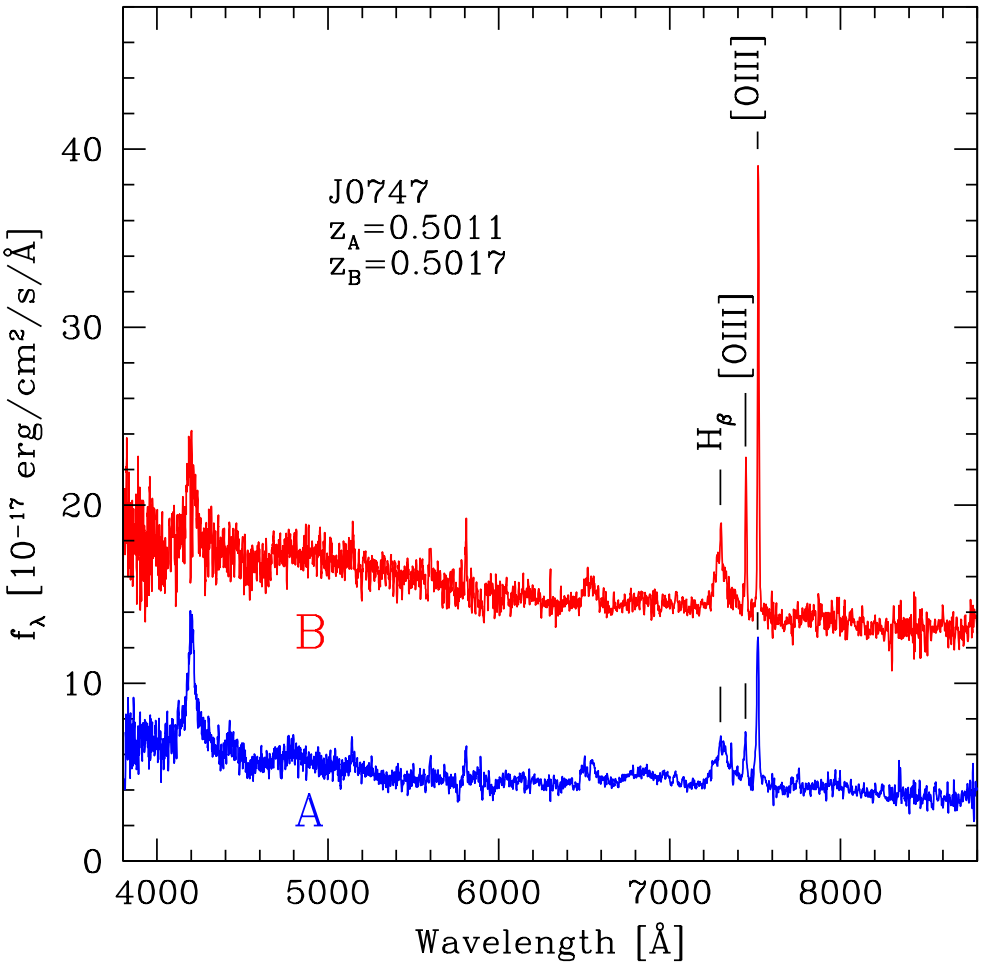

Figure 4.4.: SDSS spectra of the QSOs in pair nr. 3. For clarity of comparison, the spectrum of the QSO B is shifted upwards by $10 \cdot 10^{-17} erg\ s^{-1} cm^{-2} \mathring{A}^{-1}$.

Table 4.3.: Measurements of [O III]λ5007 emission lines.

Pair Nr a	$\lambda_{[OIII]}$ (A) [Å] b	$\lambda_{[OIII]}$ (B) [Å] c	S/N_A b	S/N_B c
1	7442.47 ± 0.63	7441.99 ± 0.26	4.4 ± 1.2	6.0 ± 0.5
2	7129.84 ± 0.44	7129.24 ± 0.32	5.8 ± 1.6	5.2 ± 1.1
3	7515.70 ± 0.26	7518.77 ± 0.30	8.6 ± 2.2	6.0 ± 2.0
4	6187.15 ± 0.24	6186.41 ± 0.22	14.1 ± 4.7	7.2 ± 2.7
5	7686.78 ± 0.37	7694.31 ± 0.26	9.5 ± 2.6	9.0 ± 2.7
6	7698.28 ± 0.30	7686.28 ± 1.27	10.6 ± 3.9	7.7 ± 1.7
7	7722.53 ± 0.47	7726.33 ± 0.20	12.7 ± 2.6	6.8 ± 1.9
8	8180.92 ± 0.06	8195.76 ± 0.61	2.7 ± 0.5	6.0 ± 1.5
9	8690.95 ± 0.33	8697.85 ± 0.70	6.5 ± 1.0	3.8 ± 1.5
10	8832.83 ± 1.10	8819.75 ± 0.04	11.7 ±4.4	12.5 ± 4.6
11	7202.80 ± 0.05	7202.88 ± 0.32	8.9 ± 1.3	10.1 ± 2.6
12	9082.84 ± 0.41	9084.48 ± 1.22	11.2 ± 2.0	6.9 ± 1.8
13	8217.60 ± 0.26	8222.40 ± 0.07	14.0 ± 2.7	2.4 ± 0.6
14	9047.04 ± 0.37	9056.06 ± 0.39	1.1 ± 0.4	4.7 ± 1.2

Notes: (a) Pair identification number. (b) and (c) Wavelengths of [O III]λ5007 emission line barycenters for QSOs A and B, respectively. (d) and (e) Signal to Noise of the spectrua of QSOs A and B, respectively.

4.3. Host galaxies

Galaxies hosting QSOs in pair were photometrically studied with the aim of outlining their properties and draw a comparison with those hosting isolated QSOs. We used the Astronomical Image Decomposition and Analysis (AIDA Uslenghi & Falomo 2008) software, an IDL package designed for QSO image analysis and fitting, to model the two QSO components and to simultaneously deconvolve the host galaxy luminosity from the nuclear source. The employed technique, that we summarize below, was applied in previous QSO host galaxies studies (Falomo et al. 2008; Decarli et al. 2012; Kotilainen et al. 2007, 2009) and is widely discussed in Falomo et al. (2014) for the imaging study of 400 low-redshift (z<0.5) SDSS QSOs in Stripe 82.

4.3.1. Modeling the nuclear source

We retrieved the i-images of QSO in pairs from the SDSS-DR10 imaging archive. The separation of the host galaxy luminosity from the nuclear source is a crucial task. The nucleus luminosity is described by the local Point Spread Function (PSF) of the image, and for its careful description a number of suitable stars in the QSO pair field have to be selected among the isolated stars in the frame (see Figure 4.5, top left panel). These stars may surround the targets as close as possible to locally model the PSF and have a large range of magnitudes, the brighter ones are also used to well characterize the

PSF wing shape with the aim of not overestimating the galaxy luminosity. In order to distinguish stars from galaxies we examined the ellipticities of the objects in the fields and required the lower ones and sharp profiles (measuring the FWHM). Each star is modeled by three bidimensional Gaussians, representing the core of the PSF, and by one exponential function depicting the extended wings of the PSF (Figure 4.5, top right). In the SDSS images the fields of view are large enough of contain the adequate amount of stars ($\sim$ 5 -10) to well derive the PFS.

Extra sources and image defects nearby the star, or in proximity of the surrounding annulus where background is evaluated, were masked out. Uncertainties in the background evaluation come from the standard error of measure in each sub-anullus. The profile fitting is performed on a circular region centered in the star, with the exclusion of the innermost part to avoid the saturated cores of bright stars. Errors involve background uncertainties, the standard deviation of residuals in the image after model subtractions and systematic effects in data reduction.

At this point we fit the QSO images with a scaled pure PSF model, after applying masks where needed.

4.3.2. Modeling the galaxy luminosity

If the profile after subtracting the PSF reveals residuals larger than PSF model uncertainties in the region around 0.5-1.5 arcsec where the nuclear contribution decreases and the galaxy luminosity rises, the nebulosity associated to the galaxy surrounding the nucleus can be resolved and a second fitting procedure is applied by using a two components model, i.e. a point source (PSF) plus a galaxy model described by a Sersic (1963) law, convolved to the proper PSF model. The Sersic model generally represents a good description of different light concentrations in galaxies and is commonly expressed as a surface-projected brightness profile such that

$$I(r) = I_e \; exp \left\{ -b_{n_s} \left[\left(\frac{r}{r_e} \right)^{1/n_s} - 1 \right] \right\} \tag{4.1}$$

where I_e is the intensity at the effective radius R_e that encloses half of the total light and n_s is a parameter called Sersic index, which controls the curvature of the stellar light profile. The smaller n_s, less centrally concentrated is the galaxy profile.

QSOs profiles which after PSF subtraction present no significant residuals are considered to have an unresolved host galaxy. The two fit outputs are compared by the $\chi^2_{PSF}/\chi^2_{PSF+host}$ ratio and visually inspected for a sure subdivision. The result is a classification of the host galaxies of the sample as *resolved* (R), *marginally resolved* (M) or *unresolved* (U) from the nuclear component. In Figure 4.5 we show an example of the adopted analysis outputs and in Figure 4.18 all the fits of our sources are reported.

4.3.3. Luminosity of the quasar pair host galaxies

For most of our sources the two component model fits better than the pure PSF profile. Statistically for resolved host galaxies $\chi^2_{PSF}/\chi^2_{PSF+host}$ ratio is above 1.1, around 1 for unresolved, and intermediate values for marginally resolved hosts. The nucleus and host

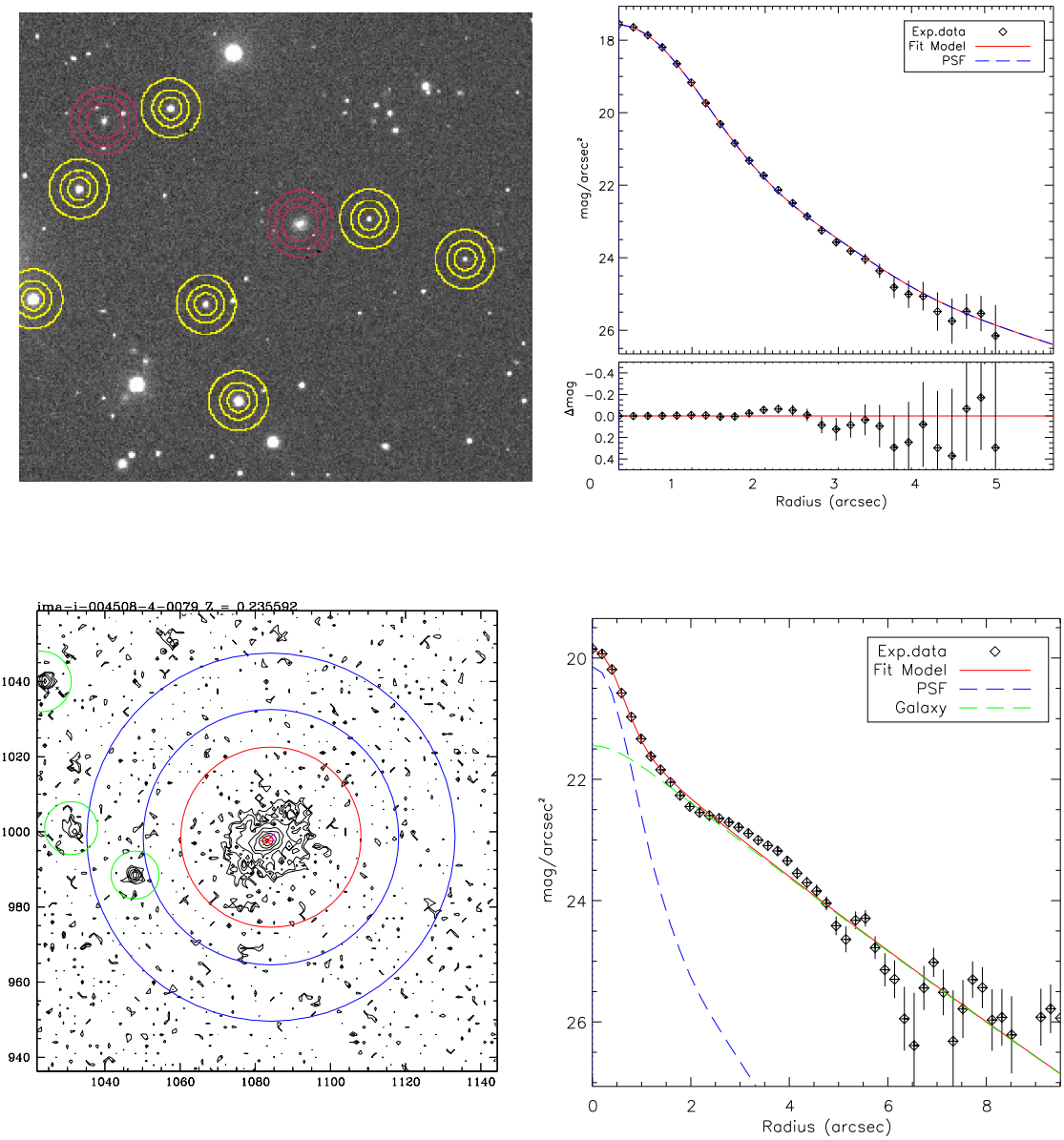

Figure 4.5.: Example of the nucleus and host galaxy luminosity decomposition performed by AIDA (see Falomo et al. 2014, for more details). Panels are related to the QSOs in the pair nr. 4 at redshift 0.2356. *Top right*: Image of the field. Stars selected for PSF modeling are in yellow circles The inner circle defines the region of the fit for each star, the outer annulus identifies the background. The red circles are the same for the two QSOs of the pair. *Top left*: Modeled light profile of the PSF. *Bottom right*: Contour plot of the QSO A. Fitting galaxy area and background annulus are marked (in red and in blue, respectively). Green circles are masks set to exclude nearby galaxies to the regions of interest. *Bottom left*: Average radial brightness profile of the QSO A fitted by the scaled PSF for the nucleus (blue dashed line) plus the the the host galaxy model convolved with the PSF (green dashed line), see the text. The overall best fit is represented by the red solid line.

Table 4.4.: Best-Fit Parameters in the modeling of the QSO images and luminosities.

QSO ID	z	χ^2_{PSF}/χ^2_{cg}	Class	i_{nuc} [mag]	i_{host} [mag]	Ellip	n_{Ser}	$M_{R,nuc}$ [mag]	$M_{R,host}$ [mag]	N/H
a	b	c	d	e	f	g	h	i	j	k
1A	0.4865	1.03	R	19.90	21.61	0.24	0.90	-22.42	-21.07	3.50
B	0.4864	1.38	R	—	20.35	0.42	1.54	—	-22.33	—
2A	0.4240	1.53	R	21.68	19.51	0.26	5.00	-20.38	-22.74	0.10
B	0.4239	1.76	R	20.16	19.03	0.01	5.00	-21.9	-23.22	0.30
3A	0.5011	1.35	R	19.19	19.55	0.32	2.45	-23.23	-23.27	1.30
B	0.5017	1.21	R	19.45	19.90	0.32	5.00	-22.97	-22.94	1.00
4A	0.2357	2.57	R	19.65	17.92	030	1.11	-20.64	-22.66	0.20
B	0.2356	1.44	R	19.29	19.68	0.44	0.90	-20.99	-20.90	1.10
5A	0.5353	1.26	R	18.90	19.76	0.35	1.65	-23.65	-23.27	1.10
B	0.5368	1.08	M	18.77	20.43	0.40	0.90	-23.79	-22.61	3.00
6A	0.5376	1.04	R	18.81	20.70	0.00	1.07	-23.74	-22.36	3.60
B	0.5352	1.07	M	18.72	20.53	0.18	0.90	-23.84	-22.51	3.40
7A	0.5420	1.51	R	18.68	19.48	0.60	1.17	-23.86	-23.55	1.30
B	0.5432	1.02	U	19.17	—	–	—	-23.37	—	—
8A	0.6340	1.08	R	20.50	19.98	0.21	2.88	-22.46	-23.64	0.30
B	0.6369	1.05	R	20.28	21.23	0.38	0.90	-22.70	-22.40	1.30
9A	0.7358	1.02	U	20.08	—	—	—	-23.01	—	—
B	0.7372	1.15	R	21.32	21.03	0.43	2.08	-22.05	-23.15	0.40
10A	0.7642	1.04	R	20.34	21.10	0.00	0.90	-23.13	-23.20	0.90
B	0.7615	1.02	R	19.25	19.69	0.72	0.90	-24.21	-24.59	0.70
11A	0.4386	1.13	M	19.35	19.34	0.49	5.00	-22.75	-22.98	0.80
B	0.4386	1.01	U	18.31	—	—-	—	-23.79	—	—
12A	0.8141	1.02	M	19.43	21.01	0.00	5.00	-24.33	-23.51	2.10
B	0.8144	1.07	R	19.99	20.27	0.83	3.35	-23.66	-24.25	0.60
13A	0.6413	1.19	R	18.29	20.04	0.63	0.90	-24.73	-23.65	2.70
B	0.6422	1.01	U	20.64	—	—	—	-22.39	—	—
14A	0.8069	1.06	R	22.05	22.27	0.90	0.90	-21.75	-22.37	0.60
B	0.8087	1.04	M	19.99	21.97	0.38	0.90	-23.82	-22.68	2.90

Notes. (a) QSO identifier. (b) Redshift from [O III]λ5007 line. (c) Ratio of χ^2 values between the best pure PSF model fit and the best PSF+galaxy model fit. (d) (R) Target with resolved galaxy, (M) marginally resolved galaxy, (U) unresolved galaxy. (e) and (f) Apparent i-magnitude (AB system) of the nucleus and host galaxy, respectively. (f) Host galaxy effective radius. (g) Host galaxy ellipticity. (h) Sersic model parameter for the host galaxy. (i) and (j) Absolute rest-frame R-band magnitude (Vega system, k-corrected and dereddered) of the nucleus and the host galaxy, respe (k) Nuclear-to-host-galaxy luminosity ratio.

Table 4.5.: Host galaxy and black hole masses estimations.

QSO ID	$log(M/L)_{host}$ $[M_\odot/L_\odot]$	$logM_{host}$ $[M_\odot]$	M_{host} $[10^{12}M_\odot]$	B/T	$logM_{bulge}$ $[M_\odot]$	M_{BH} $[10^8 M_\odot]$	$logM_{BH}$ $[M_\odot]$	$logM_{BH}$ $[M_\odot]$
a	b	c	d	e	f	g	h	i
1A	0.63	10.96	0.09	0.114	10.01	0.9	7.93	7.30
B	0.63	11.46	0.3	0.297	10.93	1.5	8.18	8.20
2A	0.65	11.64	0.4	–	11.64	2.7	8.42	8.88
B	0.65	11.83	0.7	–	11.83	3.4	8.54	9.07
3A	0.62	11.83	0.7	0.557	11.58	3.7	8.57	8.82
B	0.62	11.70	0.5	–	11.7	4.5	8.65	8.94
4A	0.71	11.67	0.5	0.174	10.92	1.9	8.29	8.18
B	0.71	10.97	0.09	0.114	10.03	0.5	7.70	7.32
5A	0.61	11.82	0.6	0.329	11.34	4.1	8.61	8.59
B	0.61	11.56	0.4	0.114	10.62	2.9	8.47	7.89
6A	0.61	11.46	0.3	0.163	10.67	2.6	8.42	7.94
B	0.61	11.52	0.3	0.114	10.58	0.9	7.93	7.85
7A	0.61	11.93	0.9	0.191	11.21	1.8	8.26	8.47
B	–	—	—	–	–	19.6	9.29	–
8A	0.59	11.94	0.9	0.680	11.78	2.5	8.40	9.01
B	0.59	11.45	0.3	0.114	10.5	5.0	8.70	7.78
9A	0.55	—	—	–	–	2.8	8.44	–
B	0.55	11.71	0.5	0.451	11.37	2.2	8.34	8.62
10A	0.55	11.73	0.5	0.114	10.78	1.1	8.05	8.05
B	0.55	12.28	1.9	0.114	11.34	7.4	8.87	8.59
11A	0.64	11.73	0.5	–	11.73	16.7	9.23	8.97
B	–	—	—	–	–	0.2	7.25	–
12A	—	11.84	0.7	–	11.84	10.1	9.00	9.07
B	0.53	12.13	1.4	0.814	12.04	3.2	8.51	9.27
13A	0.58	11.94	0.9	0.114	11	36.4	9.51	8.26
B	—	—	—	–	–	0.2	7.30	–
14A	0.53	11.38	0.3	0.114	10.44	0.5	7.73	7.72
B	0.53	11.51	0.3	0.114	10.56	2.9	8.46	7.84

Notes. (a) QSO identifier. (b) Mass to luminosity ratio of the host galaxy, assuming that the stellar population formed in a single burst of star formation at z_{burst}= 5.. (c) and (d) Stellar mass of host galaxy (upper limit, see the text). (e) Bulge to total stellar mass of the galaxy. (f) Bulge stellar mass. (g) and (h) Black hole masses derived by Vestergaard & Peterson (2006) recipe for H_β line. (i) Black hole masses from the $M_{BH} - M_{host}$ relation in Sanghvi et al. (2014) using the host masses M_{host} corrected for the disk components.

properties resulting from the best-fit image modeling analysis and individual examination are reported in Table 4.4, where 19 galaxies are resolved, 5 appear marginally resolved and 4 are unresolved. For resolved and marginally resolved galaxies we are able to derive the host magnitudes and for ten pairs we characterized the host galaxy properties of both QSOs. The Sersic index n_s for a significant fraction of QSOs in pairs tends to be ~ 1 (Table 4.4), indicating the presence of a not negligible number of disk-type host galaxy or with some disk component.

The measured i magnitudes (AB system) of the nucleus and of the host galaxy are also reported in Table 4.4, together with the rest frame Vega M_R magnitude, dereddened and k-corrected. Corrections for galactic extinction were taken from SDSS database. The host galaxies k-correction came from the elliptical galaxy spectral energy distribution of Mannucci et al. (2001), while for the nuclei we adopted the composite QSO spectrum template of Francis et al. (2001). In both the cases the i and R filter responses in color transformations are taken into account.

We find that the rest frame magnitude $M_{R,host}$ of the host galaxies ranges between -21 and -24.5 (mean -22.9 $\pm$ 0.8 ; median -23.2 $\pm$ 0.4). The $M_{R,host}$ distribution for QSOs in pairs is compared with the large sample in Falomo et al. (2014) containing QSOs with z<5 and the subsample of QSOs at $z < 0.85$ drawn from several campaigns and collected by Decarli et al. (2010), see references therein. We recover 44 observations of low-redshift (z<0.5) QSOs imagined by HST-Wild field Camera and 12 NIR ground-observed QSOs at $0.5< z <0.85$. The QSO pairs hosts have magnitudes encompassed between M* ($M^*_R = -21.2$ mag, Nakamura et al. 2003) and M*−3, with the bulk between M*-1 and M*+2, as expressed by several authors for isolated QSOs (e.g. Kotilainen et al. 2009). No obvious differences were found between the magnitude distributions represented in Figure 4.6. The indication is that the two families of QSO (individuals and in pairs) are indistinguishable from this point of view.

QSO pairs magnitude shows a overall increase with redshift, as shown in Figure 4.7.

4.3.4. Host masses of QSO pairs

We inferred the stellar mass of the host galaxies from their luminosity and presumed history. To derive the host masses the Mass to Light ratio M/L of the stellar population of the galaxies hosting QSOs a basis task is to understand how of stellar content evolves from its formation to the time of QSO activity.

Low redshift QSO are hosted in a variety of galaxies from pure ellipticals to complex/composite morphologies (see Section 4.4.3) and show an increase of the host luminosity with the redshift. A similar trend was also reported over a wider redshift range by Falomo et al. (2014) and Kotilainen et al. (2009). In addition, Decarli et al. (2010) found that the host galaxies, albeit with large spread of individual values, follow on average a similar trend.

To obtain an information about the host masses one may assume that the mass-to-light ratio passively evolves from the formation at $z = z_{burst}$ down to the present age This allow us to derive good estimations for the elliptical galaxies, for the other ones it gives an upper limit to the mass with respect the case of a diluted star formation or the occurring of other starbursts. For our purposes, at the moment, this description is acceptable. but t he evolution of M/L deserves further investigations. In this chapter, in

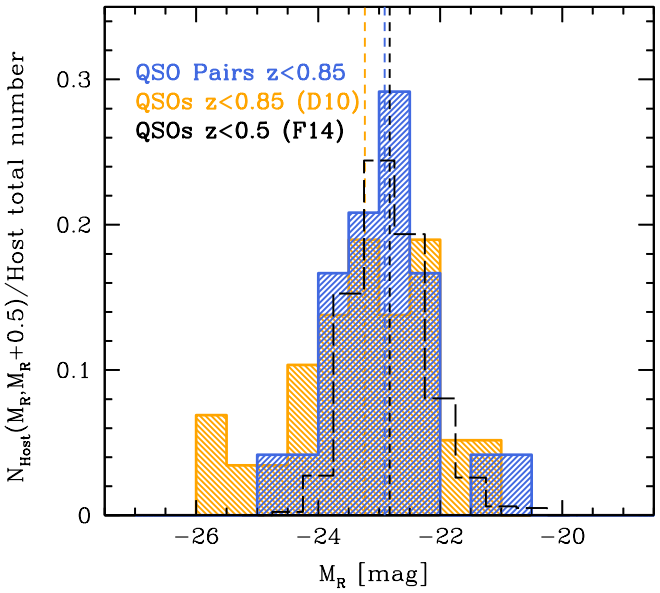

Figure 4.6.: Rest frame R-band magnitude distributions of the resolved and marginally resolved host galaxies: for QSOs in pairs (blue histogram), for the 58 isolated QSO host masses at $z < 0.85$ in Decarli et al. (2010) (yellow histogram), and for the $\sim$ 400 resolved QSOs host galaxies at redshift (z<0.5) in Falomo et al. (2014) (black line). Dashed lines mark the mean R mag of the distributions

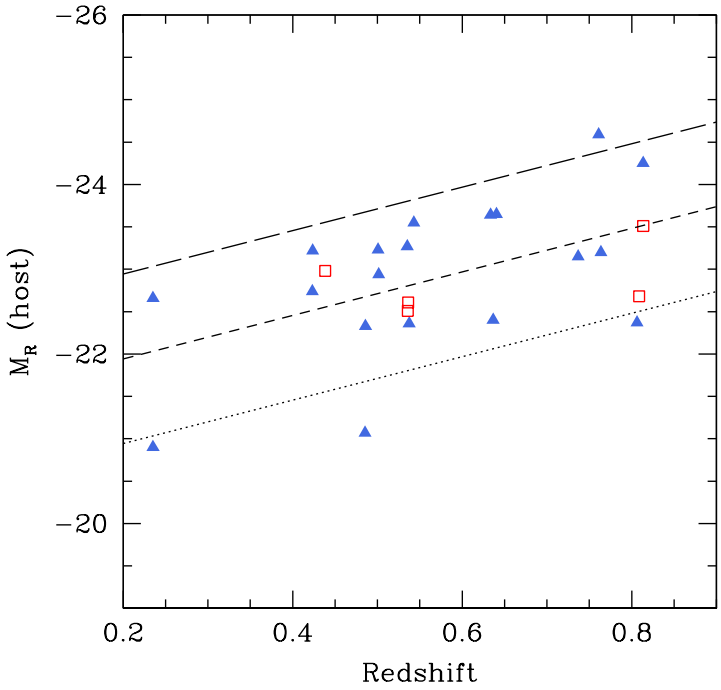

Figure 4.7.: R absolute magnitudes ($M_{R,host}$) of the resolved (blue fill triangles) and marginally resolved (red empty squares) host galaxies of QSO in pairs at different redshifts. The correlation between luminosity and z is marked by the central dashed line. The other two lines are obtained by shifting of $\pm$ 1 mag the central best fit line.

order to determine the mass of the host, we follow Kotilainen et al. (2009) and Decarli et al. (2010). We assumed the picture in which the stellar population was generated by an instantaneous star formation burst at $z_{burst} = 5$. We adopted the stellar evolution model of Bruzual & Charlot (2003) to derive the mass-to-light ratio in R-band as a function of cosmic time. By its interpolation at the redshift of the QSO we get the stellar mass of the host galaxy (for bulge-dominated galaxies). Table 4.4 summarizes the results described. The host masses are mainly concentrated between ~ 1 and $\sim 20 \cdot 10^{11} M_{\odot}$ around the average value of $6 \pm 0.2 \cdot 10^{11} M_{\odot}$ and are distributed similarly to the mentioned subsample of isolated QSOs at $z < 0.85$ in Decarli et al. (2010).

4.4. Nuclei of QSO pairs

4.4.1. Black Holes luminosities

We derive i-band (observer-frame) and rest-frame R-band magnitudes as described in Subsection 4.3.1. The nucleus absolute magnitudes $M_{R,nuc}$ span from ~ -25 to ~ -20.5 with mean $< M_{R,nuc} >= -23.0 \pm 1.1$ (median -23.1 ± 0.7). Our measurements are fully compatible with those of Falomo et al. (2014) for isolated QSO in Stripe82. It should be noted that about half of observed QSOs show a nucleus/host luminosity ratio < 1. For marginally resolved sources nucleus/host luminosity ratio is $\gtrsim 1$. A correlation between the overall luminosity of nuclei and hosts within the pairs is apparent. Least square best fit is $M_{R,host} = 0.34 \cdot M_{R,nuc} - 15.12$.

4.4.2. The mass of quasar black holes: the single-epoch spectrum approach

We estimated the M_{host} from imagine observations. To obtain the black hole masses M_{BH} the single-epoch method (see e.g. **?**, and references therein) is applied. We characterized the nuclei of the QSO pairs, following the recipes based on one-epoch spectra.

The spectrum of the AGNs, and QSOs in particular, is characterized by a strong continuum emission, resulting from the nucleus, superimposed to broad and narrow emission lines from gas clouds orbiting in different size regions from the central black hole. A continuum of stellar origin from the surrounding galaxies and galactic absorptions and emissions are also present. The continuous towards the ultraviolet region is believed due to the BH accretion. The surrounding gas, dipped in the potential well of the BH, produce emission lines by photoionization or excitation from the continuum. The motion of the clouds and the strong gravitational field lead to the broadened profiles, from which the region is termed Broad Line Region (BLR). Variabilities in the continuum reflect in a delay τ in response from the BLR photoionization. Black hole mass can be inferred from the virial paradigm using the Reverberation Mapping technique (Blandford & McKee 1982; Peterson 1993):

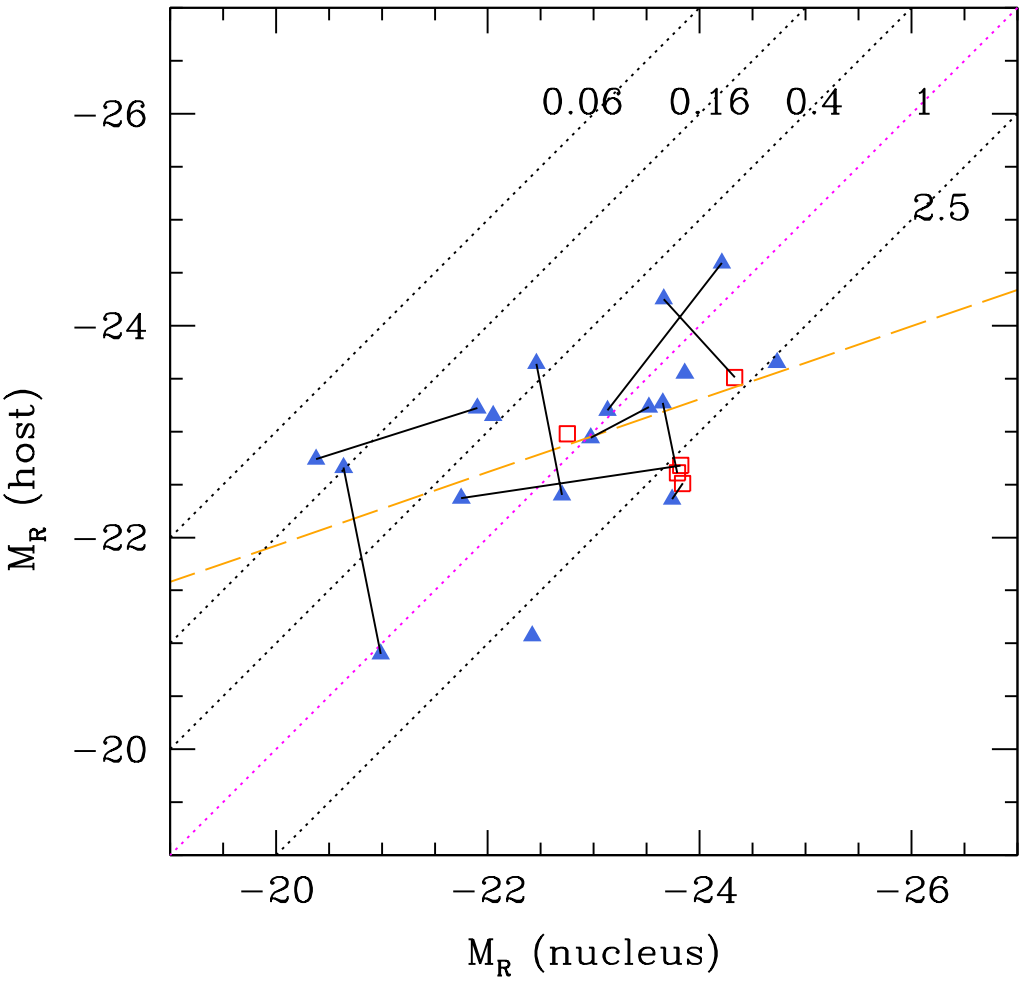

Figure 4.8.: R rest-frame magnitudes of nuclei ($M_{R,nuc}$) vs those of galaxies ($M_{R,host}$) for the resolved (filled blue triangles) and marginally resolved (open red squares) hosts in Table 4.4. Pair members are linked by a solid line. Yellow dashed line is the least squares fit for all the sources. Dotted lines trace the points of the plane in which the ratio L_{nuc}/L_{host} between the luminosities assumes the indicated constant value .

$$M_{BH} = \frac{v_{BLR}^2 \, R_{BLR}}{G} \tag{4.2}$$

where R_{BLR} is the size of the BLR as estimated by the mean emission-line lag $\tau = R_{BLR}/c$ and v_{BLR} is velocity of the emitting cloud. The virial velocity is inferred from the full width high maximum of the broad line

$$v = f \cdot FWHM \tag{4.3}$$

where f is a scale factor depending on the geometry of the BLR. Time-expensive observation campaigns, spanning many lag-cycles are needed to trace the line to continuum light curves. To date, this method has been applied to measure BLR radii in nearly 50 AGNs (e.g. Peterson et al. 2004; Denney et al. 2010; Bentz et al. 2009, 2010). This sample of reverberation mapped AGN is responsible for calibrating single-epoch M_{BH} estimates (e.g. Vestergaard 2002) for type I AGNs emission lines, is followed. through the BLR-size-to-luminosity relation. Indirectly, we can trace the black hole masses black hole masse for type I AGNs, and the assuming the continuum luminosity λL_λ as a proxy for the distance of the BLR clouds from the black hole on the basis of the correlation $R_{BLR} \propto L^\gamma$ (Kaspi et al. 2000; McLure & Jarvis 2002; Kaspi et al. 2005), where the power γ depends on the emission line used to measure the virial velocity. The great advantage of this method is the possibility of obtaining black hole mass estimates from single-epoch spectra. Various strong emission lines can be used as M_{BH} estimators: H_α, H_β, Mg_{II}, C_{IV}. We estimate the BH masses using the mass scaling relationship in Vestergaard & Peterson (2006) based on broad H_β line, suitable for our sample redshift range, and derived from detailed investigations of the BLR-size-to-L in the local universe:

$$\log M_{BH} = \log \left\{ \left[\frac{\mathrm{FWHM}(H_\beta)}{1000 \text{ km s}^{-1}} \right]^2 \left[\frac{\lambda L_\lambda (5100 \text{ Å})}{10^{44} \text{ erg sec}^{-1}} \right]^{0.50} \right\} + (6.91 \pm 0.02) \tag{4.4}$$

In Eq. 4.4 $L_\lambda(5100$ Å) and FWHM(H_β) are the optical continuum luminosity density and the full width high maximum for the H_β broad component.

4.4.3. Masses of black holes of QSO in pairs

For our sources we use the spectra retrieved from the SDSS archives, whose S/N ratios are listed in Table 4.3. We determined the black holefollowing the procedures in Decarli et al. (2010) and De Rosa et al. (2011). The non stellar continuum is defined, with respect the emission lines and the contribution of blended multiplets of Fe II, by interpolating the spectrum with a power law in wavelength windows where lines are not present. The Fe II multiplets are fitted using the empirical template of Vestergaard & Wilkes (2001) and the elliptical template of Mannucci et al. (2001) for the galaxy stellar light. The monochromatic flux λL_λ of the continuum is evaluated in a small range of 30-50 Å around 5100 Å and to evaluate the FWHM neglect the evaluation of the inner regions of the BLR for the benefit of a Sceta be affected dallla function for the fitting of the continuous and the noise of the spettr) we perform a fitting using two co-peaked gaussians, excluding the narrow line component of the H_β line.

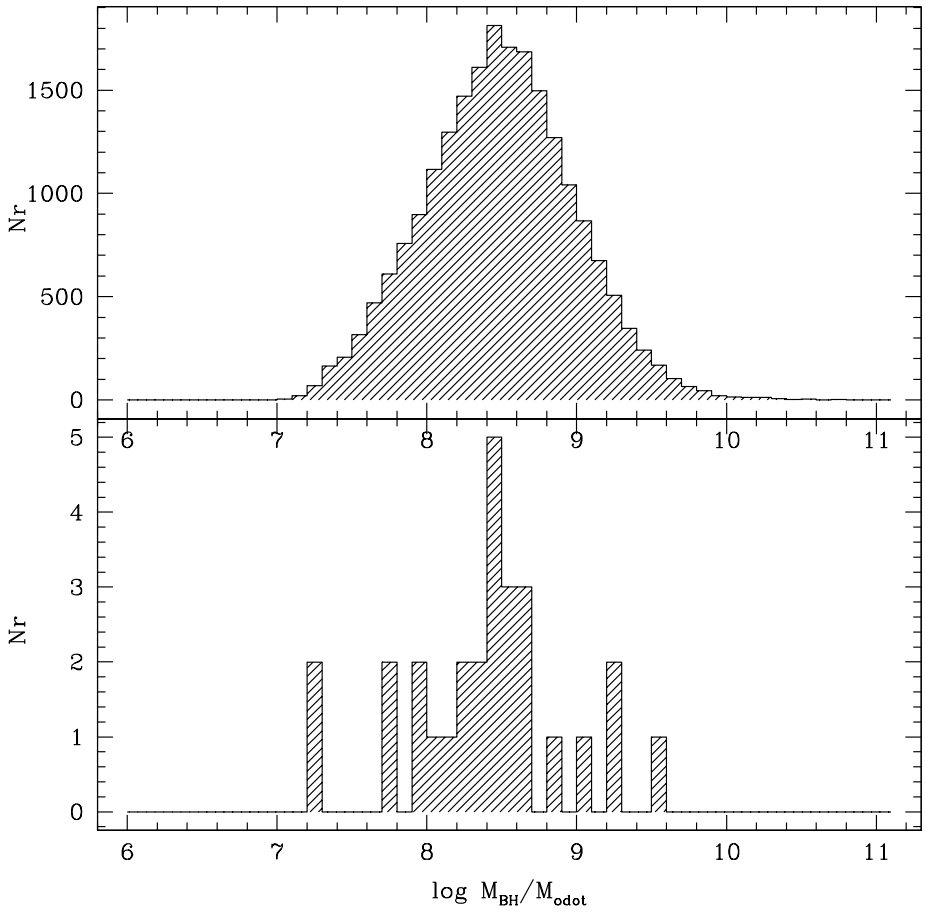

Figure 4.9.: *Top panel*: M_{BH} distribution of the subsample of QSOs in Shen et al. (2011) at z<0.85, estimated using the Vestergaard & Peterson (2006) recipe for H_β line. *Bottom panel*: M_{BH} distribution of QSOs in pairs.

Black hole masses are listed in Table 4.5, they range between $\sim 5 \cdot 10^7 M_\odot$ and . $\sim 4 \cdot 10^9 M_\odot$. The uncertainties associated with these measures of the mass are very large ($\gtrsim$ 0.4 dex) and are dominated by the dispersion of the relations between the radius of the BLR and the continuum luminosity.

Using this method Shen et al. (2011) estimated the M_{BH} from single epoch spectra for more than 100,000 QSOs from the Schneider et al. (2010) catalogue (SDSS DR7), up to z$\sim$5. We compared the BH masses of the QSO in pairs with the $\sim$ 21,000 QSOs at z<0.85 in Shen et al. (2011), having the BH masses virally estimated with the recipe for H_β. The distributions in Figure 4.9 show that that QSO pairs have BH which are representative of the total QSO population (DR7). of isolated QSOs despite the small size of our sample, and that the two families are equally distributed.

We estimated the M_{BH} of QSO pairs also by using the $M_{BH} - M_{host}$ relation reported in Sanghvi et al. (2014), holding over the entire $M_{BH} - M_{host}$ parameter space ($10^7 < M_{BH} < 10^{10.5}$ and $10^{9.5} < M_{bulge} < 10^{13}$):

$$log\frac{M_{BH}}{10^{8.5} M_\odot} = (0.97 \pm\ 0.15) \cdot log\frac{M_{host}}{10^{11.7} M_\odot} + (0.44 \pm 0.11) \tag{4.5}$$

On average virial BH masses are $\sim -50\%$ lower than those derive from Eq. 4.5.

The morphology of the host galaxies is quite complex, with spheroidal and disk component both often present. The abundance of disk-like host galaxies ($\sim$ 40-50 %) in our sample, described by a Sersic law with small index $n_s \lesssim 1$, can cause an overestimation of the bulge masses, due to the assumptions of an elliptical mass-to-light ratio in our photometric approach in deriving M_{host}. As the black hole mass is better correlated with the bulge component, a correction was applied following Sanghvi et al. (2014) to those QSOs having a disk component revealed by the Sersic index < 4. Bulge to total stellar mass can be obtained as:

$$\frac{B}{T} = \frac{n_s - 0.5}{3.5} \tag{4.6}$$

The estimations of the corrected host masses, M_{bulge} (mass of the bulge), are collected in Table 4.4. By using M_{bulge} in Eq. 4.6 on average M_{BH} measures come closer to those derived from Vestergaard & Peterson (2006) recipe, although with some dispersion, see values in Table 4.5.

It is of interest locate the QSOs in pairs in the $M_{BH} - M_{host}$ plane after disk-component correction. As it is shown in Figure 4.10 QSO pairs span the region covered by the isolated QSOs. This is an indication of the unbiased selection, and a confirmation that QSO in pairs at low redshift and with 10s-100s scale kpc separation resemble the whole set of isolated QSOs. We note that the $M_{BH} - M_{host}$ relation closely approaches the Marconi & Hunt (2003) relation for inactive galaxies (see Figure 4.10).

4.5. Galaxy environment of the QSO pairs

4.5.1. Catalogues of galaxies

In order to characterize the QSO pair environments, we analyzed the distribution of galaxies around the QSOs using SDSS DR10 catalogues. From these we obtained position and photometry of galaxies by selecting all primary objects photometrically classified

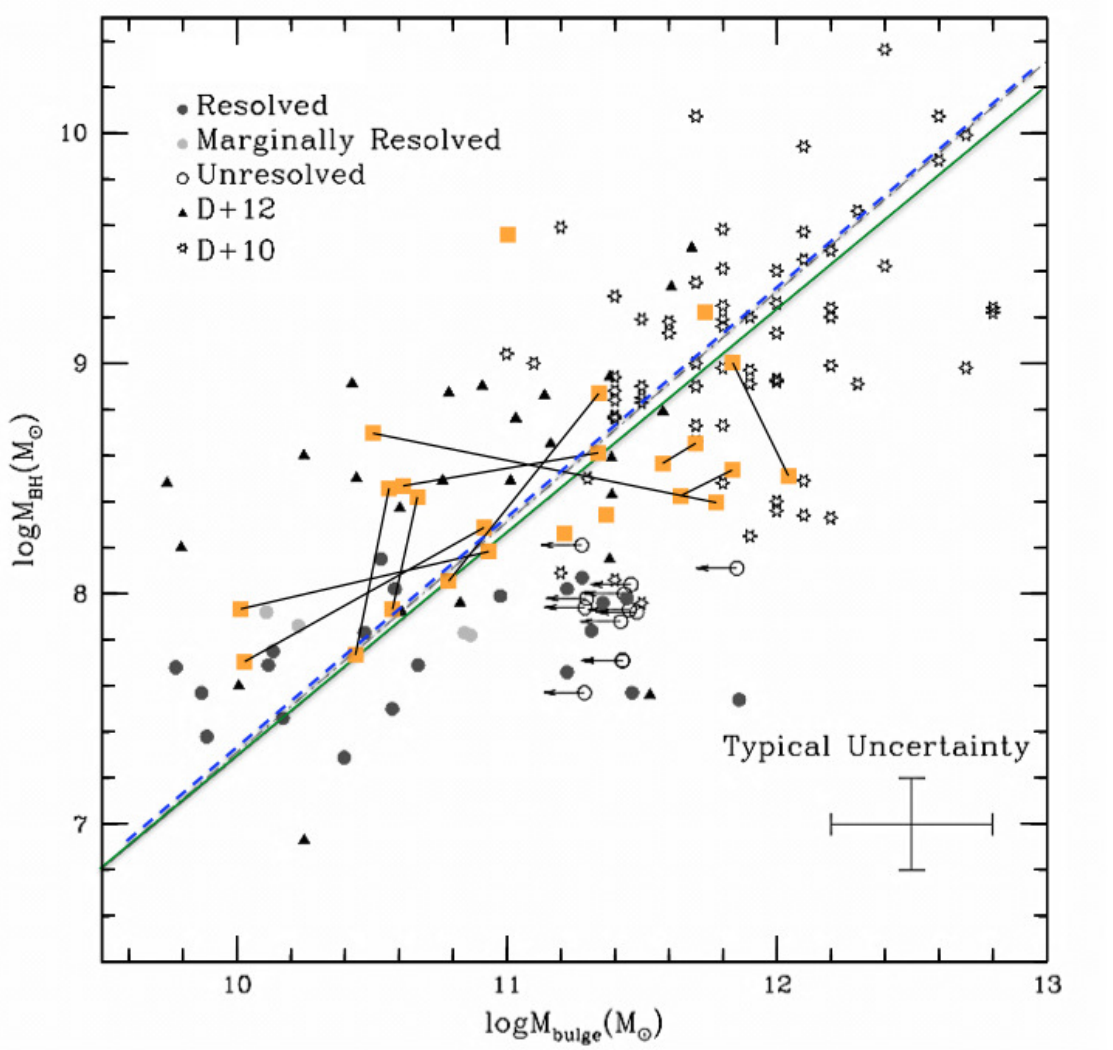

Figure 4.10.: QSOs in pairs (yellow squares) of our sample in the $M_{BH} - M_{host}$ plane, after stellar bulge correction for the disk component of the host galaxies. liar bulge with the best linear fit (dashed red line). Companions QSOs are connected with a line The other points are isolate QSOs : circles are from Sanghvi et al. (2014), stars from Decarli et al. (2010) and triangles from Decarli et al. (2012). The best bilinear regression fit is shown for the entire resolved sample of isolated QSOs as green solid line. The regression fit for the local relation for inactive galaxies by Marconi & Hunt (2003) is shown and as blue dashed line (from Sanghvi et al. (2014)). A typical error bar is shown in the lower right corner.

as galaxies. SDSS uses a classification based on the difference between the cmodelMag (composite de Vaucouleurs and exponential model) and PSF magnitude.

In each QSO pair field, we analyzed the i-band surface distributions of the SDSS galaxies and stars within a circular area of 15 arcmin radius, corresponding to a projected distance of 3.4 Mpc from the nearest pair (z=0.236) and 9.3 Mpc from the farthest (z=0.807). To estimate the completeness of the SDSS galaxy catalogues we compared the differential number counts of detected galaxies as a function of the magnitude with the very deep galaxy count data available from the Durham University Cosmology Group[4]. In particular for each field we considered as threshold the magnitude $m_{i,50\%}$ where the completeness of observed galaxies drops to 50% of that expected from Capak et al. (2007) (see Figure 4.11). The apparent i-magnitude thresholds are closely distributed around the mean value of 21.96 ± 0.09 and listed in Table 4.6 with the corresponding absolute k-corrected magnitudes. With these thresholds we can observe galaxies with magnitude M^*+2 at z < 0.3, M^*+1 at $z \lesssim 0.5$ and M^* at $z \lesssim 0.8$, see Figure 4.12, where $M^* = -21.9$ (Loveday et al. 2012).

Contextually, in order to verify the SDSS outputs both in terms of classification and photometry we measured the ellipticity and the FWHM of the pipeline-classified as galaxies and stars. We used IRAF tools to measure magnitudes of objects in four QSO pair fields characterized by different seeings. Comparisons with SDSS photometry at different radii of aperture show good matches below $i \sim 22$ mag or some more, as it is illustrated in "one to one" plots in Figure 4.13 (reported in Table 4.6). These limits all above the threshold magnitudes $m_{i,50\%}$ of our investigation.

4.5.2. Galaxy count

To evaluate the surface number density of galaxies in the background, n_{bg}, we considered the galaxies with $i < m_{i,50\%}$ and projected angular distance between 7 and 15 arcmin from the midpoint of the QSO pair. This corresponds to a minimum distance from the QSO of ∼ 1.6 Mpc for the nearest target, see Figure 4.14. The region was then divided into annuli with width of 1 arcmin. We compute n_{bg} as the median of the galaxy surface density of each annulus and the semi interquartile range is assumed as scatter and list in Table 4.6, see also Figure 4.16, top left panel. To determine the count of galaxies in the fields around the pairs a question arises of how to measure the gradient of density of galaxies with the distance from the targets, whether from the midpoint or from the position of each objects. For each QSO pair we counted the surface number density of galaxies in a number of annuli with width of 250 kpc up to 2.5 Mpc from each target and from the pair midpoint. Figures 4.14 and 4.15 illustrate the procedures for the galaxy counts.

4.5.3. Galaxy overdensity around QSOs in pairs

We study the galaxy environment following the procedure described in Karhunen et al. (2014). The galaxy overdensity of the QSO environment is measured as the ratio between the surface density of the observed galaxies in a bin of projected distance centered in r

[4]Durham University Cosmology Group, references and data in
`http://astro.dur.ac.uk/~nm/pubhtml/counts/counts.html`

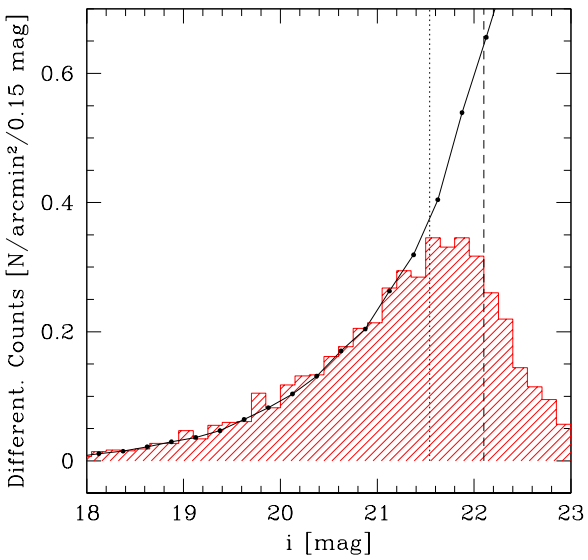

Figure 4.11.: Number counts of galaxies as a function of i-magnitude in the field of QSO pair nr. 2 (red histogram). The black solid line represents for comparison the counts from deep survey of Capak et al. (2007). The dotted and dashed vertical lines mark the median magnitude and 50% completeness threshold.

Table 4.6.: Measurements for galaxy count.

Pair Nr (a)	seeing [arcsec] (b)	$m_{i,50\%}$ [mag] (c)	$M_{i,50\%}$ [mag] (d)	n_{bg} [arcmin^{-2}] (e)	n_{bg} [Mpc^{-2}] (f)
1	1.14	21.9	-20.39	3.40 ± 0.10	26.20 ± 0.80
2	0.93	22.1	-19.85	4.01 ± 0.10	36.15 ± 2.71
3	0.99	21.9	-20.46	3.09 ± 0.16	23.16 ± 1.49
4	0.88	21.9	-18.44	2.24 ± 0.29	44.14 ± 6.02
5	1.20	21.9	-20.63	3.21 ± 0.09	22.30 ± 0.70
6	0.98	21.9	-20.64	3.27 ± 0.16	22.97 ± 1.39
7	1.09	21.8	-20.77	3.15 ± 0.15	21.98 ± 0.69
8	1.13	21.9	-21.08	3.06 ± 0.14	18.40 ± 0.59
9	0.83	22.0	-21.45	3.38 ± 0.16	17.85 ± 1.05
10	1.16	22.0	-21.55	3.41 ± 0.18	17.40 ± 1.02
11	1.14	22.0	-20.03	3.86 ± 0.10	33.88 ± 0.87
12	1.13	22.1	-21.61	4.56 ± 0.23	22.47 ± 0.98
13	0.93	22.0	-21.01	2.89 ± 0.27	17.05 ± 1.76
14	0.91	22.1	-21.59	4.10 ± 0.27	20.15 ± 1.47

Notes: (a) QSO pair identification number . (b) Seeing of the image containing the QSO pair. (c) Apparent SDSSi-magnitude threshold. (d) Absolute magnitude corresponding to $m_{i,50\%}$. (e) and (f) Background surface number density of galaxies in arcmin^{-2} and in Mpc^{-2}, respectively.

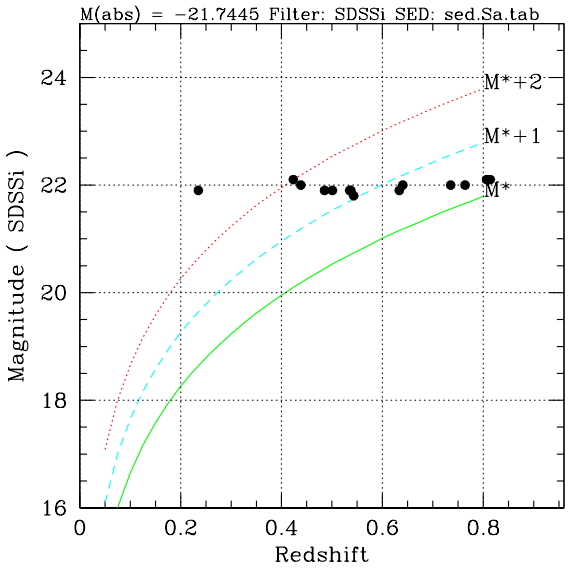

Figure 4.12.: Apparent i magnitude thresholds as function of the redshift of the pairs. Lines represent the apparent i magnitude of M* (solid green line), M*+1 (cyan dashed line) and M*+2 (red dotted line) at different redshift. Lines are derived from Montero-Dorta & Prada (2009).

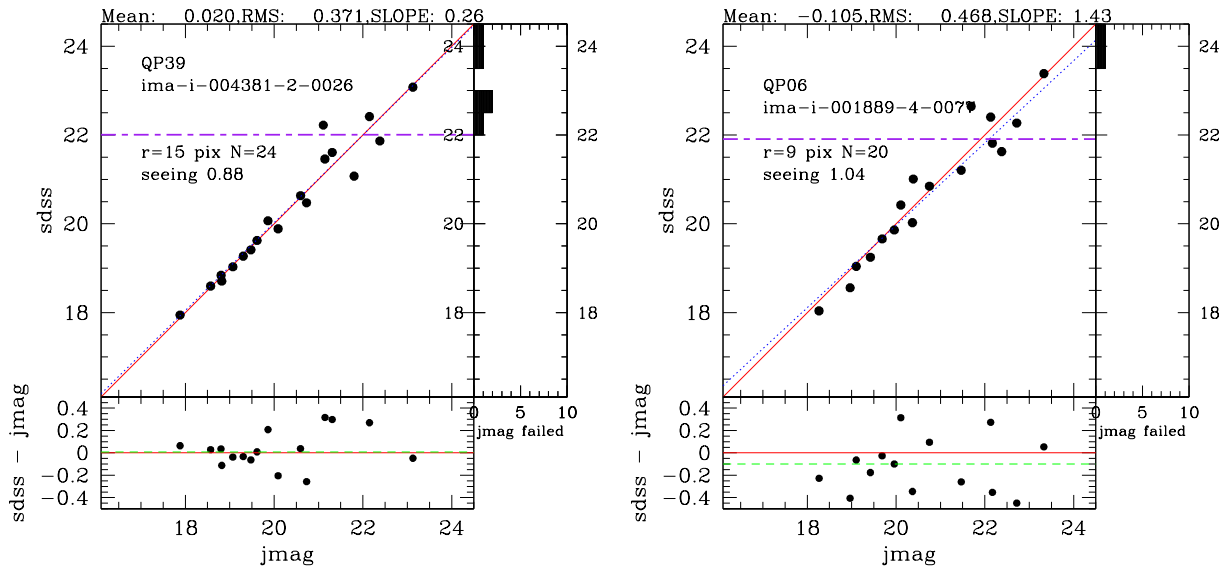

Figure 4.13.: Examples of SDSS and IRAF galaxy photometry comparison on images at different seeings and using different radii of aperture. Histograms on the right report the number of failed IRAF-recipes measurements in bins of SDSS photometry. Purple dashed lines mark the 50% galaxy completeness limits. *Left panel*: Seeing 0.88 and aperture radius 15 pixels. *Right panel:* Seeing 1.04 and aperture radius 9 pixels.

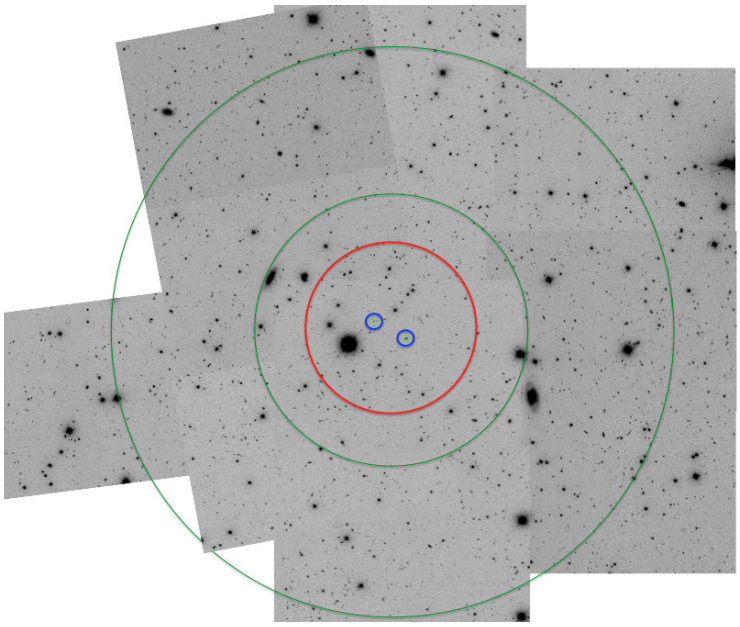

Figure 4.14.: Galaxy count regions around QSO pairs: Background region is encompassed between the two green radii, located at 7 and 15 arcmin from the midpoint of the QSO pair. Blue circles mark the two sources and the environment inner region $<$ 1 Mpc at the redshift of the pairs is enclosed in the red circle. The figure refers to the QSO pair nr. 4, z=0.235.

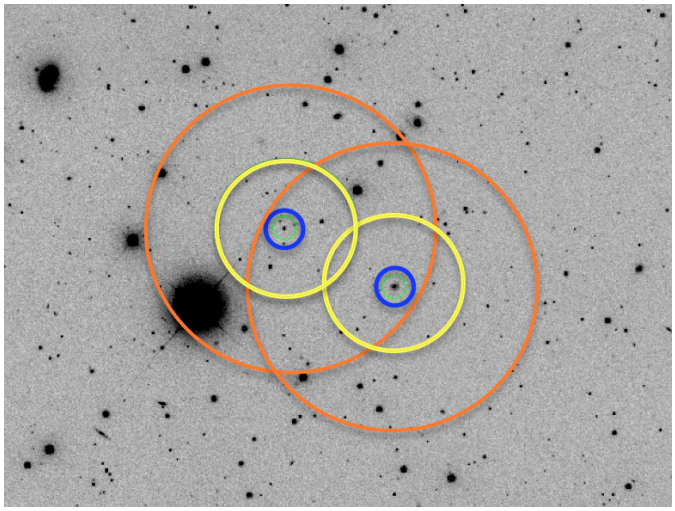

Figure 4.15.: Galaxy count regions around QSO pairs: 250 kpc and 500 kpc wide annuli around both QSOs in the pair (yellow and orange circle, respectively). For a comparison with the mean environment around isolated QSOs (Section 4.5.4), the excess of galaxies with respect the background, if present in the overlapping region defined by the same radius, is equally subdivided to each QSO. The figure refers to the QSO pair nr. 4, z=0.235.

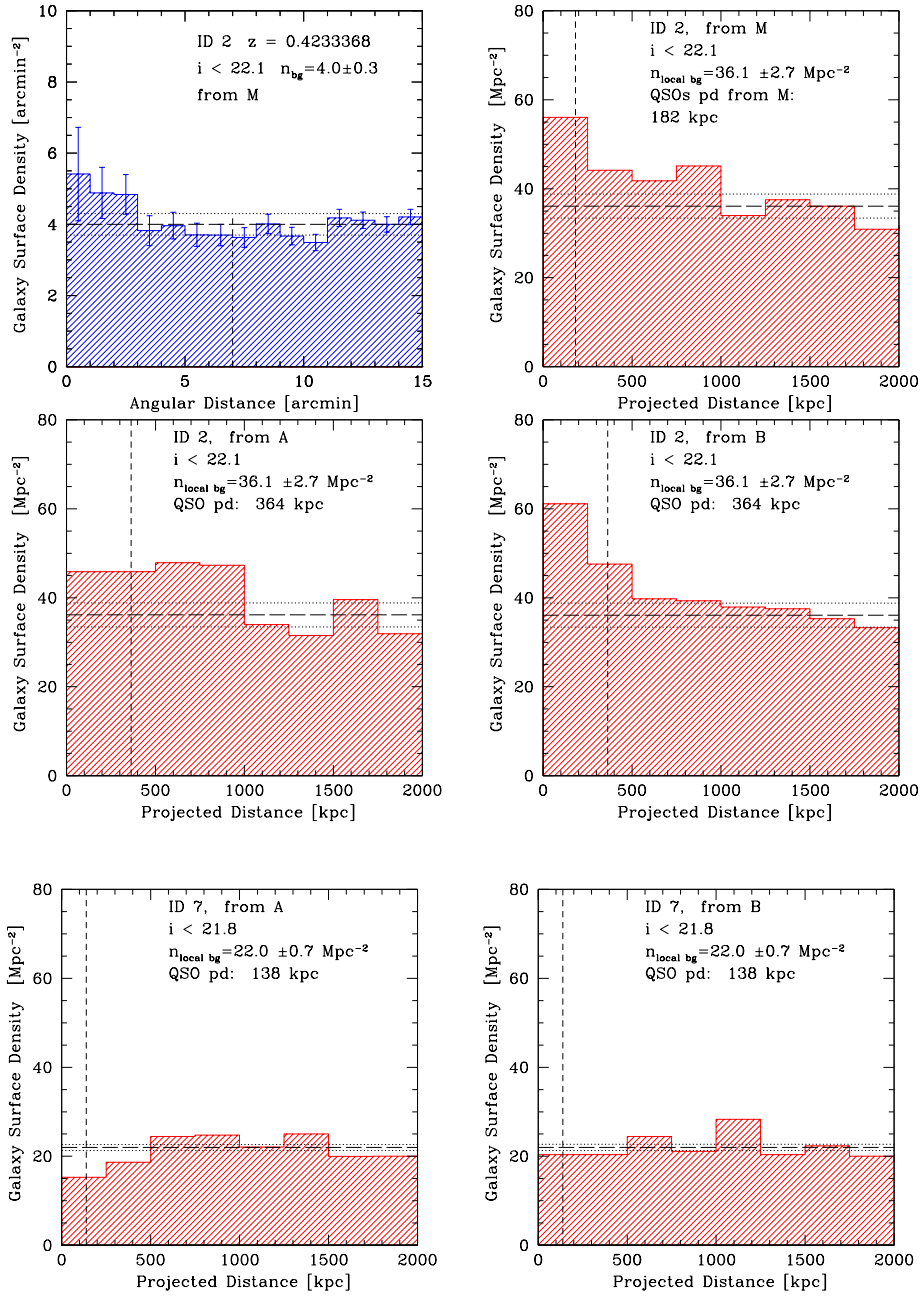

Figure 4.16.: Examples of surface density distributions of galaxies in the field of our QSO pairs. *Top and central panels*: Blue histogram is the differential surface density distribution of galaxies (i $< m_{50\%}$) with the angular distance, within a radius of 15 arcmin from the midpoint M of the two QSOs of the pairs n. 2. We consider as background the median of the surface galaxy densities evaluated in 1 arcmin wide bins of angular distance between this value and 15 arcmin. The vertical dashed line marks the distance of 7 arcmin from M. The background galaxy density n_{bg} and its uncertainty are marked in all the panels of this figure by the horizontal dashed line and the dotted lines, respectively. Red histograms: Differential surface density distributions of galaxies (i$< m_{50\%}$) within 2000 kpc at the redshift of the foreground QSO, starting from M and from the position of each QSO . In all the panels, the vertical dashed line marks the position of the second QSO when the projected distance axis starts from QSO A or QSO B; the lines mark the position of both the QSOs when the horizontal axis starts from M. *Lower panels*: the same of central panels for the QSO pair nr. 7.

and that of the background: $n_{obs}(r)/n_{bg}$. A variety of galaxy distributions surround the QSO pairs (see Figure 4.16) exhibiting in some cases sub densities in proximity of both the QSOs (e.g. QSO pairs nr. 9, Table 4.6) or asymmetric distributions around the two QSOs (e.g. QSO pair nr. 12). We note that the region within 500 kpc include all the QSOs in our pairs and their immediate environments. On average, there is an evidence of overdensity signal within $\sim$ 1 Mpc from the QSO pairs.

Results of the cumulative overdensity as a function of the projected distance from the pair midpoint are shown in Table 4.11 and in Figure 4.19.

Table 4.7.: Statistics of galaxy in the QSO pair environments/1. Example of the galaxy overdensity estimation around single QSOs in pairs within 250 kpc and overdensity within 500 kpc.

Pair Nr (a)	$O_{0,25}(A)$ (b)	$O_{0,25}(B)$ (c)	$N_{0,25}(A)$ (d)	$N_{0,25}(B)$ (e)	N_I (f)	$N_{bg,I}$ (g)	$\mathcal{N}_{0.25}$(A) (h)	$\mathcal{N}_{0.25}$(B) (i)	$G_{0,25}(A)$ (j)	$G_{0,25}(B)$ (k)	$G_{0,5}(A)$ (l)	$G_{0,5}(B)$ (m)
1	1.36 ± 0.04	1.17 ± 0.04	7	6	0	0.6	7.0	6.0	1.36 ± 0.04	1.17 ± 0.02	1.21 ± 0.04	0.68 ± 0.02
2	1.27 ± 0.10	1.69 ± 0.13	9	12	3	1.4	8.1	11.1	1.14 ± 0.05	1.56 ± 0.08	1.14 ± 0.09	1.28 ± 0.10
3	1.54 ± 0.10	1.76 ± 0.11	7	8	7	4.4	5.4	6.4	1.20 ± 0.08	1.42 ± 0.09	1.04 ± 0.12	1.04 ± 0.15
4	0.46 ± 0.06	0.69 ± 0.09	4	6	0	0.5	4.0	6.0	0.46 ± 0.04	0.69 ± 0.04	0.89 ± 0.04	1.10 ± 0.04
5	2.06 ± 0.06	1.37 ± 0.04	9	6	6	3.5	7.7	4.7	1.75 ± 0.07	1.07 ± 0.07	1.27 ± 0.07	1.21 ± 0.07
6	1.11 ± 0.07	1.55 ± 0.09	5	7	1	0.6	4.8	6.8	1.06 ± 0.03	1.50 ± 0.07	0.87 ± 0.04	0.92 ± 0.07
7	0.46 ± 0.01	0.70 ±0.02	2	3	2	3.0	2.0	3.0	0.46 ± 0.09	0.70 ± 0.10	0.75 ± 0.15	0.87 ± 0.14
8	1.94 ± 0.06	1.11 ± 0.04	7	4	2	0.8	6.4	3.4	1.76 ± 0.07	0.93 ± 0.05	1.11 ± 0.07	1.25 ± 0.05
9	0.86 ± 0.05	0.86 ± 0.05	3	3	3	3.1	2.7	3.0	0.86 ± 0.04	0.86 ± 0.06	1.21 ± 0.04	0.93 ± 0.05
10	1.46 ± 0.09	1.76 ± 0.10	5	6	3	2.2	4.5	5.5	1.32 ± 0.06	1.61 ± 0.06	1.27 ± 0.07	1.13 ± 0.07
11	1.35 ± 0.03	1.35 ± 0.03	9	9	1	0.3	8.6	8.6	1.30 ± 0.03	1.30 ± 0.04	1.15 ± 0.04	1.07 ± 0.04
12	0.27 ± 0.01	1.59 ± 0.07	1	7	1	2.4	1.0	7.0	0.23 ± 0.05	1.59 ± 0.06	0.88 ± 0.05	1.51 ± 0.06
13	2.99 ± 0.31	2.99 ± 0.31	10	10	9	3.6	7.0	7.0	2.09 ± 0.03	2.09 ± 0.03	1.41 ± 0.02	1.33 ± 0.03
14	0.25 ± 0.02	1.01 ± 0.07	1	4	0	0.0	1.0	4.0	0.25 ± 0.03	1.01 ± 0.03	0.57 ± 0.03	0.70 ± 0.03

Notes: (a) QSO pair identification number . (b) and (c) Galaxy overdensity within 250 kpc from the QSO A and B, respectively, on the basis of the counts reported in columns (d) and (e). (f) Number of galaxies in the overlapping region. (g) Number of background galaxies + (1-σ) in the overlapping region. (h) and (i) Number of galaxies within 250 kpc after subdivision of excess galaxies with respect those in (g) to each QSO. (j) and (k) Galaxy overdensity within 250 and 500 kpc from the QSO A and B, corrected for the superposition of the companion environment. (l) and (m) The same within 500 kpc.

Table 4.8.: Comparison of the mean overdensity within 250 kpc around isolate QSOs from literature.

Serber et al. (2006)		Strand et al. (2008)	Karhunen et al. (2014)			
QSOs	L* Gal.	QSOs	Full sam.	Res. QSOs	Full contr.	Match. contr.
(a)	(b)	(c)	(d)	(e)	(f)	(g)
$M_i \lesssim -22$ $z \lesssim 0.4$	$M_i \lesssim -22$ $z \lesssim 0.4$	$-24.2 \lesssim M_i \lesssim -22$ $0.08 \lesssim z \lesssim 0.4$	$M_i \lesssim -24$ $0.1 < z < 0.5$	$M_i \lesssim -24$ $0.1 < z < 0.5$	$M_i \lesssim -24$ $0.1 < z < 0.5$	$M_i \lesssim -24$ $0.1 < z < 0.5$
1.57 ± 0.01	1.51 ± 0.01	1.41 ± 0.03	1.11 ± 0.04	1.12 ± 0.04	1.30 ± 0.08	1.40 ± 0.11

Notes: The mean overdensity is evaluated: (a), (c) and (d) around the full sample of QSOs; (b) around L* galaxies; (e) around QSOs with resolved host galaxies; (f) around inactive galaxies matching in redshifts with the full sample; (g) around inactive galaxies matching in redshift and spanning the same luminosity of resolved QSO hosts.

4.5.4. Comparison with isolated quasars and galaxies.

In order to take into account the contribution of galaxies on their position around the pair we considered the galaxies in annuli of 250 kpc projected distance width from the positions of both the QSOs A and B. The mean cumulative overdensities in the regions resulting from jointing the two same-radius circles from the QSOs is plotted in Figure4.17, top panel, where it is compared with the overdensity results around isolate quasars, drawn from the subsample of Karhunen et al. (2014) with i < 22 mag to take into account only galaxies matching in luminosity with ours.

In order to try a comparison with the isolated QSOs, in the case that the annuli around the two QSO are overlapping (see Figure 4.15), we have subdivided the excess galaxies in common to an equal number for each QSOs. This yields a distribution $G(r)$ which may deviate from the galaxy density of the field around the pair, as illustrated in the example in Table 4.7, especially when the two objects are close enough. The companion QSO host is excluded from the count with a view to keeping separated the environments. Results within 250 and 500 kpc are listed in Table 4.6.

The average cumulative overdensity distribution $G_{ave}(r)$ for the 28 QSOs is reported in Figure 4.17, bottom panel. On average, the galaxy overdensity around one single QSO in pair is indistinguishable from that of isolated QSOs. For each QSO in our sample we report in Table 4.6 the galaxy overdensity $G_{0.25}$ and $G_{0.5}$ inside radii of 250 and 500 kpc, respectively. For a full comparison with recent works, in Table 4.8 we report the overdensities within 250 kpc found around low-redshift isolated QSOs by Serber et al. (2006), Strand, Brunner, & Myers (2008) and Karhunen et al. (2014).

4.5.5. Galaxy overdensity dependence on QSO projected separation

As a natural consequence, on average we expect that close separations between the two QSOs should result in a high richness of galaxies at low projected distances. To aim this, we computed the galaxy overdensity around of the six pairs that are separated by less than 180 kpc and compare it with that expected under the assumption that

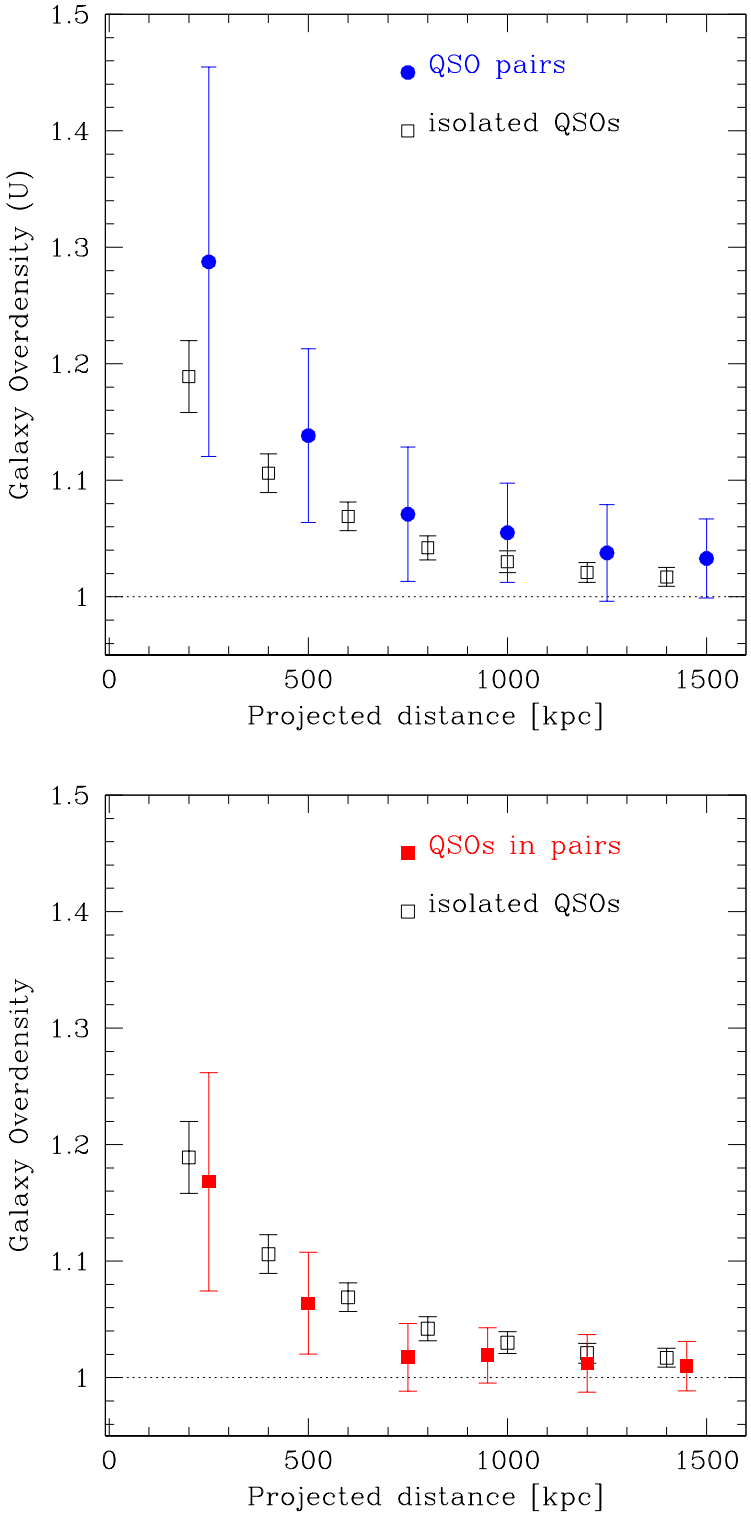

Figure 4.17.: *Top panel:* Mean cumulative overdensity of galaxies in the jointed circular areas with the same radius from each QSO. *Bottom panel:* Mean cumulative overdensity of galaxies around the individual QSOs in pairs, corrected for the superposition of the companion environment. The mean cumulative overdensity around isolated QSOs with i < 22 mag derived from the full QSO sample in Karhunen et al. (2014) is plotted for a comparison.

Table 4.9.: Observed and expected galaxy surface overdensities.

r (a)	$O_{obs,R_\perp<180}$ (b)	$O_{exp,full\ sample}$ (c)	$O_{exp,R_\perp<180}$ (d)	$O_{exp,R_\perp>180}$ (e)
250	1.598 ± 0.336	1.336 ± 0.188	1.568 ± 0.306	1.162 ± 0.234
750	1.103 ± 0.110	1.034 ± 0.058	1.104 ± 0.090	0.984 ± 0.076
1500	1.086 ± 0.035	1.020 ± 0.042	1.104 ± 0.040	0.956 ± 0.064

Notes: (a) Projected distance within which cumulative distribution is evaluated. (b) Observed cumulative mean galaxy distribution in the fields around the closer pairs (from M). (c), (d) and (e) Expected cumulative mean galaxy overdensity around the whole closer QSO pairs, derived assuming that each individual QSO of the full sample, only of the closer pairs and only of the larger pairs, respectively, contributes to the average value of galaxies.

each individual QSO contributes to the average value of galaxies (as given in Fig. 4.17, bottom panel).

The comparison, see Figure 4.18, and Table 4.9), suggests that closer QSO pairs may be in richer environments than those at larger separation, see Chapter 5.

We performed a Kolmomgorov-Smirnov test (KS test, see e.g Chakravarti et al 1967) comparing the galaxy overdensity distribution of QSO pairs with $R_\perp < 180$ kpc to that of QSO pairs with larger separations. For the cumulative galaxy overdensity up to 1500 kpc the KS test yields the probability p=0.08, see Figure 4.20. This indicates that the suggestion should be confirmed by a significantly larger sample. The mean overdensities around the pairs related to the two subsamples with QSO at closer and larger separations are plotted in Figure 4.19, right panel. On this issue see also Chapter 5.

4.6. Discussion

In the hierarchical scenario, quasars and physically bound quasar associations are expected to be located in regions with a higher density of galaxies on small scales than that of normal galaxy, where mergers are more likely to take place. Quasar pairs are usually believed to be a first tracer of clustering. With the aim of clarifying this issue, we have investigated the properties of the environments of a sample of 14 physical low-redshift QSO pairs.

We found that the QSOs in pairs are on average in regions of modest galaxy overdensity extending up to ~ 0.5 Mpc, with a weak signal up to $\sim$1 Mpc. This overdensity may be interpreted on average as a superposition of the overdensity around each QSO, i.e. if we divide the excess of galaxies (with respect the background) in the overlapping projected area, the overdensity is indistinguishable from that of a homogeneous sample of isolated QSOs (Karhunen et al. 2014), that is matched in host galaxy luminosity. In Karhunen et al. (2014) a complete comparison of the environments around isolated QSOs and inactive galaxies in the Stripe82 (Figure 4.21), matching in redshift and luminosity with

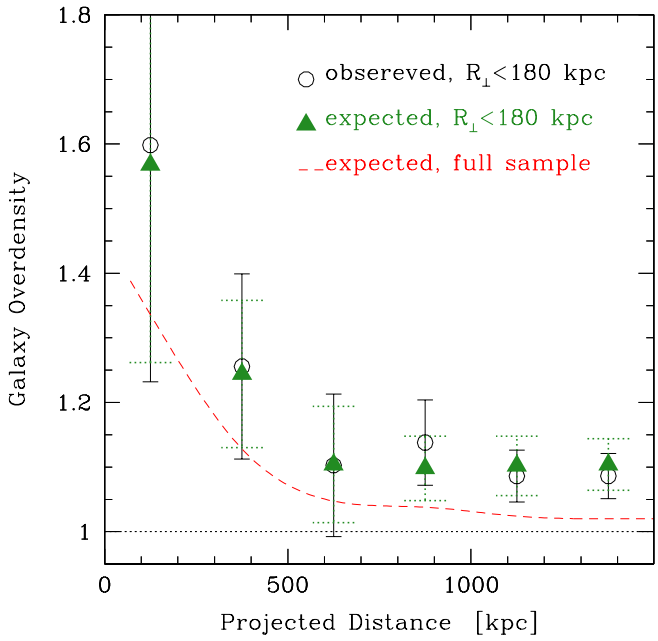

Figure 4.18.: Mean cumulative overdensity detected around the six QSO pairs with $0 < R_{\perp} < 180$ kpc (from the QSO midpoint, empty circles). The expected galaxy overdensity around a whole QSO pair, derived under the assumption that each individual QSO in the sample contributes to the average (i.e. from overdensity in Figure 4.17) , is plotted with the red dashed line. If we only consider the individual QSOs in the closer pairs ($R_{\perp} < 180$ kpc), the expected mean overdensity is represented by the full green triangles.

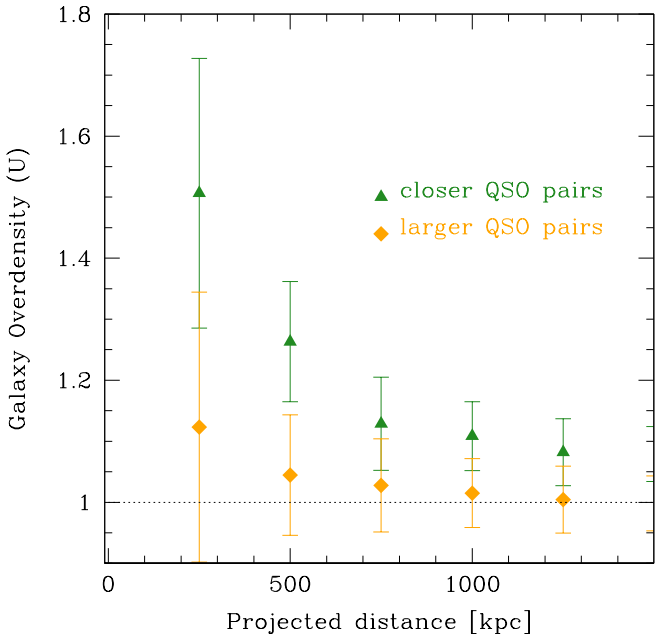

Figure 4.19.: The mean cumulative overdensity distribution of galaxies around the QSO pairs at larger (180< $R_{\perp}$ <600 kpc) and closer $R_{\perp}$ <180 kpc) separations between the two QSO companions .

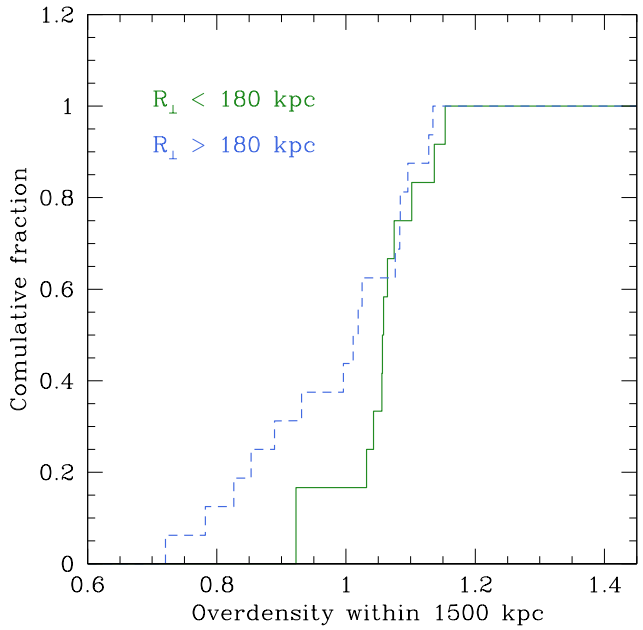

Figure 4.20.: Kolmogorov-Smirnow test comparing the galaxy overdensity distribution around the QSO pairs with separation< 180 kpc to that of QSO pairs with larger separations. The overdensity are evaluated within 1500 kpc from each pair.

the quasar host galaxies, is presented, showing that the QSO environments is comparable to that of the inactive galaxies. It means that quasars are not in richer environments than inactive galaxies. We therefore infer that, on average, the environment of QSO pairs is similar to that of inactive galaxies. The main result is, therefore, the indication that at the scale of our investigation (<1-2 Mpc) the rare activation of two QSOs with small physical separation does not require any extraordinary galaxy environment and that the quasar activity could be a common phase in the life of normal galaxies. In addition, we note that for the closest QSO pairs there is a suggestion of a larger overdensity. roughly commensurated to the sum of the average individual QSO environments. We note that only one QSO pair, nr. 13 J1553, is found inhabits a particular abundant environment with$O_{0.5} \sim 6O_{0.5,ave}$, which is also the pair with the smallest projected separation between the two QSO components ($\sim$ 40 kpc).

Although the number of known QSO pair candidates (e.g. Hennawi et al. 2006; Myers et al. 2008) is much larger than that in our sample, at present a direct comparison with other results is not possible. For instance, the extended sample of QSO pairs of Hennawi et al. (2006) covers a wide redshift range (up to z=3, majority of pairs at z>1), for which a detailed environmental study is not available and would require a major observational effort on large telescopes. Recently Green et al. (2011) studied the environments around 7 close QSO pairs ($R_\perp < 40$ kpc in our adopted cosmology) in a redshift range comparable with ours. They searched for extended X-ray emission as evidence for a local group - or cluster-sized dark matter halo associated with these QSO pairs, and found none. From their near-IR images they are unable to detect the emission from the host galaxies,

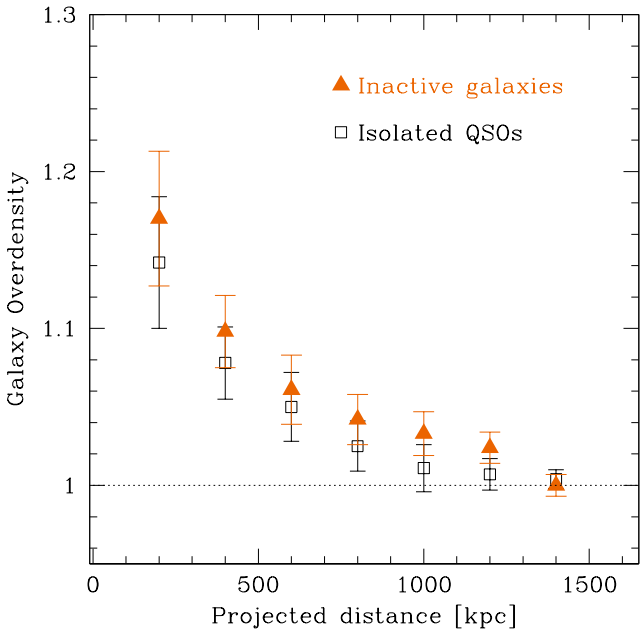

Figure 4.21.: Environment around isolated QSOs and galaxies in the Stripe 82 from Karhunen et al. (2014), with z< 0.5 and i<22.8. The mean cumulative overdensity as a function of distance is plotted for the full sample of $\sim$ 400 QSOs at redshift < 0.5 in the SDSS Stripe82 (empty squares), derived from the Schneider et al. (2010) catalogue. The overdensity of the control samples of $\sim$ 600 objects spectroscopically identifies ad galaxies, with the same cut of redshift is also given with blue triangles. The average magnitude threshold i = 22.8. Similar distributions are obtained considering $\sim$ 300 QSOs in Stripe 82 with resolved galaxies and using as control sample a likewise number of inactive galaxies closely matching in redshifts and in luminosity with the QSO host galaxies.

or signature of mergers and/or disturbed morphology, Moreover, due to the relatively bright magnitude limits of SDSS images at the redshift of these pairs, only the most luminous galaxies possibly associated to the QSOs could be detected using their DWCM technique (Distance and error-Weighted Color Mean, Green et al. 2011). Within these limits, their results that QSO pairs avoid rich cluster environments are qualitatively in agreement with our findings. We are going to investigate the environment of the Green sample in Chapter 5.

Moreover, due to the relatively bright magnitude limits of SDSS images at the redshift of these pairs, only the most luminous galaxies possibly associated to the QSOs could be detected using their DWCM technique (Distance and error-Weighted Color Mean, Green et al. 2011). Within these limits, their results that QSO pairs avoid rich cluster environments are qualitatively in agreement with our findings.

Table 4.10.: Comparison of the minimum virial mass of the the QSO pairs with the total mass of their host galaxies.

Pair Nr (a)	$M_{vir,min}$ $[10^{12} M_\odot]$ (b)	$M_{host,A} + M_{host,B}$ $[10^{12} M_\odot]$ (c)
1	< 0.12	0.4
2	< 0.15	1.1
3	0.20 ± 0.06	1.2
4	< 0.25	0.6
5	1.9 ± 0.2	1.0
6	20 ± 4	0.6
7	0.7 ± 0.2	(1.7)
8	25 ± 2	1.2
9	1.1 ± 0.3	(1.0)
10	8 ± 1	2.4
11	< 0.02	(1.1)
12	< 0.36	2.0
13	0.30 ± 0.04	(1.8)
14	12 ± 2	0.6

Notes: (a) QSO pair identification number. (b) Minimun virial mass of the binary system. When values are not enough constrained, the 1-σ upper limits are given. (c) Total mass of the QSO host galaxies in the pair. In the cases where only one QSO is resolved (see Table 4.4), we consider as the total mass the twice that of the resolved QSO and give it in brackets

4.6.1. Virial mass of the quasar pairs

Since the environment around pairs is relatively poor, it is of interest to compare it with the minimum mass of the binary system of the two QSOs, assuming it is gravitationally bound. We computed the minimum virial mass associated to each pair as

$$M_{vir} = C \, \frac{\Delta V_\parallel^2 \, R_\perp}{G} \tag{4.7}$$

where the orbit-plane orientation parameter C takes the minimum value =1 (average value $< C >$=3.4, see Farina, Falomo, & Treves 2011). We compared M_{vir} with the total mass of the host galaxies (see Table 4.5), evaluated following Kotilainen et al. (2009) and Decarli et al. (2010). While in most cases the $M_{vir,min}$ is less than or similar to the total mass of the host galaxies, in a least 3 cases out of 14 $M_{vir,min}$ exceeds the sum of the masses of the hosts by a factor $\gtrsim 10$ (see Table 4.10 and figure 4.22). Because the environment is not particularly rich in the first 500 kpc, this is suggestive of a huge dark matter contribution (see also Farina, Falomo, & Treves 2011).

Following the recipes in Farina, Falomo, & Treves (2011), we evaluated the density of

galaxies brighter than the magnitude threshold associated to a clusters having as mass the minimum virial mass of the pair systems, and assuming different mass-light (M/L) ratio. The galaxies in the clusters are assumed to follow the Schechter (Schechter 1976) luminosity function and describe a King-like profile with a virial radius from Girardi et al. (1998). In Figure 4.23 the observed density excess of galaxy (with respect the background) within 500 kpc is compared with that expected. We didn't find indication of overdensity over 2-σ, except than 5 QSP pairs. For two of these cases a M/L ratio $\gtrsim$ 10 is required to take into account the difference of the velocities between the two QSOs. A number of 4 QSO pairs, for which we don't measure appreciable overdensities in the fields ($>$ 500 kpc) require similar M/L and then an additive mass to be bound systems. The values of M/L are compatible with those derive from scaling relations between the optical luminosity and the cluster mass (e.g. Popesso et al. 2005). In particular, the QSO pair nr. 6, for the high virial mass and the low richness of galaxies of its environment needs a M/L $\sim$ 80, and may be it is not a physical pair.

However, because of the exiguity of our sample, to reach a firm conclusion on the environment and dynamical properties of QSO pairs, a detailed spectroscopic and imaging investigation of a larger and homogeneous sample is required.

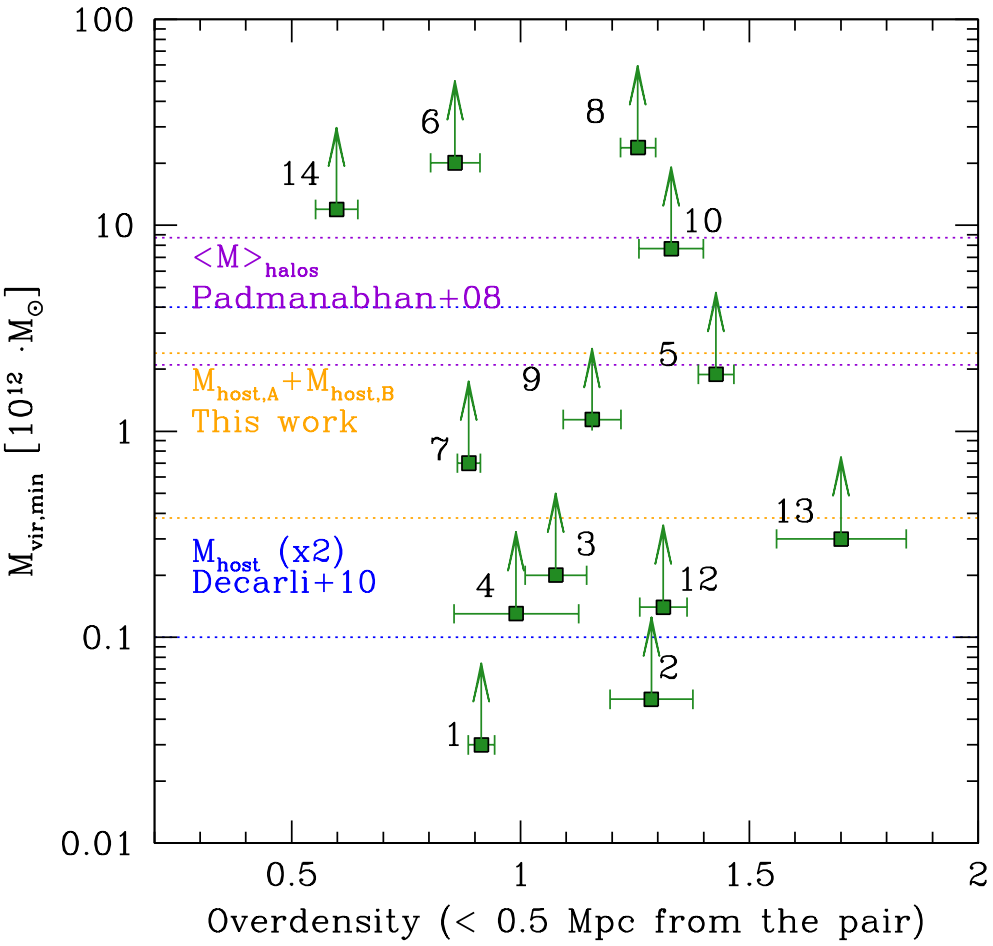

Figure 4.22.: The minimum dynamical mass $M_{vir,min}$ is plotted vs the mean overdensity within 0.5 Mpc from the pair. This value is taken as an indicator of the excess of galaxy around the pair. Blue dotted lines include the host masses multiplied by 2 reported in Decarli et al. 2010 and based on galactic luminosity of objects at $z < 1$ ($M_{host} \sim 0.1 - 2 \cdot 10^{12} M_\odot$). Dotted purple lines mark the range of the mean halo masses around $z < 0.6$ QSOs ($1.9 - 6.1 \cdot h^{-1} M_\odot$) derived by Padmanabhan et al. (2009). Yellow dotted lines encompass the range of variably of the sum $M_A + M_B$ of the pair member masses in this chapter. ID numbers mark the QSO pairs.

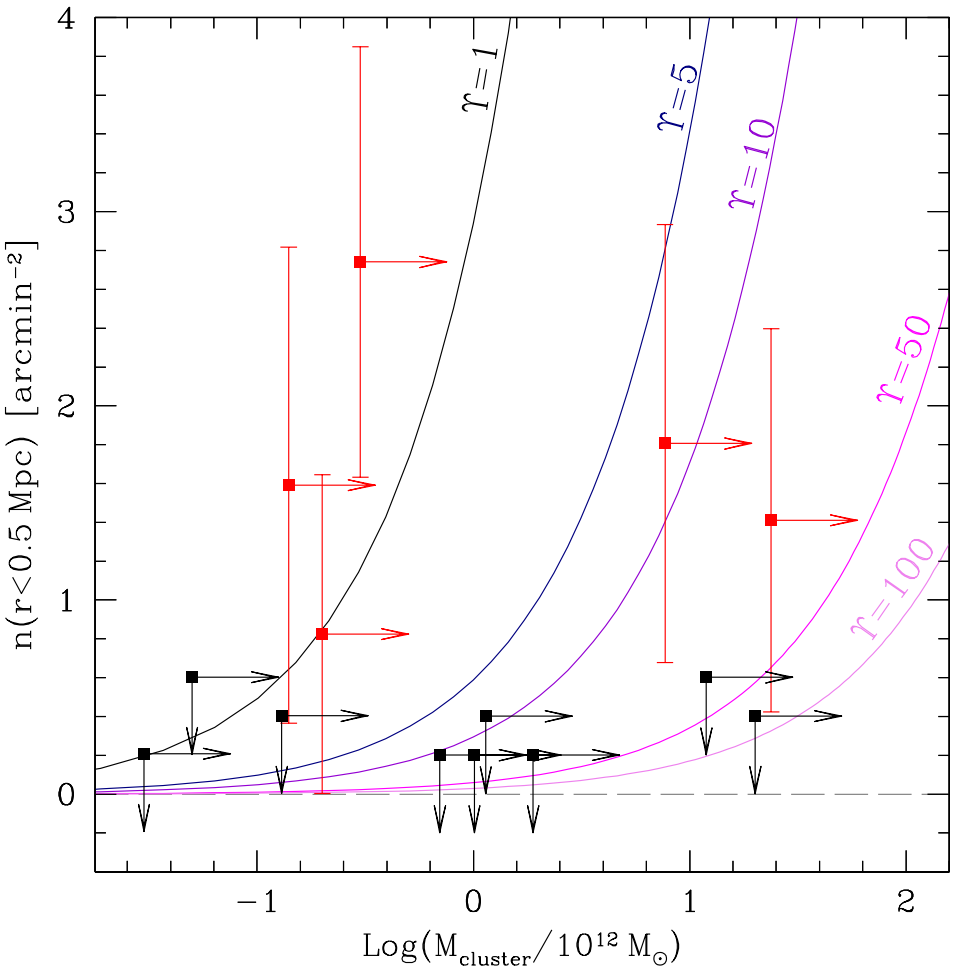

Figure 4.23.: Mass to light ratio expected for the clusters harboring the quasar pairs as a function of the minimum virial mass of the cluster and the density excess of galaxy in the environment. Lines mark the loci where the M/L ratio assumes the constant values reported. Red points are the QSO pairs with $< O_{0,500} > +2 \cdot \sigma \geqslant 1$. Black points refer to the pairs with no evidences of overdensity, for which we assumed an upper limit of galaxy excess of 2 σ above the background.

4.7. Supplemental material

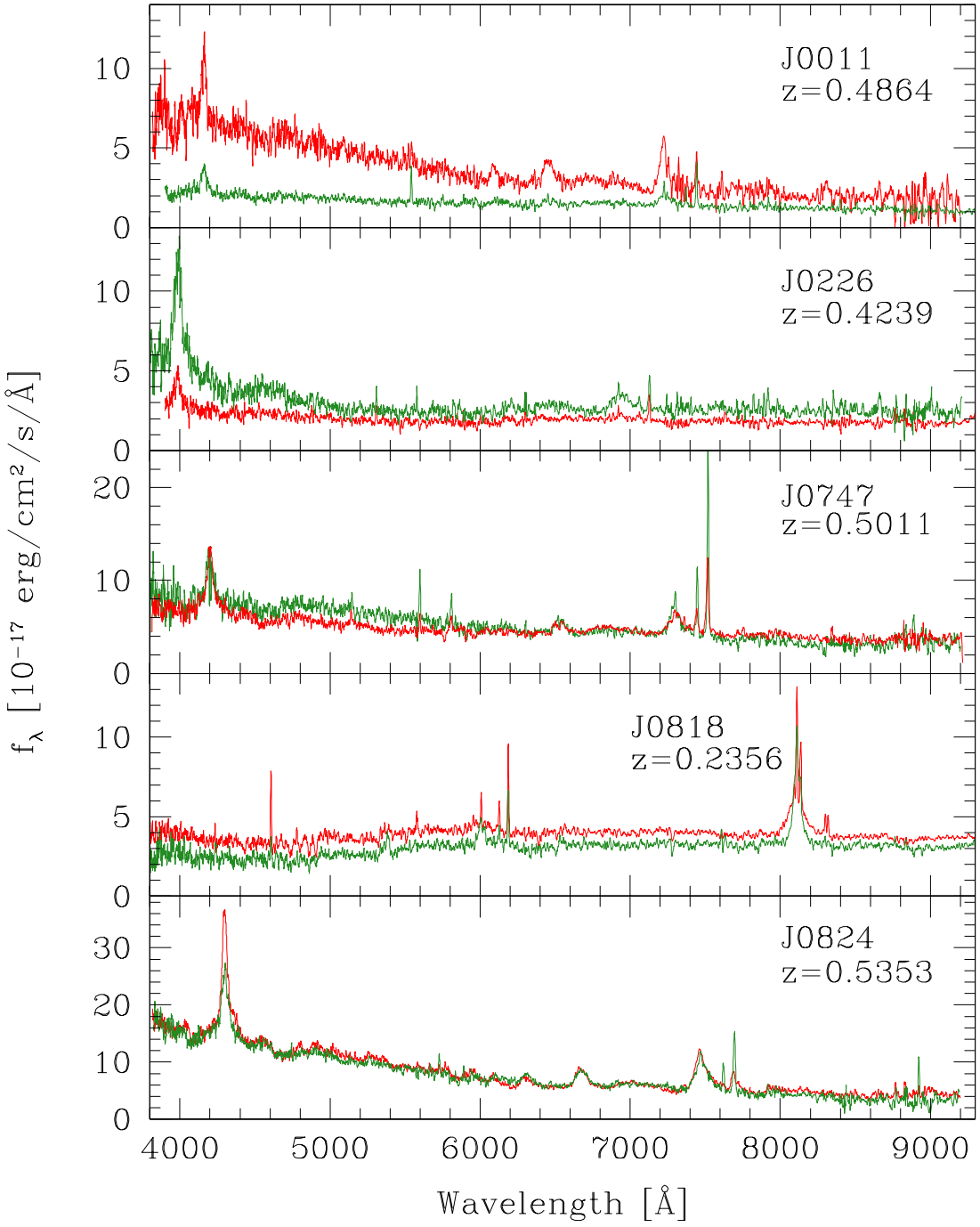

Figure 4.17.: SDSS Spectra of the QSO pairs listed in Table 4.2. Spectra ID in figure are derived from the QSO names. A kernel 3 filter is applied.

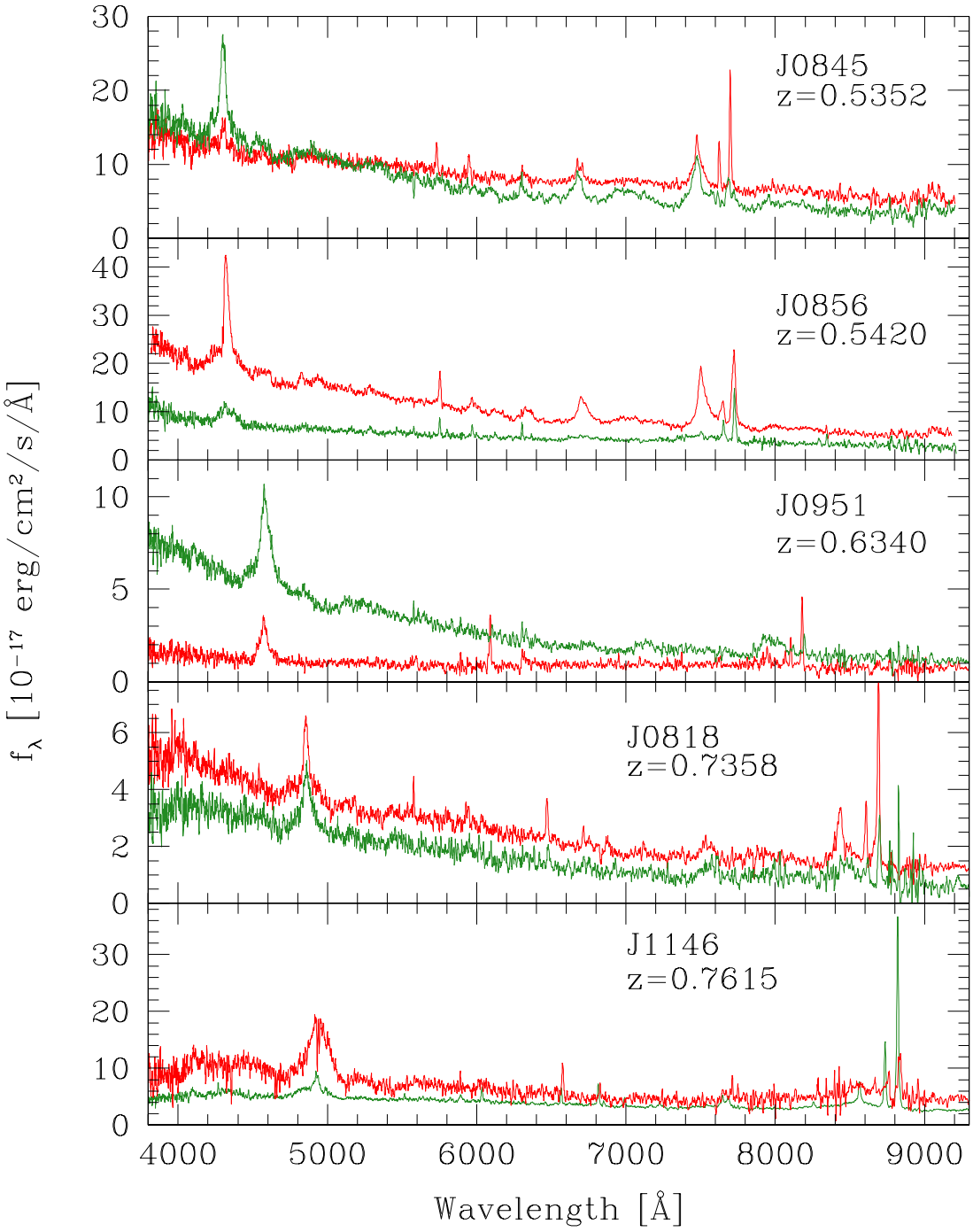

Figure 4.17.: — Continued

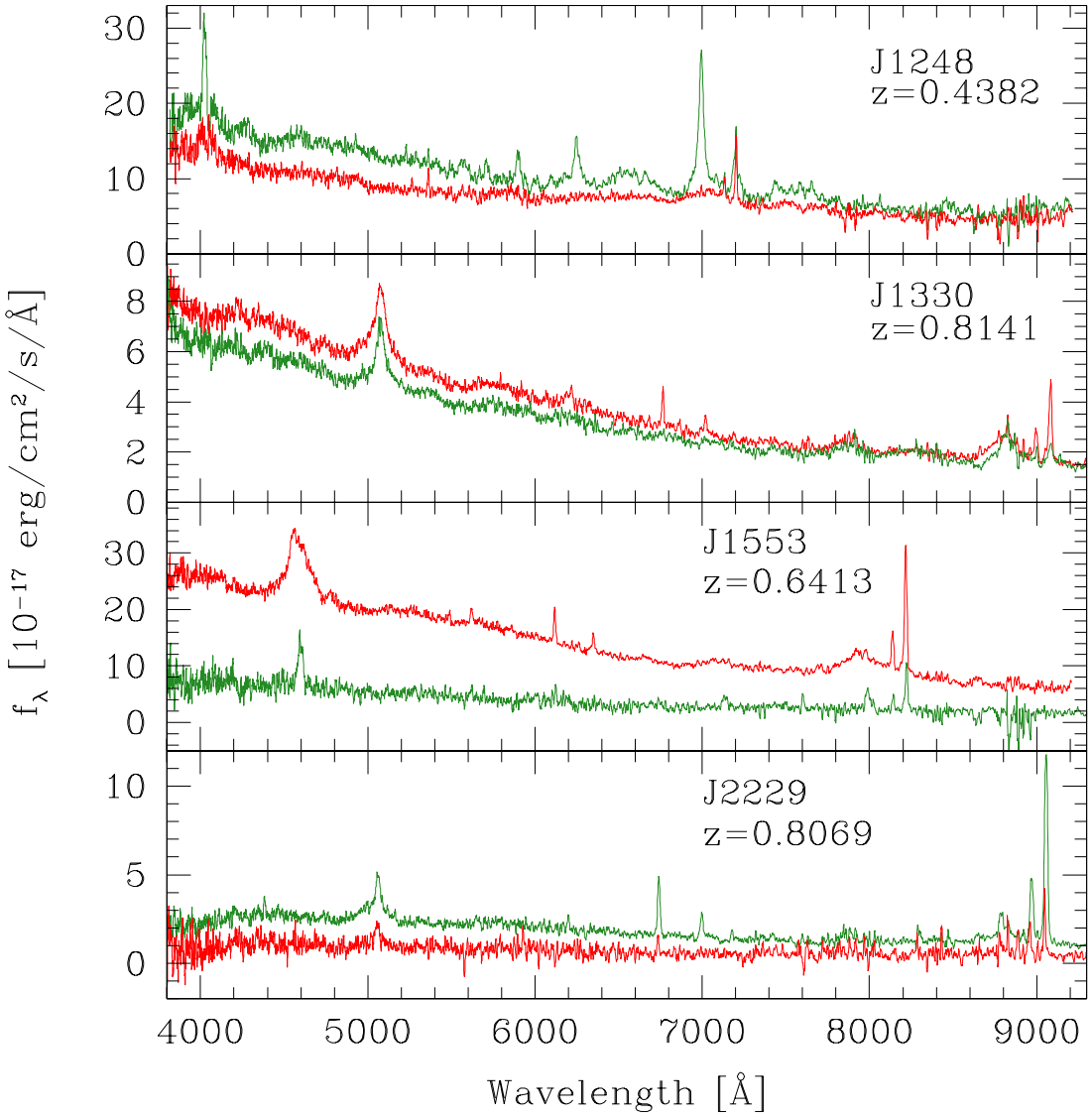

Figure 4.17.: — Continued

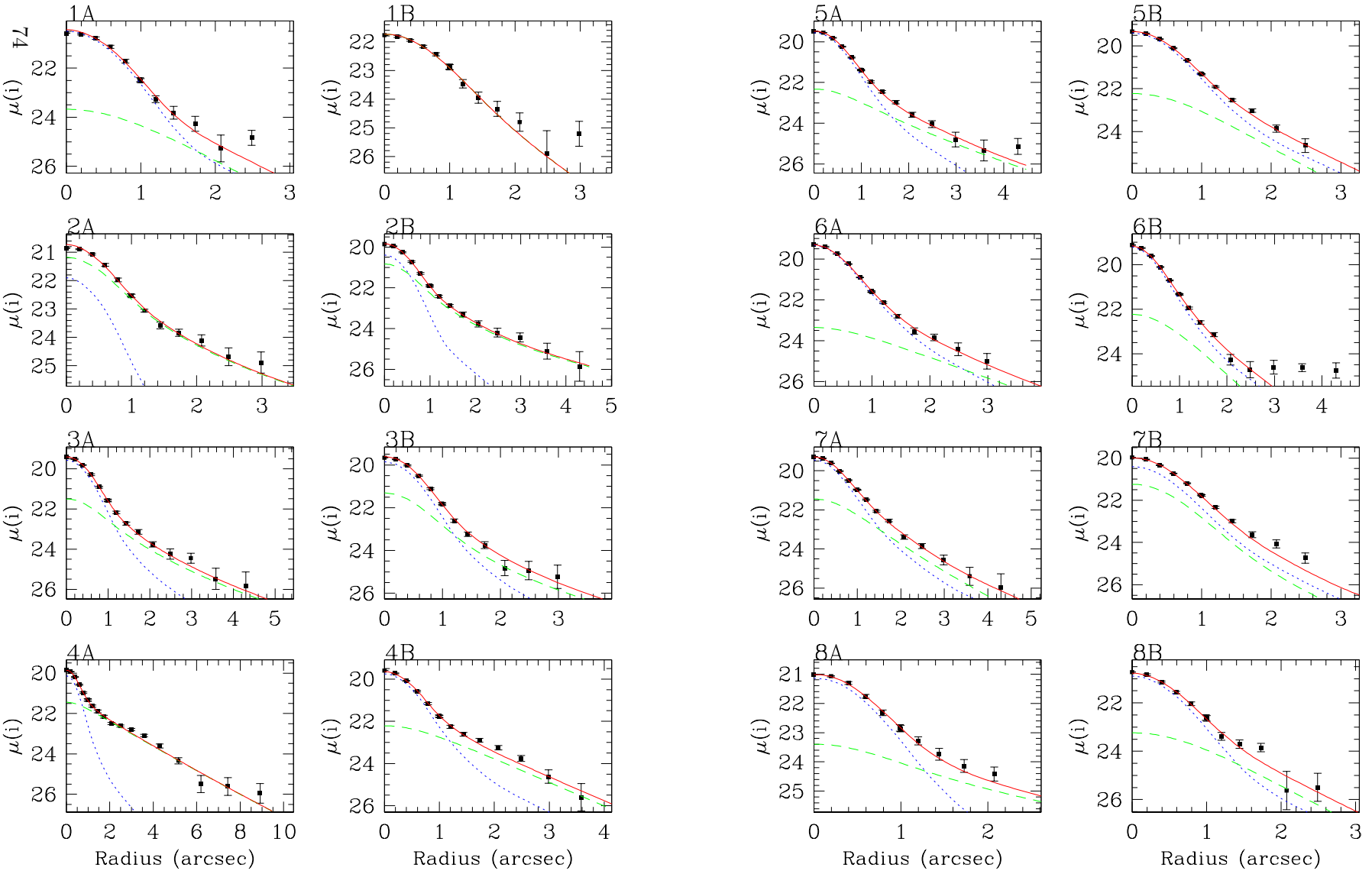

Figure 4.18.: Average radial brightness profile of the two QSOs in each pairs listed in Table 4.2, fitted by the scaled PSF for the nucleus (blue dotted line) plus the the the host galaxy model convolved with the PSF (green dashed line), see the text. The overall best fit is represented by the red solid line.

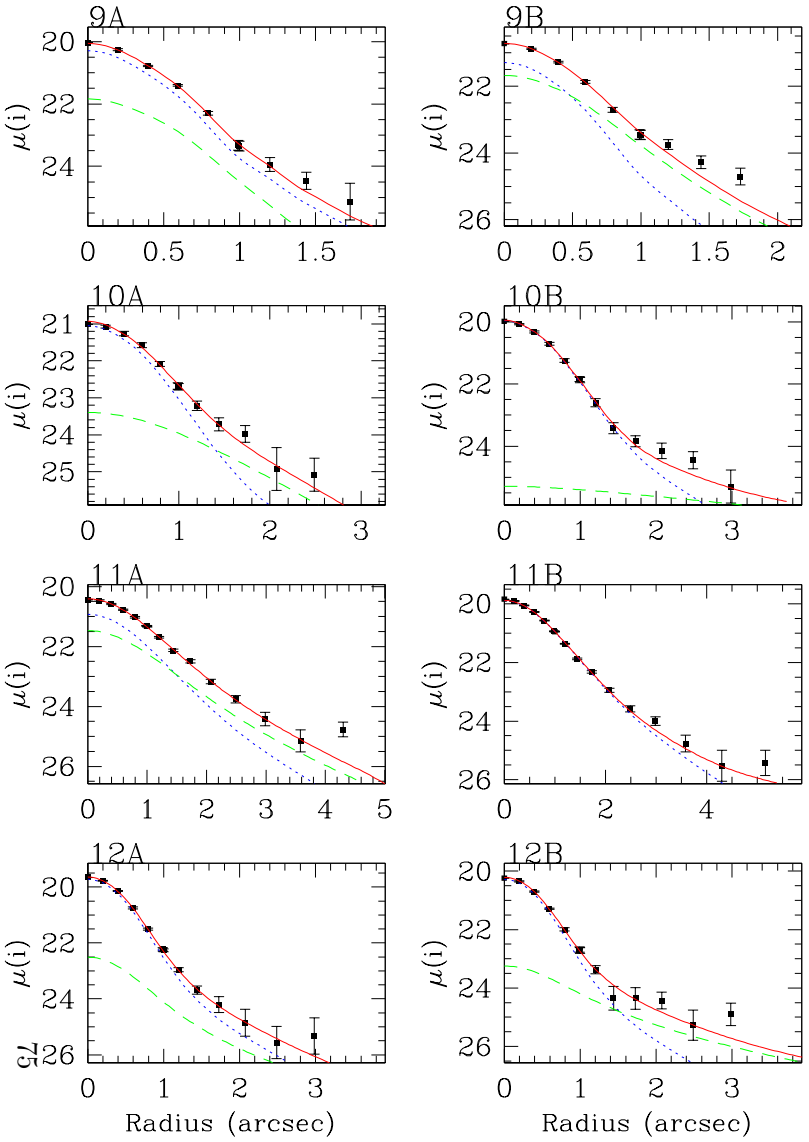
9A
9B
10A
10B
11A
11B
12A
12B
μ(i)
Radius (arcsec)

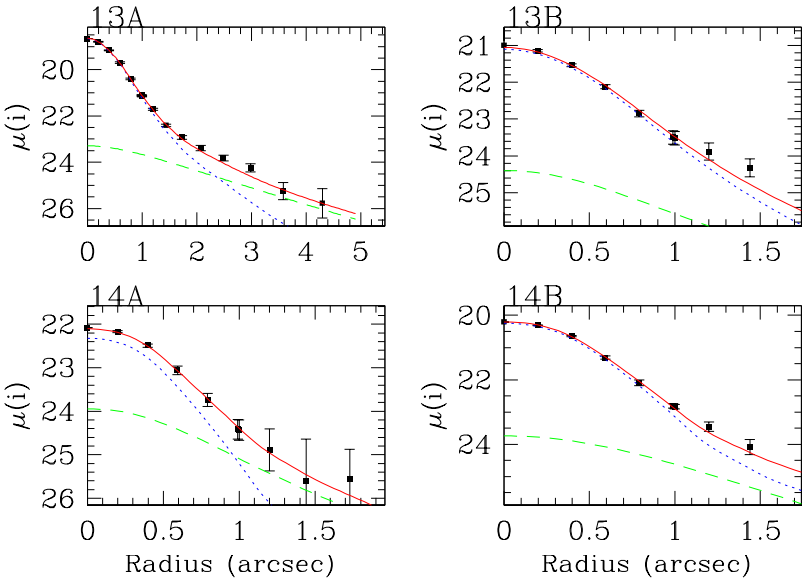
13A
13B
14A
14B
μ(i)
Radius (arcsec)

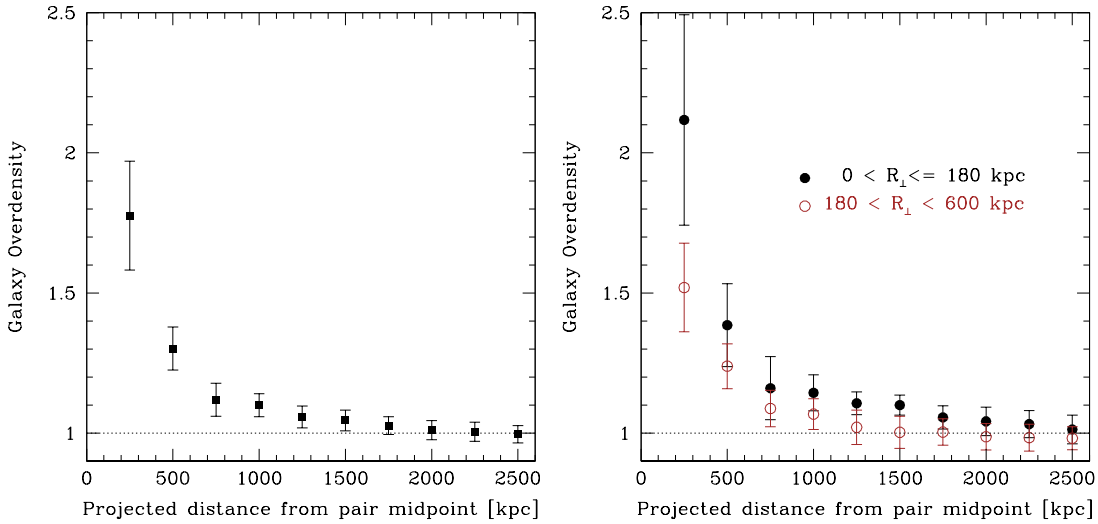

Figure 4.19.: SDSS i-band mean cumulative overdensity of galaxies from the midpoints of the QSO pairs. QSOs host galaxies are included in the counts. *Right panel:* Full sample (black squares). *Left panel*: Mean cumulative overdensity of the 6 pairs with $0 < R_{\perp} < 180$ kpc (black full circles) and of the 8 pairs with $180 \leqslant R_{\perp} < 600$ kpc (brown empty circles).

Table 4.11.: Statistics of galaxy in the QSO pair environments / 2. around the midpoint of the QSO pair.

Pair Nr (a)	$N_{0,25}(M)$ (g)	$N_{0,5}(M)$ (h)	$O_{0,25}(M)$ (i)	$O_{0,5}(M)$ (j)
1	7	26	1.36 ± 0.04	1.26 ± 0.04
2	13	39	1.83 ± 0.14	1.37 ± 0.10
3	10	23	2.20 ± 0.14	1.27 ± 0.08
4	10	37	1.15 ± 0.16	1.07 ± 0.15
5	11	26	2.51 ± 0.08	1.49 ± 0.05
6	10	23	2.22 ± 0.14	1.28 ± 0.08
7	4	15	0.93 ±0.03	0.87 ± 0.03
8	7	21	1.94 ± 0.06	1.45 ± 0.05
9	5	17	1.43 ± 0.08	1.21 ± 0.07
10	7	21	2.05 ± 0.12	1.54 ± 0.09
11	7	36	1.05 ± 0.03	1.35 ± 0.03
12	7	24	1.59 ± 0.07	1.36 ± 0.06
13	12	26	3.59 ± 0.37	1.94 ± 0.20
14	4	12	1.01 ± 0.07	0.76 ± 0.06

Notes: (a) QSO pair identification number . (b) Seeing of the image containing the QSO pair. (c) Apparent SDSSi-magnitude threshold. (d) Absolute magnitude corresponding to $m_{i,50\%}$. (e) and (f) Background surface number density of galaxies in arcmin^{-2} and in Mpc^{-2}, respectively. (g) and (h) Count of galaxies in the region within 250 and 500 kpc, respectively, taken staring from the QSO pair midpoint. (i) and (j) Galaxy overdensity in the region within 250 and 500 kpc , respectively, from the QSO pair midpoint.

5. Ongoing programs

5.1. Summary

The availability of large samples of spectroscopic quasars (more than 300,000) have allowed the discovery of a number of quasar pairs that according to transverse separation and redshift are likely physically bound (e.g. Hennawi et al. 2006; Myers et al. 2007b, and Chapter 3). While the properties of these pairs are generally poorly studied (see Chapter 2), they represent an important tool for constraining quasar evolution, in particular their environment. In Chapter 4 we studied the environment around a sample of low-redshift QSO pairs with separations of 10 - 100 kpc scale. We found that, on average, galaxy overdensity around quasars in the pair is indistinguishable from that around isolated quasars. We then inferred the indication that at the scale of our investigation ($\lesssim$2 Mpc) the activation of two QSOs does not require any extraordinary galaxy environment.

Further investigations on QSO pairs are deemed necessary to secure more evidence and reach firmer conclusions. In particular, we intend to enlarge the sample with the aim of exploring the environmental dependence of properties on the QSO separation and the cosmological evolution of the clustering of galaxies around QSOs, exploring larger redshifts.

In this Chapter we examinein detail the environment of the seven very close QSO pairs reported by Green et al. (2011) (Section 5.2) and already mentioned in Chapter 4. We then describe the observations taken from Nordic Optical telescope (NOT) at the near-infrared wavelengths , with the aim to exploring the environment of QSO pairs at a deeper level than the SDSS images and to reaching at higher redshift objects (Section 5.3), the analysis and interpretation of which are ongoing.

5.2. Close QSO pairs

5.2.1. Sample

To investigate the suggestion of a dependence of the overdensity on the QSO separations, we search for good confidence spectroscopic close pairs in previous works. Candidates were drawn from the sample of seven spatially resolved QSO pairs in Green et al. (2011), targeted as part of a complete sample of binary quasars with small transverse separations (< 40 kpc).

The QSOs Green et al. (2011) were selected from the photometrically classified Type 1 QSOs quasar catalogue of Richards et al. (2009). All pairs of objects with component separation (2".9−6"), UV-excess, and g < 20.85 were targeted for follow up spectroscopy. The sample was originally supplemented with the pair J0740+2926, discovered as binary QSO in the SDSS Quasar Lens Search (SQLS, Inada et al. 2012; Oguri et al. 2012, and references therein) and included in the sample of close QSO pairs of Hennawi et al. (2006). Because of similar properties and origin, we also add the QSO pair J1138, again from Hennawi et al. (2006). The sample is presented in Table 5.2.

Distances between the two QSOs in the pairs are small , corresponding to a few tens kpc. At this angular separation, there is a risk of lensing contaminations in the sample. On the basis of the considerations in Hennawi et al. (2006), Green et al. (2011) and Inada et al. (2010)we consider all pairs as binary QSOs rather than lenses, see however, the comments of Myers et al. (2008).

5.2.2. Spectroscopy

All these pairs have been spectroscopically identified as broad-line QSO pairs in previous works (Hennawi et al. 2006; Myers et al. 2008; Green et al. 2010, 2011) by follow-up spectroscopy of the objects which lack a SDSS spectrum (see details in the notes to the objects in Table 5.2). Redshifts from the SDSS or from dedicated observations are reported in Table 5.2.

From SDSS archives we retrieve the spectra for at least one object in the other pairs, but not for the QSO pair J1158, for which we found none. All the SDSS spectra are reported in Figure 5.1. From all the QSOs at z<0.85 with available spectra in SDSS, we evaluated the redshifts from [OIII]λ5007 forbidden emission lines using the line barycenter method, as described in Sect.4.2.2, with uncertainties ranging from 2 to $8 \cdot 10^{-5}$. Measurement details are in Table 5.3. The mean redshift of the sample is 0.723.

In further analysis involving redshifts, we will consider the values derived from O[III]λ5007 lines when available, while for the other sources we refer to those obtained in Hennawi et al. (2006), Myers et al. (2008) and Green et al. (2010, 2011), assuming uncertainties 0.002 and 0.0002 for redshifts with 3 and 4 decimals, respectively. We derived the difference of systemic velocities $\Delta v_{\parallel}$ and the minimum viral mass $M_{vir,min}$ (Eq. 3.7 and Eq. 4.7), which are listed in Table 5.4.

Following our adopted cosmology, $R_{\perp}$ is <40 kpc and $\Delta v_{\parallel} \lesssim 600$ km/s. For the pair J1138, for which the individual redshifts are not available, we adopt $\Delta v_{\parallel}$=840 km/s as given in Hennawi et al. (2006). On the basis of the considerations in the Chapter 3 and for the enhanced clustering at these scales with respect to that expected on the

low separations, the probability that these 8 close pairs are physical systems is very high ($\sim$ 98 %). Moreover, both the small-separated QSO pairs collections of Hennawi et al. (2006) and Myers et al. (2008), containing parts of this sample, have revealed an enhancement of clustering at tens kpc scale with respect that expected on the from large separation measurements.

5.2.3. The environment: preliminary analysis

We retrieve the images of all the QSO pair fields from the SDSS archives. Catalogs of photometric objects primary classified as galaxies by the SDSS recipes in an area of 15 arcmin from each QSO pair were compiled. Angular and projected distances of all the galaxy from the pair were computed at the redshift of the foreground QSO. As fully described in Sect. 4.5.3 we measure the surface overdensity of galaxies at different distances. Statistics of counts are reported in Table 5.5, with photometrical thresholds and seeings. The mean cumulative overdensity of galaxies in the QSO fields is plotted in Figure 5.2 as a function of the distance from the QSO pair.

We found that the pairs of close binary quasars here investigated are surrounded by a number of galaxies, lower, on average, than those discussed in the previous chapter. Our findings of poor galaxy environment around those close pairs under examination is consistent with the results of Green et al. (2011), which are also confirmed by the study of the X-rays images of the fields. This is against the suggestion outlined in Section 4.6.

Due to the mean higher redshift and similar seeings around the close QSO pairs we can explore galaxies brighter than those in the sample of 14 pairs discussed in Chapter 4, hereafter *main sample* (mean rest frame magnitude thresholds are $< M_{50\%} >= -20.7 \pm 0.2$ in the main sample and $< M_{50\%} >= -21.4 \pm 0.3$ in the close pair sample). Although the images are on average less deep, we believe that a comparison of the overdensities with previous results is possible and that the average environment is quite poor in the vicinity of these pairs of QSOs. If we exclude the host galaxies from the count, within 250 kpc the mean overdensity of galaxies drops to 1.06 (value that the main sample show at $\sim$ 1000 kpc) with respect the main sample and remains constant up to the distance of our investigation (2000 kpc).

In particular, in Chapter 4 we found an interesting case in terms of richness of galaxies. It concerns the environment of the closest QSO pairs of the main sample, QSO pair nr.13, as we noted in Section 4.6. This pair (z$\sim$0.64) has a projected QSO separation $R_{\perp} \sim 40$ kpc and host-excluded overdensity from the midpoint $O_{0.25}(M) \sim 3$ and $O_{0.5} \sim 1.8$, derived from the presence of 10 galaxies within 250 kpc and 24 galaxies within 500 kpc. In the current sample, the QSO pair J1158 (z $\sim$0.60) also shows a remarkable density of galaxies with respect to background, at similar magnitude threshold and despite a worse seeing, indicating that a variety of situations could be present even at very small separations and that there is no apparent correlation, at the moment, which is linking the environment to the existence of two simultaneous nearby QSOs.

To probe the galactic environment around these intriguing binary QSOs, they are proposed for spectroscopy and imaging at Gran Telescopio Canarias (GTC, see Section 5.4). From the images we can derive morphology and a more accurate distribution of galaxies in the fields, its richness and distribution. In addition, the image observations

could also allow us to derive a direct estimate of the masses of the host galaxies of the QSOs, and to detect, if present, the signatures of the eventual merger episode that affects the host galaxy of the pairs.

Table 5.1.: Properties of low-redshift close QSO pair sample.

Pair ID	A	z_A	r_A [mag]	B	z_B	r_B [mag]	$z_{A,[OIII]}$	$z_{B,[OIII]}$	$\Delta\theta$ [arcsec]	$R_\perp$ [kpc]	$\Delta V_\parallel$. [km/s]
(a)	(b)	(c)	(d)	(e)	(f)	(g)	(h)	(i)	(j)	(k)	(l)
J0740	J074013.42+292645.7	0.978 (H)	19.47	J074013.44+292648.3	0.9803 (S)	18.27	—	—	2.6	20.8	349 ± 155
J0813	J081312.63+541649.8	0.7814 (G11)	20.08	J081313.10+541646.9	0.7792 (S)	17.18	—	0.77946	5.0	37.4	327 ± 37
J1138	J113808.87+680736.6	— (H*)	19.87	J113809.20+680738.6	0.7687 (S)	17.86	—	0.77030	2.7	20.1	840 ± —
J1158	J115822.77+123518.5	0.5996 (M)	19.85	J115822.98+123520.3	0.5957 (M)	20.12	—	—	3.6	23.7	733 ± 54
J1254	J125454.86+084652.1	0.4401 (G10)	19.43	J125455.09+084653.9	0.4392 (G10)	17.08	0.44042	0.43753	3.9	21.8	601 ± 15
J1418	J141855.41+244108.9	0.5728 (S)	19.21	J141855.53+244104.7	0.5751 (M)	20.13	0.57359	—	4.5	29.4	287 ± 40
J1508	J150842.19+332802.6	0.8773 (S)	17.80	J150842.21+332805.5	0.878 (H)	20.19	—	—	2.9	22.5	112 ± 163
J1606	J160602.80+290048.8	0.7701 (S)	18.35	J160603.01+290050.8	0.7692 (M)	18.25	0.77107	—	3.5	25.6	317 ± 36

Notes: (a) Pair identification number. (b) and (e) SDSS QSO name. (c) and (f) QSO redshifts from literature and references:
S: SDSS;
G10: Green et al. (2010) using Magellan/IMACS;
G11: Green et al. (2011), by Kitt Peak National Observatory (KPNO) using R-C spectrograph on the Mayall 4 m telescope and the KPC-10A grating;
M: Myers et al. (2008), from Spectrograph on the Mayall 4m at KPNO;
H: Hennawi et al. (2006), obtained by Astrophysical Research consortium (ARC) 3.5m telescope at the Apache Point Observatory;
(H*): Hennawi et al. (2006) reported the redshift of the SDSS target and their difference of radial velocities, that we add in column (k).
(d) and (g) SDSS dereddered r-band magnitude. (h) and (i) redshifts from [OIII] line positions on SDSS spectra. (j) Angular projected separation between the two QSOs of the pair. (k) Traverse separation at the pair redshift (foreground QSO). (l) Radial velocity difference.

Table 5.2.: Properties of low-redshift close QSO pair sample.

Pair ID	A	z_A	r_A [mag]	B	z_B	r_B [mag]	$z_{A,[OIII]}$	$z_{B,[OIII]}$	$\Delta\theta$ [arcsec]	$R_\perp$ [kpc]	$\Delta V_\parallel$. [km/s]
(a)	(b)	(c)	(d)	(e)	(f)	(g)	(h)	(i)	(j)	(k)	(l)
J0740	J074013.42+292645.7	0.978 (H)	19.47	J074013.44+292648.3	0.9803 (S)	18.27	—	—	2.6	20.8	349 ± 155
J0813	J081312.63+541649.8	0.7814 (G11)	20.08	J081313.10+541646.9	0.7792 (S)	17.18	—	0.77946	5.0	37.4	327 ± 37
J1138	J113808.87+680736.6	— (H*)	19.87	J113809.20+680738.6	0.7687 (S)	17.86	—	0.77030	2.7	20.1	840 ± —
J1158	J115822.77+123518.5	0.5996 (M)	19.85	J115822.98+123520.3	0.5957 (M)	20.12	—	—	3.6	23.7	733 ± 54
J1254	J125454.86+084652.1	0.4401 (G10)	19.43	J125455.09+084653.9	0.4392 (G10)	17.08	0.44042	0.43753	3.9	21.8	601 ± 15
J1418	J141855.41+244108.9	0.5728 (S)	19.21	J141855.53+244104.7	0.5751 (M)	20.13	0.57359	—	4.5	29.4	287 ± 40
J1508	J150842.19+332802.6	0.8773 (S)	17.80	J150842.21+332805.5	0.878 (H)	20.19	—	—	2.9	22.5	112 ± 163
J1606	J160602.80+290048.8	0.7701 (S)	18.35	J160603.01+290050.8	0.7692 (M)	18.25	0.77107	—	3.5	25.6	317 ± 36

Notes: (a) Pair identification number. (b) and (e) SDSS QSO name. (c) and (f) QSO redshifts from literature and references:
S: SDSS;
G10: Green et al. (2010) using Magellan/IMACS;
G11: Green et al. (2011), by Kitt Peak National Observatory (KPNO) using R-C spectrograph on the Mayall 4 m telescope and the KPC-10A grating;
M: Myers et al. (2008), from Spectrograph on the Mayall 4m at KPNO;
H: Hennawi et al. (2006), obtained by Astrophysical Research consortium (ARC) 3.5m telescope at the Apache Point Observatory;
(H*): Hennawi et al. (2006) reported the redshift of the SDSS target and their difference of radial velocities, that we add in column (k).
(d) and (g) SDSS dereddered r-band magnitude. (h) and (i) redshifts from [OIII] line positions on SDSS spectra. (j) Angular projected separation between the two QSOs of the pair. (k) Traverse separation at the pair redshift (foreground QSO). (l) Radial velocity difference.

Table 5.3.: [O III]λ5007Å emission lines positions for the close QSO pairs in Table 5.2 and redshifts.

QSO ID	S/N	$\lambda_{[OIII]}$ [Å]
a	b	c
J0740 B	14	—
J0813 B	24	8909.46 ± 0.40
J1138 B	21	8863.61 ± 0.76
J1254 A	33	7211.94 ± 0.25
J1254 B	13	7197.50 ± 0.22
J1418 A	9	7878.72 ± 0.29
J1508 A	10	—
J1606 A	15	8867.48 ± 0.34

Notes: [O III]λ5007Å emission lines are evaluated for only the objects at z<0.85 with available public SDSS spectra.

Table 5.4.: Minimum virial masses of the system of close QSO pairs.

Pair ID	$M_{vir,min}$ $[10^{12}M_{\odot}]$
(a)	(b)
J0740	0.60 ± 0.53
J0813	0.93 ± 0.21
J1138	3.40 ± —
J1158	2.97 ± 0.43
J1254	1.84 ± 0.09
J1418	0.57 ± 0.16
J1508	0.07 ± 0.20
J1606	0.59 ± 0.14

Notes: (a) QSO pair identification number. (b) Minimun virial mass of the binary system.

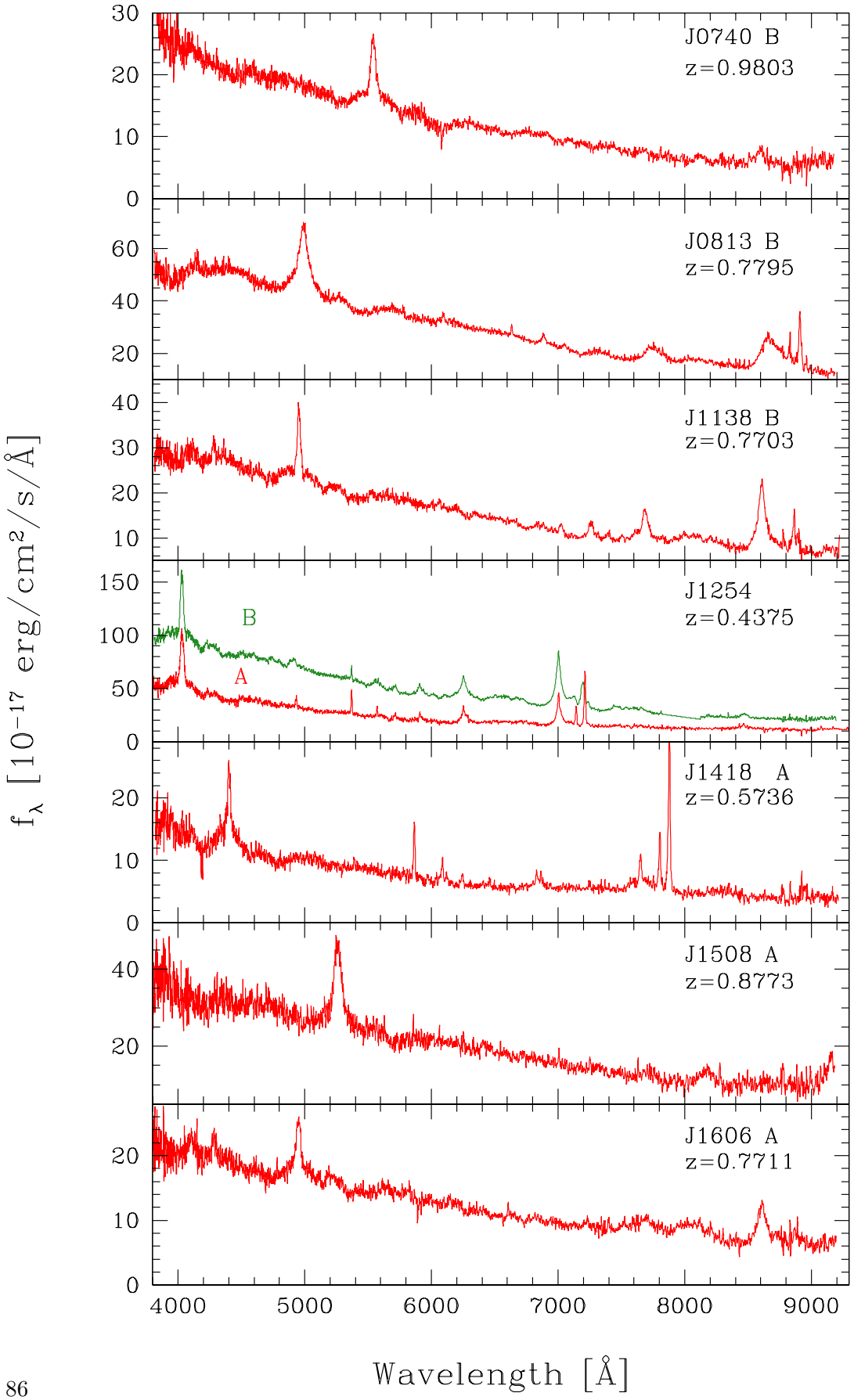

Figure 5.1.: SDSS spectra of close QSO pairs in Table 5.2. For clarity the flux of QSO J1254 A is multiplied by 4, and the redshift reported is that of the foreground QSO B.

Table 5.5.: Statistics of galaxy in the environment of close QSO pairs in Table 5.2 / 1. Galaxy overdensity around the midpoint of the QSO pair.

						Hosts included				Hosts excluded			
Pair Nr	seeing [arcsec]	$m_{i,50\%}$ [mag]	$M_{i,50\%}$ [mag]	n_{bg} [arcmin^{-2}]	n_{bg} [Mpc^{-2}]	$N_{0,25}$	$N_{0,5}$	$O_{0,25}$	$O_{0,5}$	$N_{0,25}$	$N_{0,5}$	$O_{0,25}$	$O_{0,5}$
(a)	(b)	(c)	(d)	(e)	(f)	(g)	(h)	(i)	(j)	(k)	(l)	(m)	(n)
J0740	1.13	21.7	-22.43	2.09 ± 0.11	9.21 ± 0.44	5	11	2.77 ± 0.22	1.52 ± 0.07	3	9	1.66 ± 0.08	1.25 ± 0.06
J0813	1.09	21.8	-21.81	3.23 ± 0.10	16.10 ± 0.50	6	12	1.90 ± 0.05	0.95 ± 0.03	4	10	1.27 ± 0.04	0.79 ± 0.02
J1138	1.44	21.7	-21.87	2.60 ± 0.22	13.21 ± 1.02	4	12	1.54 ± 0.10	1.16 ± 0.09	2	10	0.77 ± 0.06	0.96 ± 0.07
J1158	1.24	21.8	-21.03	2.85 ± 0.22	18.21 ± 1.26	9	26	2.52 ± 0.25	1.82 ± 0.13	7	24	1.96 ± 0.14	1.68 ± 0.12
J1254	1.17	21.9	-20.14	3.21 ± 0.22	27.69 ± 1.73	8	22	1.47 ± 0.13	1.01 ± 0.06	6	20	1.10 ± 0.07	0.92 ± 0.06
J1418	1.07	22.1	-20.62	3.53 ± 0.15	22.81 ± 1.30	3	18	0.67 ± 0.02	1.01 ± 0.06	1	16	0.22 ± 0.01	0.89 ± 0.05
J1508	0.74	21.9	-21.99	3.58 ± 0.24	16.76 ± 0.93	4	15	1.22 ± 0.07	1.14 ± 0.06	2	13	0.61 ± 0.03	0.99 ±0.05
J1606	0.94	22.2	-21.37	4.25 ± 0.37	21.33 ± 2.03	6	19	1.43 ± 0.18	1.14 ± 0.11	4	17	0.96 ± 0.09	1.02 ± 0.10

Notes: (a) QSO pair identification number . (b) Seeing of the image containing the QSO pair. (c) Apparent SDSSi-magnitude threshold. (d) Absolute magnitude corresponding to $m_{i,50\%}$, at the redshift of the QSO pair.. (e) and (f) Background surface number density of galaxies in arcmin^{-2} and in Mpc^{-2}, respectively. (g) and (h) Count of galaxies in the region within 250 and 500 kpc, respectively, from the QSO pair midpoint; host galaxies are included in the count. (i) and (j) Galaxy overdensity in the region within 250 and 500 kpc , respectively, from the QSO pair midpoint, hosts are included. (k), (l), (m), and (n) are the same as the previous 4 columns when the host galaxies are excluded.

5.3. NOT observations.

In order to explore a range of higher redshifts, we obtained dedicated observations with near-infrared imaging at the 2.5 m Nordic Optical Telescope (NOT), located at Roque de los Muchachos, La Palma, Canarias (Spain).

With these observations we can detect and measure faint galaxies in the field around the selected QSOs. We reach 22-23 mag in J band, i.e. we can detect galaxies that are about 2 magnitudes fainter than the characteristic luminosity M* of the galaxy luminosity function. In this way galaxies in the rest frame R band down to M*+2 can be explored. The images will allow us to derive host galaxy morphology, luminosity and mass. The analysis of the distribution of galaxies in the field of the QSO pair can be compared with the one in the background measured in the same frames to study richness and distribution of the galaxy environment to a deeper level than our previous works.

5.3.1. Sample selection

The collected material regards QSO physical pairs candidates suitable to be observed from NOT location and obtained as explained in Chapter 3. The pairs are selected with the following criteria:

1. $0.7 < z < 1.2$: in this z range, J-band images will allow us to probe the brightest part of the galaxy SEDs;

2. high probability of being physical pairs with respect to chance superpositions (see Chapter 3). In the selected redshift window the number of observed quasar pairs with respect to those expected from chance superpositions increases from 7 to 20 times when
   - projected distance $R_\perp < 400\ kpc$
   - For $1000 < \Delta V_r < 1500\ km/s$, we restricted $R_\perp \leqslant 260$ kpc.

3. Spectra from public releases (see Figure 5.17) are visually inspected in order to remove erroneous classifications or redshift determinations by automatic pipelines (see Chapter 4).

Under the conditions listed above, we found 34 quasar pairs observable from La Palma, quite evenly distributed in redshift: 14 pairs at $0.7 < z < 0.9$, 10 at $0.9 < z < 1.2$, 10 at $1.2 < z < 1.6$.

5.3.2. Observations

We were granted three nights to image QSO pairs from La Palma using the NOTCam on the NOT. NOTCam NIR detector has 1024x1024 pixels spanning a ~ 4 x 4 arcmin^2 field of view with 0."234 pixel-1 pixel scale. We observed in J band (1.25 μm), corresponding to $\sim 0.65 - 0.75\mu$m rest-frame wavelength at the mean redshift of the sample.

At this stage, the observation of 16 QSO pairs at intermediate redshift t (z$<$ 1.2, z_{ave} =0.791) has been completed and this first sample listed in Table 5.6. Angular and

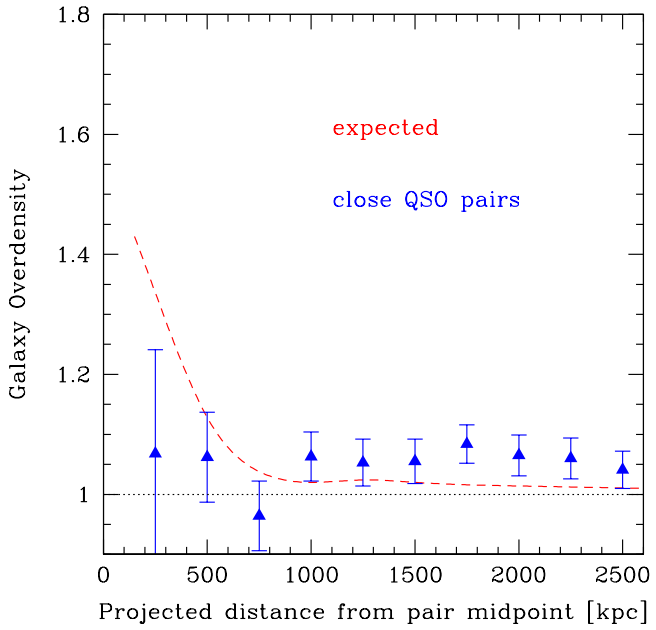

Figure 5.2.: Mean integral ovedensity of galaxies of the close QSO pairs in Table 5.2, from the midpoint of the QSO pairs (triangles). For comparison, the expected galaxy overdensity, derived for close QSO pairs in Section 4.5.5 is plotted as dashed line (see also Figure 4.18).

projected separations between the QSOs and the difference of their radial velocities are also tabled. The remaining pairs are scheduled for the current observing period.

In the field of view, we searched for stars in the Two Micron All Sky Survey (2MASS) point source catalogue (Skrutskie et al. 2006) and found that each frame contained at least one star in 2MASS , which we used to calibrate the astrometry of each frame.

Data analysis and result interpretations are ongoing.

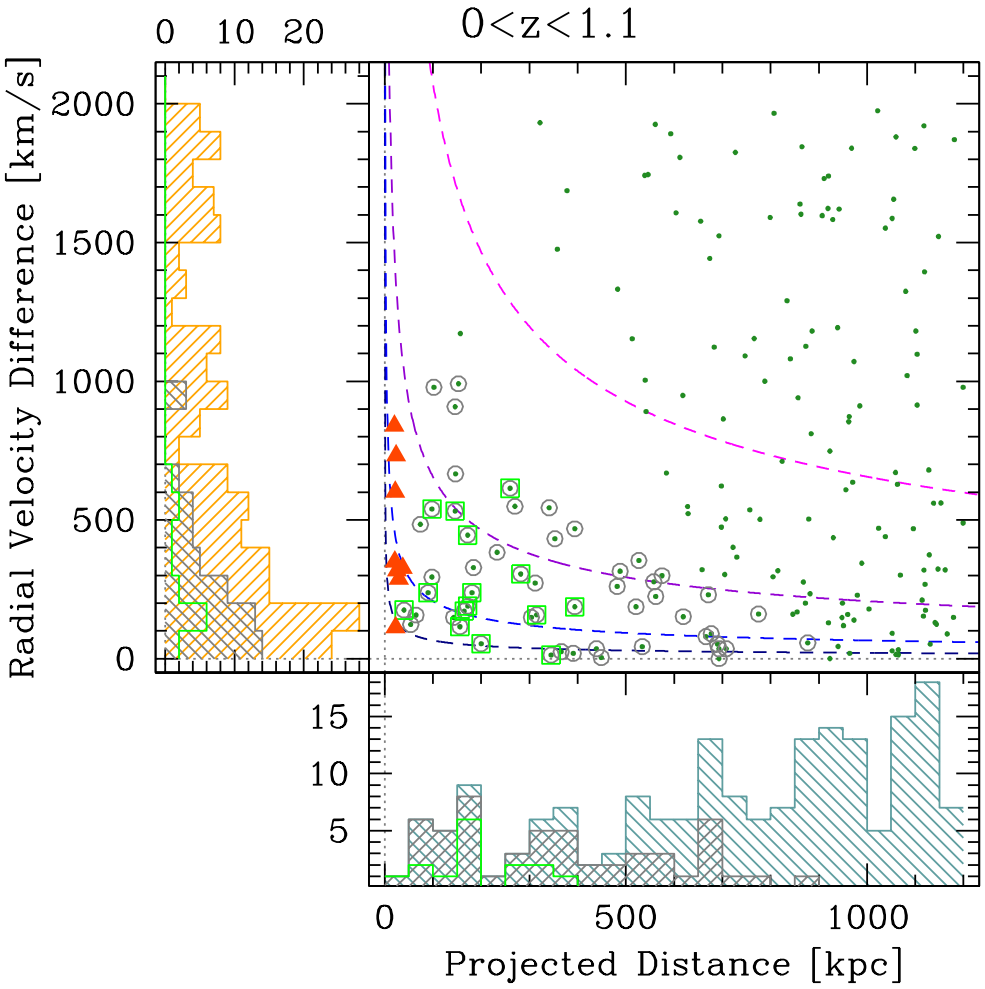

Figure 5.3.: Distribution in the $R_\perp - \Delta V_\parallel$ plane of the QSO physical pairs candidates discussed in this chapter. The panel contains the physical pair candidates at redshift z<1.1 (grey circles) from Table 3.2). Grey histograms are the $R_\perp$ and $\Delta V_\parallel$ distributions. Light blue and orange histograms are the same for the pairs with $R_\perp < 1200$ kpc and $\Delta V_\parallel < 2000$ km/s (green dots). Pairs selected for observations at NOT are marked with light green squares, and distribution are illustrate in green histograms. The sample of the close pairs discussed in Section 4.2 are also included as dark orange triangles to completeness od information. Iso-minimun-virial-masses from Eq. 3 , see Section 4.6, are drawn by dashed lines. From top to bottom iso-minimun-virial-mass values are $M_{vir,min} = 10^{14} M_\odot$, $10^{13} M_\odot$, $10^{12} M_\odot$, and $10^{11} M_\odot$ (from magenta line to blue line).

Table 5.6.: Properties of NOT sample.

Pair ID	A	z_A	r_A [mag]	B	z_B	r_B [mag]	$\Delta\theta$ [arcsec]	$R_\perp$ [kpc]	$\Delta V_\parallel$ [$km\ s^{-1}$]
(a)	(b)	(c)	(d)	(e)	(f)	(g)	(h)	(i)	(j)
J1137	SDSS J113725.69+141101.3	0.7358	19.99	SDSS J113726.12 +141111.4	0.7372	20.56	12.4	90	238
J1146	SDSS J114603.49+334614.3	0.7642	20.32	SDSS J114603.76 +334551.9	0.7615	19.42	23.3	172	445
J1158	2QZ J115814.79−003403.8	0.7930	19.09	SDSS J115817.24 −003430.7	0.7931	20.91	46.2	345	13
J1207	2QZ J120700.96+011539.5	0.9660	18.99	2QZ J120701.39 +011504.4	0.9640	20.34	35.5	282	305
J1217	2QZ J121734.24+005522.2	0.9015	19.84	2QZ J121736.94 +005522.6	0.9019	20.15	40.5	316	63
J1226	SDSS J122624.08−011234.5	0.9212	17.28	2QZ J122625.57 −011319.8	0.9204	19.73	50.5	394	125
J1231	SDSS J123145.16+000319.1	0.9079	21.55	2SLAQJ123145.44 +000326.6	0.907	21.48	8.5	67	142
J1247	SDSS J124702.52+402410.1	0.7236	19.85	SDSS J124703.60 +402415.0	0.7205	18.81	13.5	98	539
J1311	SDSS J131157.58+255648.6	1.0062	20.05	SDSS J131159.93 +255650.4	1.0103	19.55	32.4	260	614
J1328	SDSS J132821.74+351738.5	0.6857	18.50	SDSS J132823.66 +351739.0	0.6847	19.86	23.3	165	171
J1330	SDSS J133046.35+373142.8	0.8141	19.27	SDSS J133048.58 +373146.6	0.8144	19.86	26.5	200	54
J1455	SDSS J145553.92+181912.1	1.0714	18.34	SDSS J145555.06 +181901.6	1.0722	21.36	19.1	156	115
J1537	SDSS J153708.94+381905.6	0.7455	21.48	SDSS J153710.51 +381851.7	0.7461	18.78	23.5	172	189
J1553	SDSS J155330.22+223010.2	0.6413	18.31	SDSS J155330.55 +223014.3	0.6422	20.82	5.8	40	175
J1604	SDSS J160406.95+431445.6	0.8066	20.94	SDSS J160408.90 +431455.7	0.8078	20.67	24.0	177	199
J1647	SDSS J164732.53+350524.9	0.8644	20.45	SDSS J164733.23 +350541.6	0.8607	19.93	18.8	145	596

Notes: (a) Pair identificator. (b) and (f) QSO name. (c) and (g) Coordinates of the QSOs from SDSS. (d) and (h) Quasar redshifts derived from SDSS, 2QZ, 2SLAQ. For the QSOs already studied in Chapter 4 (nr. 1, 2, 10, 13) the redshifts are derived from [OIII] line positions, see Table 4.2. (e) and (i) SDSS r-band apparent magnitude of the quasar A and B, respectively. (j) Angular separation of the QSO pair. (k) Proper traverse separation. (l) Radial velocity difference.

5.4. Future programs

To further expand our investigation and in order to prove the galaxy environment up to M*+1, and possibly M* + 2, we need to exploit optimal signal-to-noise optical spectroscopy and high quality images of the QSO fields. Dedicated observations are required.

- A sample of 34 QSO pairs at higher redshift ($0.7 < z < 1.6$), and already described in Section 5.3, was drawn in the J deep images (R rest-frame) using NOTCam on NOT 2.5 m telescope.
- Multicolor imaging of sample of 20 pairs at $z < 1$ was obtained with BUSCA-Calar Alto (CAHA, 2.2 m) telescope in U, B, R, I bands.
- We have request for observing time for spectra and R and I band imaging of selected 25 QSO pairs at $z < 1$ from OSIRIS-Gran Telescopio CANARIAS (GTC, 10.4 m) to map B and V rest-frame targets.

New high quality spectra will allow us to obtain accurate values of ΔV_r (down to ∼30 km/s) and provide a firm lower limit to the systemic velocity of the QSO pair for a number of QSOs with low S/M spectra in public releases and to improve our current estimations. It is of interest to compare the minimum virial mass of the QSO pairs with the total mass of the pair based on the mass of their host galaxies to explore if possible excesses of mass may be due to a group or cluster of galaxy or, otherwise, they could be explained with QSO host galaxies surrounded by dark matter halos.

From the images we can derive the richness and distribution of the galaxy environment, the host galaxy morphology and peculiarities. We can also to detect, if present, the signatures of the eventual merger episode that affects the host galaxy of the pairs. When multi-band observations are present, we can use colors as indicators of current star formation of both the host galaxies of the QSOs and those in their environment. We will also take advantage of multi-band images to constrain the number of galaxies surrounding the QSOs and take the estimations of photometric redshifts to get rid of fore- and back-ground sources. We could reconstruct the luminosity functions of the galaxies selected in this way, and compare them to those of known clusters and groups of galaxies.

5.5. Supplemental material

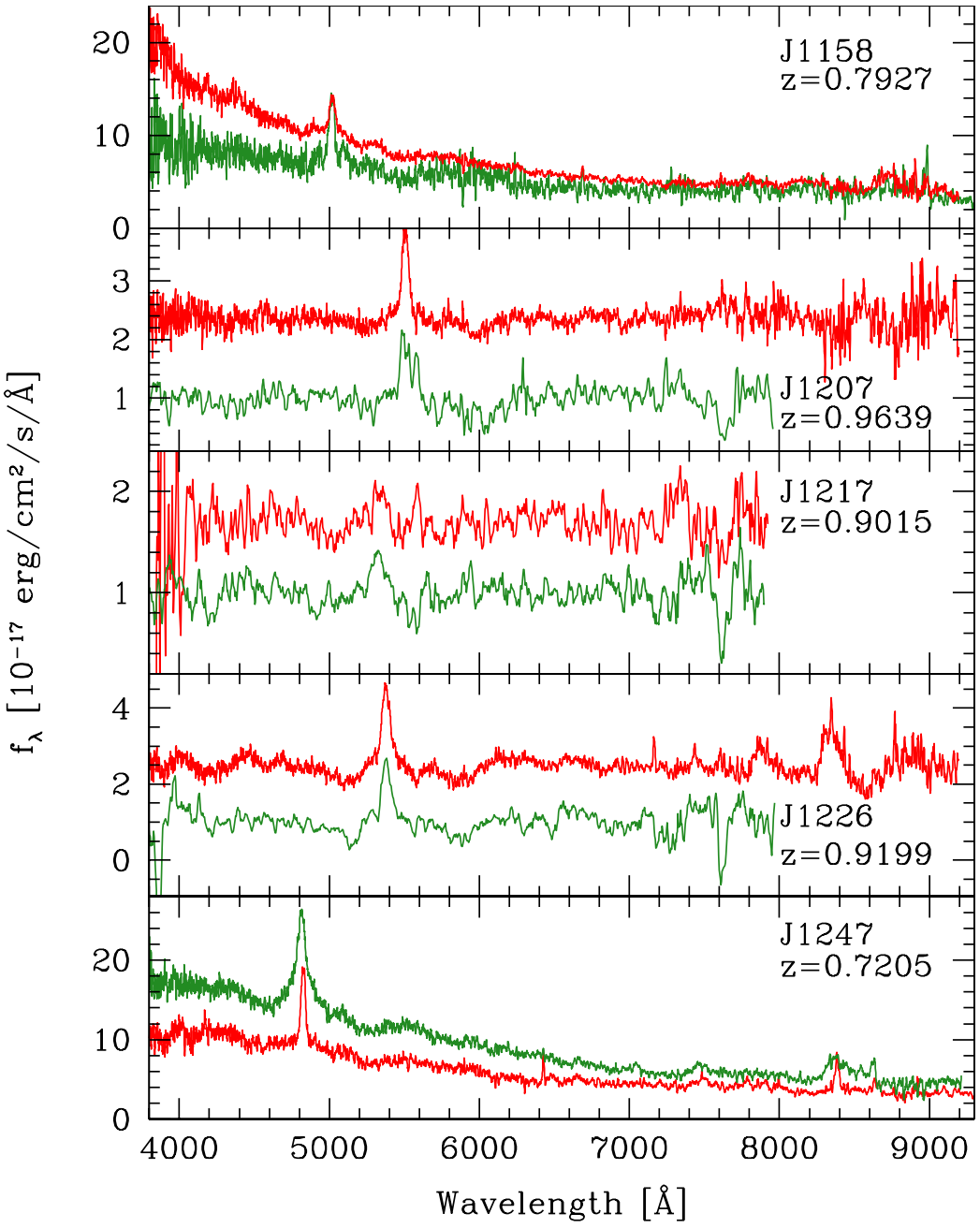

Figure 5.17.: Spectra of the QSO pairs listed in Table 4.2. The spectra in the QSO pairs J1207 and J1217 and one spectrum in the pair J 1226 derived from the Second Quasar Redshift (2QZ) survey release and are given in normalized form. The other spectra are taken from the SDSS archives. A kernel 3 filter is applied. For readability the fluxes of QSOs J1158 B, J1328 B, J1455 B, J1537 A are multiplied by 5, and that of QSO J1247 A is multiplied by 2.

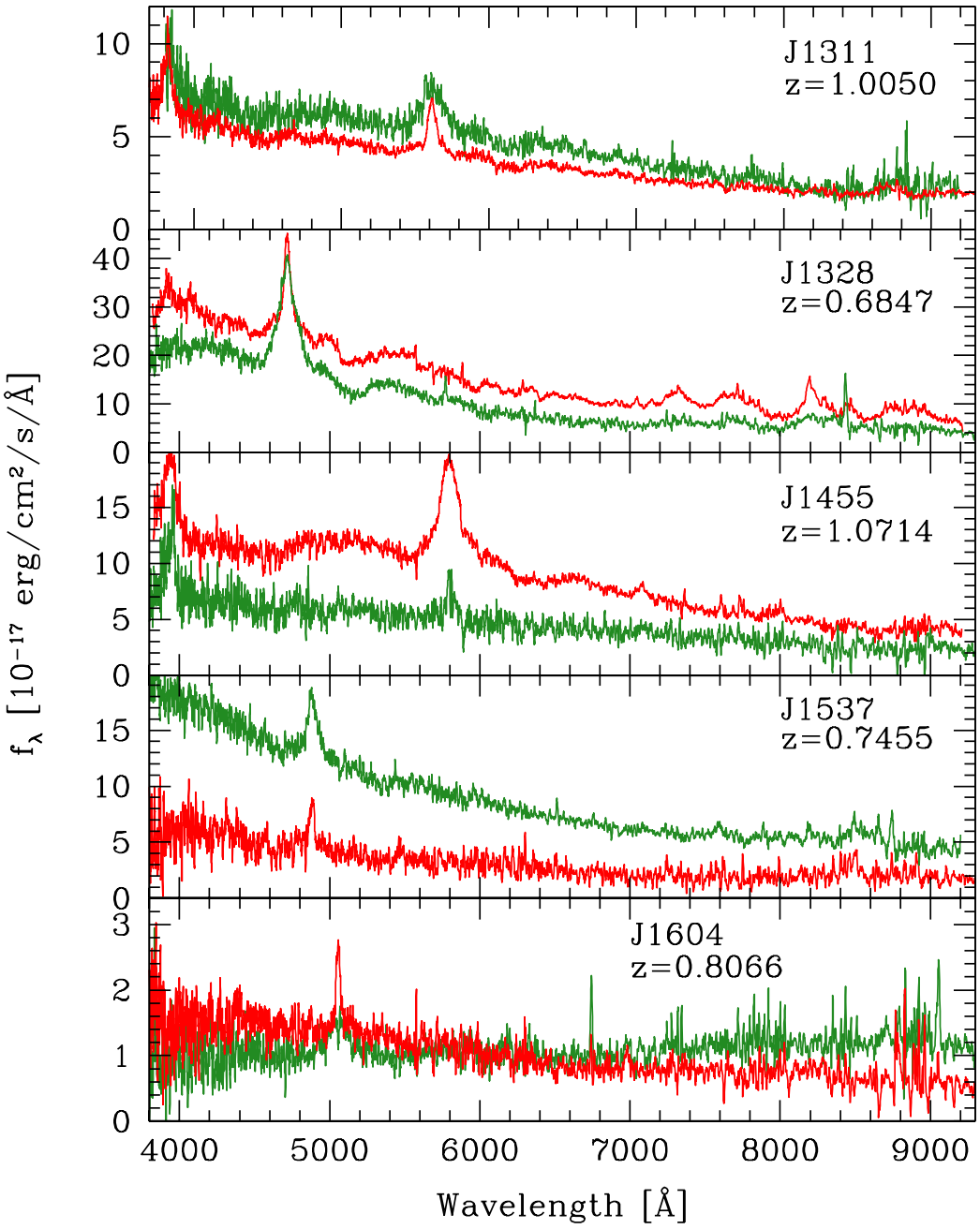

Figure 5.17.: — Continued

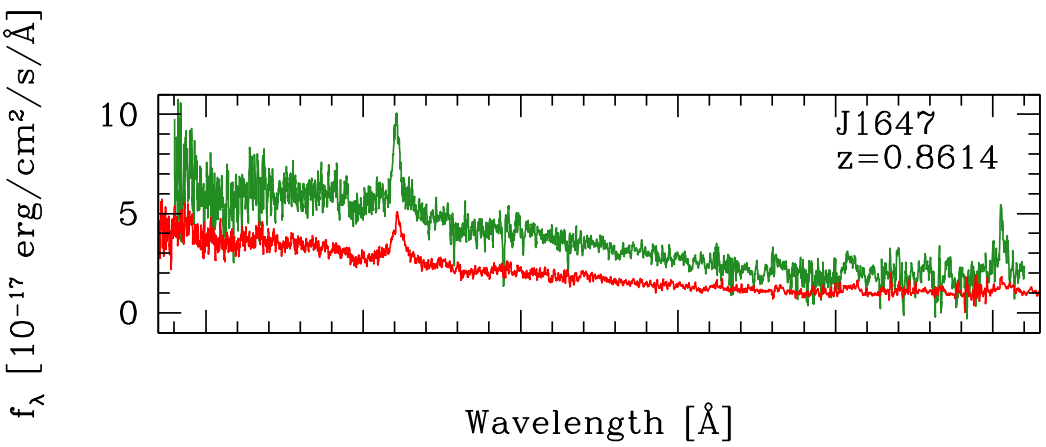

Figure 5.17.: — Continued

Part II.

Blazar photometry

6. Blazar photometry

6.1. Summary

Here we summarize results of the optical-NIR photometry of six BL Lac objects, PKS 0537-441, PKS 0735+17, OJ 287, PKS 2005-489, PKS 2155-304, W Comae, and of the flat spectrum radio quasar (FSRQ) PKS 1510-089 as a part of a photometric monitoring program in the near-infrared/optical bands started in 2004 with the REM telescope. All sources are Fermi blazars.

All this material is reported in the paper of Sandrinelli et al. 2014, A&A, 562, A79, attached as an appendix to this thesis (Part III).

Long but sparse exposures have been obtained through the REM telescope, located at the ESO premises of La Silla (Chile), which was built with the main purpose of promptly observing the gamma ray bursts detected by the *Swift* mission. The REM software system (Covino et al. 2004) is able to manage complex observational strategies in a fully autonomous way. Being robotic is very well fitted for systematic observations of extensive duration.

REM can take simultaneous NIR-optical images of the same source and several observations are sometimes obtained in the same night interval. We have considered the optical and NIR data in VRIJHK bands (from 0.55 to 2.15 μm), collected from April 2005 to June 2012. Systematic monitoring, independent of the activity of the source, guarantees large sample size statistics, and allows an unbiased view of different activity states on weekly or daily time scales for the whole timeframe and on nightly timescales for some epochs.

Our purpose is to investigate flux and spectral variability on short and long time scales. We were probing the synchrotron component where the first peak of the SED is located. As is apparent from the literature (see e.g. Bonning et al. 2012, and references therein) and from our results , the variability pattern of blazars in the optical is rather complex. On time scales of days or months, one can explore modifications in the jet structure or accretion disk, and possibly their interaction. On the other hand, when the time scales are hours, we are close to the scales of the expected radius of the central black hole (e.g. Urry & Padovani 1991). General and special relativistic effects become dominant.

Variability $\gtrsim 3$ mag is observed in PKS 0537-441, PKS 1510-089 and PKS 2155-304, the largest ranges spanned in the near-infrared. The color intensity plots show rather different morphologies. The spectral energy distributions in general are well fitted by a power law, with some deviations that are more apparent in low states. Some variability episodes during a night interval are well documented for PKS 0537-441 and PKS 2155-304. For the latter source the variability time scale implies a large relativistic beaming factor.

In spring 2014 a paper by Zhang et al. (2014) was circulated where, using archived materials from various astronomical groups, the existence of a quasi-periodicity of T_1 in PKS2155-304 was proposed. We therefore reconsidered our REM light curves of this source and were able to confirm the results of Zhang et al. (2014). Moreover, we retrieved the γ-ray light curves from the *Fermi* archives and found a significant signal at $T = 2T_1$. Our results are published in Sandrinelli et al., ApJL, 793, L1, 2014, in which we described the methods for search for periodicity and discuss the issues of alias. (see also Section 6.5). This paper too is included in the Part III.

In this Chapter we consider some progress that has taken place in this program over recent months.

1. The REM light curves of a number of blazars were produced (see Section 6.2, and Tables 6.1 and 6.2).

2. The light curve of 3C 279, which contains a large number of observations, was analyzed. It is reported in detail in Section 6.3.

3. We have Fourier analyzed the REM photometry of all the seven objects in Sandrinelli et al. (2014a) and the photometry of 3C 279. Moreover, when available, we have considered the data from the *Fermi* archives. The most interesting results are those regarding 3C 279, which we have reported in Section 6.4. In the same paragraph we summarize the recent findings about the quasi-periodicity of the BL Lac PKS2155-304.

6.2. TeV Blazar Photometry

We have compared the REM archives[1] with the list of the blazars observed in the TeV bands (from TeVCat[2]). Apart from the objects reported in Sandrinelli et al. (2014a), there are 18 objects in the REM archives which contain observations for at least ~ 10 nights in a single band. They are selected for photometry and are listed in Tables 6.1 and 6.2 with the number of observations and the monitoring periods.

We followed the same procedures described in Sandrinelli et al. (2014a), watching out for dubious images and erroneous calibrations. Aperture photometry was performed by means of comparison stars in the fields reported in *Two Micron All Sky Survey Catalog*[3] (2MASS, Skrutskie et al. 2006) for NIR frames. For optical standard stars, calibrated sequences from several authors were followed, depending on the blazar field.

By far the one object which was been most frequently monitored by REM is 3C 279 and the results are given in the next paragraph. The other objects are not discussed here.

6.3. 3C 279 variability

REM data on 3C 279 spans from 2005-03-02 to 2011-06-30. As optical standard stars we consider some of the calibrated stars in González-Pérez et al. (2001). The properties of the light curves, plotted in Figure 6.1 in the six bands, are reported in Table 6.3. The flux values in the Table are given after de-reddening with the galactic extinction coefficients taken from Schlafly & Finkbeiner (2011).

It is apparent that during all the REM monitoring the light curves are strongly variable. The observed amplitude of variability ($\Delta m = m_{max} - m_{min}$) is larger than 4 magnitudes. The curves show monotonic trends that last some months.

The color-intensity plots (Figure 6.2) were derived from our data using quasi-simoultaneous H and R magnitudes with very short time-lapses ($\lesssim 5$ min). Usually, FSRQ exhibit an elongated shape, that we called "banana like" in our previous work, with a trend indicating a general bluer-when-fainter or redder-when-brighter track, consistent with FSRQs having luminous accretion disks, as also evidenced by their typically strong spectral emission lines. 3C 279 shows a hybrid behavior which closely resembles the case of PKS0537-441, see Sandrinelli et al. (2014a). A redder-when-brighter trend arises from fainter states, probably when the redder (with respect to the bluer disk component) jet synchrotron emission increases, or alternatively, when the combination of the emission detected became bluer for the increase of the disk emission. In 3C 279, over H ~ 12 (K ~ 12.5) an additional brightening of the source results in reverting the I-K color toward blue color, while R-H color is roughy achromatic. This effect may be due to more energetic electrons accompanying further brightening of the jet (see also Bonning et al. 2012).

The availability of six filters allow us to construct the spectral flux and the energy distributions (SED), that are reported in Figure 6.3 for a variety of source states. Some

[1] REM data are available at `http://www.rem.inaf.it`

[2] `http://tevcat.unichicago.edu/`

[3] `http://www.ipac.caltech.edu/2mass/`

Table 6.1.: TeV blazar sample

Source	ra [h:m:s]	dec [d:m:s]	Type	z
(a)	(b)	(c)	(d)	(e)
1ES0229+200	02:32:48.6	+20:17:17.5	HBL	0.14
RBS0413	03:19:47	+18:45:42	HBL	0.19
PKS0447-439	04:49:28.2	-43:50:12	HBL	–
PKS0548-322	05:50:38.4	-32:16:12.9	HBL	0.069
1ES1101-232	11:03:36.5	-23:29:45	HBL	0.186
Markarian421	11:04:27.3	+38:12:31	HBL	0.031
1ES1215+303	12:17:52.1	+30:07:01	HBL	0.13
1ES1218+304	12:21:26.3	+30:11:29	HBL	0.182
WComae	12:21:31.7	+28:13:59	IBL	0.102
3C 279	12:56:11.1	-05:47:22	FSRQ	0.536
1ES1312-423	13:14:58.5	-42:35:49	HBL	0.105
PKS1424+240	14:27:00	+23:47:40	IBL	–
PKS1510-089	15:12:52.2	-09:06:21.6	FSRQ	0.361
PG1553+113	15:55:44.7	+11:11:41	HBL	0.5
H1722+119	17:25:04.3	+11:52:15	HBL	–
PKS2005-489	20:09:27.0	-48:49:52	HBL	0.071
PKS2155-304	21:58:52.7	-30:13:18	HBL	0.116
H2356-309	23:59:09.4	-30:37:22.7	HBL	0.165

Notes: (d) Classification of the spectral energy distribution: LBL means low synchrotron peaked ($\nu_S < 10^{14}$ Hz, where ν_S is the synchrotron peak frequency) , IBL intermediate synchrotron peaked ($10^{14} Hz < \nu_S < 10^{15}$ Hz), and HBL high synchrotron peaked ($\nu_S > 10^{15}$ Hz) blazars; from Abdo et al. (2010). FSRQ means that the source flat spectrum radio quasar
(e) Redshift.

Table 6.2.: REM observation of the TeV blazar sample

Source	N NIR	N Opt	N_{night} NIR	N_{night} Opt	Start	End
(a)	(b)	(c)	(d)	(e)	(f)	(g)
1ES0229+200	106	198	27	45	2010-11-18	2014-01-02
RBS0413	75	82	24	26	2007-09-27	2009-01-26
PKS0447-439	206	239	27	21	2008-06-12	2012-11-10
PKS0548-322	141	242	27	21	2005-03-24	2012-04-12
1ES1101-232	148	171	46	54	2004-06-11	2009-07-27
Markarian421	168	160	9	8	2006-05-14	2013-04-20
1ES1215+303	38	53	16	16	2009-02-03	2009-06-10
1ES1218+304	32	116	7	12	2005-03-24	2007-01-31
WComae	599	837	141	87	2005-03-24	2012-02-26
3C 279	1613	1771	197	188	2005-03-02	2011-06-30
1ES1312-423	53	114	9	10	2008-03-17	2008-07-09
PKS1424+240	110	128	24	19	2009-06-20	2013-04-03
PKS1510-089	1529	785	444	395	2006-01-27	2013-03-21
PG1553+113	556	782	105	80	2005-04-08	2013-07-01
H1722+119	59	60	18	17	2009-03-02	2009-07-17
PKS2005-489	1133	1778	196	261	2005-04-20	2012-02-27
PKS2155-304	1459	3980	410	555	2004-06-02	2014-10-24
H2356-309	141	229	47	66	2006-07-16	2009-07-26

Notes: (b) and (c) Number of observations in Near-Infrared and optical bands, respectively. (d) and (e) Number of night-average photometric NIR and optical points. Numbers refer to H and R band, respectively (f) and (g) Start date and end date of observations (evaluated for H band).

Table 6.3.: Properties of the NIR-optical light curves of 3C 279

Filter	Magnitude range [mag]	Δm [mag]	Mean mag. [mag]	Mode [mag]	Median [mag]	Standard deviation [mag]	Flux Range [mJy]	F_{max}/F_{min}
K	9.57 - 13.33	3.76	11.00	10.56	10.77	0.76	3.14 - 100.39	32.00
H	10.07 - 14.24	4.17	12.10	12.18	12.02	0.91	2.13 - 98.77	46.47
J	10.90 - 15.21	4.32	12.77	13.14	12.55	0.82	1.31 - 69.55	53.21
I	12.09 - 16.10	4.02	14.07	13.53	13.97	0.78	0.92 - 37.10	40.36
R	12.66 - 16.58	3.92	14.64	15.09	14.62	0.73	0.77 - 28.47	37.05
V	13.11 - 16.83	3.72	15.01	15.06	15.00	0.68	0.73 - 22.57	30.82

deviation from the the power-law trend occur in the lower states toward larger frequencies.

6.4. Quasi-periodicities of BL Lacs: the case of 3C 279.

All the objects in Sandrinelli et al. (2014a) plus 3C279, which is described in this thesis, have been analyzed for periodicity. Since we are interested in investigating month-scale periodicities, we considered the light curves based on nightly averages. We adopted the same search methods described in Sandrinelli, Covino, & Treves (2014b) for PKS2155-304, i.e. the Date Compensated Discrete Fourier Transform (DC DFT, Ferraz-Mello 1981, Foster 1995), and the Lomb-Scargle (LS) algorithms (Scargle 1982). These methods are very suitable in the search for periodicity because they are expressly designed to include the unevenly spaced data from astronomical observations. Since these methods are both based on DFT, at a later stage we also analyzed the data applying the Phase Dispersion Minimization (PDM) (PDM, Stellingwerf 1978), which is an improved extension of the statistical Jurkevich (Jurkevich 1971) technique. All the candidate periods are analyzed against false alarms, see Subsection 6.5.2. The techniques employed are described in Section 6.5.1.

For MeV-GeV emitters, we also examined the *Fermi*[4] light curves as provided by the automatic standard analysis procedure. Light curves cover the interval 2008/08/06 (54684 MJD) to 2014/06/09 (56817 MJD). We took one week integrations and selected the two energy ranges 100 MeV - 300 GeV and 300 MeV - 1 GeV. The data was searched again with LS, DC DFT and PDM. Among the investigate sources, apart from PKS2155-304, 3C 279 provides results of some interest.

A period of $\sim$ 240 days is found, recurring with a good significance in the Fourier spectra optical wavelengths. A similar one is found in γ-ray curves. In NIR spectra, a period of $\sim$ 330 days also emerges. We listed the results of our our analysis of the 240-days candidate period in Table 6.4. Power spectra and folded curves are given in

[4] `http://fermi.gsfc.nasa.gov/ssc/data/access/lat/msl_lc/`

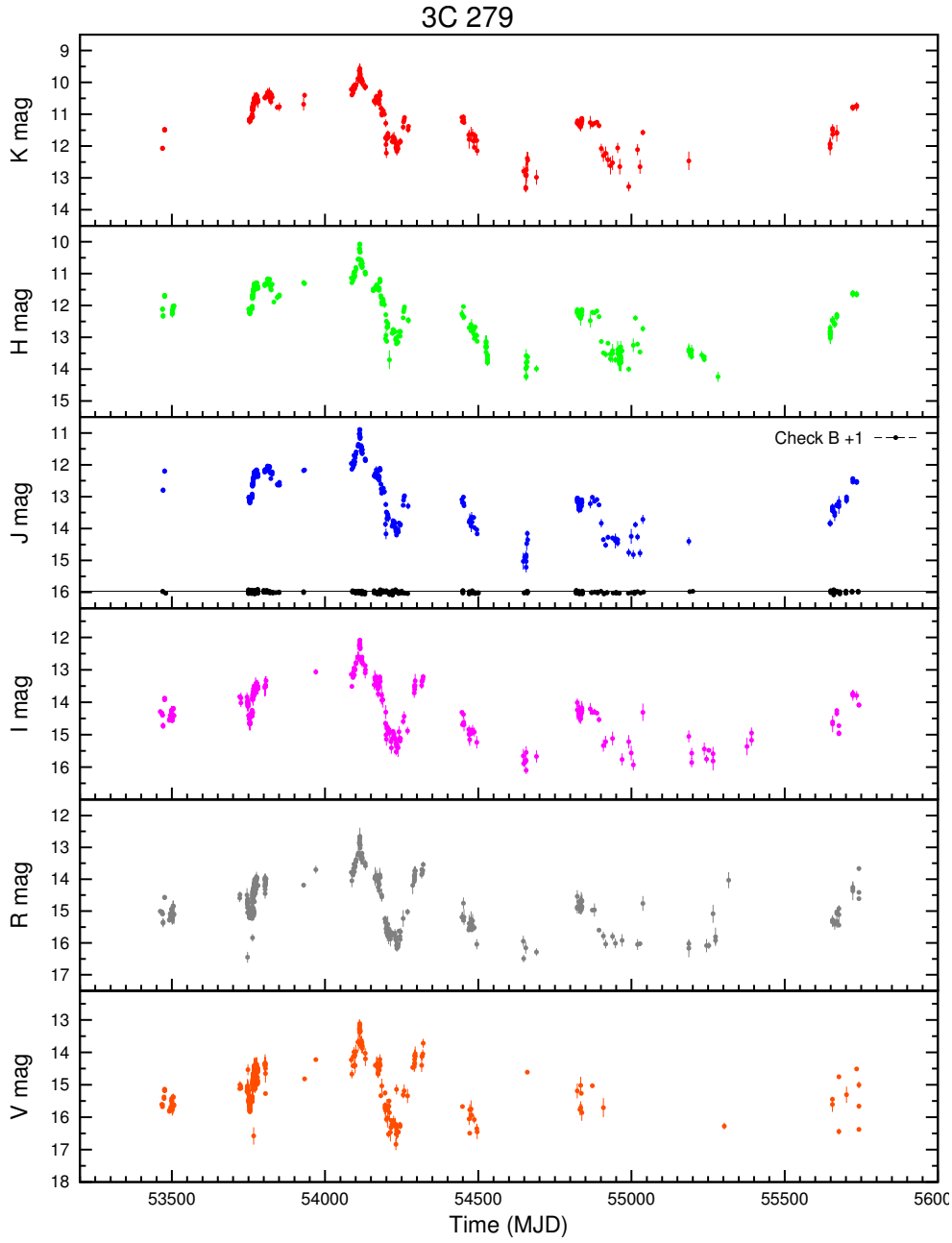

Figure 6.1.: REM near-infrared and optical nightly averaged light curves of the seven target sources. The light curve of the check star is reported in J band (black points) with the indicated displacements Δm.

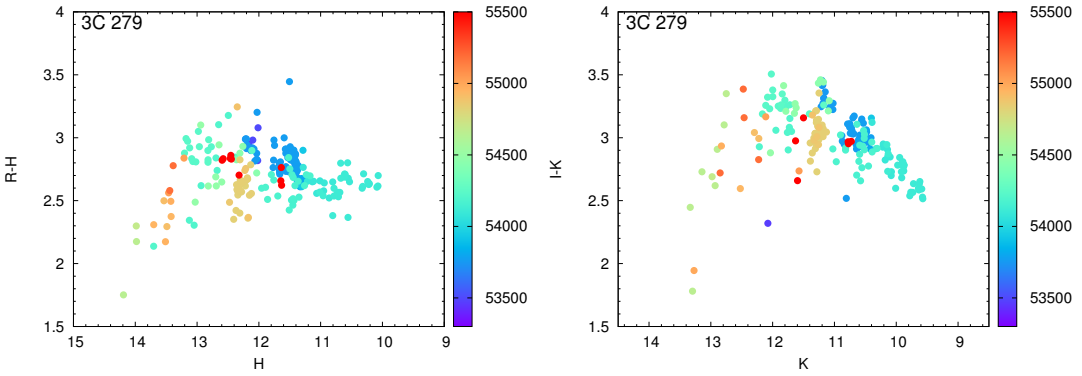

Figure 6.2.: Color intensity diagrams for 3C 279. The color of each point is related to the epoch of detections of corresponding data, according to the bar at the right. Error bars are omitted for readability.

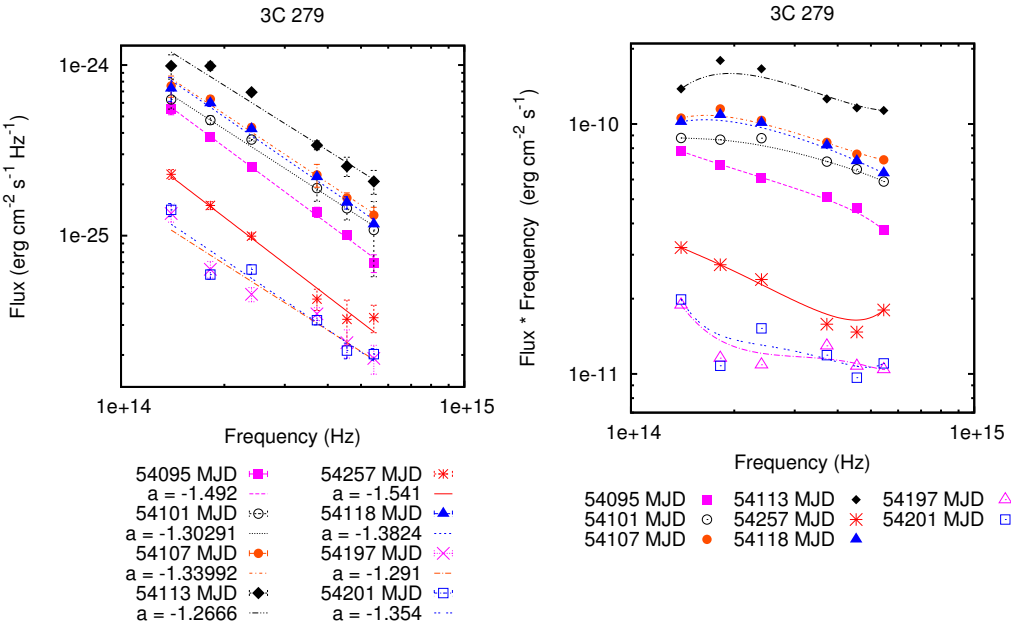

Figure 6.3.: Spectral flux distribution (*left panel*) and spectral energy distribution (*right panel*). or 3C 279 in NIR-optical bands. The lines in the left panel are power low fits and corresponding slopes α are reported. In the right panel the lines are help for the eye.

Table 6.4.: Period analysis of T $\sim$ 240 in 3C 279

			DC-DFT				LS		
Band	N_{obs}	N_{night}	T [days]	Power	p-value	A [mag]	T [days]	Power	p-value
(a)	(b)	(c)	(d)	(e)	(f)	(g)	(h)	(i)	(j)
V	643	169	255	35.85	$< 1 \cdot 10^{-6}$	0.76	243	35.59	$< 5 \cdot 10^{-7}$
R	638	188	243	34.66	$< 1 \cdot 10^{-6}$	0.75	243	34.78	$< 5 \cdot 10^{-7}$
I	510	183	241	30.75	$< 1 \cdot 10^{-6}$	0.74	245	30.64	$< 5 \cdot 10^{-7}$
J	491	178	245	27.63	$< 1 \cdot 10^{-6}$	0.73	242	27.30	$< 5 \cdot 10^{-7}$
H	609	197	244	29.77	$< 1 \cdot 10^{-6}$	0.73	244	28.62	$< 5 \cdot 10^{-7}$
K	401	170	245	28.19	$< 1 \cdot 10^{-6}$	0.67	241	29.03	$2 \cdot 10^{-5}$
average			246	31.17		0.73	243	30.98	
$\gamma 1$	–	321	231	13.17	$< 1 \cdot 10^{-6}$	0.34	231	13.18	$4.8 \cdot 10^{-3}$
$\gamma 2$	–	316	233	11.55	$< 1 \cdot 10^{-6}$	0.29	231	11.54	$2.8 \cdot 10^{-2}$
average			232	12.36		0.32	231	12.36	

Notes: (a) Band or range of energy; $\gamma 1$ is the 100 MeV - 300 GeV range and $\gamma 2$ is the 300 MeV -1 GeV range. (b) Number of observations. (c) Number of night-average photometric points, or one-week integrations for γ-rays. (d) Period corresponding to the maximum frequency in the DC DFT technique. (e) Power of maximum frequency in the DC DFT technique. (f) DC-DFT p-value. (g) Amplitude. (h) Period corresponding to the maximum frequency in the LS period gram (i) Power of maximum frequency in the LS period gram. (j) LS p-value.

figure 6.4 and the PDM periodograms in Figure 6.5.

For the sake of comparison with PKS2155-304 we report in Figure 6.6 the Fourier power spectra and the folded curves regarding the signals at $T_1 \sim = 315$ days and the peaks at $T_2 \sim$ 630-640 days found in the *Fermi* light curves, which is consistent with twice T_1. For details, peak frequencies and discussion on beat periods we refer the reader to Sandrinelli, Covino, & Treves (2014b) attached in Part III of this thesis. PDM periodograms are also reported (Figure 6.7).

6.5. Supplemental material

6.5.1. Methods of period estimation

A variety of astrophysical phenomena can produce periodic times-series curves. Time-series curves of astrophysical objects are inherently noisy measurements: photon noise, atmospheric conditions and other factors can introduce random variations into the photometric magnitude of the observations. The intervals at which the measurements are taken are also generally uneven. Periodograms are used as a tool to identify and extract any intrinsic periodic signal from the data. There are currently three algorithms that

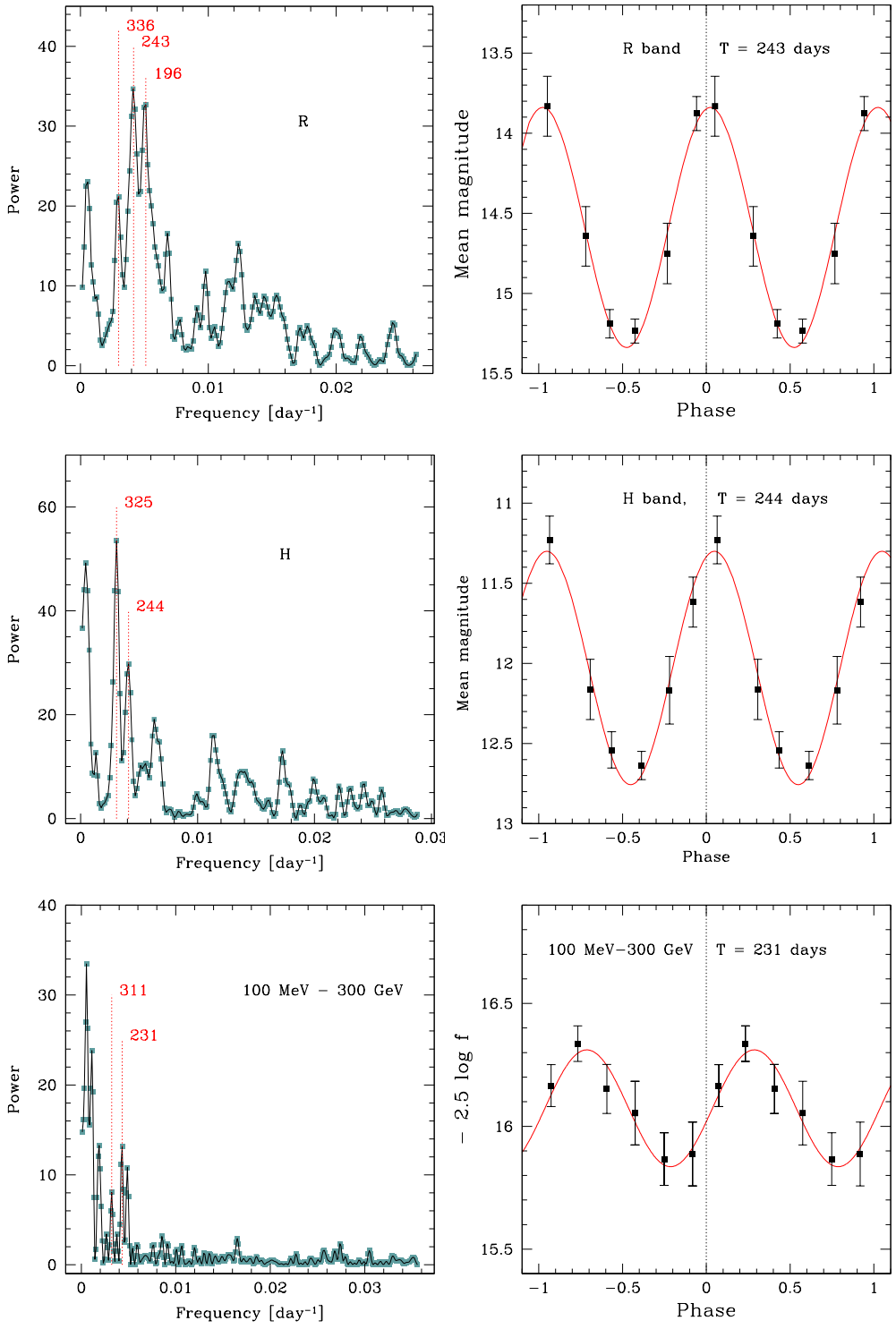

Figure 6.4.: DC DFT analysis of the period candidate T ∼ 240 days in 3C 279. *Left panels:* Power spectra, computed with the DC DFT approach, in R and H bands and in 100 MeV - 300 GeV range. Periods in days corresponding to the prominent peaks are marked. *Right panels:* Folded light curves. Error bars are the standard errors of the average. Flux f is in photon cm^{-2} s^{-1}. The initial time for folding cycles is 2008/04/29 (54585 MJD) for the NIR-optical light curves and 2011/09/06 (55810 MJD) for the γ-ray light curve. Power spectra and folded curves in the remaining bands are very similar and are omitted from the figure.

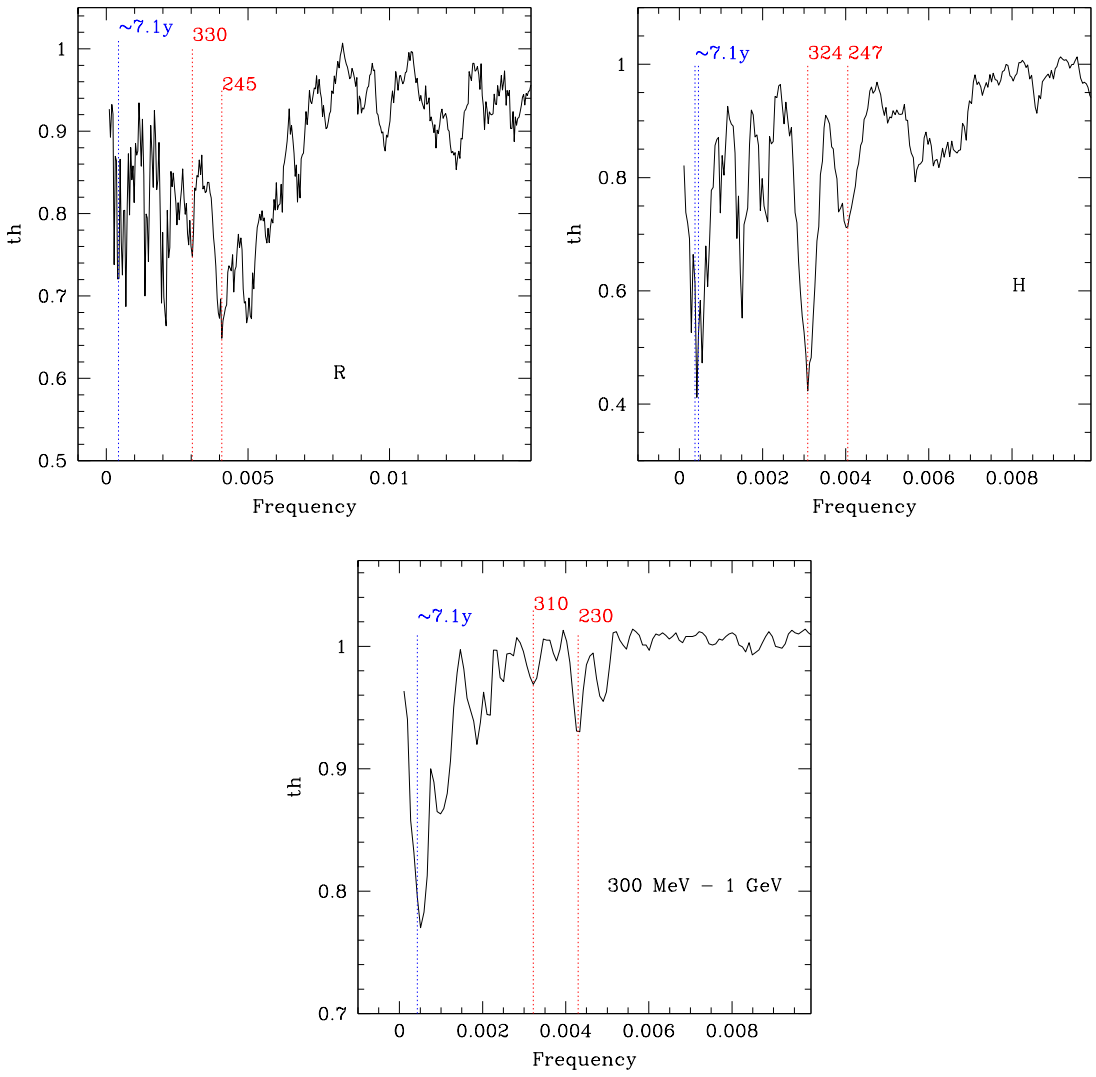

Figure 6.5.: PDM periodogram of 3C 279. The period candidates $T_1 \sim 240$ days and $T_2 \sim 320$ days are marked in Θ statistic parameter vs frequency plots derived in R-band, H-band and 300 MeV-1 GeV light curves, respectively,. The lower the Θ is, more the period is reliable. The ~ 7.1 y claimed by Fan & Lin (1999) is apparent. We note that a 7 years interval is close to the total length of NIR-optical observations. A signal at ~ 200 days also emerges.

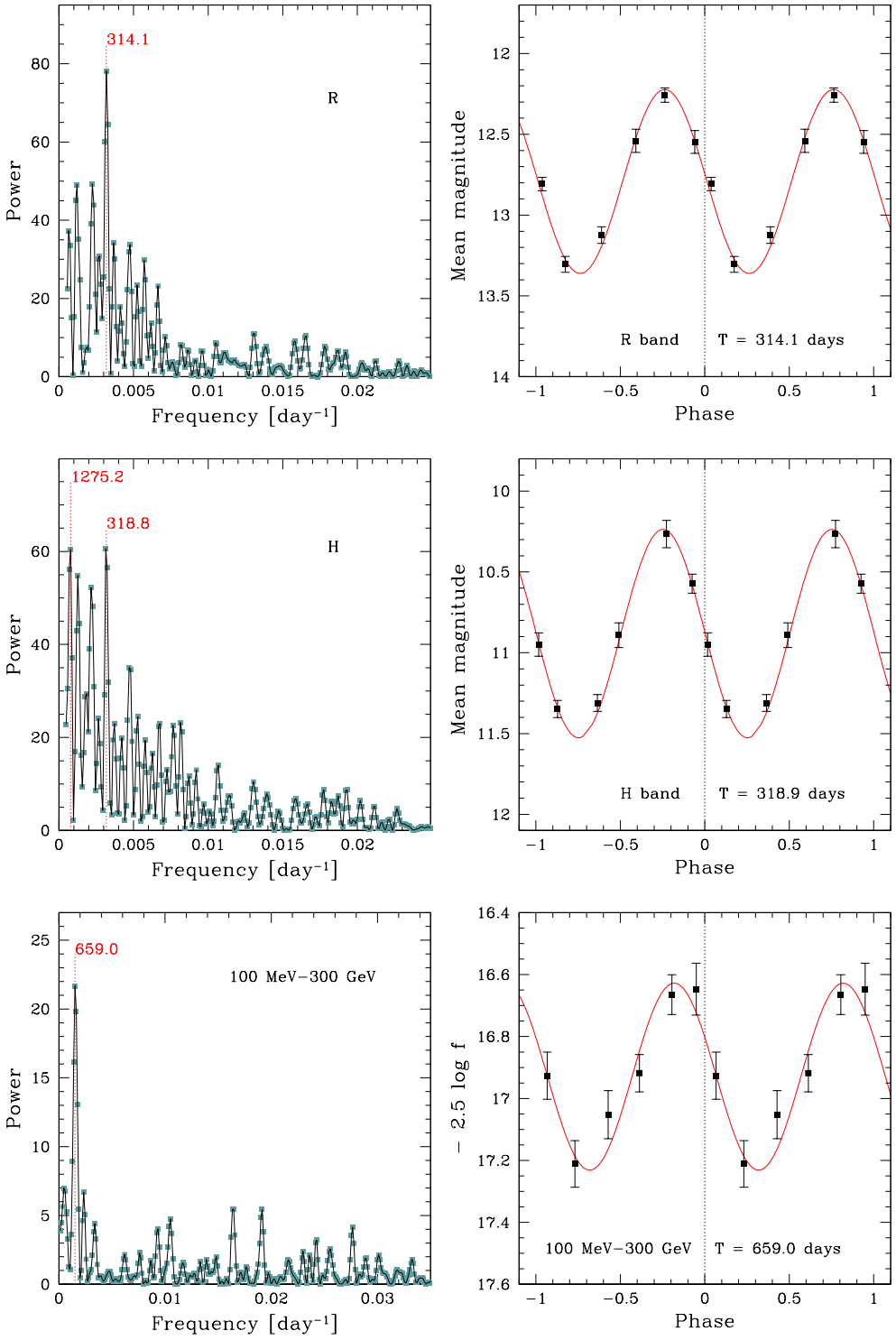

Figure 6.6.: DC DFT analysis of the period candidates $T_1 \sim 315$ days in NIR-optical light-curves and $T_2 \sim 640$ days in PKS2155-304. *Left panels:* Power spectra in R and H bands and in 100 MeV - 300 GeV range. Periods in days corresponding to the most prominent peaks are marked. *Right panels:* Folded light curves. Error bars are the standard errors of the average. Flux f is in photon cm^{-2} s^{-1}. The initial time for folding cycles is the same for all the curves (2009/07/28, 55040 MJD). Power spectra and folded curves in the remaining bands are very similar and are omitted from the figure.

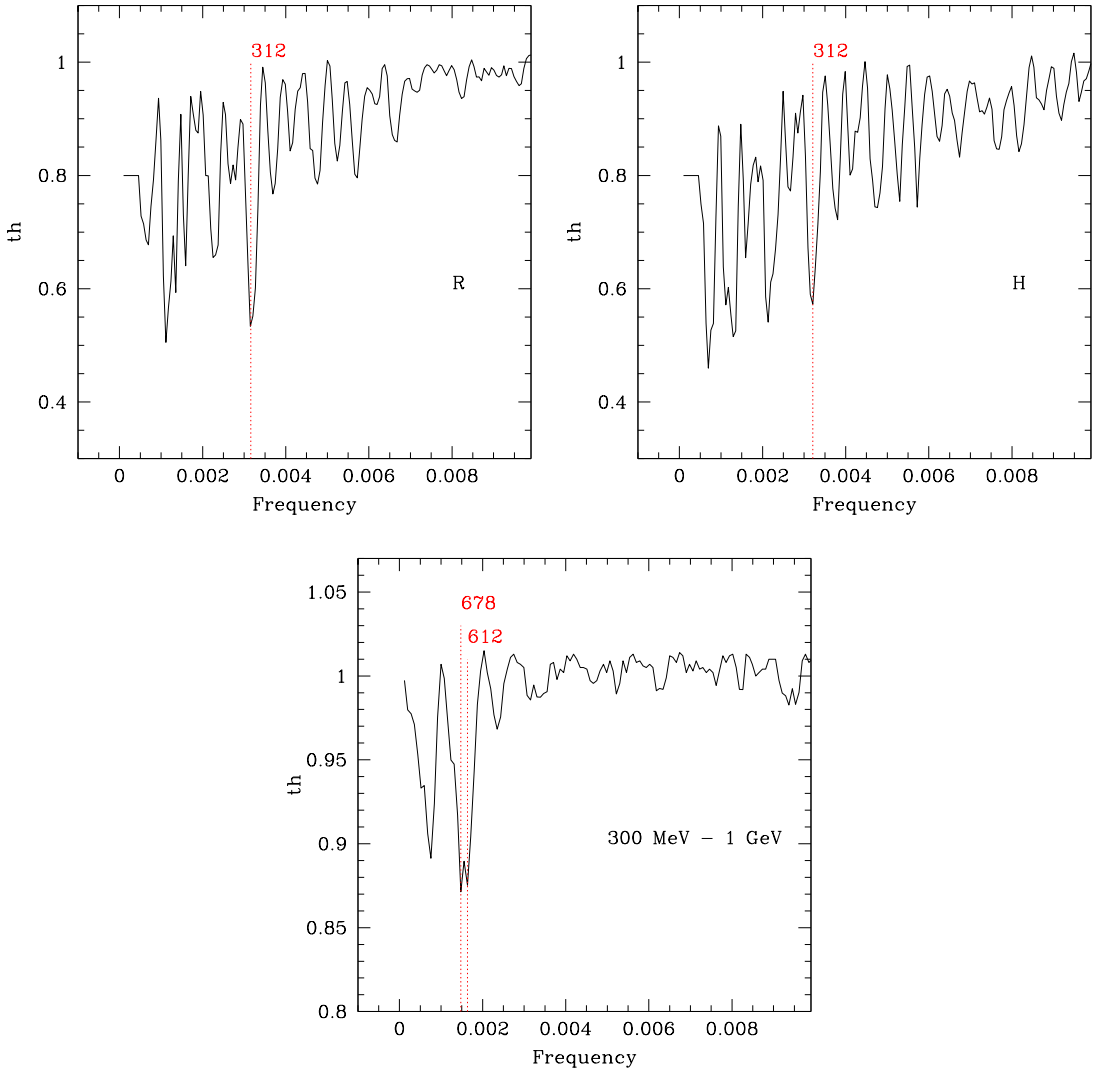

Figure 6.7.: PDM analysis results. The period candidates $T_1 \sim 315$ days in NIR-optical light-curves and $T_2 \sim 640$ days in PKS2155-304 are marked in Θ statistic parameter vs frequency plot. More the period is true, lower is the Θ local minimum (see Sandrinelli, Covino, & Treves 2014b, for details on other peaks).

we have used to calculate periodograms. In our search for periodicities we applied the methods described below:

- Lomb-Scargle (LS, Scargle 1982), optimized using the Horne & Baliunas (1986)
- Date Compensated Discrete Fourier Transform (DCDFT, Ferraz-Mello 1981)
- Phase Dispersion Minimization (PDM, Stellingwerf 1978)

We address to the indicated references for details.

Both LS and DCDFT are based on Discrete Fourier Transform (DFT) as a basic tool of spectral analysis and attempt to represent a set of observations in a linear combination of sinusoidal functions with different periods, amplitudes and phases. The basis of sinusoidal functions transforms the data from the time domain to the frequency domain. DFT techniques usually assume evenly spaced data points in the time series, but this is rarely the case with astrophysical time-series data. Both methods have derived algorithms for transform coefficients that are similar to the DFT in the limit of evenly spaced observations. Although LS periodogram decomposes the data into a series of sine and cosine functions, it is similar to least-squares statistical methods, aiming at minimizing the difference between observed and modeled data. LS assume an exponential distribution of power values in the limit of a large number of observations, and a binomial distribution for a small number of observations.

DC DFT calculates the power spectrum of unequally-spaced data using a so-called date compensated discrete Fourier transform. This transform is defined so as to include the uneven spacing of the dates of observation and weighting of the corresponding data. Accurate determination of the spectral peak heights allows one to filter harmonics discriminating among the spectrum peaks that correspond to independent periodicities from those that are just aliases of those periodicities.

PDM method incorporates all the data directly into the test statistic and is thus well suited to small data sets. It is an extension of the Jurkevich technique (Jurkevich 1971) and is a classical method for distinguishing between possible periods, by finding the period that produces the least observational scatter around the mean light curve. PDM first folds the observation data on a series of trial frequencies. For each trial frequency, the full phase interval (0, 1) is divided into a user defined number of bins. The variance of each of these bins is calculated, giving a measure of the scatter around the mean light curve, defined by the means of the data in each sample. The PDM statistics Θ is calculated by dividing the overall variance of all the samples by the variance of the original (unbinned) dataset. This process is repeated for each next trial frequency. The local minima in the Θ vs frequency plot (periodogram) indicate the period candidates. The lower Θ, more reliable the period is. If the period is not true Θ will be approximately equal to one. Swingler (1989) reported that statistical or epoch folding periodogram methods may be regarded as being approximation to the Furrier methods and their statistical performance is generally inferior.

6.5.2. Check test for significance and alias.

In our search we performed tests to check the significance of the dominant period: The dominant period is the most prominent period resulting from the analysis. It corresponds with the highest peak (e.g. in LS, DCDFT) or deepest valley (e.g. in PDM) in the periodgraph, depending on the selected period analysis method. The dominant period is not necessarily the true period (or exact period) of the object under analysis. Some peaks or valleys arise from aliasing, others may be harmonics of the main (fundamental) frequency.

Aliases are artifacts derived from the interval sampling between observations or sampling rate, and cause false peaks in the analysis. An alias masquerades as another period, where the data seemingly fits as well as the correct period. It differs from the true period by an integral fraction. If a sinusoid of frequency f is sampled s times per day, with s = f/2, the resulting samples will also be compatible with a sinusoid of frequency f∼2s. Each sinusoid becomes an alias for the other. To avoid aliasing, we check the signal does not contain any sinusoidal component with a frequency greater than s/2. This is equivalent to saying that the sampling frequency s must be strictly greater than twice the signal's bandwidth (i.e., the difference between the maximum and minimum frequencies of its sinusoidal components).

We also check for the significance of the period by calculating the False Alarm Probability (FAP) for dominant periods. Many of the FAP algorithms presented in literature had been demonstrated to be unreliable. Heck, Manfroid, & Mersch (1985) demonstrated the F-test (test for long-term trends) of the PDM method is incorrect. Cumming, Marcy, & Butler (1999) demonstrated the Horne & Baliunas (1986) equation for the number of independent frequencies is incorrect. This equation is used in Lomb-Scargle false alarm probabilities. To assess the dominant period statistical significance we have executed a Monte Carlo Permutation Test. Permutation tests are special cases of randomization tests that use randomly generated numbers for statistical inference. This test executes the selected period analysis calculation repeatedly, each time shuffling the magnitude values of the observations to form a new, randomized observation set, but keeping the observation times fixed. For our test the number of interactions was always N=200. In all cases we obtained a 99.9 % confidence interval for the p-values reported in the Table 6.4 and for PKS2155-304 resulting from trying all possible permutations.

Part III.

Publications

7. List of publications and full papers

⋆ **Sandrinelli A.**, Falomo R., Treves A., Farina E.P., & Uslenghi, M., 2014, MNRAS, **444**, 1835, *The environment of low redshift quasar pairs.*

⋆ **Sandrinelli A.**, Covino S., & Treves A., 2014, ApJ, **793**, L1, *Quasi-periodicities of the BL Lac Object PKS 2155-304.*

⋆ **Sandrinelli A.**, Treves A., Falomo R., Farina E. P., Foschini L., Landoni M., & Sbarufatti B., 2014, AJ, **146**, 163, *Spectroscopy of Optically Selected BL Lac Objects and their γ-ray emission.*

⋆ **Sandrinelli A.**, Covino S., & Treves A., 2014, A&A, **562**, 79, *Long and short term variability of seven blazars in six near-infrared/optical bands.*

⋆ J. Aleksic S., Ansoldi L. A., ... **Sandrinelli A.**, ... (MAGIC Collaboration), 2014, A&A, **569**, 46, *MAGIC gamma-ray and multi-frequency observations of flat spectrum radio quasar PKS 1510-089 in early 2012.*

Full papers are attached below.

Monthly Notices
of the
ROYAL ASTRONOMICAL SOCIETY

MNRAS **444,** 1835–1841 (2014) doi:10.1093/mnras/stu1526

The environment of low-redshift quasar pairs

A. Sandrinelli,[1,2,3]★ R. Falomo,[4] A. Treves,[1,2,3] E. P. Farina[5] and M. Uslenghi[6]

[1]*Università degli Studi dell'Insubria, Via Valleggio 11, I-22100 Como, Italy*
[2]*INAF–Osservatorio Astronomico di Brera, Via Emilio Bianchi 46, I-23807 Merate, Italy*
[3]*INFN–Istituto Nazionale di Fisica Nucleare, Sezione Milano Bicocca, Dipartimento di Fisica G. Occhialini, Piazza della Scienza 3, I-20126 Milano, Italy*
[4]*INAF–Osservatorio Astronomico di Padova, Vicolo dell Osservatorio 5, I-35122 Padova, Italy*
[5]*Max Planck Institut für Astronomie, Königstuhl 17, D-69117 Heidelberg, Germany*
[6]*INAF–IASF via E. Bassini 15, I-20133 Milano, Italy*

Accepted 2014 July 28. Received 2014 July 28; in original form 2014 June 9

ABSTRACT

We investigate the properties of the galaxy environment of a sample of 14 low-redshift ($z < 0.85$) quasar (QSO) physical pairs extracted from Sloan Digital Sky Survey Data Release 10 archives. The pairs have a systemic radial velocity difference $\Delta V_{\parallel} \leq 600$ km s^{-1} (based on [O III]5007 Å line) and projected distance $R_{\perp} \leq 600$ kpc. The physical association of the pairs is statistically confirmed at a level of ∼90 per cent. For most of the images of these QSOs we are able to resolve their host galaxies that turn out to be on average similar to those of QSOs not in pairs. We also found that QSOs in a pair are on average in region of modest galaxy overdensity extending up 0.5 Mpc from the QSO. This galaxy overdensity is indistinguishable from that of a homogeneous sample of isolated QSOs at the same redshift and with similar host galaxy luminosity. These results, albeit derived from a small (but homogeneous) sample of objects, suggest that the rare activation of two QSOs with small physical separation does not require any extraordinary environment.

Key words: galaxies: clusters: general – quasars: general.

1 INTRODUCTION

It is widely accepted that all massive galaxies contain a supermassive black hole in their centres. However, only a small fraction of them become active and for a very short time with respect to the evolution time of the galaxies. The mechanism that activates and fuels the nuclei of galaxies is still not well understood. The leading processes thought to be responsible for transforming a dormant massive black hole into a luminous quasar (QSO) are dissipative tidal interactions and galaxy mergers (e.g. Di Matteo, Springel & Hernquist 2005; Callegari et al. 2011, and references therein). Galaxy formation is known to be heavily influenced by the environment, with galaxies in clusters tending to be elliptical and deprived of most of their gaseous content (e.g. Silk & Wyse 1993; Kormendy et al. 2009), and in a number of cases showing signature of interactions and mergers (e.g. Bennert et al. 2008; McIntosh et al. 2008). What is the effective role of these interactions and of the large-scale environment for the triggering and/or fuelling the nuclear activity is not yet clear.

The investigation of QSO environments at various scales (from few kpc to Mpc) and at different cosmic epochs compared with that of normal galaxies still represents an important opportunity to unveil the link between nuclear activity and the immediate environment. The studies of galaxy clustering around QSOs (Stockton 1978; Yee & Green 1984, 1987) and other active galaxies (e.g. Wake et al. 2004) aim to characterize the properties of the environment and to compare them with the environment of non-active galaxies. The emerging picture is not homogeneous. Most of the papers conclude that QSOs reside in regions of galaxy density that are higher than average, albeit with significant difference among various objects. Only in rare cases QSOs are found in relatively rich environments (Stockton 1978; Yee & Green 1984) and the typical environment is a modest group or a poor cluster of galaxies.

Contrasting results emerge when the QSO environments are compared with those of non-active galaxies, depending on the properties of the sample (nuclear luminosity, redshift, radio loudness, etc.). Some differentiation emerges from the comparison of radio loud and radio quiet QSOs. Ellingson, Yee & Green (1991) studied a sample of radio loud quasars (RLQs) and radio quiet quasars (RQQs) at $0.3 < z < 0.6$ and found that the environments around RLQs are significantly denser than those around RQQs. However, Fisher et al. (1996) and McLure & Dunlop (2001) find no difference between the environments of RLQs and RQQs. More recently from the analysis of a large QSO data set at $z < 0.4$ from Sloan Digital Sky Survey (SDSS) Serber et al. (2006) found that the overdensity around the QSOs is larger than that around typical L^* galaxies. However, a more complete comparison of QSOs and inactive galaxies

★ E-mail: asandrinelli@yahoo.it

environments by Karhunen et al. (2014), that includes a matching of the samples in terms of both redshift and galaxy luminosity, shows that the galaxy number density of the QSO environments is comparable to that of the inactive galaxies.

Another important issue about the environment of QSOs is that they are found clustered similarly to galaxies in the local Universe (e.g. Porciani, Magliocchetti & Norberg 2004; Croom et al. 2005, and reference therein). At high redshift the clustering is more difficult to measure but there are indications that its strength would be higher than at the present epoch (e.g. Porciani et al. 2004). The clearest sign of QSO clustering is the finding of QSO pairs, see e.g. the pioneering work of Djorgovski (1991) and the analysis on the Veron-Cetty & Veron (2000) catalogue by Zhdanov & Surdej (2001). Hennawi et al. (2006) found a large sample of QSO pair candidates in a wide range of redshift but a detailed study of the environment was not carried out. Most of these QSO pairs (∼80 per cent) are at $z > 1$ hindering observations of their environment. A number of high-redshift QSO pairs have also been discovered by Hennawi et al. (2010).

Detailed study of the environment of a QSO pair at $z \sim 1.3$ has been reported by Djorgovski et al. (1987). Boris et al. (2007) investigated the environment of four QSO pairs at $z \sim 1$ with separations $\gtrsim$1 Mpc. They found one pair in a particularly high-density region, some evidences for galaxy cluster in the proximity of other two, while one pair appears isolated. A more systematic study was presented by Farina, Falomo & Treves (2011, hereafter F11) for six low-redshift physical QSO pairs from the SDSS data set. They reported a pair in a moderately rich group of galaxies together with dynamical evidence of additional mass to make the pairs bound systems. More recently, Green et al. (2011) searched for signatures of galaxy clusters and hot inter cluster medium associated with seven close ($R_\perp < 25$ kpc) QSO pairs. Because of low-quality images they fail to resolve the host galaxies and to set stringent limits to the galaxy environments. Nevertheless from their observations there is no evidence that these pairs are in rich cluster environments.

Rare examples of QSO associations with more than two objects have been reported (Djorgovski et al. 2007; Farina et al. 2013) but the limited number prevents performance of a statistical analysis.

In this paper, we explore the galaxy environments and the dynamical properties around 14 low-redshift QSO physical pairs derived from SDSS Data Release 10 (SDSS-III DR10, Ahn et al. 2014) spectroscopic and imaging data sets. For these systems, we perform a detailed analysis of their host galaxies and of the clustering of galaxies around the pairs. We are then able to compare the properties of these environments with those of a homogeneous sample of QSOs not in pair spanning the same range of redshift and host galaxy luminosities. Finally, from the difference of systemic velocity of each pair (derived from [O III]λ5007 emission lines, hereafter [O III]) we set constraints on the total minimum mass of the systems based on the dynamic of the pair.

In this work, we assume a concordant cosmology: $H_0 = 70$ km s^{-1} Mpc^{-1}, $\Omega_m = 0.30$ and $\Omega_\Lambda = 0.70$.

2 THE SAMPLE OF QUASAR PHYSICAL PAIRS

We searched for QSO pair candidates from a data set of ∼260 000 QSOs drawn from the SDSS combining the QSO spectroscopic catalogues of Schneider et al. (2010) and of Pâris et al. (2014). We restricted the search to the ∼40 000 QSOs with $z < 0.85$, in order to derive redshifts from [O III] narrow emission line, which is a much better indicator of the systemic velocity of the QSO host galaxy (Hewett & Wild 2010; Liu et al. 2014).

To search for QSO pair candidates we computed the number N_{obs} of QSOs in the catalogue that have $\Delta V_\parallel < \Delta V_{\parallel,limit}$ and $R_\perp < R_{\perp,limit}$, where $\Delta V_{\parallel,limit}$ and $R_{\perp,limit}$ are fixed values, and compared with the number N_{exp} of expected random association using the redshift permutation method (e.g. Zhdanov & Surdej 2001). It consists in maintaining fixed the positions of the QSOs, permuting randomly the redshifts. 10 000 runs were performed. We repeated the search with various value of $\Delta V_{\parallel,limit}$ and $R_{\perp,limit}$ in order to optimize the number of candidates with respect to the number of chance associations. It turns out that the best choice is $R_\perp < 600$ kpc and $\Delta V_\parallel < 600$ km s^{-1}. For this combination, we find 26 QSO pair candidates of which only 3–4 (∼14 per cent) are expected to be false pairs (random associations).

At this stage of the selection $\Delta V_\parallel$ was determined from SDSS redshifts. We inspected the spectra of all candidates to ensure that the systemic $\Delta V_\parallel$ could be reliably derived from [O III] lines. For two dubious classifications we removed two QSO pair candidates, another one for the lack of the [O III] wavelength region in one spectrum. Because of poor signal-to-noise ratio, 8 pair candidates have the [O III] line position hardly measurable for at least one QSO. For the remaining pairs, the [O III] line position was measured with procedure described in F11, where the centroid was evaluated as the median of the barycentres of the line above different flux thresholds and the interquartile range as uncertainty. In one case $\Delta V_\parallel$ from [O III] did not satisfy the condition <600 km s^{-1}, which instead was fulfilled by the SDSS redshifts, and the pair candidate was removed.

In our sample of 14 QSO pairs, we then expect that 1–2 pairs could be chance superpositions. We can assume that the selected sample is mostly composed of physically associated objects where the QSO velocities are due to gravitational binding. The final list of the QSO pair candidates is reported in Table 1 and details on [O III] line measurements are given in Table 2. None of our QSO pairs are present in catalogues of lensed QSOs (CfA-Arizona Space Telescope LEns Survey of gravitational lenses, CASTLE;[1] SDSS Quasar Lens Search, SQLS[2]). Moreover detailed comparison between the spectra of each pair exhibits clear differences that exclude the possibility of gravitational lensing. The redshifts of these QSO pairs are $0.23 \lesssim z \lesssim 0.82$, with $z_{ave} = 0.58 \pm 0.16$. An example of the SDSS spectra of a selected QSO pair is given in Fig. 1.

3 HOST GALAXIES

We retrieved the *i* images of QSO pairs from the SDSS DR10 imaging archive. Analysis was made using the Astronomical Image Decomposition and Analysis software (Uslenghi & Falomo 2008). Our procedure for the study of the QSO host galaxies follows closely that adopted by Falomo et al. (2014) for the imaging study of 400 low-redshift ($z < 0.5$) SDSS QSOs in Stripe 82. In particular, the analysis provides the decomposition of the QSO components, nucleus and host galaxy (see Fig. 2), resulting in 19 QSOs with resolved host galaxies (R), five marginally resolved (M), and four objects unresolved (U); for 10 pairs we are able to characterize the host galaxy properties of either QSOs. The measured *i* magnitudes (AB system) of the nucleus and of the host galaxy are reported in Table 3, together with the rest-frame Vega M_R absolute magnitude, dereddened and *k*-corrected. Corrections for galactic extinction were taken from SDSS data base and *k*-corrections from

[1] http://www.cfa.harvard.edu/castles/
[2] http://www-utap.phys.s.u-tokyo.ac.jp/~sdss/sqls/index.html

Table 1. Properties of low-redshift QSO pair sample.

Pair Nr (a)	A (b)	z_A (c)	i_A (mag) (d)	B (e)	z_B (f)	i_B (mag) (g)	$\Delta\theta$ (arcsec) (h)	$R_\perp$ (kpc) (i)	$\Delta V_\parallel$ (km s^{-1}) (j)
1	J001103.18+005927.2	0.4865	19.75	J001103.48+010032.6	0.4864	20.62	652	390	19 ± 28
2	J022610.98+003504.0	0.4240	19.54	J022612.41+003402.2	0.4239	19.09	66.0	360	25 ± 24
3	J074759.02+431805.3	0.5011	18.84	J074759.65+431811.4	0.5017	19.09	8.9	60	123 ± 18
4	J081801.47+205009.9	0.2357	17.45	J081808.77+204910.1	0.2356	18.81	118.1	440	36 ± 16
5	J082439.83+235720.3	0.5353	18.71	J082440.61+235709.9	0.5368	18.61	15.5	90	294 ± 19
6	J084541.18+071050.3	0.5376	18.73	J084541.52+071152.3	0.5352	18.60	62.3	390	468 ± 51
7	J085625.63+511137.0	0.5420	18.38	J085626.71+511117.8	0.5432	19.18	22.5	140	148 ± 21
8	J095137.01−004752.9	0.6340	20.23	J095139.39−004828.7	0.6369	20.02	49.8	350	544 ± 23
9	J113725.69+141101.3	0.7358	20.03	J113726.12+141111.4	0.7372	20.53	12.4	90	238 ± 28
10	J114603.49+334614.3	0.7642	20.11	J114603.76+334551.9	0.7615	19.23	23.3	170	445 ± 38
11	J124856.55+471827.7	0.4386	18.62	J124903.33+471906.0	0.4386	18.30	79.4	450	4 ± 15
12	J133046.35+373142.8	0.8141	19.32	J133048.58+373146.6	0.8144	19.82	26.4	200	54 ± 43
13	J155330.22+223010.2	0.6413	18.22	J155330.55+223014.3	0.6422	20.65	5.9	40	175 ± 12
14	J222901.08+031139.8	0.8069	21.69	J222902.03+031024.7	0.8087	19.88	76.5	570	299 ± 19

Notes. (a) Pair identification number. (b) and (e) SDSS QSO name. (c) and (f) QSO redshifts derived from [O III] line positions. (d) and (g) *i*-band apparent magnitude of the QSO A and B, respectively. (h) Angular separation of the pair. (i) Proper traverse separation $R_\perp$. (j) Radial velocity difference.

Table 2. Measurements of [O III]λ5007 Å emission lines based on the median of the barycentre of the line (see the text).

Pair Nr (a)	$\lambda_{[O\,III]}$ (A) (Å) (b)	$\lambda_{[O\,III]}$ (B) (Å) (c)
1	7442.47 ± 0.63	7441.99 ± 0.26
2	7129.84 ± 0.44	7129.24 ± 0.32
3	7515.70 ± 0.26	7518.77 ± 0.30
4	6187.15 ± 0.24	6186.41 ± 0.22
5	7686.78 ± 0.37	7694.31 ± 0.26
6	7698.28 ± 0.30	7686.28 ± 1.27
7	7722.53 ± 0.47	7726.33 ± 0.20
8	8180.92 ± 0.06	8195.76 ± 0.61
9	8690.95 ± 0.33	8697.85 ± 0.70
10	8832.83 ± 1.10	8819.75 ± 0.04
11	7202.80 ± 0.05	7202.88 ± 0.32
12	9082.84 ± 0.41	9084.48 ± 1.22
13	8217.60 ± 0.26	8222.40 ± 0.07
14	9047.04 ± 0.37	9056.06 ± 0.39

Notes. (a) Pair identification number. (b) and (c) Emission line centres of [O III]λ5007 emission line for QSOs A and B, respectively.

templates of Mannucci et al. (2001) and Francis et al. (2001) for host galaxies and nuclei, respectively.

The average absolute magnitudes M_R(nuc) of the nuclei is -23.0 ± 1.1 (median -23.1 ± 0.7), similar to the nuclear luminosities of isolated QSOs (e.g. Falomo et al. 2014). We find that the absolute magnitude M_R(host) of the host galaxies range between -21 and -24.5 (mean -22.9 ± 0.8; median -22.9 ± 0.5). The distribution of M_R(host) is comparable within similar redshifts to that reported for QSOs that are not in pairs (Falomo et al. 2014), indicating that the two families of QSO (individuals and in pairs) are indistinguishable from this point of view. Note that for ∼60 per cent of the objects the observations in the *i* filter include the [O III] emission line. This might contaminate the measurement of the host galaxy luminosity (e.g. because of scattered light from the nucleus). However, the same effect would be present also in the case of single QSOs at similar redshifts.

4 GALAXY ENVIRONMENT OF THE QUASAR PAIRS

In order to characterize the QSO pair environments, we analysed the distribution of galaxies around the QSOs using SDSS DR10 catalogues. From these, we obtained position and photometry of galaxies by selecting all primary objects photometrically classified as galaxies. In each QSO pair field, we analysed the *i*-band surface distribution of the galaxies within a circular area of 15 arcmin radius, corresponding to a projected distance of 3.4 Mpc from the nearest pair ($z = 0.236$) and 9.3 Mpc from the farthest ($z = 0.807$).

To estimate the completeness of the SDSS galaxy catalogues we compared the differential number counts of detected galaxies as a function of the magnitude with the very deep galaxy count data available from the Durham University Cosmology Group.[3] In particular, for each field we considered as threshold the magnitude $m_{i,\,50\,\mathrm{per\,cent}}$ where the completeness of observed galaxies drops to 50 per cent of that expected from Capak et al. (2007; see Fig. 3).

The apparent *i*-magnitude thresholds are closely distributed around the mean value of 21.96 ± 0.09 and listed in Table 4 with the corresponding absolute *k*-corrected magnitudes. At these thresholds we can observe galaxies with magnitude M^*+2 at $z < 0.3$, M^*+1 at $z \lesssim 0.5$ and M^* at $z \lesssim 0.8$.

In order to study the galaxy environment we followed the procedure described by Karhunen et al. (2014). To evaluate the surface number density of galaxies in the background, $n_{\rm bg}$, we considered the galaxies with $i < m_{i,\,50\,\mathrm{per\,cent}}$ and projected angular distance between 7 and 15 arcmin from the mid-point of the QSO pair. This corresponds to a minimum distance from the QSO of ∼1.6 Mpc for the nearest target. The region was then divided into annuli with width of 1 arcmin and we compute $n_{\rm bg}$ as the median of the galaxy surface density of each annulus and the semi-interquartile range is assumed as scatter (see Table 4). Finally, for each QSO we counted the surface number density of galaxies in a number of annuli with width of 250 kpc around the target. The galaxy overdensity of the QSO environment is the ratio between this number density and that of the background. In order to take into account the contribution of

[3] Durham University Cosmology Group, references and data in http://astro.dur.ac.uk/∼nm/pubhtml/counts/counts.html

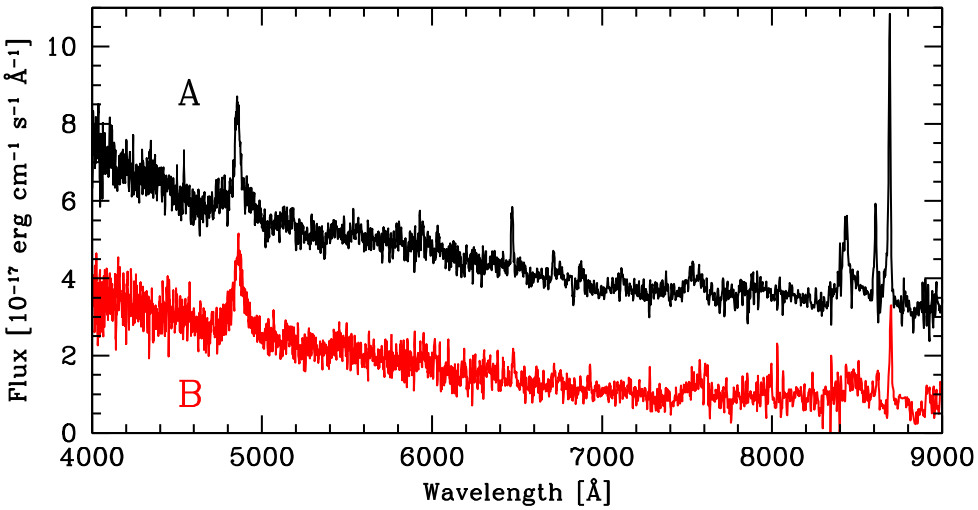

Figure 1. SDSS spectra of the QSOs in pair nr. 9 at $z = 0.736$. For clarity of comparison, the spectrum of the QSO A is shifted upwards.

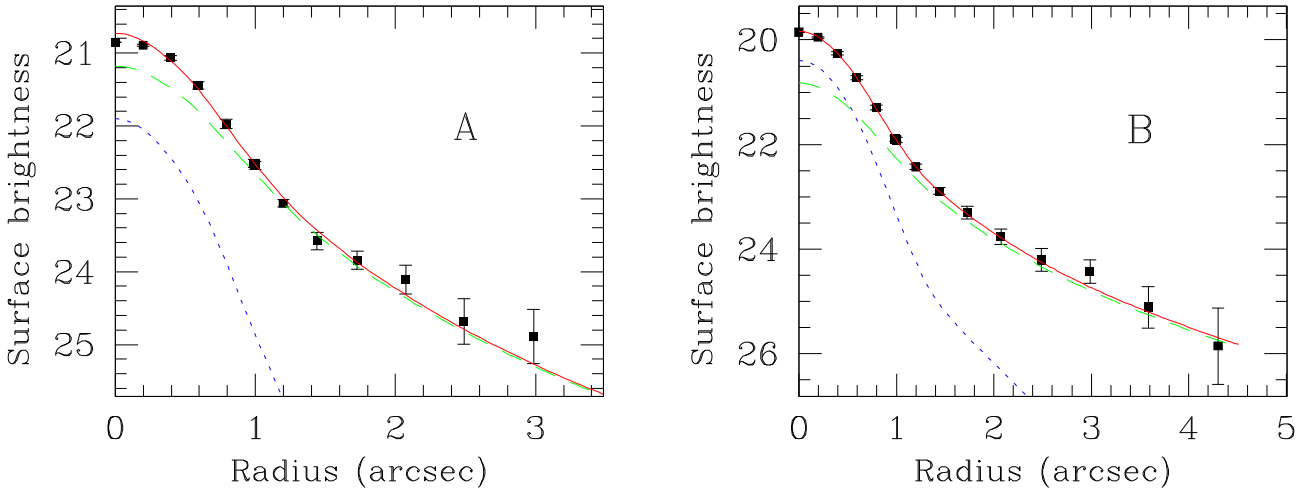

Figure 2. Examples of the QSO host galaxies decomposition for the QSO pair nr. 2. Left-hand panel: average radial brightness profile of the QSO A (square dots) fitted by the scaled point spread function (PSF) (dotted line) plus the host galaxy model convolved with the PSF (dashed line), see the text. The best fit is represented by the solid line. Right-hand panel: the same for the QSO B.

galaxies in the field around the QSO pair in the case that the annuli around the two QSO are overlapping, we have subdivided the excess galaxies in common to an equal number for each QSOs. The average cumulative overdensity distribution for the 28 QSOs is reported in Fig. 4, left-hand panel, and compared with that of isolated QSOs derived by Karhunen et al. (2014). We find that on average the galaxy overdensity around QSOs in pair is indistinguishable from that of isolated QSOs. For each QSO in our sample we report in Table 4 the galaxy overdensity inside a radius of 500 kpc.

It is of interest to probe whether the galaxy overdensity depends on the separation of the QSO pairs. To this aim, we computed the galaxy overdensity of the six pairs that are separated by less than 180 kpc and compare it with that expected under the assumption that each individual QSO contributes to the average value of galaxies (as given in Fig. 4, left-hand panel). The comparison (see Fig. 4, right-hand panel) suggests that closest QSO pairs may be in richer environments than those at larger separation. We performed a Kolmogorov–Smirnov (KS) test comparing the galaxy overdensity distribution of QSO pairs with $R_\perp < 180$ kpc to that of QSO pairs with larger separations. For the cumulative galaxy overdensity up to 1500 kpc the KS test yields the probability $p = 0.08$. This indicates that the suggestion should be confirmed by a significantly larger sample.

5 SUMMARY AND CONCLUSIONS

We have investigated the properties of the environments of a sample of 14 physical low-redshift QSO pairs. We found that the QSOs in pairs are on average in regions of modest galaxy overdensity extending up to ∼0.5 Mpc. This overdensity is indistinguishable from that of a homogeneous sample of isolated QSOs (Karhunen et al. 2014) that is matched in redshift and host galaxy luminosity. We note that for the closest QSO pairs there is a suggestion of a larger overdensity roughly commensurated to the sum of the average individual QSO environments.

Although the number of known QSO pair candidates (e.g. Hennawi et al. 2006; Myers et al. 2008) is much larger than that in our sample, a direct comparison with other results is at present not possible. For instance, the extended sample of QSO pairs of Hennawi et al. (2006) covers a wide redshift range (up to $z = 3$,

Table 3. Properties of nuclei and host galaxies.

QSO ID (a)	Class (b)	i_{nuc} (mag) (c)	i_{host} (mag) (d)	M_R(nuc) (mag) (e)	M_R(host) (mag) (f)	M(host) (10^{12} M$_\odot$) (g)
1A	R	19.90	21.61	−22.42	−21.07	0.09
1B	R	–	20.35	–	−22.33	0.3
2A	R	21.68	19.51	−20.38	−22.74	0.4
2B	R	20.16	19.03	−21.9	−23.22	0.7
3A	R	19.19	19.55	−23.23	−23.27	0.7
3B	R	19.45	19.90	−22.97	−22.94	0.5
4A	R	19.65	17.92	−20.64	−22.66	0.5
4B	R	19.29	19.68	−20.99	−20.90	0.09
5A	R	18.90	19.76	−23.65	−23.27	0.6
5B	M	18.77	20.43	−23.79	−22.61	0.4
6A	R	18.81	20.70	−23.74	−22.36	0.3
6B	M	18.72	20.53	−23.84	−22.51	0.3
7A	R	18.68	19.48	−23.86	−23.55	0.9
7B	U	19.17	–	−23.37	–	–
8A	R	20.50	19.98	−22.46	−23.64	0.9
8B	R	20.28	21.23	−22.7	−22.40	0.3
9A	U	20.08	–	−23.01	–	–
9B	R	21.32	21.03	−22.05	−23.15	0.5
10A	R	20.34	21.10	−23.13	−23.20	0.5
10B	R	19.25	19.69	−24.21	−24.59	1.9
11A	M	19.35	19.34	−22.75	−22.98	0.5
11B	U	18.31	–	−23.79	–	–
12A	M	19.43	21.01	−24.33	−23.51	0.7
12B	R	19.99	20.27	−23.66	−24.25	1.4
13A	R	18.29	20.04	−24.73	−23.65	0.9
13B	U	20.64	–	−22.39	–	–
14A	R	22.05	22.27	−21.75	−22.37	0.3
14B	M	19.99	21.97	−23.82	−22.68	0.3

Notes. (a) QSO identifier. (b) Resolved (R), marginally resolved (M), unresolved (U). (c) and (d) Apparent i magnitude (AB system) of the nucleus and host galaxy. (e) and (f) Absolute R-band magnitude (Vega system, k-corrected and dereddened) of the nucleus and host galaxy. (g) Mass of the host galaxy (see the text).

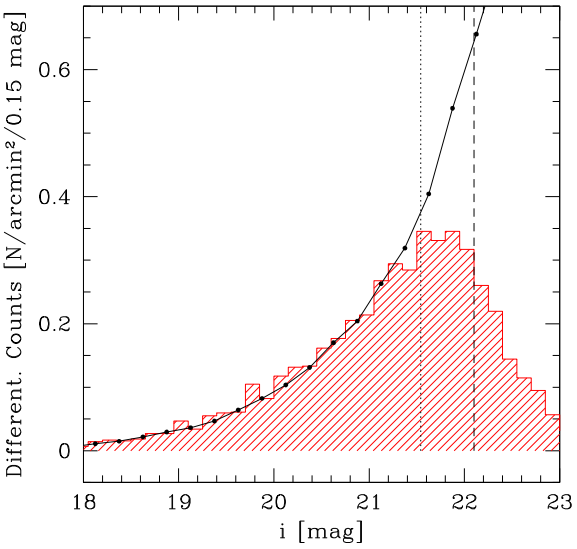

Figure 3. Number counts of galaxies as a function of i-magnitude in the field of QSO pair nr. 2 (shallow histogram). The black solid line represents for comparison the counts from deep survey of Capak et al. (2007). The dotted and dashed vertical lines mark the median magnitude and 50 per cent completeness threshold.

majority of pairs at $z > 1$), for which a detailed environmental study is not available and would require a major observational effort on large telescopes. Recently, Green et al. (2011) studied the environments around seven close QSO pairs ($R_\perp < 30$ kpc) in a redshift range comparable with ours. They searched for extended X-ray emission as evidence for a local group – or cluster – sized dark matter halo associated with these QSO pairs, and found none. In potential contrast to our results, they did not detect a significant optical/infrared galaxy density enhancement. Moreover, due to the relatively bright magnitude limits of SDSS images at the redshift of these pairs, only the most luminous galaxies possibly associated with the QSOs could be detected using their Distance and error-Weighted Colour Mean technique (Green et al. 2011). Within these limits, their results that QSO pairs avoid rich cluster environments are qualitatively in agreement with our findings.

Since the environment around pairs is relatively poor, it is of interest to compare it with the minimum mass of the binary system (the two QSOs) assuming it is gravitationally bound. Following F11, we computed the minimum virial mass associated with each pair and compared it with the total mass of the host galaxies (see Table 3), evaluated following Kotilainen et al. (2009) and Decarli et al. (2010). While in most cases $M_{vir,min}$ is less than or similar to the total mass of the host galaxies, in three cases (out of 14) $M_{vir,\,min}$ exceeds the sum of the masses of the hosts by a factor of $\gtrsim$10 (see

Table 4. Statistics of galaxy in the QSO pair environments.

Pair Nr (a)	$m_{i,\,50\,\mathrm{per\,cent}}$ (mag) (b)	$M_{i,\,50\,\mathrm{per\,cent}}$ (mag) (c)	n_{bg} (arcmin^{-2}) (d)	n_{bg} (Mpc^{-2}) (e)	$G_{0,\,5}(A)$ (f)	$G_{0,\,5}(B)$ (g)
1	21.9	−20.76	3.40 ± 0.10	26.20 ± 0.80	1.22 ± 0.04	0.68 ± 0.02
2	22.1	−20.14	4.01 ± 0.10	36.15 ± 2.71	1.14 ± 0.09	1.28 ± 0.10
3	21.9	−20.86	3.09 ± 0.16	23.16 ± 1.49	1.04 ± 0.12	1.04 ± 0.15
4	21.9	−18.62	2.24 ± 0.29	44.14 ± 6.02	0.89 ± 0.04	1.10 ± 0.04
5	21.9	−21.07	3.21 ± 0.09	22.30 ± 0.70	1.27 ± 0.07	1.21 ± 0.07
6	21.9	−21.08	3.27 ± 0.16	22.97 ± 1.39	0.87 ± 0.04	0.92 ± 0.07
7	21.8	−21.22	3.15 ± 0.15	21.98 ± 0.69	0.75 ± 0.15	0.87 ± 0.14
8	21.9	−21.67	3.06 ± 0.14	18.40 ± 0.59	1.11 ± 0.07	1.25 ± 0.05
9	22.0	−22.22	3.38 ± 0.16	17.85 ± 1.05	1.21 ± 0.04	0.93 ± 0.05
10	22.0	−22.41	3.41 ± 0.18	17.40 ± 1.02	1.27 ± 0.07	1.13 ± 0.07
11	22.0	−20.34	3.86 ± 0.10	33.88 ± 0.87	1.15 ± 0.04	1.07 ± 0.04
12	22.1	−22.68	4.56 ± 0.23	22.47 ± 0.98	0.88 ± 0.05	1.51 ± 0.06
13	22.0	−21.61	2.89 ± 0.27	17.05 ± 1.76	1.41 ± 0.02	1.33 ± 0.03
14	22.1	−22.63	4.10 ± 0.27	20.15 ± 1.47	0.57 ± 0.03	0.70 ± 0.03

Notes. (a) QSO pair identification number. (b) Apparent SDSS *i*-magnitude threshold. (c) Absolute magnitude corresponding to $m_{i,\,50\,\mathrm{per\,cent}}$. (d) and (e) Background surface number density of galaxies in arcmin^{-2} and in Mpc^{-2}, respectively. (f) and (g) Galaxy overdensity in the region within 500 kpc from the QSO, see the text.

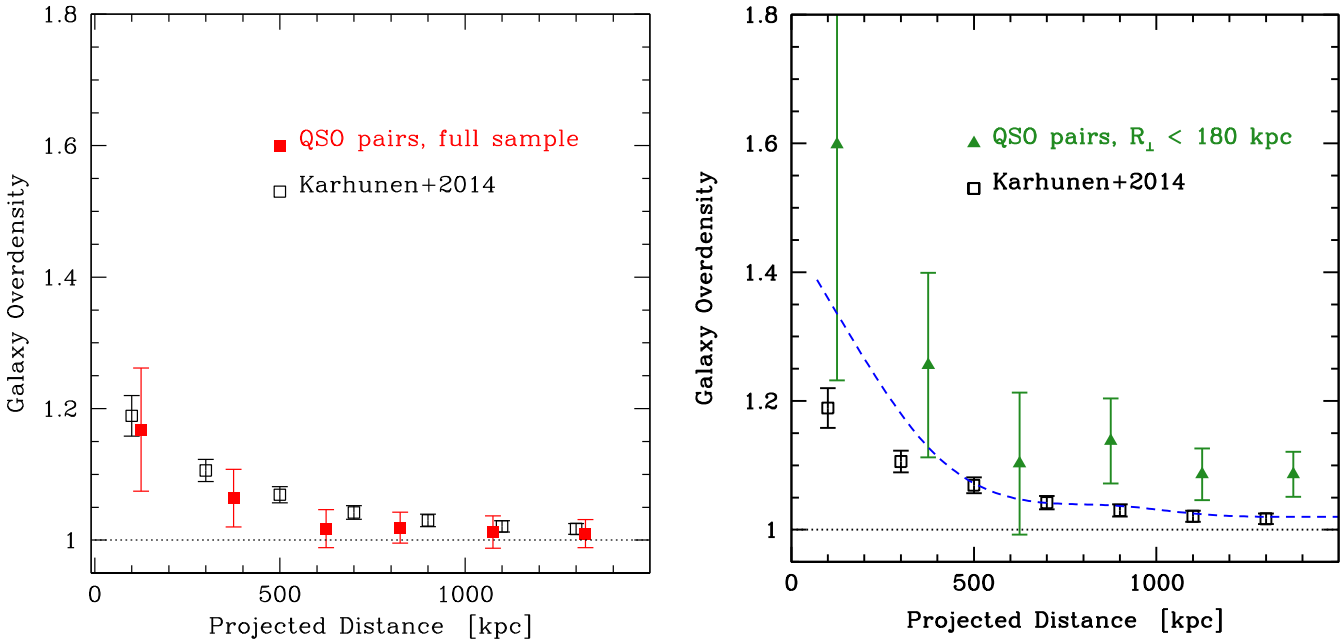

Figure 4. Left-hand panel: SDSS *i*-band mean cumulative overdensity of galaxies around the QSOs in pairs, corrected for the superposition of the companion environment (filled squares) as a function of the projected distance from the QSOs. Right-hand panel: same as the left-hand panel for whole QSO pairs with $0 < R_{\perp} < 180$ kpc (filled triangles). The expected galaxy overdensity around the whole QSO pairs, derived from the galaxy overdensity in the left-hand panel is plotted with the dashed line. In both the panels, the mean cumulative overdensity around isolated QSOs from the subsample at $i < 22$ mag derived by Karhunen et al. (2014) is plotted for a comparison (open squares).

Table 5). This is suggestive of a huge dark matter contribution (see also F11). However, because of the exiguity of our sample, to reach a firm conclusion on the environment and dynamical properties of QSO pairs, a detailed spectroscopic and imaging investigation of a larger and homogeneous sample is required.

ACKNOWLEDGEMENTS

We thank the referee for her/his constructive report which enabled us to improve our paper. We acknowledge the support of the Italian Ministry of Education (grant PRIN-MIUR 2010-2011).

Table 5. Comparison of the minimum virial mass of the QSO pairs with the total mass of their host galaxies.

Pair Nr (a)	$M_{\rm vir,\,min}$ ($10^{12}\,M_\odot$) (b)	$M_{\rm host,\,A}+M_{\rm host,\,B}$ ($10^{12}\,M_\odot$) (c)
1	(0.03 ± 0.09)	0.4
2	(0.05 ± 0.10)	1.1
3	0.20 ± 0.06	1.2
4	(0.13 ± 0.12)	0.6
5	1.9 ± 0.2	1.0
6	20 ± 4	0.6
7	0.7 ± 0.2	(1.7)
8	25 ± 2	1.2
9	1.1 ± 0.3	(1.0)
10	8 ± 1	2.4
11	(0.00 ± 0.02)	(1.1)
12	(0.14 ± 0.22)	2.0
13	0.30 ± 0.04	(1.8)
14	12 ± 2	0.6

Notes. (a) QSO pair identification number. (b) Minimum virial mass of the binary system. Values encompassed by bracket are not enough constrained. (c) Total mass of the QSO host galaxies in the pair. In the cases where only one QSO is resolved (see Table 3; in brackets), we consider the total mass to be twice that of the resolved QSO.

EPF acknowledges funding through the ERC grant Cosmic Dawn.

Funding for SDSS-III has been provided by the Alfred P. Sloan Foundation, the Participating Institutions, the National Science Foundation, and the U.S. Department of Energy Office of Science. The SDSS-III web site is http://www.sdss3.org/.

SDSS-III is managed by the Astrophysical Research Consortium for the Participating Institutions of the SDSS-III Collaboration including the University of Arizona, the Brazilian Participation Group, Brookhaven National Laboratory, Carnegie Mellon University, University of Florida, the French Participation Group, the German Participation Group, Harvard University, the Instituto de Astrofisica de Canarias, the Michigan State/Notre Dame/JINA Participation Group, Johns Hopkins University, Lawrence Berkeley National Laboratory, Max Planck Institute for Astrophysics, Max Planck Institute for Extraterrestrial Physics, New Mexico State University, New York University, Ohio State University, Pennsylvania State University, University of Portsmouth, Princeton University, the Spanish Participation Group, University of Tokyo, University of Utah, Vanderbilt University, University of Virginia, University of Washington, and Yale University.

REFERENCES

Ahn C. P. et al., 2014, ApJS, 211, 17
Bennert N., Canalizo G., Jungwiert B., Stockton A., Schweizer F., Peng C. Y., Lacy M., 2008, ApJ, 677, 846
Boris N. V., Sodré L., Jr, Cypriano E. S., Santos W. A., de Oliveira C. M., West M., 2007, ApJ, 666, 747
Callegari S., Kazantzidis S., Mayer L., Colpi M., Bellovary J. M., Quinn T., Wadsley J., 2011, ApJ, 729, 85
Capak P. et al., 2007, ApJS, 172, 99
Croom S. M. et al., 2005, MNRAS, 356, 415
Decarli R., Falomo R., Treves A., Kotilainen J. K., Labita M., Scarpa R., 2010, MNRAS, 402, 2441
Di Matteo T., Springel V., Hernquist L., 2005, Nature, 433, 604
Djorgovski S., 1991, in Crampton D., ed., ASP Conf. Ser. Vol. 21, The Space Distribution of Quasars. Astron. Soc. Pac., San Francisco, p. 349
Djorgovski S., Perley R., Meylan G., McCarthy P., 1987, ApJ, 321, L17
Djorgovski S. G., Courbin F., Meylan G., Sluse D., Thompson D., Mahabal A., Glikman E., 2007, ApJ, 662, L1
Ellingson E., Yee H. K. C., Green R. F., 1991, ApJ, 371, 49
Falomo R., Bettoni D., Karhunen K., Kotilainen J. K., Uslenghi M., 2014, MNRAS, 440, 476
Farina E. P., Falomo R., Treves A., 2011, MNRAS, 415, 3163 (F11)
Farina E. P., Montuori C., Decarli R., Fumagalli M., 2013, MNRAS, 431, 1019
Fisher K. B., Bahcall J. N., Kirhakos S., Schneider D. P., 1996, ApJ, 468, 469
Francis P. J., Drake C. L., Whiting M. T., Drinkwater M. J., Webster R. L., 2001, Publ. Astron. Soc. Aust., 18, 2
Green P. J., Myers A. D., Barkhouse W. A., Aldcroft T. L., Trichas M., Richards G. T., Ruiz Á., Hopkins P. F., 2011, ApJ, 743, 81
Hennawi J. F. et al., 2006, AJ, 131, 1
Hennawi J. F. et al., 2010, ApJ, 719, 1672
Hewett P. C., Wild V., 2010, MNRAS, 405, 2302
Karhunen K., Kotilainen J. K., Falomo R., Bettoni D., 2014, MNRAS, 441, 1802
Kormendy J., Fisher D. B., Cornell M. E., Bender R., 2009, ApJS, 182, 216
Kotilainen J. K., Falomo R., Decarli R., Treves A., Uslenghi M., Scarpa R., 2009, ApJ, 703, 1663
Liu X., Shen Y., Bian F., Loeb A., Tremaine S., 2014, ApJ, 789, 140
Mannucci F., Basile F., Poggianti B. M., Cimatti A., Daddi E., Pozzetti L., Vanzi L., 2001, MNRAS, 326, 745
McIntosh D. H., Guo Y., Hertzberg J., Katz N., Mo H. J., van den Bosch F. C., Yang X., 2008, MNRAS, 388, 1537
McLure R. J., Dunlop J. S., 2001, MNRAS, 321, 515
Myers A. D., Richards G. T., Brunner R. J., Schneider D. P., Strand N. E., Hall P. B., Blomquist J. A., York D. G., 2008, ApJ, 678, 635
Pâris I. et al., 2014, A&A, 563, A54
Porciani C., Magliocchetti M., Norberg P., 2004, MNRAS, 355, 1010
Schneider D. P. et al., 2010, AJ, 139, 2360
Serber W., Bahcall N., Ménard B., Richards G., 2006, ApJ, 643, 68
Silk J., Wyse R. F. G., 1993, Phys. Rev., 231, 293
Stockton A., 1978, ApJ, 223, 747
Uslenghi M., Falomo R., 2008, in Di Gesu V. et al., eds, Modelling and Simulation in Science. World Scientific, Hackensack, NJ, p. 313
Veron-Cetty M.-P., Veron P., 2000, VizieR Online Data Catalog, 7215, 0
Wake D. A. et al., 2004, ApJ, 610, L85
Yee H. K. C., Green R. F., 1984, ApJ, 280, 79
Yee H. K. C., Green R. F., 1987, ApJ, 319, 28
Zhdanov V. I., Surdej J., 2001, A&A, 372, 1

This paper has been typeset from a TEX/LATEX file prepared by the author.

The Astrophysical Journal Letters, 793:L1 (4pp), 2014 September 20 doi:10.1088/2041-8205/793/1/L1

QUASI-PERIODICITIES OF THE BL LACERTAE OBJECT PKS 2155−304

A. Sandrinelli[1,2,3], S. Covino[2], and A. Treves[1,2,3]
[1] Università degli Studi dell′ Insubria, Via Valleggio 11, I-22100 Como, Italy; asandrinelli@yahoo.it
[2] INAF-Osservatorio Astronomico di Brera, Via Emilio Bianchi 46, I-23807 Merate, Italy
[3] INFN-Istituto Nazionale di Fisica Nucleare, Sezione Milano Bicocca, Dipartimento di Fisica G. Occhialini, Piazza della Scienza 3, I-20126 Milano, Italy
Received 2014 July 15; accepted 2014 July 29; published 2014 August 29

ABSTRACT

We have searched for periodicities in our *VRIJHK* photometry of PKS 2155−304, which covers the years 2005–2012. A peak of the Fourier spectrum with high significance is found at $T \sim 315$ days, confirming the recent findings by Zhang et al. The examination of the gamma-ray light curves from the *Fermi* archives yields a significant signal at $\sim 2T$, which, while nominally significant, involves data spanning only $\sim 6T$. Assuming a black hole mass of $10^9\ M_\odot$, the Keplerian distance corresponding to the quasi-period T is $\sim 10^{16}$ cm, about 50 Schwarzschild radii.

Key words: BL Lacertae objects: general – BL Lacertae objects: individual (PKS 2155−304) – galaxies: active – methods: statistical

Online-only material: color figure

1. INTRODUCTION

Variability is one of the main tools for constraining models of BL Lac objects. The timescales can be so short (e.g., hours, minutes) that even taking into account relativistic beaming effects, they can shed light on sizes comparable with the gravitational radius of the black hole that is supposed to lie at their center (e.g., Urry & Padovani 1991). Variability on a month/year timescale is a probe of the relativistic jet structure, indicating, for instance, a global helicoidal pattern and a possible stratification in the direction perpendicular to the jet axis (e.g., Marscher et al. 2008). This kind of variability is essentially nonperiodic, describing turbulent mechanisms that may ultimately have been triggered by some instability in the accretion process (e.g., Ulrich et al. 1997).

Up to now, the only strong claim of periodicity in emission of a BL Lac object was raised in the case of OJ 287, where, based on optical records extending for a century, a period of 12 yr was suggested (Sillanpaa et al. 1988). It may be interpreted as a Keplerian period of a system with two black holes of masses $1.7 \times 10^{10}\ M_\odot$ and $1.4 \times 10^8\ M_\odot$ and orbital semi-major axes of 0.056 pc (Lehto & Valtonen 1996). Note, however, that this periodicity is still widely discussed (e.g., Hudec et al. 2013).

In this Letter, we concentrate on the case of the BL Lac object PKS 2155−304 ($z = 0.116$, $V \sim 13$), which is a prototype of the class and one of the most intensely observed objects since its discovery in the 1970s. It is a highly variable source, and numerous multifrequency observations from radio to TeV are now available (e.g., Aharonian et al. 2007; Foschini et al. 2008, and references therein). Possible quasi-periodicities on various timescales have been reported. Urry et al. (1993) found a repetition timescale of 0.7 days in ultraviolet and optical bands in a campaign lasting about one month. Lachowicz et al. (2009), using a few days of data from *XMM-Newton*, proposed a quasi-periodicity of 4.6 h, with a rather convincing sinusoidal folded light curve. Fan & Lin (2000) collected a miscellaneous set of data from ∼17 yr of UBVRI observations and found evidence of quasi-periodicity at 4 and 7 yr.

More recently, Zhang et al. (2014) made a collection of rather inhomogeneous optical data over the last 35 yr. In particular, they produced an *R*-band light curve with ∼8000 points derived from the photometrical data of 25 different astronomical groups. This light curve was searched for periodicity with various procedures, namely, epoch-folding (Leahy et al. 1983), the Jurkevich method (Jurkevich 1971), and the discrete correlation function (Edelson & Krolik 1988), that yielded, with high significance, a quasi-period $T \sim 317$ days.

In Section 2, we consider for periodicities our homogeneous optical–NIR photometry of PKS 2155−304 (Sandrinelli et al. 2014), which was not included in the Zhang et al. (2014) data collection. We then examine the archived *Fermi* γ-ray curves (Section 3). Conclusions are drawn in Section 4.

2. REM DATA

Our photometric study of PKS 2155−304 was obtained with the Rapid Eye Mounting Telescope (REM, 60 cm; Zerbi et al. 2004; Covino et al. 2004) in the *VRIJHK* bands from 2005 May 18 (MJD 53508) to 2012 May 29 (MJD 56076). Results and details about reduction and analysis procedures are thoroughly discussed in Sandrinelli et al. (2014). Instrumental magnitudes were obtained via aperture photometry. Calibration was performed by means of comparison stars in the field reported in the Two Micron All Sky Survey Catalog[4] (2MASS; Skrutskie et al. 2006) for NIR images and in Hamuy & Maza (1989) for the optical. Check stars were used in all CCD frames. Though the photometry is fully automatized, a direct eye check of the data was performed. Several frames were excluded because the target or the reference stars were at the border, or other obvious problems were apparent.

Since we are interested in a long periodicity, we considered light curves based on nightly averages. We searched for periodicity using the Date Compensated Discrete Fourier Transform (DC DFT; Ferraz-Mello 1981; Foster 1995) and the Lomb–Scargle (LS) algorithms (Scargle 1982). Results are reported in Table 1 and in Figure 1. The Fourier spectra of the photometry in the VIJK filters are very similar to those in R and H and are not reported in the figure.

[4] http://www.ipac.caltech.edu/2mass/

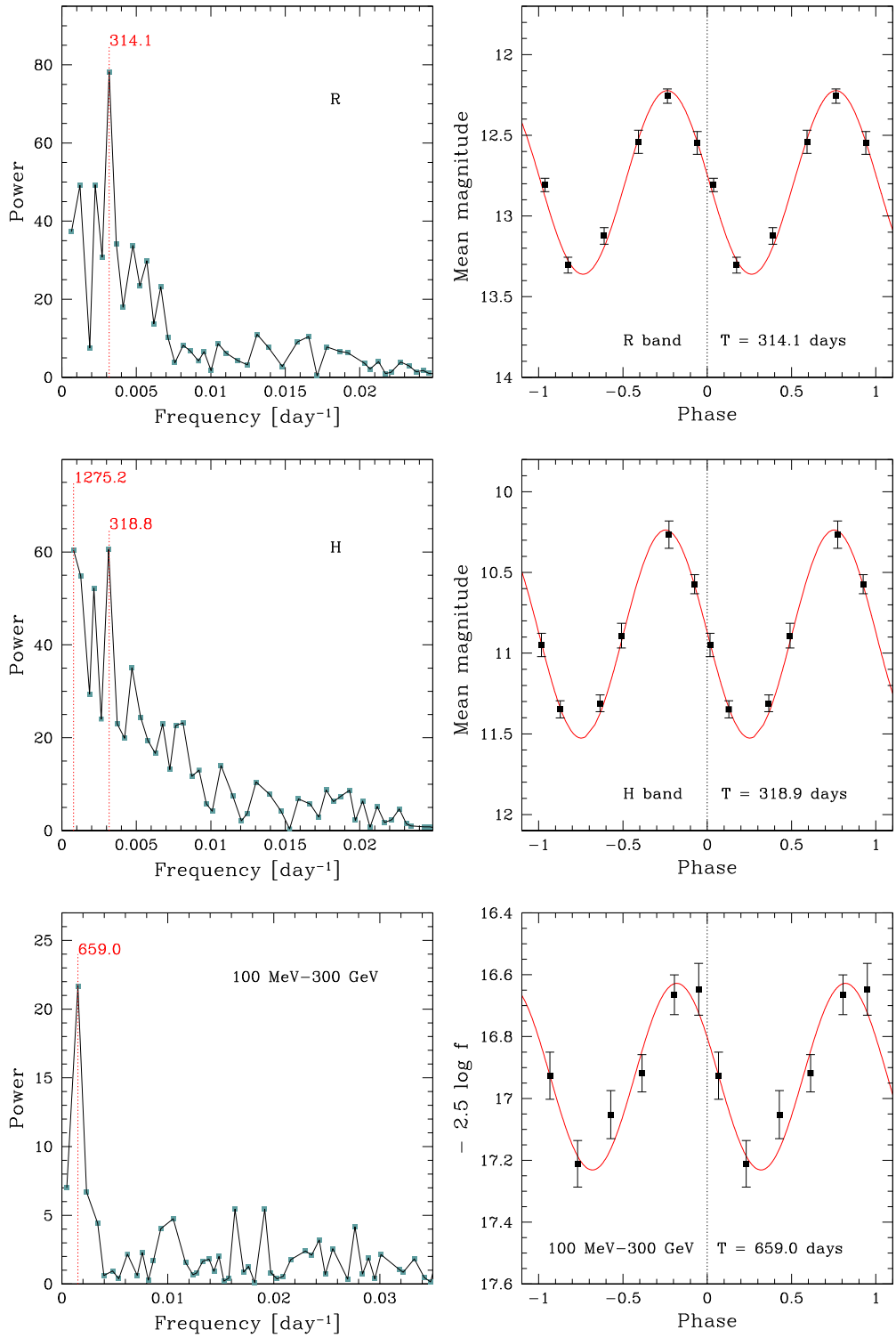

Figure 1. Left panels: power spectra, computed with the DC DFT approach, in the *R* and *H* bands and in the 100 MeV–300 GeV range. Periods in days corresponding to the prominent peaks are marked. Right panels: folded light curves. Error bars are the standard errors of the average. Flux *f* is in photon cm^{-2} s^{-1}. The initial time for folding cycles is the same for all the curves (2009 July 28, 55040 MJD).

(A color version of this figure is available in the online journal.)

Our most prominent peaks are in the range of T_1 = 306–319 days, and their significance is high. In the NIR Fourier spectra, other noticeable peaks appear at ∼461 days and at ∼1270 days (∼4 · T_1). Folded light curves based on DC-DFT[5] periods are shown in Figure 1, where data are divided in $T_1/6$ width bins. The folded light curves are clearly sinusoidal, with an amplitude of ∼0.6 mag. Therefore, we basically confirm the results of Zhang et al. (2014) with completely independent optical and NIR data.

[5] http://www.aavso.org

Table 1
Period Analysis

Band	N_{obs}	N_{night}	LS			DC-DFT			
			T (days)	Power	p-value	T (days)	Power	A (mag)	p-value
(a)	(b)	(c)	(d)	(e)	(f)	(g)	(h)	(i)	(j)
V	1938	275	306	75.42	$<5 \times 10^{-7}$	309	81.15	0.65	$<1 \times 10^{-6}$
R	1903	297	309	74.54	$<5 \times 10^{-7}$	314	78.14	0.60	$<1 \times 10^{-6}$
I	1743	281	315	77.85	$<5 \times 10^{-7}$	316	76.24	0.58	$<1 \times 10^{-6}$
J	547	274	317	62.21	$<5 \times 10^{-7}$	316	62.99	0.65	$<1 \times 10^{-6}$
H	646	258	314	62.32	$<5 \times 10^{-7}$	319	60.50	0.64	$<1 \times 10^{-6}$
K	455	243	318	61.09	$<5 \times 10^{-7}$	317	62.03	0.71	$<1 \times 10^{-6}$
100 MeV–300 GeV	–	305	650	22.02	8.4×10^{-7}	659	21.67	0.30	1.6×10^{-5}
300 MeV–1 GeV	–	295	625	12.28	1.4×10^{-2}	621	12.26	0.16	5.7×10^{-5}

Notes. (a) Band or range of energy. (b) Number of observations. (c) Number of night-average photometric points or one-week integrations for γ-rays. (d) Period corresponding to the maximum frequency in the LS periodogram. (e) Power of maximum frequency in the LS periodogram. (f) LS p-value. (g) Period corresponding to the maximum frequency in the DC-DFT technique. (h) Power of maximum frequency in the DC-DFT technique. (i) Amplitude. (j) DC-DFT p-value.

3. FERMI DATA

PKS 2155−304 is a well-known γ-ray emitter (average photon flux $f_{1-100\ \mathrm{GeV}} = 2.35 \pm 0.06 \times 10^{-8}$ photon cm^{-2} s^{-1} and photon index $\Gamma_{100\ \mathrm{MeV}-100\ \mathrm{GeV}} = 1.84 \pm 0.02$; Nolan et al. 2012). We considered the *Fermi*[6] light curves as provided by the automatic standard analysis procedure. Light curves cover the interval 2008 August 6 (54684 MJD) to 2014 June 9 (56817 MJD). We took one week integrations and selected the energy ranges 100 MeV–300 GeV and 300 MeV–1 GeV. The data were searched again with LS and DC-DFT (Table 1 and Figure 1). It is apparent that the periodicity peaks at $T_2 \sim$ 630–640 days, which is consistent with twice the optical/NIR period T_1. Note, however, that the folded light curves cover a time interval of only $\sim 3 \cdot T_2$, so this must be considered a tentative result at this time. Moreover, the present data do not allow us to comment about a possible phase shift of optical and γ-ray bands

4. DISCUSSION

The simple fact that we recover the $T_1 \sim 317$ day period of Zhang et al. (2014) on independent data, although with an overlap of the observing time interval, makes their claim of this quasi-periodicity more robust. The discovery of a possible quasi-periodicity at $T_2 \sim 2\ T_1$ in γ-rays is intriguing and per se an indirect confirmation of T_1. At this stage, because of the limited number of monitored periods, it is impossible to discriminate between a quasi-periodicity and a real period. Note that the *Fermi* satellite follows this source with no interaction with Sun constraints so that the light curve is not annually biased. For the optical–NIR data, $T_1 \sim 317$ days can be distinguished from a 1 yr period, given the length of our data train and this distinction is even stronger for the data collected by Zhang et al. (2014). In fact, in our Fourier spectra (Figure 1, top and central panels on the left) the power associated with a 1 yr periodicity is significantly lower than that at T_1.

In principle, it is also possible that T_1 is a beat frequency, for instance, with a 1 yr period. In this case the "true" period could be ∼168 days (0.46 yr) or ∼2246 days (6.15 yr). The former period does not appear in our power spectra, while the latter is comparable to the duration of our optical observations. Further information on the quasi-periodicity may come from unpublished archived observations, which we expect to be numerous since the source is a rather common target. Additional *Fermi* data will show whether our tentative quasi-periodicity in γ-rays holds up long enough to be fully convincing. Of interest would also be a detailed study of the X-ray light curves beyond that performed by Lachowicz et al. (2009). This will be a delicate business. In fact, because of the nature of most X-ray observations, a combination of data from numerous different instruments is required.

One can assume a mass of the black hole in PKS 2155−304 $\sim 10^9\ M_\odot$, as proposed by Falomo et al. (1991) and Kotilainen et al. (1998) on the basis of the absolute magnitude of the host galaxy. If T_1 (T_2) were a real periodicity, one could consider a Keplerian frame that yields an orbital radius of 1.3×10^{16} cm (2×10^{16} cm), ∼40 (70) Schwarzschild radii. The tidal effects on a star orbiting the supermassive black hole at such a radius would be very relevant, a subject which deserves further investigation.

We thank the referee for the prompt and competent report which enabled us to improve this Letter.

We acknowledge the support of the Italian Ministry of Education (grant PRIN-MIUR 2009, 2010, 2011). This work has also been supported by ASI grant I/004/11/0.

[6] http://fermi.gsfc.nasa.gov/ssc/data/access/lat/msl_lc/source/PKS_2155-304

REFERENCES

Aharonian, F., Akhperjanian, A. G., Bazer-Bachi, A. R., et al. 2007, ApJL, 664, L71
Covino, S., Stefanon, M., Sciuto, G., et al. 2004, Proc. SPIE, 5492, 1613
Edelson, R. A., & Krolik, J. H. 1988, ApJ, 333, 646
Falomo, R., Giraud, E., Melnick, J., et al. 1991, ApJL, 380, L67
Fan, J. H., & Lin, R. G. 2000, A&A, 355, 880
Ferraz-Mello, S. 1981, AJ, 86, 619
Foschini, L., Treves, A., Tavecchio, F., et al. 2008, A&A, 484, L35
Foster, G. 1995, AJ, 109, 1889
Hamuy, M., & Maza, J. 1989, AJ, 97, 720
Hudec, R., Bašta, M., Pihajoki, P., & Valtonen, M. 2013, A&A, 559, A20
Jurkevich, I. 1971, Ap&SS, 13, 154
Kotilainen, J. K., Falomo, R., & Scarpa, R. 1998, A&A, 336, 479
Lachowicz, P., Gupta, A. C., Gaur, H., & Wiita, P. J. 2009, A&A, 506, L17
Leahy, D. A., Darbro, W., Elsner, R. F., et al. 1983, ApJ, 266, 160
Lehto, H. J., & Valtonen, M. J. 1996, ApJ, 460, 207
Marscher, A. P., Jorstad, S. G., D'Arcangelo, F. D., et al. 2008, Natur, 452, 966

Nolan, P. L., Abdo, A. A., Ackermann, M., et al. 2012, ApJS, 199, 31
Sandrinelli, A., Covino, S., & Treves, A. 2014, A&A, 562, A79
Scargle, J. D. 1982, ApJ, 263, 835
Sillanpaa, A., Haarala, S., Valtonen, M. J., Sundelius, B., & Byrd, G. G. 1988, ApJ, 325, 628
Skrutskie, M. F., Cutri, R. M., Stiening, R., et al. 2006, AJ, 131, 1163
Ulrich, M.-H., Maraschi, L., & Urry, C. M. 1997, ARA&A, 35, 445
Urry, C. M., Maraschi, L., Edelson, R., et al. 1993, ApJ, 411, 614
Urry, C. M., & Padovani, P. 1991, ApJ, 371, 60
Zhang, B.-K., Zhao, X.-Y., Wang, C.-X., & Dai, B.-Z. 2014, RAA, in press (arXiv:1405.6858)
Zerbi, F. M., Chincarini, G., Ghisellini, G., et al. 2004, Proc. SPIE, 5492, 1590

The Astronomical Journal, 146:163 (7pp), 2013 December doi:10.1088/0004-6256/146/6/163

SPECTROSCOPY OF OPTICALLY SELECTED BL LAC OBJECTS AND THEIR γ-RAY EMISSION

A. Sandrinelli[1,2,3], A. Treves[1,2,3], R. Falomo[4], E. P. Farina[1,3], L. Foschini[2], M. Landoni[1,2,3], and B. Sbarufatti[2,5]
[1] Università degli Studi dell'Insubria, Via Valleggio 11, I-22100 Como, Italy; angela.sandrinelli@brera.inaf.it
[2] INAF-Osservatorio Astronomico di Brera, Via Emilio Bianchi 46, I-23807 Merate, Italy
[3] INFN-Istituto Nazionale di Fisica Nucleare, Sezione Milano Bicocca, Dipartimento di Fisica G. Occhialini, Piazza della Scienza 3, I-20126 Milano, Italy
[4] INAF-Osservatorio Astronomico di Padova, Vicolo dell Osservatorio 5, I-35122 Padova, Italy
[5] Department of Astronomy and Astrophysics, Pennsylvania State University, University Park, PA 16801, USA
Received 2013 July 9; accepted 2013 October 5; published 2013 November 13

ABSTRACT

We present Very Large Telescope optical spectroscopy of nine BL Lac objects of unknown redshift belonging to the list of optically selected radio-loud BL Lac candidates. We explore their spectroscopic properties and possible link with gamma-ray emission. From the new observations we determine the redshifts of four objects from faint emission lines or from absorption features of their host galaxies. In three cases we find narrow intervening absorptions from which a lower limit to the redshift is inferred. For the remaining two featureless sources, lower limits to the redshift are deduced from the absence of spectral lines. A search for γ counterpart emission shows that six out of the nine candidates are *Fermi* γ-ray emitters and we find two new detections. Our analysis suggests that most of the BL Lac objects still lacking redshift information are most likely located at high redshifts.

Key words: BL Lacertae objects: general – galaxies: distances and redshifts

Online-only material: supplemental data

1. INTRODUCTION

BL Lac objects are active galactic nuclei (AGNs) characterized by strong and rapid flux variability, polarization, and either weakness or an absence of spectral emission lines. Along with flat spectrum radio quasars, BL Lac objects represent a type of radio-loud object called blazars. As proposed in the seminal paper of Blandford & Rees (1978), blazars are AGNs with relativistic jets pointing close to the direction of the observer. They are the dominant population in the extragalactic γ-ray sky at both GeV and TeV energies. At radio frequencies, BL Lac objects display strong core compact flat spectrum emissions. In the optical range, the synchrotron continuum is boosted by relativistic beaming resulting in a depression of the equivalent width of the spectral lines, especially in the high-state spectra, often making the detection of redshift a challenging task and a central issue in γ astronomy.

The first complete surveys of BL Lac objects were performed in the radio band considering the flatness of the radio spectrum (e.g., Stickel et al. 1991) as a distinguishing feature. In X-rays BL Lac surveys were a sub-product of "complete" sky surveys (see, e.g., Stocke et al. 1985, 1991). The Palomar Green survey (Green et al. 1986), aimed at building a complete list of quasars based on their colors, yielded four bright BL Lac objects. The optical spectroscopy was a necessary further step, since the commonly used criterion for defining a BL Lac is the line equivalent widths EW < 5 Å (e.g., Marcha et al. 1996). The detection of these weak features requires spectroscopy of adequate spectral resolution and signal-to-noise ratio (S/N). Observations with medium aperture telescopes provided redshifts for a number of BL Lac objects (e.g., Falomo et al. 1987b, 1987a; Falomo 1990; Stickel et al. 1993; Veron 1994; Marcha et al. 1996; Carangelo et al. 2003) but for many of these objects, in particular those with a strong nuclear component, the redshifts remained unknown. With 8 m class telescopes the situation improved as demonstrated among the recent systematic spectroscopic campaigns such as our study of 69 BL Lac objects in the southern sky with ESO−VLT+FORS2, which yielded 23 new redshifts of BL Lac objects basically selected in the Giommi/Padovani list (Padovani & Giommi 1995) before the launch of *Fermi* (Sbarufatti et al. 2005a, 2005b, 2006a, 2006b, 2009; Landoni et al. 2013, spectra and redshifts are available in electronic form on our Web site http://www.oapd.inaf.it/zbllac/).

In the last decade in parallel with the activity related to high-energy emission, substantial progress in discovering new BL Lac objects and their redshifts has been derived from large optical spectroscopic surveys in combination with data from radio and X-ray catalogs. Plotkin et al. (2008, hereafter P08) selected 501 BL Lac candidates by combining observations from the Faint Images of the Radio Sky at Twenty-Centimeters (FIRST; Becker et al. 1995) radio survey with the Sloan Digital Sky Survey (SDSS) Data Release 5 spectroscopic data base, using the criteria of featureless or weak-feature spectra and Ca II H/K depression less than 40%. A substantial fraction of sources, (∼60%) lack reliable spectroscopic redshifts. Recently, using different telescopes, Shaw et al. (2013, hereafter S13) produced spectra of most of the 475 *Fermi* BL Lac candidates (Ackermann et al. 2011), obtaining redshifts for ∼44% of the sample and constraining z for nearly all remaining objects. However, in order to characterize the general properties of the BL Lac population it is highly desirable to define a homogeneous sample of BL Lac objects not biased by the properties introduced by the selection of X-ray and radio surveys. For instance, Collinge et al. (2005) compiled a large optically selected sample (386 targets) from 2860 deg^2 of the SDSS, chosen to have quasi-featureless optical spectra and low proper motions. Some radio-quiet sources were found, almost all without X-ray counterparts in the *ROSAT* All-Sky Survey (RASS; Voges et al. 1999). Plotkin et al. (2010a, hereafter P10) expanded the Collinge sample through a complex sieving procedure of SDSS DR7 (Abazajian et al. 2009), and recovered 723 purely optically selected BL Lac objects, included a fraction of 86 radio-quiet objects, the majority of which are unlikely bona fide BL Lac objects, but rather a distinct class of quasars

Table 1
Journal of Observations

Source	R.A. (h:m:s)	Decl. (d:m:s)	Date	r (mag)	Exp.Time (min)	N	Seeing (arcsec)	S/N
(a)	(b)	(c)	(d)	(e)	(f)	(g)	(h)	(i)
J003808.50+001336.5	00 38 08.503	+ 00 13 36.53	2009 Jun 13	19.30	90	6	0.6	50
J125032.58+021632.1	12 50 32.581	+ 02 16 32.173	2009 Apr 30	19.22	45	3	0.9	30
J135120.84+111453.0	13 51 20.847	+ 11 14 53.02	2009 Jun 24	18.58	45	3	1.0	100
J144052.93+061016.1	14 40 52.94	+ 06 10 16.2	2009 Jun 24	17.17	45	3	1.1	140
J145507.44+025040.2	14 55 07.443	+ 02 50 40.25	2009 Aug 12	19.40	45	3	0.7	35
J163716.73+131438.8	16 37 16.737	+ 13 14 38.80	2009 Apr 29	18.95	45	3	1.2	90
J214406.27-002858.1	21 44 06.271	− 00 28 58.19	2009 May19	19.20	45	3	0.7	15
J224448.09-000619.3	22 44 48.095	− 00 06 19.49	2009 Aug 15	19.11	45	3	0.5	90
J224730.19+000006.4	22 47 30.196	+ 00 00 06.463	2009 Sep 09	18.26	45	3	1.1	45

Notes. (a) Object ID. (b), (c) ICRS right ascension and declination coordinates (J2000). (d) Date of observation. (e) r apparent point-spread function magnitude from SDSS DR7. (f) Total exposure time. (g) Number of collected spectra. (h) Seeing during the observation. (i) S/N evaluated as the average over the whole spectrum range, avoiding the regions affected by emission or absorption features.

with intrinsically weak emission lines (Plotkin et al. 2010b; Wu et al. 2012). Approximately ∼80% of the whole P10 sample match with radio sources in the FIRST/NRAO VLA Sky Survey (Condon et al. 1998), and ∼40% match with RASS X-ray sources. Spectroscopic redshifts are given for ∼36% of the radio-loud subsample.

For this elusive class of objects the adopted selection criteria can affect the redshift distributions of the BL Lac objects and cause different cosmological evolution scenarios (see, e.g., the discussions in Bade et al. 1998 and Giommi et al. 2012). Radio-selected BL Lac objects seem to display a positive evolution (i.e., either the number density or the luminosity shows a decrease with cosmic time), while a negative evolution or no evolution at all was proposed for X-ray-selected objects (Rector et al. 2000; Rector & Stocke 2001; Caccianiga et al. 2002; Beckmann et al. 2003; Padovani et al. 2007; Ajello et al. 2009; Giommi et al. 2009, 2012, and references therein). A continuum trend from slightly positive-evolution low-peaked BL Lac objects to strong negative-evolution high-peaked BL Lac objects was proposed (Rector et al. 2000), and was thought to be related to the X-ray to radio flux ratio (Giommi et al. 1999, 2012). Statistics concerning the evolution of BL Lac objects suffer from redshift incompleteness, making the increase in objects with reliable redshifts from homogeneous and unbiased selections a core issue (see also Shaw et al. 2013 for a discussion).

In this paper we present optical spectroscopy of a small sample (nine targets) of BL Lac objects with unknown redshifts belonging to the P08 catalog of radio-selected BL Lac objects. We note that our sample is also entirely included in the P10 catalog of optically selected BL Lac objects. We describe our observations and analysis of spectra in Section 2 together with the new redshifts; then we search for counterparts in the *Fermi* Gamma-ray Space Telescope archives (Section 3). A summary and conclusions are given in Section 4.

Throughout the paper we adopt the following concordant cosmology: $H_0 = 70\,\mathrm{km\,s^{-1}\,Mpc^{-1}}$, $\Omega_m = 0.30$, and $\Omega_\Lambda = 0.70$.

2. OPTICAL SPECTROSCOPY

2.1. Sample Observations and Data Analysis

Within about 200 P08 BL Lac objects with unknown redshift, we selected a small sample of 15 with the only requirement that they be relatively bright objects ($r < 19.4$), well observable from Paranal (Chile) ESO premises and classified as high-confidence BL Lac objects. We stress that these objects are all included among the P10 radio-loud BL Lac candidates, selected on the only basis of their optical properties, thus we can consider them to be a posteriori optically selected. We collected optical spectra of only 9 sources (see Table 1) out of 15 because of weather conditions.

Spectra were gathered with FORS2 mounted on the Antu Very Large Telescope (VLT) of the ESO in Paranal. Observations were performed with the grism 300 V and the 2″ wide slit, yielding a spectral resolution at the central wavelength of $R = \lambda/\Delta\lambda \sim 350$ and covering 3800–8200 Å spectral range, exploiting the better S/N of the VLT. The seeing in the nights of observations ranged from 0.″5 to 1.″2, with an average of ∼0.″9, as reported in Table 1. Standard IRAF[6] tools were used for the data reduction. We adopted the same procedures described in previous works (e.g., Sbarufatti et al. 2005a, 2005b), including bias subtraction and flat fielding. For each target we obtained three or six individual spectra with typical total exposure times of 45 or 90 minutes, respectively, to correct for the effect of cosmic rays and provide independent checks of each signature (see Table 1). Individual spectral frames are combined by taking the median from which a one-dimensional spectrum is extracted. The wavelength calibration was achieved using the spectra of a helium neon argon lamp and typical uncertainties are ∼1 Å. Spectra are corrected for Galactic reddening according to the Schlegel et al. (1998) maps and assuming $R_V = 3.1$ (e.g., Cardelli et al. 1989).

2.2. The Optical Spectra

The extracted spectra and the normalized spectra with respect to the continuum are reported in both Figure 1 and on our previously mentioned Web site. For each spectrum the S/N is given in Table 1. The continuum was fitted with a power law, defined as $F_\lambda \propto \lambda^{-\alpha_\lambda}$. The resulting optical spectral indices are given in the Table 2 as α_ν ($F_\nu \propto \nu^{-\alpha_\nu}$, where $\alpha_\nu = 2 - \alpha_\lambda$) for consistency and easy comparison with the bulk of the literature. We find $0.73 < \alpha_\nu < 1.44$ corresponding to an average value of $\alpha_{\nu\mathrm{ave}} = 1.17$, consistent with both the average spectral index $\alpha_\nu = 1.15$ and the dispersion of 0.69 reported by P10.

[6] IRAF (Tody 1986) is distributed by the National Optical Astronomy Observatory, which is operated by the Association of Universities for Research in Astronomy, Inc., under cooperative agreement with the National Science Foundation.

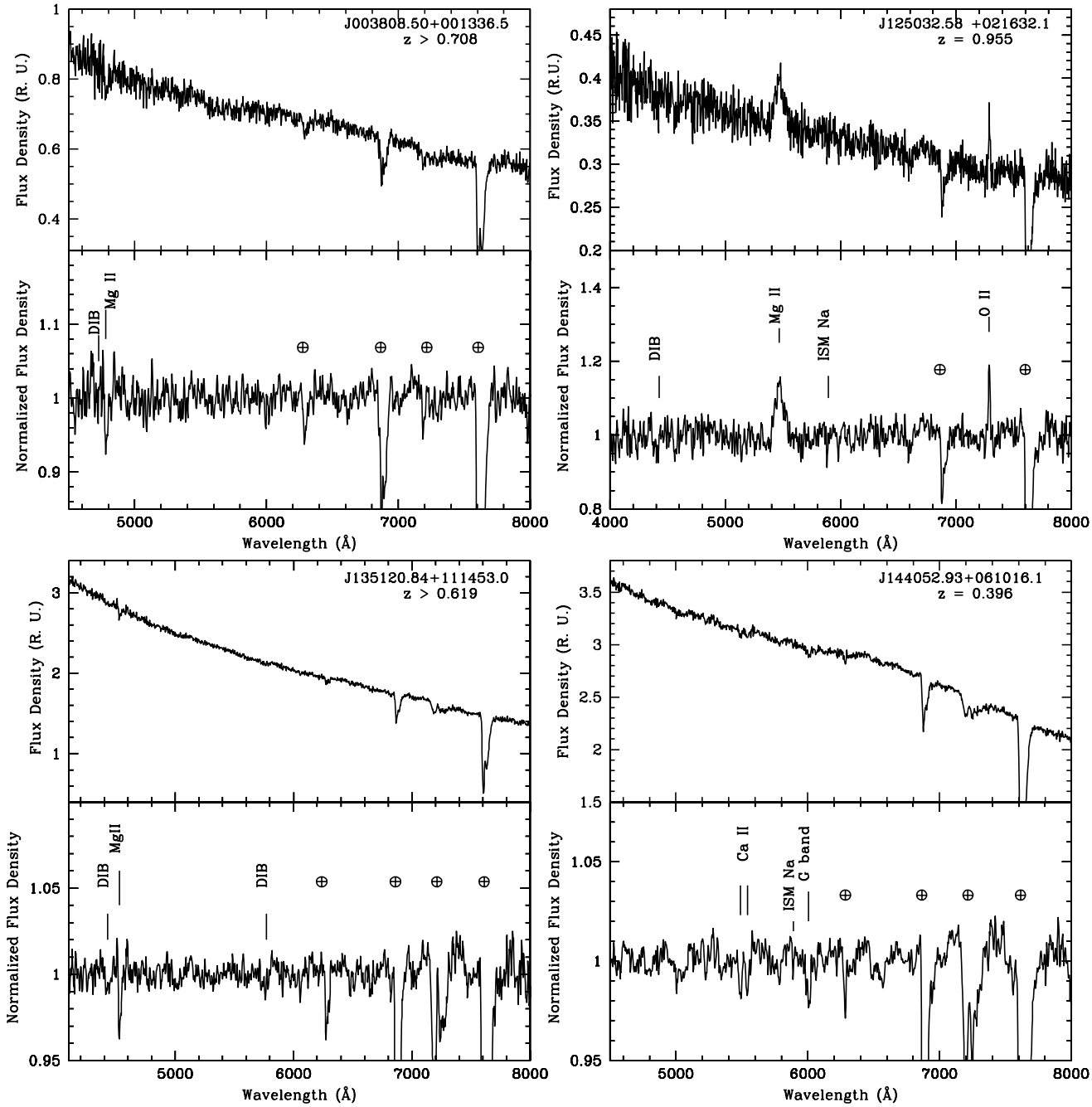

Figure 1. Spectra of the objects in the observer frame. Top panel: flux density spectrum in relative units (R.U.); Bottom panel: slightly smoothed normalized spectrum (3 pixel kernel). Telluric bands are flagged by ⊕, spectral lines are marked by line identifications, absorption features from interstellar medium (ISM) of our galaxy are labeled by ISM, and diffuse interstellar bands by DIB.

(Supplemental data for this figure are available in the online journal.)

In order to search for very weak spectral lines, we evaluated the minimum observable equivalent width (EW_{min}). Dividing the spectrum into 25 Å bins, as fully described in Sbarufatti et al. (2005b), we objectively define the EW_{min} as twice the rms of the distribution of all the observer-frame EWs measured in each bin. The absorption and emission features with EWs greater than this threshold are carefully inspected. ID labels mark the successful identifications in Figure 1 and in Table 2, where EW_{min} and line properties are also reported. For four sources we were able to obtain a redshift from the detection absorption/emission lines associated with the BL Lac host galaxy. In three cases, we observed absorption intervening features which, interpreted as Mg II 2800, allow us to set a lower limit for the redshift. In two cases the spectrum is featureless, thus we calculated a lower limit for z using the method described by Sbarufatti et al. (2005b, 2006b). Briefly, recalling that both nonthermal jets and the host galaxy contribute to the observed flux and assuming that BL Lac host galaxies are giant ellipticals with $M_R^{\rm host} = -22.90 \pm 0.50$ and standard absorption lines, one can infer a z-dependent relationship between the observed EW and emitted $EW_{rest} = EW/(1+z)$. The absence of lines puts $EW < EW_{min}$, providing a lower limit for z. In Table 2 we also report the upper limit of the redshift from the lack of Lyα absorptions as $z_{upper} = \lambda_{lim}/1216\,\text{Å} - 1 + \Delta z$, where Δz is derived

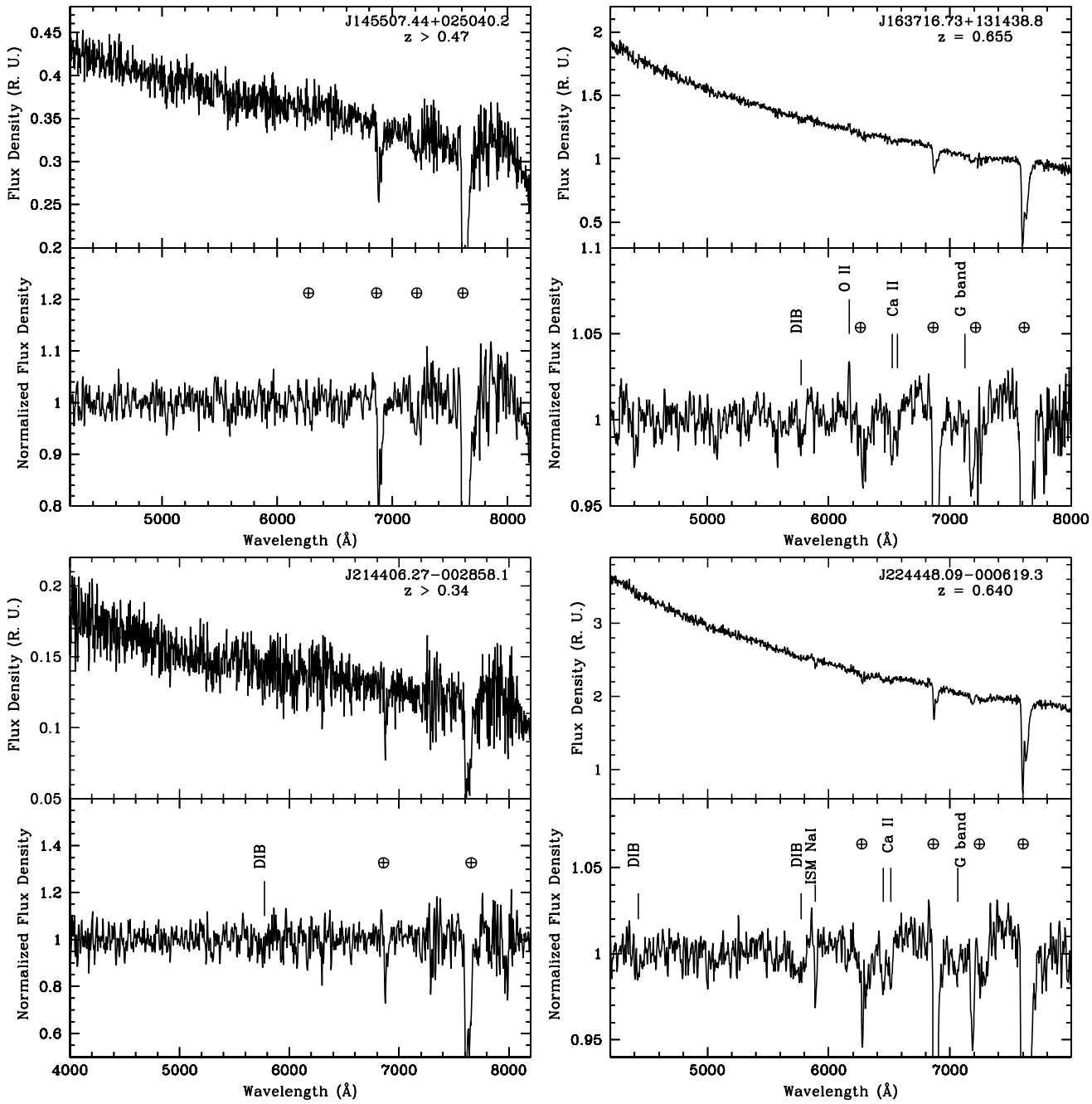

Figure 1. (Continued)

from the probability of not detecting any absorber close to the blue limit wavelength $\lambda_{\rm lim}$ of the spectrum, taking into account the redshift dependence of Lyα forest absorber density and its EW scaling (see Shaw et al. 2013, and references therein).

In the following we report further information about individual sources.

2.3. Notes on Individual Sources

J003808.50+001336.5. The spectrum shows a feature at $\lambda = 4780$ Å. We ascribed to a Mg II λ2798 intervening system absorption, which places the source at $z > 0.708$. This feature is, however, only detected at the 2σ level. We also note that the Mg II doublet is unresolvable with our observations. To complement our observations we retrieved all the spectra from the SDSS. This target was observed three times from MJD 51793 to 55444 with S/N $\sim$ 10 and no reliable redshift is available.

J125032.58+021632.1. Mg II λ2798 and O II λ3727 emission lines are apparent, securing the source at $z = 0.995$. A tentative redshift of 0.953, warning-flagged for multiple equal χ^2 best fits, was assigned to the source by the redshift fitting procedure in the SDSS DR9 based on a spectrum of S/N $\sim$ 10 where the Mg II feature is loosely visible and detectable. For this optically selected BL Lac candidate the rest-frame Mg II equivalent width is $\mathrm{EW_{rest}} = 6.1 \pm 0.4$ Å, which makes its inclusion in the BL Lac class marginal. To evaluate a more physical discriminant parameter, the optical beaming factor δ, as discussed by Farina et al. (2012) and Landoni et al. (2013), was calculated. This parameter quantifies the contribution of the thermal disk to the total luminosity (Decarli et al. 2011). $\delta = 6.0 \pm 3.6$ identifies the

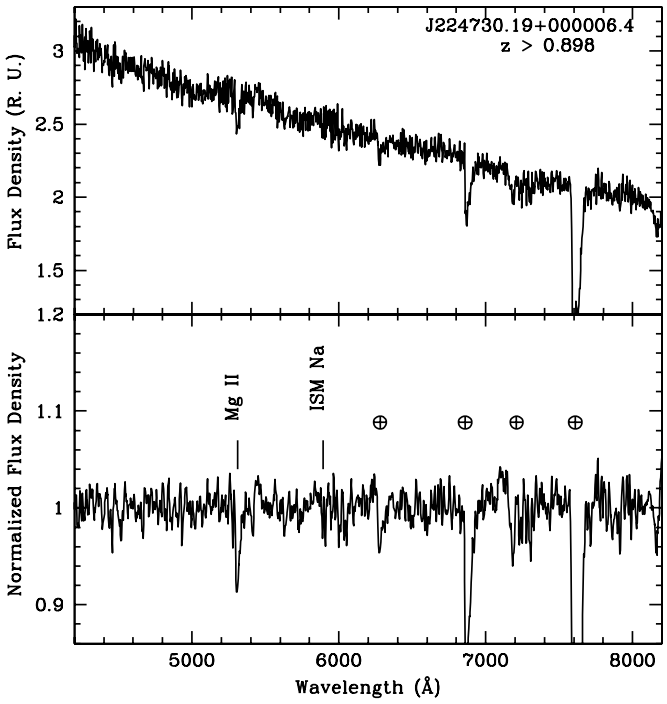

Figure 1. (Continued)

source as a BL Lac just above the intermediate region between pure QSOs ($\delta \simeq 1$) and BL Lac objects ($\delta \gtrsim 4$) (Landoni et al. 2013).

J135120.84+111453.0. An absorption feature at $\lambda = 4530$ Å is detected. If the interpretation is in terms of a Mg II λ2798 intervening system, the redshift lower limit is 0.619. This absorption feature at $\lambda = 4530$ Å was also recently observed by Shaw et al. (2013).

J144052.93+061016.1. Our spectrum exhibits Ca II H/K λλ3934, 3968 and *G*-band λ4305 absorption lines from the underlying host galaxy at $z = 0.396$. Two optical spectra were gathered by SDSS on MJD 53494 and 55686 and the inferred redshifts are noted as unreliable. Shaw et al. (2013) detected an absorption feature $\lambda \sim 3685$ Å, which, interpreted as Mg II, set a lower limit at 0.316.

J163716.73+131438.7. In our spectrum we detect a narrow emission line at $\lambda = 6170$ Å. This is most probably a real feature, since it clearly appears on each of the three individual spectra. It can be identified with O II λ2737 at $z = 0.656$. At the same redshift two absorption lines ascribed to Ca II H/K λλ3934, 3968 are apparent. In addition, the position of an absorption at $\lambda = 7124$ Å, encompassed by two H_2O telluric bands, is consistent with *G*-band absorption at the same redshift of the other lines. Our redshift is one of the highest ever detected in the optical range using host galaxy absorption lines.

J214406.27−002858.1. Because of the featureless spectrum, a redshift lower limit of ~ 0.34 is derived from $EW_{min} = 1.36$ Å. Unreliable redshifts were assigned by the SDSS.

J224448.09−000619.3. We clearly detected Ca II H/K λλ3934, 3968 absorptions at redshift $z = 0.641$. The position of an absorption at $\lambda = 7057$ Å in a region inside the H_2O telluric bands, is consistent with *G*-band λ4305 absorption at the same redshift as Ca II doublet wavelengths. No reliable redshift was obtained by the SDSS.

J224730.18+000006.4. We distinctly observed an absorption feature at $\lambda = 5311$ Å with an EW $= +3.0 \pm 0.1$ Å, which was interpreted as a Mg II λ2798 intervening system setting $z > 0.898$. There is no evidence of the emission line feature detected by Shaw et al. (2013) at $\lambda \sim 5460$ Å and taken as Mg II at $z = 0.949$. We suspect this feature to be instrumental

Table 2
Spectral Line Parameters

Source	z	α_ν	EW_{min} (Å)	Line ID	λ_{line} (Å)	Type	FWHM (km s^{-1})	EW (Å)
(a)	(b)	(c)	(d)	(e)	(f)	(g)	(h)	(i)
J003808.50+001336.5	$0.708 < z \lesssim 2.7$	1.14	0.78	Mg II	4780	a	900 ± 200	$+1.6 \pm 0.3$
J125032.58+021632.1	0.955	1.44	1.05	Mg II	5469	e	4500 ± 200	-12.1 ± 0.8
				O II	7288	e	700 ± 200	-3.6 ± 0.8
J135120.84+111453.0	$0.619 < z \lesssim 2.4$	0.73	0.31	Mg II	4530	a	1500 ± 300	$+1.0 \pm 0.2$
J144052.93+061016.1	0.396	1.08	0.28	Ca II	5491	g	1500 ± 600	$+0.4 \pm 0.1$
				Ca II	5542	g	1000 ± 200	$+0.4 \pm 0.1$
				G band	6008	g	1750 ± 50	$+0.93 \pm 0.04$
J145507.44+025040.3	$0.47 < z \lesssim 2.5$	1.44	0.79	featureless	...	...	...	...
J163716.73+131438.7	0.655	1.19	0.40	O II	6170	e	900 ± 100	-0.8 ± 0.2
				Ca II	6523	g	1100 ± 100	$+0.7 \pm 0.07$
				Ca II	6566	g	800 ± 300	$+0.4 \pm 0.09$
				G band	7124	g	800 ± 200	$+0.8 \pm 0.2$
J214406.27−002858.1	$0.34 < z \lesssim 2.5$	1.36	1.45	featureless	...	...	...	...
J224448.09−000619.3	0.640	0.88	0.35	Ca II	6450	g	1300 ± 100	$+0.75 \pm 0.05$
				Ca II	6511	g	1300 ± 300	$+0.7 \pm 0.1$
				G band	7057	g	1200 ± 300	$+0.55 \pm 0.07$
J224730.18+000006.4	$0.898 < z \lesssim 2.5$	1.27	0.52	Mg II	5311	a	1800 ± 100	$+3.0 \pm 0.1$

Notes. (a) Object ID. (b) Average redshift from the single lines or limits: lower limits from intervening systems or following Sbarufatti et al. (2005b) for featureless spectra; upper limits from the absence of Lyα absorptions following Shaw et al. (2013), and references therein. (c) Spectral index of the continuum, defined by $F_\nu \propto \nu^{-\alpha_\nu}$. (d) Minimum detectable equivalent width (observer frame). (e) Line identification. (f) Wavelength at the center of the feature. (g) Type of feature: e: emission line; g: host galaxy absorption line; a: intervening system absorption line. (h) FWHM of the line. (i) Line equivalent width (observer frame).

Table 3
Fermi LAT Detections for the Target Objects

Source	*in* 2LAC	2 FGL name	R.A. (deg)	Decl. (deg)	Error (deg)	$F_{0.1-100\ \mathrm{GeV}}$ x10^{-9} (ph cm^{-2} s^{-1})	Photon Index	TS	Time	$f_{0.1-100\ \mathrm{GeV}}$ x10^{-8} (ph cm^{-2} s^{-1})	Photon Index	TS_h
(a)		(b)	(c)	(c)	(d)	(e)	(f)	(g)	(h)	(i)	(j)	(k)
J003808.50+001336.5	Y	J0038.1+0015	9.542	0.265	0.217	1.6 ± 0.7	-1.78 ± 0.15	42	2009 Oct 09	1.80 ± 0.16	1.74 ± 0.04	24
J125032.58+021632.1	...	...	192.578	2.308	0.095	2.2 ± 1.1	-1.85 ± 0.17	35	2009 Nov 08	2.07 ± 0.54	1.93 ± 0.13	15
J135120.84+111453.0	Y	J1351.4+1115	207.867	11.256	0.110	$<2\ (5\sigma)$	...	...	2012/04/26	1.16 ± 0.84	1.63 ± 0.30	24
J144052.93+061016.1	Y	J1440.9+0611	220.248	6.189	0.099	9.6 ± 2.1	2.1 ± 0.1	148	2008 Dec 13	2.72 ± 1.3	1.93 ± 0.23	34
J145507.44+025040.2	...	...	...	...	...	$<2\ (5\sigma)$	...	...	...	...	...	
J163716.73+131438.8	...	...	249.37	13.20	0.12	$< 2\ (5\sigma)$	...	...	2011/09/29	10.2 ± 4.4	3.69 ± 0.60	9
J214406.27-002858.1	...	...	...	...	...	$<2\ (5\sigma)$	...	...	...	...	...	
J224448.09-000619.3	...	...	...	...	...	$<2\ (5\sigma)$	...	...	...	...	...	
J224730.19+000006.4	Y	J2247.2−0002	341.811	−0.049	0.152	$<2\ (5\sigma)$	...	...	2012/07/25	1.99 ± 1.3	1.93 ± 0.30	16

Notes. (a) Object ID. (b) *Fermi* LAT designation in two-year catalog. (c) γ counterpart coordinates. (d) 95% error radius. (e) Integral photon flux in 0.1–100 GeV range. (f) Photon index defined as $\nu F_\nu \propto \nu^{-\Gamma+2}$. (g) Test statistic (Mattox et al. 1996). (h) Time of highest significance observation: measures derived from 30 days integration around the date (±15 days) in Column (h). (i) Highest significance photon flux. (j) Photon index of highest significance observation. (k) Highest test statistic.

since it appears in other spectra reported by Shaw with the same spectrograph.

3. HIGH-ENERGY EMISSION OF THE SOURCES

The *Fermi* Second Source Catalog (2LAC; Nolan et al. 2012) lists the 1873 significant sources detected by the Large Area Telescope (LAT; Atwood et al. 2009) during *Fermi*'s first two years of sky survey observations. Most of them are jet-dominated AGNs. Among them, more than 400 *Fermi* BL Lac objects attest to their large contribution to the γ emission background among the brightest extragalactic sources. To fully describe our small sample of optically selected BL Lac objects, the detections of the target objects at high and very high energy were investigated. A comparison with TevCat[7] (Horan & Wakely 2008) indicates that there are no TeV counterparts. This is not surprising, since measured redshifts or lower limits to the redshift are beyond the extragalactic background light horizon, with the exception of J144052.93+061016.1.

We cross-correlated the *Fermi* archived events available online[8] with the positions of our sources to update them with respect to the LAT 2 release. As shown in Table 3, four of our sources were entered in the 2LAC catalog (LAT AGN Catalog; Ackermann et al. 2011). We analyzed all the available 57 month survey data from the start of *Fermi* activity on 2008 August 4 (MJD 54682) to 2013 April 8 (MJD 56390), with the aim of updating the values of flux and photon indices, tracing the light curves, and looking for new detections. We used the `LAT Science Tools v. 9.27.1`, the Instrument Response Function `P7SOURCE_V6`, and the corresponding background files, following standard procedures.[9] For each source, we selected all the events of class 2 ("source" type) included in a circular region centered on the optical coordinates and with radius 10°. The final source list was determined by applying a significance threshold.

Two new γ-ray sources appeared: J125032.58+021632.1 and J163716.73+131438.8. Some targets, although included in the 2LAC, have not been detected on the basis of their γ fluxes over the entire 57 month period, but due to the variability they are found on a monthly scale. In Table 3 the integrated photon flux in the 0.1–100 GeV range or upper limit, the photon index, and Test Statistic (TS, Mattox et al. 1996) are given for the entire observation time in the central columns, while the right columns refer to monthly detections with the highest TS. We considered as valid the results of the likelihood of TS $\geqslant 9$, corresponding to about 3σ.

In order to compare these results with the whole dataset, we have correlated the list of 637 radio-loud optically selected BL Lac objects of P10 with 2LAC, finding 125 positional coincidences, corresponding to ∼20 % of the objects. In the sample examined here we observed a higher percentage, possibly as a consequence of the imposed magnitude limit, and the choice of SDSS lineless objects, which can be indicative of strong beaming. We have therefore selected 194 P10 objects that are lineless and have $r < 19.4$, and found 69 correlations with 2LAC, corresponding to ∼35 %, which is consistent with our findings.

4. SUMMARY AND CONCLUSIONS

We obtained optical spectroscopy of a small sample of BL Lac objects with unknown redshifts. On the basis of the γ properties the objects appear representative of the parent sample. In one case a broad line emission was found; in others absorptions from the host galaxy or intervening material were detected. For two objects the spectrum remained featureless, and in these cases the redshift should be $z \gtrsim 0.4$. New surveys have allowed us to derive the spectroscopic redshifts of a large number of BL Lac objects with high S/N spectra. Nevertheless a significant fraction of unknown z objects remains. The new redshifts are higher compared to those from recently assembled large samples (P08, P10, S13). If tentative attributions and lower limits are included, redshift medians for high-confidence BL Lac objects are 0.39 in P08, 0.43 in the P10 radio-loud subsample, 0.32 in S13, and 0.64 for our objects. Although ours is a small sample, it suggests that a significant fraction of most unknown z objects is probably at high z and significantly beamed. Larger redshift completeness fractions and homogeneous and unbiased selections could also better define the picture of cosmological evolution. A search for γ counterpart emission shows that six out of nine objects are *Fermi* γ-ray emitters and we also found two new detections. High z and high-beamed BL Lac objects merit a

[7] http://tevcat.uchicago.edu/
[8] http://fermi.gsfc.nasa.gov/ssc/data/access/lat/2yr_catalog/
[9] http://fermi.gsfc.nasa.gov/ssc/data/analysis/scitools/

new approach and capabilities for deriving their redshifts. In the region of $z \sim 0.1$–0.7 a very effective technique was introduced in the far-UV (1135–1800 Å) with *HST*+COS (e.g., Stocke et al. 2011; Danforth et al. 2010, 2013), for constraining z quite stringently using intervening intergalactic medium absorbers detected in Lyα and in Lyβ and/or metal lines. An interesting possibility is deriving z lower limits for BL Lac objects at redshift $z > 1.5$ by searching for weak and narrow Lyα absorption in the optical range from the ground as performed and adopted in UV spectra. Good candidates can also be found in the sample presented here. High-resolution spectroscopy combined with large-diameter telescopes is required.

REFERENCES

Abazajian, K. N., Adelman-McCarthy, J. K., Agüeros, M. A., et al. 2009, ApJS, 182, 543
Ackermann, M., Ajello, M., Allafort, A., et al. 2011, ApJ, 743, 171
Ajello, M., Costamante, L., Sambruna, R. M., et al. 2009, ApJ, 699, 603
Atwood, W. B., Abdo, A. A., Ackermann, M., et al. 2009, ApJ, 697, 1071
Bade, N., Beckmann, V., Douglas, N. G., et al. 1998, A&A, 334, 459
Becker, R. H., White, R. L., & Helfand, D. J. 1995, ApJ, 450, 559
Beckmann, V., Engels, D., Bade, N., & Wucknitz, O. 2003, A&A, 401, 927
Blandford, R. D., & Rees, M. J. 1978, PhyS, 17, 265
Caccianiga, A., Maccacaro, T., Wolter, A., Della Ceca, R., & Gioia, I. M. 2002, ApJ, 566, 181
Carangelo, N., Falomo, R., Kotilainen, J., Treves, A., & Ulrich, M.-H. 2003, A&A, 412, 651
Cardelli, J. A., Clayton, G. C., & Mathis, J. S. 1989, ApJ, 345, 245
Collinge, M. J., Strauss, M. A., Hall, P. B., et al. 2005, AJ, 129, 2542
Condon, J. J., Cotton, W. D., Greisen, E. W., et al. 1998, AJ, 115, 1693
Danforth, C. W., Keeney, B. A., Stocke, J. T., Shull, J. M., & Yao, Y. 2010, ApJ, 720, 976
Danforth, C. W., Nalewajko, K., France, K., & Keeney, B. A. 2013, ApJ, 764, 57
Decarli, R., Dotti, M., & Treves, A. 2011, MNRAS, 413, 39
Falomo, R. 1990, ApJ, 353, 114
Falomo, R., Maraschi, L., Treves, A., & Tanzi, E. G. 1987a, in Liege Int. Astrophys. Colloq. 27, Observational Astrophysics with High Precision Data (Liege: Univ. de Liege), 153
Falomo, R., Maraschi, L., Treves, A., & Tanzi, E. G. 1987b, ApJL, 318, L39
Farina, E. P., Decarli, R., Falomo, R., Treves, A., & Raiteri, C. M. 2012, MNRAS, 424, 393
Giommi, P., Colafrancesco, S., Padovani, P., et al. 2009, A&A, 508, 107
Giommi, P., Menna, M. T., & Padovani, P. 1999, MNRAS, 310, 465
Giommi, P., Padovani, P., Polenta, G., et al. 2012, MNRAS, 420, 2899
Green, R. F., Schmidt, M., & Liebert, J. 1986, ApJS, 61, 305
Horan, D., & Wakely, S. 2008, AAS/High Energy Astrophysics Division Meeting, 10, 41.06
Landoni, M., Falomo, R., Treves, A., et al. 2013, AJ, 145, 114
Marcha, M. J. M., Browne, I. W. A., Impey, C. D., & Smith, P. S. 1996, MNRAS, 281, 42
Mattox, J. R., Bertsch, D. L., Chiang, J., et al. 1996, ApJ, 461, 396
Nolan, P. L., Abdo, A. A., Ackermann, M., et al. 2012, yCat, 219, 90031
Padovani, P., & Giommi, P. 1995, MNRAS, 277, 1477
Padovani, P., Giommi, P., Landt, H., & Perlman, E. S. 2007, ApJ, 662, 182
Plotkin, R. M., Anderson, S. F., Brandt, W. N., et al. 2010a, AJ, 139, 390
Plotkin, R. M., Anderson, S. F., Brandt, W. N., et al. 2010b, ApJ, 721, 562
Plotkin, R. M., Anderson, S. F., Hall, P. B., et al. 2008, AJ, 135, 2453
Rector, T. A., & Stocke, J. T. 2001, AJ, 122, 565
Rector, T. A., Stocke, J. T., Perlman, E. S., Morris, S. L., & Gioia, I. M. 2000, AJ, 120, 1626
Sbarufatti, B., Ciprini, S., Kotilainen, J., et al. 2009, AJ, 137, 337
Sbarufatti, B., Falomo, R., Treves, A., & Kotilainen, J. 2006a, A&A, 457, 35
Sbarufatti, B., Treves, A., & Falomo, R. 2005a, ApJ, 635, 173
Sbarufatti, B., Treves, A., Falomo, R., et al. 2005b, AJ, 129, 559 (Paper I)
Sbarufatti, B., Treves, A., Falomo, R., et al. 2006b, AJ, 132, 1 (Paper II)
Schlegel, D. J., Finkbeiner, D. P., & Davis, M. 1998, ApJ, 500, 525
Shaw, M. S., Romani, R. W., Cotter, G., et al. 2013, ApJ, 764, 135
Stickel, M., Fried, J. W., & Kuehr, H. 1993, A&AS, 98, 393
Stickel, M., Padovani, P., Urry, C. M., Fried, J. W., & Kuehr, H. 1991, ApJ, 374, 431
Stocke, J. T., Danforth, C. W., & Perlman, E. S. 2011, ApJ, 732, 113
Stocke, J. T., Liebert, J., Schmidt, G., et al. 1985, ApJ, 298, 619
Stocke, J. T., Morris, S. L., Gioia, I. M., et al. 1991, ApJS, 76, 813
Tody, D. 1986, Proc. SPIE, 627, 733
Veron, P. 1994, A&A, 283, 802
Voges, W., Aschenbach, B., Boller, T., et al. 1999, A&A, 349, 389
Wu, J., Brandt, W. N., Anderson, S. F., et al. 2012, ApJ, 747, 10

A&A 562, A79 (2014)
DOI: 10.1051/0004-6361/201321558

Astronomy & Astrophysics

Long and short term variability of seven blazars in six near-infrared/optical bands⋆

A. Sandrinelli[1,2], S. Covino[2], and A. Treves[1,3]

[1] Università dell'Insubria, via Valleggio 11, 22100 Como, Italy
[2] INAF, Osservatorio Astronomico di Brera, via Bianchi 46, 23807 Merate (LC), Italy
e-mail: angela.sandrinelli@brera.inaf.it
[3] Affiliated to INAF, INFN, ICRA

Received 24 March 2013 / Accepted 19 July 2013

ABSTRACT

Context. We present the light curves of six BL Lac objects, PKS 0537-441, PKS 0735+17, OJ 287, PKS 2005-489, PKS 2155-304, and W Comae, and of the flat spectrum radio quasar PKS 1510-089, as a part of a photometric monitoring program in the near-infrared/optical bands started in 2004. All sources are Fermi blazars.
Aims. Our purpose is to investigate flux and spectral variability on short and long time scales. Systematic monitoring, independent of the activity of the source, guarantees large sample size statistics, and allows an unbiased view of different activity states on weekly or daily time scales for the whole timeframe and on nightly time scales for some epochs.
Methods. Data were obtained with the REM telescope located at the ESO premises of La Silla (Chile). Light curves were gathered in the optical/near-infrared *VRIJHK* bands from April 2005 to June 2012.
Results. Variability $\gtrsim$3 mag is observed in PKS 0537-441, PKS 1510-089 and PKS 2155-304, the largest ranges spanned in the near-infrared. The color intensity plots show rather different morphologies. The spectral energy distributions in general are well fitted by a power law, with some deviations that are more apparent in low states. Some variability episodes during a night interval are well documented for PKS 0537-441 and PKS 2155-304. For the latter source the variability time scale implies a large relativistic beaming factor.

Key words. BL Lacertae objects: general – galaxies: photometry – galaxies: active

1. Introduction

Blazars are active galactic nuclei (AGNs) characterized by spectra extending from radio to GeV and TeV bands, high variability and polarization. An important subclass is that of BL Lac objects, where contrary to other species of AGNs, emission lines are very weak, if not absent. Ever since the seminal paper of Blandford & Rees (1978), the basic model of these sources requires nonthermal emission from a relativistic jet, which is pointed in the observer's direction. The thermal emission associated to an accretion disk or to the broad emission line region is only a fraction of that from the jet. The jet emission is most probably dominated by synchrotron radiation of relativistic electrons and by Compton emission through the scattering of electrons off synchrotron photons or thermal ones. This gives rise to the typical "two-peaked shape" of the spectral energy distribution (SED), when studied over a broad energy band. The variability, which is present at all bands, is a basic tool for constraining the model, since it gives information on the size of the emitting region and on the relativistic beaming factor, which transforms the quantities measured in the observer frame into those of the emitting region.

Here we present optical-NIR photometry of seven blazars, therefore we are probing the synchrotron component, where the first peak of the SED is located. As is apparent from the literature and from our results (see e.g. Impiombato et al. 2011; Bonning et al. 2012, and references therein), the variability pattern of blazars in the optical is rather complex. On time scales of days or months, one can explore modifications in the jet structure or accretion disk, and possibly their interaction. On the other hand, when the time scales are hours, we are close to the scales of the expected radius of the central black hole. General and special relativistic effects become dominant.

Long but sparse exposures have been obtained through the REM telescope, which being robotic is very well fitted for systematic observations of extensive duration. The telescope, the CCD cameras, and the photometry procedures are described in Sect. 2 and the blazar sample in Sect. 3. The variability on time scales larger than one day is presented in Sect. 4 and short term variability in Sect. 5. A discussion of the results is given in Sect. 6.

2. Telescope, camera and photometric procedures

The Rapid Eye Mounting Telescope (REM, Zerbi & Rem Team 2001; Covino et al. 2004) is a robotic telescope located at the ESO Cerro La Silla observatory (Chile). It was built with the main motivation to promptly observe the gamma ray burst detected by the *Swift* mission. REM has a Ritchey-Chretien configuration with a 60 cm $f/2.2$ primary and an overall $f/8$ focal

⋆ Full Table 3 is only available at the CDS via anonymous ftp to cdsarc.u-strasbg.fr (130.79.128.5) or via http://cdsarc.u-strasbg.fr/viz-bin/qcat?J/A+A/562/A79

Table 1. Blazar sample.

Source	Coordinates [1] RA Dec [h:m:s] [d:m:s]	Optical Class [2]	SED Class [3]	Redshift	TeV Source [4]	References
PKS 0537-441	05:38:50.35 − 44:05:09.05	BL Lac	LSP	0.896		(a)
PKS 0735+17	07:38:07.39 +17:42:18.00	BL Lac	LSP	0.424		
OJ 287	08:54.48.87 + 20.06:30.64	BL Lac	LSP	0.3060		(b)
PKS 1510-089	05:12:50.53 − 09 :05:59.83	FSRQ	LSP	0.3599	Y	(c)
PKS 2005-489	20:09:25.39 − 4 8:49:53.72	BL Lac	HSP	0.071	Y	
PKS 2155-304	21:58:52.07 − 30:13:32.12	BL Lac	HSP	0.117	Y	(d)
W Comae	12:21:31.69 + 28:13.58.50	BL Lac	ISP	0.1029	Y	(e)

Notes. [1] ICRS coordinates (J2000) and redshifts from SIMBAD[1]; [2] Class from Massaro et al. (2012); [3] Classification of the spectral energy distribution: LSP means low synchrotron peaked ($\nu_S < 10^{14}$ Hz, where ν_S is the synchrotron peak frequency), ISP intermediate synchrotron peaked (10^{14} Hz $< \nu_S < 10^{15}$ Hz), and HSP high synchrotron peaked ($\nu_S > 10^{15}$ Hz) blazars; from Abdo et al. (2010); [4] TeV Sources from TeVCat [2].

References. (a) Zhang et al. (2013); Impiombato et al. (2011); D'Ammando et al. (2010a, 2011a, 2013); Pucella et al. (2010); Impiombato et al. (2008); Pian et al. (2007); Dolcini et al. (2005). (b) D'Ammando et al. (in prep.). (c) D'Ammando et al. (2011a,b,c, 2010a,b,c). (d) Covino et al. (2010); Impiombato et al. (2008); Foschini et al. (2008); Dolcini et al. (2007). (e) D'Ammando et al. (2011a,b, 2010a).

ratio in a fast-moving alt-azimuth mount that provides two stable Nasmyth focal stations. The two cameras, REMIR (Conconi et al. 2004) for near-IR and ROSS (Tosti et al. 2004) for the optical, both have a field of view of 10 × 10 arcmin and imaging capabilities with the usual NIR (z, J, H, and K) and Johnson-Cousins VRI filters. They allow us to obtain nearly simultaneous data. The REM software system (Covino et al. 2004) is able to manage complex observational strategies in a fully autonomous way.

In this paper we consider optical and NIR data in *VRIJHK* bands (from 0.55 to 2.15 μm), collected from April 11, 2005 (53 471 MJD) to June 30, 2012 (56 108 MJD). Instrumental magnitudes were obtained via aperture photometry, using aperture radii of 5 arcsec and typically with 300 s integration time in the optical and 150 s integration time in the NIR. Calibration was performed by means of comparison stars in the field reported in Two Micron All Sky Survey Catalog (2MASS)[3] (Skrutskie et al. 2006) for NIR frames. For optical standard stars, calibrated sequences from several authors were followed, depending on the blazar field. Among the calibrated stars we chose a *reference* star, present in each frame, and a *check* star for each source of the sample. The check star can change depending on its positions in the frames. When the check star differed from its mean value by more than 2.5σ, the image was discarded. Dubious and mainly low-state images were visually inspected in order to remove frames affected by inhomogenous background, bad tracking, etc., to obtain a clean photometric sample. Interesting episodes were similarly carefully inspected.

3. The blazar sample

The seven blazars presented here (Table 1) are all bright, well studied objects. Among the sources of the class monitored by REM[4] (~60), they were chosen with the basic criterion of having the largest extensions of the total coverage. Six sources are BL Lac objects, and one is a flat spectrum radio quasar (FSRQ). The redshift is known for all of them. They are all Fermi gamma ray sources and four of them were detected in the TeV band as shown in Table 1. Recently a strong but complex correlation between optical and gamma rays has been demonstrated (e.g. Chatterjee et al. 2013). Some REM photometry on the target sources has already been published.

In Fig. 1 we report some images of the CCD fields where the target, the reference, and the check stars are indicated. The magnitudes of the reference and the check stars are given in Table 2 for V, R, and I optical filters. The procedure described in the previous section was followed.

4. Long term variability

The light curves resulting from the averaging of the single measurements on each night are presented in Fig. 2 and in Table 3. A full version of Table 3 is available at the CDS. If more data are present in a night interval, weighted averaged magnitudes are taken. The standard errors of source and of the check star added in quadrature with the mean instrumental and calibration error is assumed as uncertainty. For each source the corresponding check star light curve is reported in the J filter and in the other bands the curve for the check star is very similar.

The properties of the light curves are reported in Table 4, where the flux values are given after dereddening with the coefficient reported in Table 5. All seven sources are strongly variable. The amplitude of variability is larger than four magnitudes in the NIR bands of PKS 0537-441and PKS 1510-089, decreasing in the optical. For the BL Lacs PKS 0735+17, OJ 287, PKS 2005-489, and W Comae, the variability is 1−2 mag, while the case of PKS 2155-304 is intermediate. The curves are spiky, with monotonic trends that can last for months. There are flares of various intensities and shapes, and their classification appears arduous. As an example we select in Fig. 3 the prominent flare that occurred in PKS 1510-089 and lasted for nine days around May 10, 2009 (54 961 MJD) while the source was brightening for 120 days. The source K flux dramatically rose from ~10 to 73.8 mJy in about six days before decaying in four days to the original value. The noticeable event was also observed simultaneously by Sasada et al. (2011) and Bonning et al. (2012).

[1] http://simbad.u-strasbg.fr/
[2] http://tevcat.uchicago.edu/
[3] http://www.ipac.caltech.edu/2mass/
[4] REM data are available at http://www.rem.inaf.it

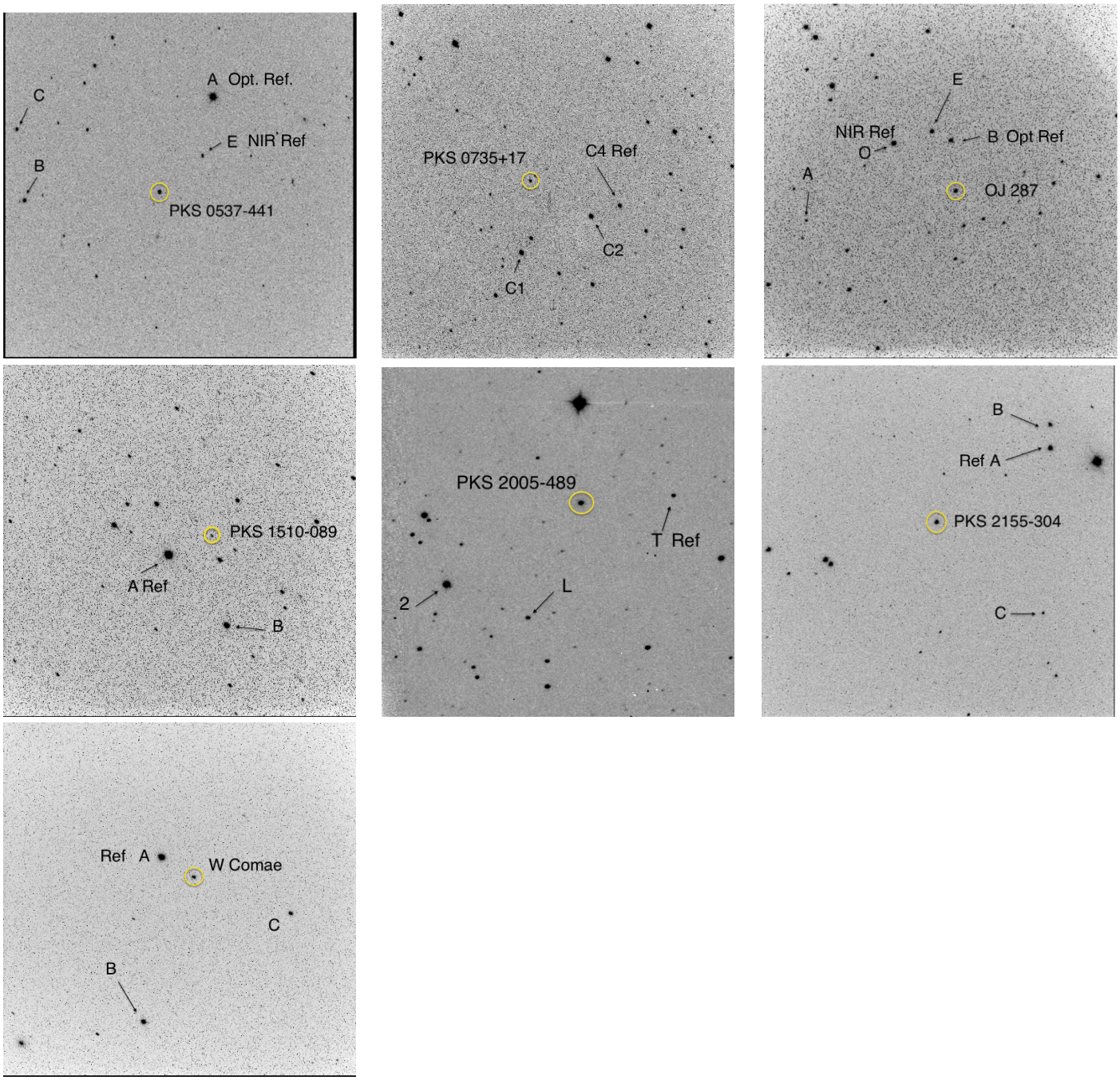

Fig. 1. Charts for the seven targets in *R* filter.

We also characterized the variability of all the light curves through the fractional variability amplitude $\sigma_{\rm rms}$ defined as

$$\sigma^2_{\rm rms} = \frac{1}{N\mu^2} \sum \left[(F_i - \mu)^2 - \sigma_i^2 \right], \quad (1)$$

where N is the number of flux values F_i, with measurement uncertainties σ_i, and μ is the average flux. The evaluation of $\sigma_{\rm rms}$ gives a measure of the intrinsic variability amplitude and it represents the averaged amplitude of observed variations as a percentage of the flux corrected for the effects of measurement noise. It is discussed, for example, in Nandra et al. (1997), Edelson et al. (2002), and Vaughan et al. (2003). From Table 6 and Fig. 4 it is apparent that in terms of $\sigma_{\rm rms}$ the most variable source is PKS 1510-089, followed by PKS 0537-441 and PKS 2155-304, consistently with the variability indicated by the secular excursion of the source magnitude (see above). The dependence of $\sigma_{\rm rms}$ on the spectral band is modest in the BL Lacs objects and is possibly in part due to the dishomogeneity in the coverage. The FSRQ PKS 1510-048 is more variable at longer wavelengths. The latter behavior with smoother trends is also pointed out by Bonning et al. (2012).

The dependence of $\sigma_{\rm rms}$ on flux was also investigated. The *H* and *R* light curves were divided into four flux intervals containing approximatively the same number of points. Average fluxes and $\sigma_{\rm rms}$ are evaluated for each interval, and no clear trend $\sigma_{\rm rms}$ vs. F is apparent. The results are collected in Table 7. We note that our results do not agree with the finding by

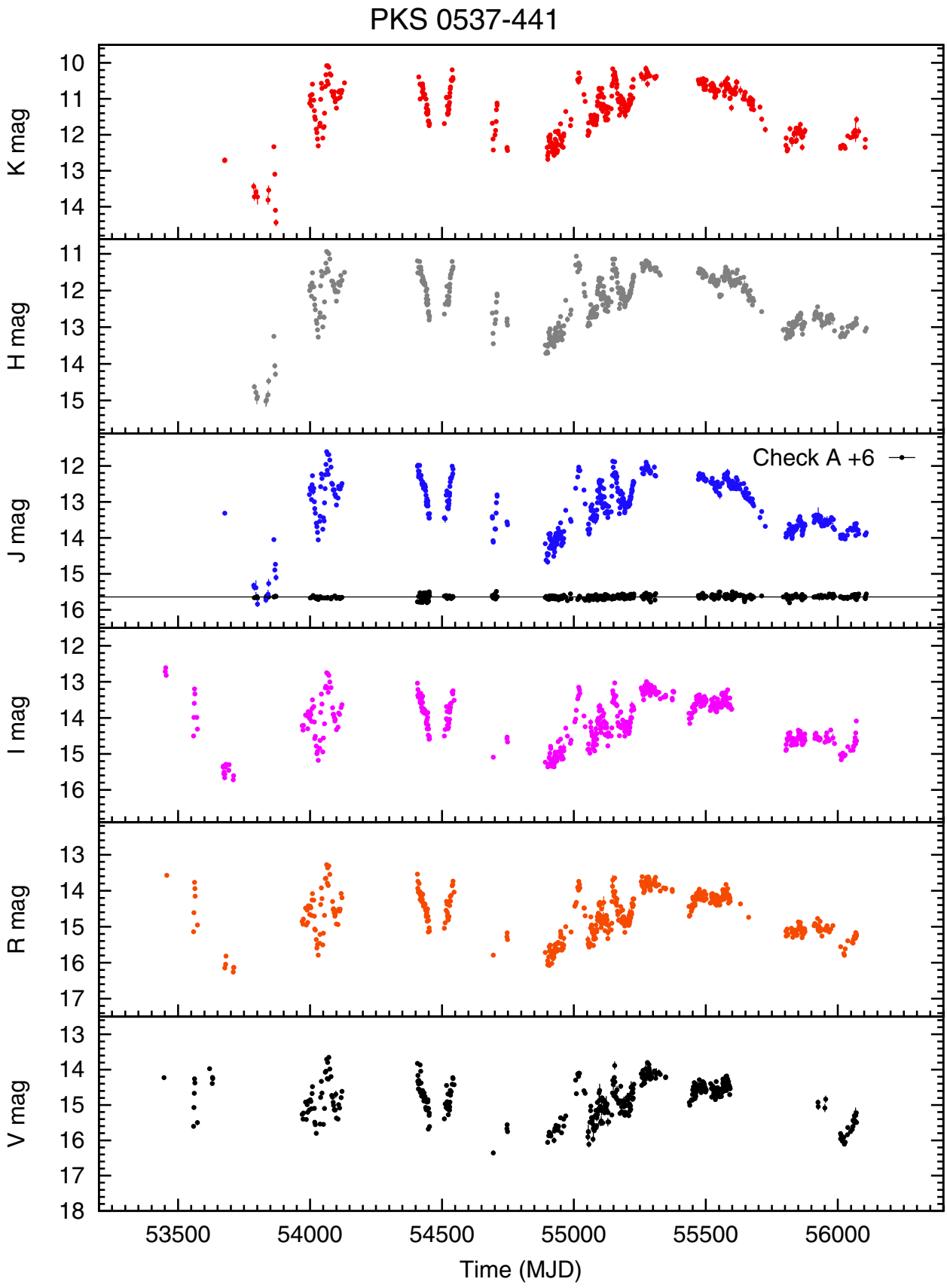

Fig. 2. REM near-infrared and optical nightly averaged light curves of the seven target sources. The light curve of the check star is reported in *J* band (black points) with the indicated displacements Δm.

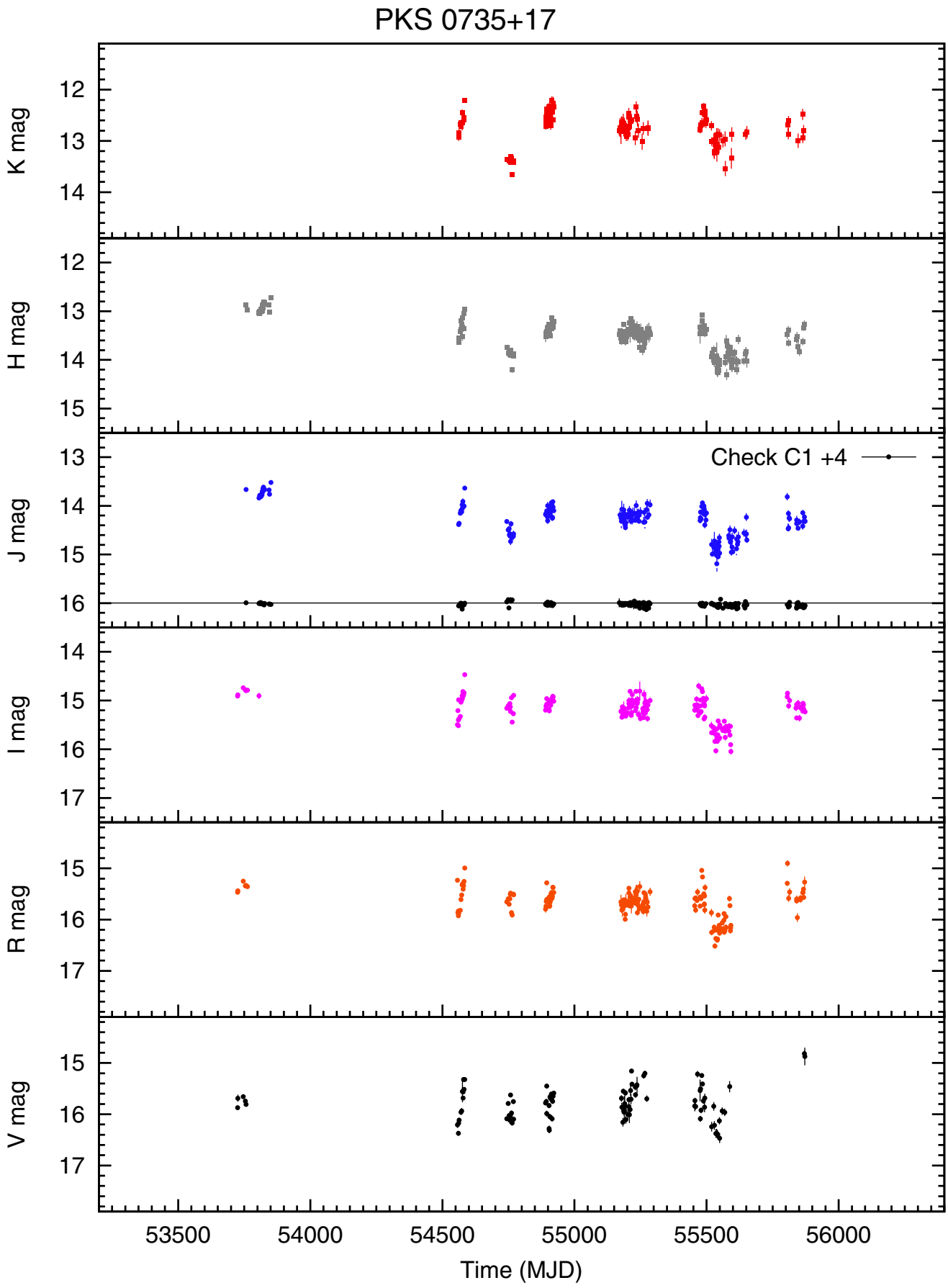

Fig. 2. continued.

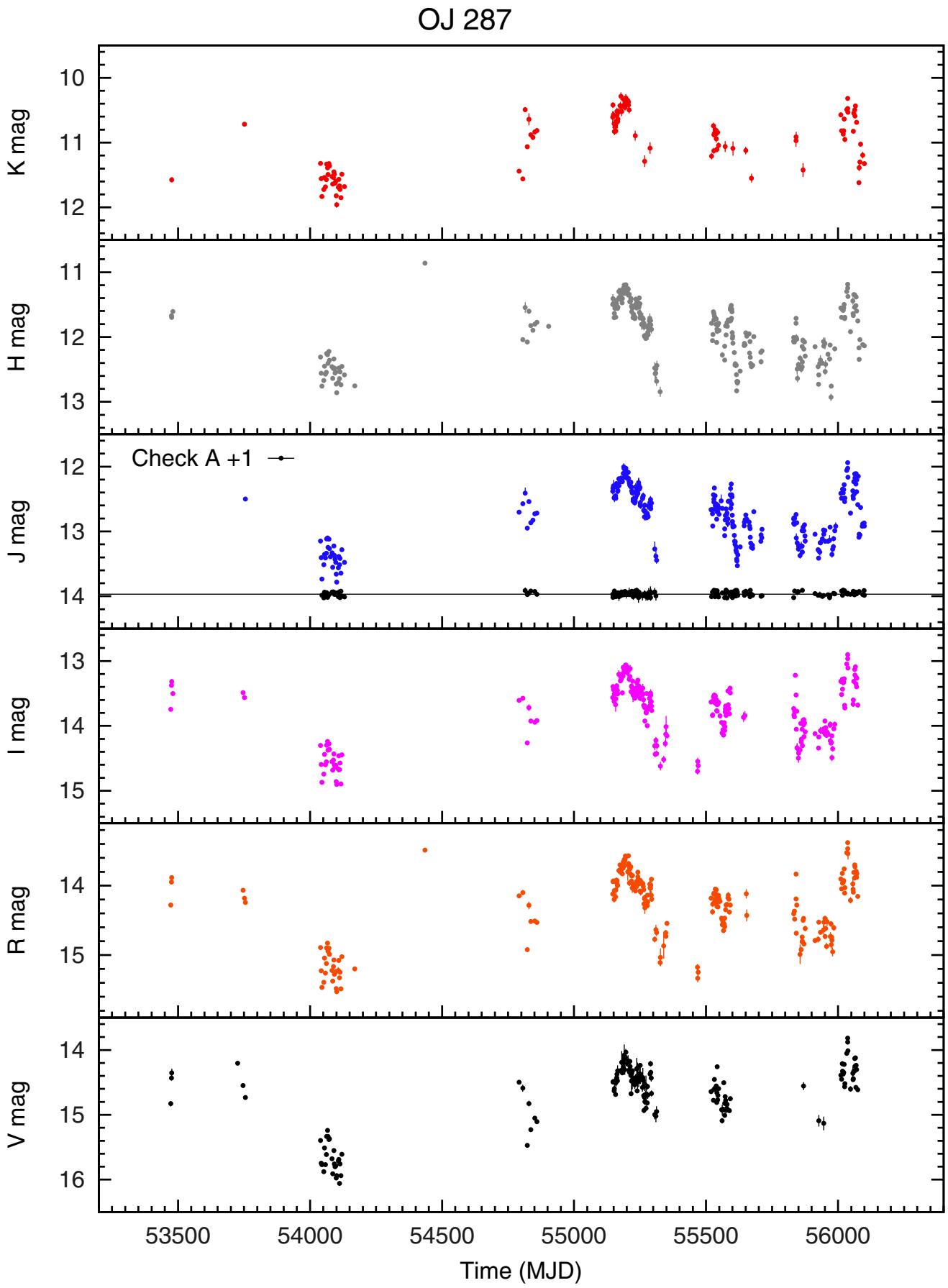

Fig. 2. continued.

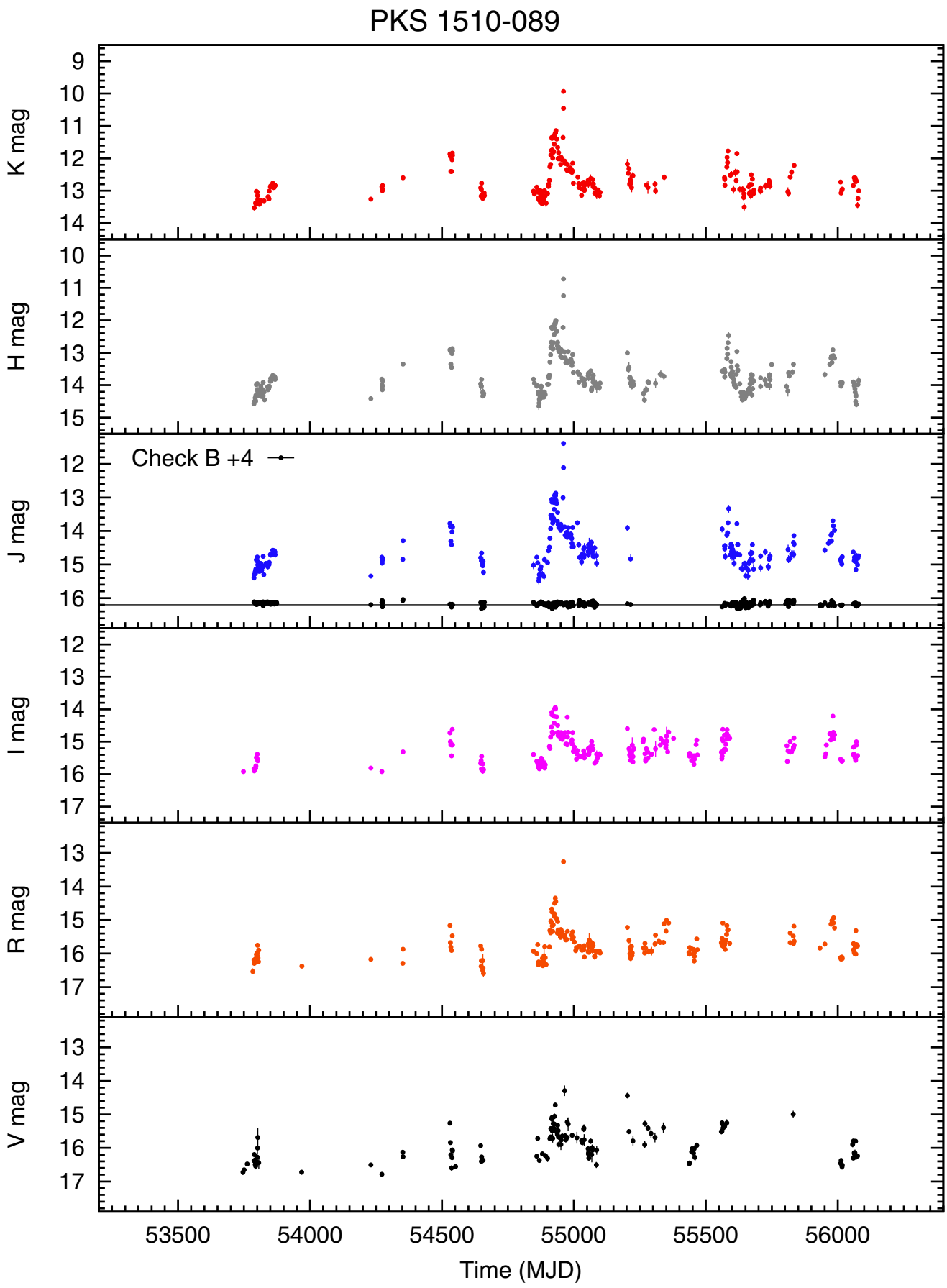

Fig. 2. continued.

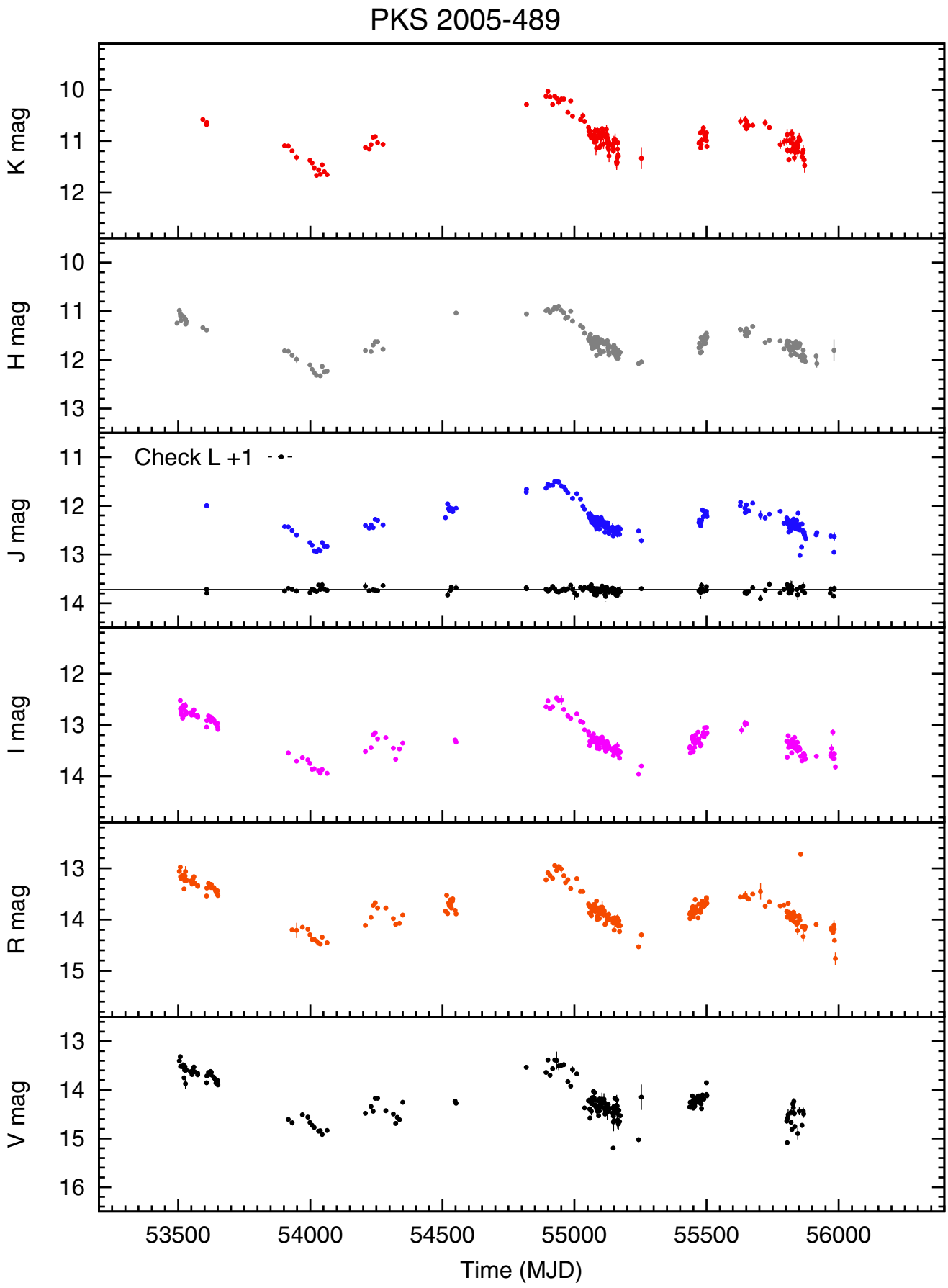

Fig. 2. continued.

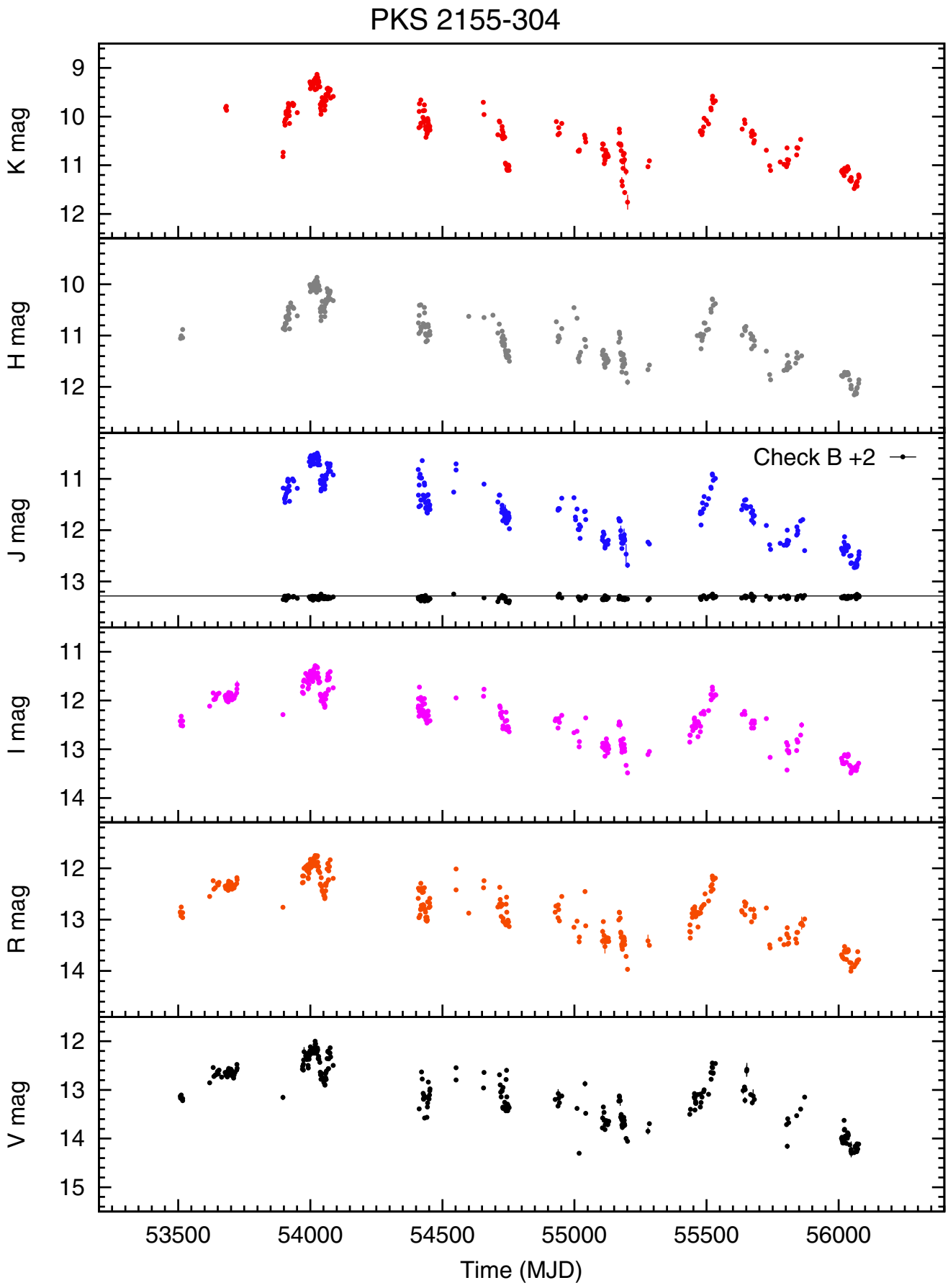

Fig. 2. continued.

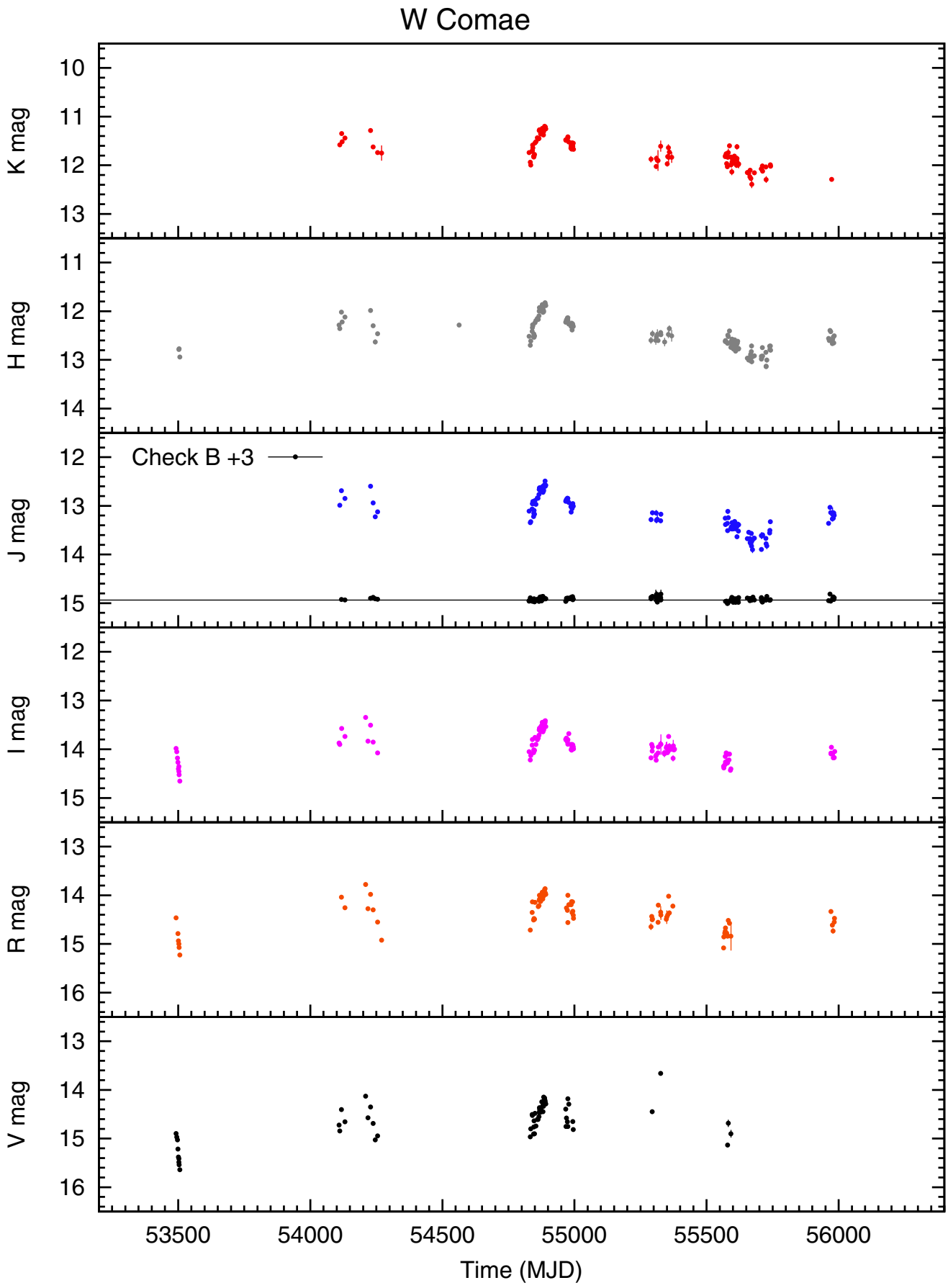

Fig. 2. continued.

Table 2. *V*, *R*, *I* comparison stars in the fields of our sample.

Source	Star	Coordinates RA Dec [h:m:s] [d:m:s]	*V*	$\sigma(V)$	*R*	$\sigma(R)$	*I*	$\sigma(I)$	References
PKS 0537-441	A (Opt Ref)	05:39:04.51 – 44:06:38.2	10.680	0.010	10.400	0.010	10.120	0.010	1
	B	05:38:49.33 – 44:01:30.0	13.200	0.010	12.870	0.010	12.540	0.010	1
	C	05:38:59.97 – 44:01:19.1	14.080	0.010	13.710	0.010	13.340	0.010	1
	E (NIR Ref)	05:38:55.70 – 44:06:19.6	14.843	0.035	14.151	0.034	13.585	0.023	6
PKS 0735+17	C1	07:38:00.57 + 17:41:19.7	13.26	0.04	12.89	0.04	12.57	0.04	2
	C2 (Ref)	07:38:08.55 + 17:40:29.2	13.31	0.04	12.79	0.04	12.32	0.04	2
OJ 287	O (NIR Ref)	08:54:53.38 + 20:04:44.8	14.192	0.003	13.707	0.002	13.262	0.004	3
	B (Opt Ref)	08:54:54.45 + 20:06:13.6	14.627	0.003	14.315	0.003	13.999	0.004	3
	E	08:54:55.20 + 20:05:42.3	14.974	0.003	14.632	0.003	14.304	0.004	3
PKS 1510-089	A (Ref)	15:12:46.16 – 09:05:23.0	11.571	0.001	11.195	0.002	10.847	0.001	3
	B	15:12:53.19 – 09:03:42.4	13.282	0.016	12.992	0.022	12.687	0.019	3
PKS 2005-489	T (Ref)	20:09:40:03 – 48:50:21.8	14.92	–	14.39	–	13.86	0.06	4 (*V*, *R* band); 6 (*I* band)
	L	20:09:19.04 – 48:46:43.1	14.41	–	13.89	–	13.45	0.09	4 (*V*, *R* band); 6 (*I* band)
	2	20:09:05.42 – 48:47:20.8	11.92	0.03	11.33	0.03	10.79	0.03	6
PKS 2155-304	A (Ref)	21:59:02.49 – 30:10:46.6	12.050	0.010	11.670	0.010	11.300	0.020	1
	B	21:59:05.34 – 30:10:51.0	13.000	0.010	12.470	0.020	12.020	0.020	1
	C	21:58:42.33 – 30:10:27.4	14.280	0.010	13.920	0.020	13.560	0.020	1
W Comae	A (Ref)	12:21:33.66 + 28:13:04.1	12.08	0.02	11.72	0.04	11.40	0.04	5
	B	12:21:13.83 + 28:13:04.3	13.03	0.07	12.69	0.05	12.37	0.05	6
	C	12:21:28.61 + 28:16:37.7	14.81	0.04	13.86	0.04	12.68	0.04	5

Notes. Stars used as references are marked with Ref; NIR Ref and Opt Ref specify that the reference stars change between NIR and optical bands. The check star can change depending on its positions in the frames.

References. (1) Hamuy & Maza (1989); (2) Ciprini et al. (2007); (3) González-Pérez et al. (2001); (4) Rector & Perlman (2003); (5) Fiorucci & Tosti (1996); (6) this work.

Table 3. Photometry of the seven target objects.

Source	Filter	Time of observation [MJD]	Average magnitude [mag]	Magnitude error [mag]
PKS0537-441	*K*	53 453	10.685	0.031
PKS0537-441	*K*	53 676	12.716	0.044
PKS0537-441	*K*	53 677	12.699	0.049
....	....	....	....	....

Notes. The full table is available at the CDS.

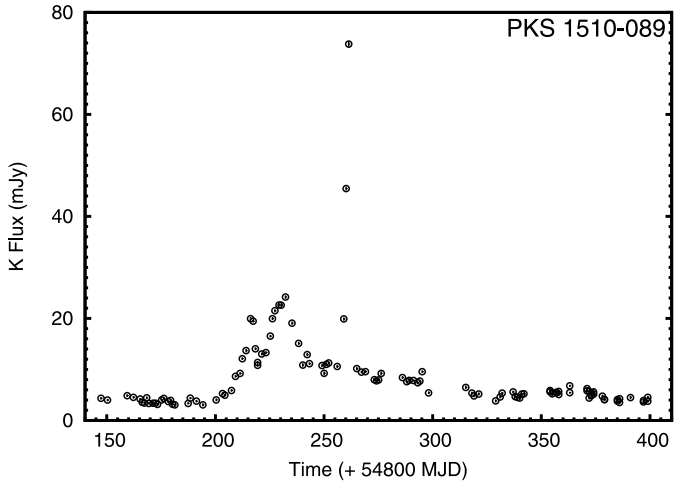

Fig. 3. Active state of PKS 1510-089 and the flare occurring around 54 961 MJD.

Edelson et al. (2013) of a clear correlation between rms and flux of the BL Lac object W2R1926+42 observed by *Kepler* satellite.

For each source the general behavior of the light curves is similar in the various filters. Nevertheless, color-intensity plots are of some interest. We selected epochs when the time lapse between *R* and *H* observations was less than six minutes. The $R-H$ color vs. the *H* magnitude is reported in Figs. 5 and 6. It is apparent that the plots are rather different. PKS 1510-089 exhibits a banana-like shape, with a general trend indicating bluer color for decreasing flux. The same tendency appears in PKS 0537-441, and in PKS 0735+17. On the other hand, OJ 287 and PKS 2005-489 trace a circular spot, or rather an atoll shape. In the case of PKS 2155-304 the spot is distorted in the intensity direction. The shape of the color-intensity plots may be very different if one only considers a fraction of the overall collection of data (see the bars at the right of the figures).

The case of the flare of PKS 1510-089 around 54 961 MJD marked in Fig. 5 is illustrative of the complexity of the

Table 4. Properties of the light curves.

Source	Timeframe in H band ([MJD])	Filter	Magnitude range [mag]	Variability amplitude Δm [mag]	Average magnitude [mag]	Mode [mag]	Median [mag]	Standard deviation [mag]	Flux range [mJy]	F_{max}/F_{min}
PKS 0537-441	2005/11/03–2012/06/30	K	10.06–14.57	4.51	11.30	10.6	11.15	0.74	1.14–63.07	55.32
	(53677–56108)	H	10.93–15.45	4.52	12.28	11.8	12.18	0.73	0.70–45.16	64.51
		J	11.58–15.84	4.26	13.09	12.5	13.01	0.71	0.74–37.41	50.55
		I	12.59–15.75	3.16	14.08	13.6	14.06	0.63	1.29–23.79	18.44
		R	13.27–16.28	3.01	14.65	14.2	14.65	0.61	1.04–16.64	16.00
		V	13.11–16.36	3.25	14.83	14.6	14.78	0.53	1.18–23.49	19.91
PKS 0735+17	2006/01/19–2011/11/05	K	12.14–13.65	1.51	12.78	12.7	12.71	0.32	2.35–9.41	4.00
	(53754–55870)	H	12.72–14.30	1.58	13.52	13.4	13.46	0.34	2.02–8.65	4.28
		J	13.52–15.19	1.67	14.28	14.2	14.23	0.34	1.34–6.27	4.68
		I	14.47–16.04	1.57	15.19	15.1	15.14	0.28	0.98–4.20	4.29
		R	14.90–16.52	1.62	15.68	15.6	15.64	0.28	0.83–3.68	4.43
		V	14.72–16.46	1.74	15.79	15.7	15.79	0.32	1.05–5.24	4.99
OJ 287	2005/04/11–2012/06/21	K	10.27–11.96	1.69	10.99	10.4	10.88	0.46	11.12–52.94	4.76
	(53471–56099)	H	10.84–12.93	2.09	11.92	11.7	11.84	0.44	7.10–48.82	6.88
		J	11.94–13.78	1.84	12.74	12.3	12.69	0.42	4.90–26.76	5.46
		I	12.90–14.90	2.00	13.79	13.5	13.70	0.45	2.80–17.64	6.30
		R	13.38–15.52	2.14	14.31	14.0	14.19	0.48	2.05–14.74	7.19
		V	13.82–16.06	2.24	14.69	14.4	14.55	0.49	1.51–11.91	7.89
PKS 1510-089	2006/01/27–2012/06/01	K	9.93–13.78	3.85	12.67	12.8	12.82	0.56	2.14–73.8	34.49
	(53783–56079)	H	10.72–14.80	4.08	13.74	14.0	13.89	0.59	1.31–56.58	43.19
		J	11.39–15.57	4.18	14.54	14.7	14.69	0.61	1.00–47.17	47.17
		I	13.95–15.97	2.02	15.21	15.4	15.28	0.40	1.18– 7.62	6.46
		R	13.26–16.69	3.43	15.73	15.9	15.79	0.44	0.83–19.44	23.42
		V	14.29–16.93	2.64	15.90	16.2	15.94	0.50	0.83– 9.44	11.37
PKS 2005-489	2005/04/20–2012/02/25	K	10.03–11.67	1.64	10.96	11.1	10.98	0.32	14.61–66.42	4.55
	(53480–55982)	H	10.88–12.33	1.45	11.64	11.7	11.69	0.29	12.55–47.53	3.79
		J	11.45–13.01	1.56	12.32	12.4	12.37	0.28	10.17–42.85	4.21
		I	12.09–13.96	1.87	13.27	13.3	13.34	0.31	6.99–38.97	5.58
		R	12.72–14.76	2.04	13.76	13.9	13.83	0.34	4.42–28.81	6.52
		V	12.98–15.20	2.22	14.19	14.2	14.27	0.39	3.61–27.92	7.73
PKS 2155-304	2005/05/18–2012/05/29	K	9.08–11.57	2.49	10.03	9.3	10.55	0.62	15.92–157.49	9.89
	(53508–56076)	H	9.81–12.16	2.35	10.94	11.6	11.43	0.62	14.40–124.96	8.68
		J	10.44–12.75	2.32	11.40	10.6	11.35	0.63	12.57–106.07	8.44
		I	11.17–13.53	2.36	11.92	11.9	11.90	0.37	9.78–85.69	8.77
		R	11.63–14.04	2.41	12.40	12.3	12.32	0.41	7.88–72.53	9.20
		V	11.98–14.30	2.32	12.68	12.6	12.63	0.39	7.49–64.43	8.47
W Comae	2005/05/12–2012/02/26	K	11.20–12.39	1.19	11.71	11.3	11.72	0.30	7.47–22.42	3.00
	(53502–55983)	H	11.83–13.14	1.31	12.48	12.7	12.53	0.33	5.84–19.60	3.36
		J	12.49–14.15	1.66	13.17	13.4	13.17	0.37	3.48 –16.07	4.62
		I	13.35–14.67	1.33	13.93	14.0	13.97	0.28	3.42–11.61	3.39
		R	13.78–15.24	1.46	14.36	14.0	14.34	0.33	2.64–10.11	3.83
		V	13.97 –15.66	1.69	14.65	14.4	14.64	0.39	2.16–10.22	4.73

Table 5. Absorption coefficients.

	λ [μm]	PKS 0537-441	PKS 0735+17	OJ 287	PKS 1510-089	PKS 2005-489	PKS 2155-304	W Comae
A_K	2.15	0.0137	0.0124	0.0103	0.0369	0.0205	0.0080	0.0085
A_H	1.64	0.0212	0.0192	0.0160	0.0571	0.0317	0.0124	0.0132
A_J	1.25	0.0328	0.0297	0.0248	0.0883	0.0491	0.0192	0.0204
A_I	0.804	0.0685	0.0620	0.0517	0.1845	0.1026	0.0400	0.0426
A_R	0.659	0.0946	0.0856	0.0714	0.2548	0.1417	0.0552	0.0589
A_V	0.55	0.1162	0.1051	0.0878	0.3128	0.1740	0.0678	0.0723

Notes. Extinction values are derived from the NASA/IRPAC Infrared Science Archive (Schlegel et al. 1998). Cardelli et al. (1989) formulae were used to calculate the absorption coefficients, assuming the extinction to reddening ratio $Av/E(B-V) = 3.1$. Those formulae are available at http://dogwood.physics.mcmaster.ca/Acurve.html

Table 6. NIR-optical fractional variability amplitude $\sigma_{\rm rms}$ of the blazar sample (×100%).

Source	Class	K	H	J	I	R	V
PKS 0537-441	BL Lac	54 ± 2	57 ± 2	57 ± 2	55 ± 2	52 ± 2	47 ± 2
PKS 0735+17	BL Lac	25 ± 2	30 ± 2	29 ± 2	23 ± 1	25 ± 1	31 ± 2
OJ 287	BL Lac	39 ± 3	38 ± 2	37 ± 2	37 ± 2	39 ± 2	36 ± 2
PKS 1510-089[a]	FSRQ	92 ± 4	104 ± 4	115 ± 5	43 ± 2	69 ± 4	52 ± 4
PKS 1510-089[b]		61 ± 3	69 ± 3	68 ± 3	44 ± 2	45 ± 2	47 ± 4
PKS 2005-489	BL Lac	32 ± 2	29 ± 2	29 ± 1	31 ± 1	33 ± 1	38 ± 2
PKS 2155-30	BL Lac	57 ± 3	54 ± 2	54 ± 2	48 ± 2	49 ± 2	49 ± 2
W Comae	BL Lac	26 ± 2	31 ± 2	33 ± 2	25 ± 2	28 ± 2	34 ± 3

Notes. [(a)] All data; [(b)] because of inhomogenous sampling, the flare occurring on 54 956−54 969 MJD was removed.

Table 7. NIR-optical fractional variability amplitude $\sigma_{\rm rms}$ dependence on flux.

PKS 0537-441			PKS 1510-089			PKS 2155-304		
Filter	Average flux [mJy]	$\sigma_{\rm rms}$ (×100%)	Filter	Average flux [mJy]	$\sigma_{\rm rms}$ (×100%)	Filter	Average flux [mJy]	$\sigma_{\rm rms}$ (×100%)
H	5.7 ± 0.13	27.5 ± 1.7	H	2.08 ± 0.02	7.9 ± 1.1	H	22.6 ± 0.5	17.3 ± 1.6
	10.6 ± 0.2	19.0 ± 1.2		2.74 ± 0.02	–		35.7 ± 0.6	13.7 ± 1.2
	18.4 ± 0.2	12.3 ± 0.8		3.53 ± 0.04	6.3 ± 1.0		54 ± 1	15.6 ± 1.4
	27.1 ± 0.3	15.1 ± 0.8		8.8 ± 0.8	81 ± 7		91 ± 2	16.5 ± 1.5
R	2.31 ± 0.05	23.8 ± 1.5	R	1.31 ± 0.02	10.2 ± 0.3	R	13.0 ± 0.3	17.0 ± 1.4
	3.80 ± 0.04	11.5 ± 0.9		1.73 ± 0.01	–		21.7 ± 0.2	9.4 ± 0.8
	6.14 ± 0.06	11.1 ± 0.8		2.14 ± 0.02	5.9 ± 1.0		31.8 ± 0.5	13.7 ± 1.1
	9.3 ± 0.2	19.0 ± 1.2		3.9 ± 0.4	64 ± 7		48.4 ± 0.9	16.0 ± 1.3

Notes. No evaluation is reported when $\sigma^2_{\rm rms}$ is dominated by errors, resulting in a negative value.

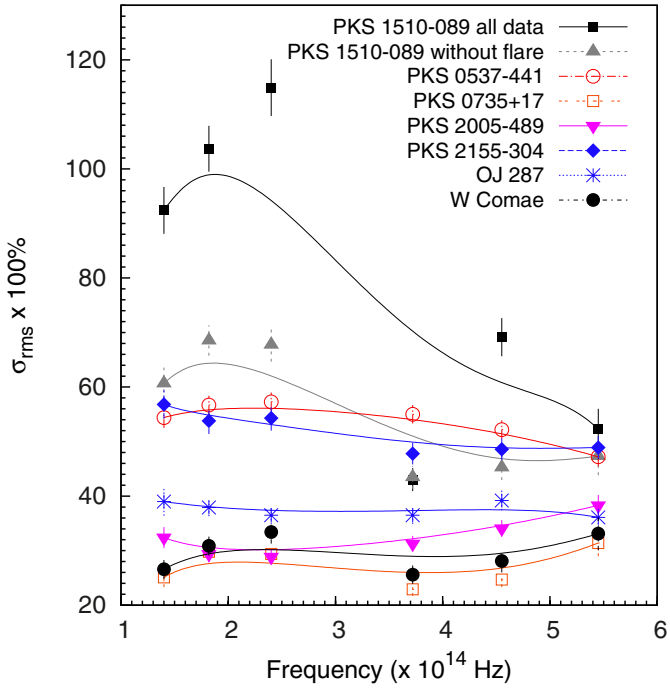

Fig. 4. Fractional variability amplitude vs. frequency. The lines are a help to the eye.

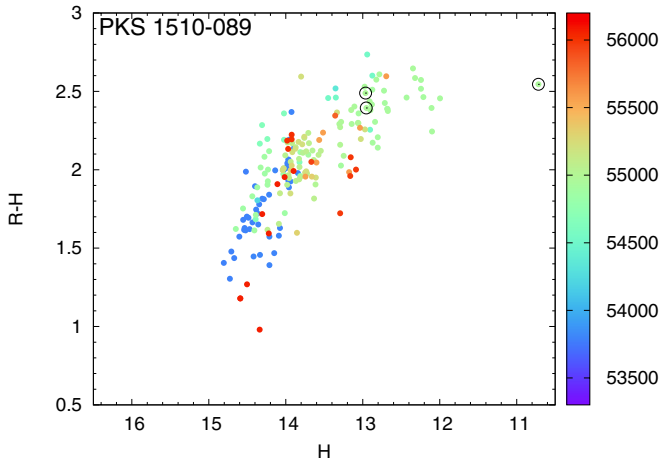

Fig. 5. Color-intensity diagram for PKS 1510-089. The color of each point is related to the epoch of detection, according to the bar on the right. The circles encompass the points referring to the flare observed around 54 961 MJD. Error bars are omitted for readability.

color-intensity dependence. During both the rising and falling phases of the flare, $R - H$ remained constant and $J - K$ was decreasing by ∼0.5, indicating a bluer color for increasing intensity. This result may be relevant in order to reconcile the achromaticity of the flare reported by Bonning et al. (2012) on the basis of the $B - J$ color vs. J, and the suggestion by Sasada et al. (2011) of bluer values for higher intensity indicated by the $V - J$ vs. V plot.

The availability of six filters allows the construction of the spectral flux distributions and the SEDs that are reported in Fig. 7. In all sources the highest states are well fitted by a single power law, and deviations may appear in the lowest states.

5. Rapid events in the light curves

REM observations of blazars, and specifically of the seven sources considered here, contain data deriving from proposals with various scientific goals. A large fraction of the observations

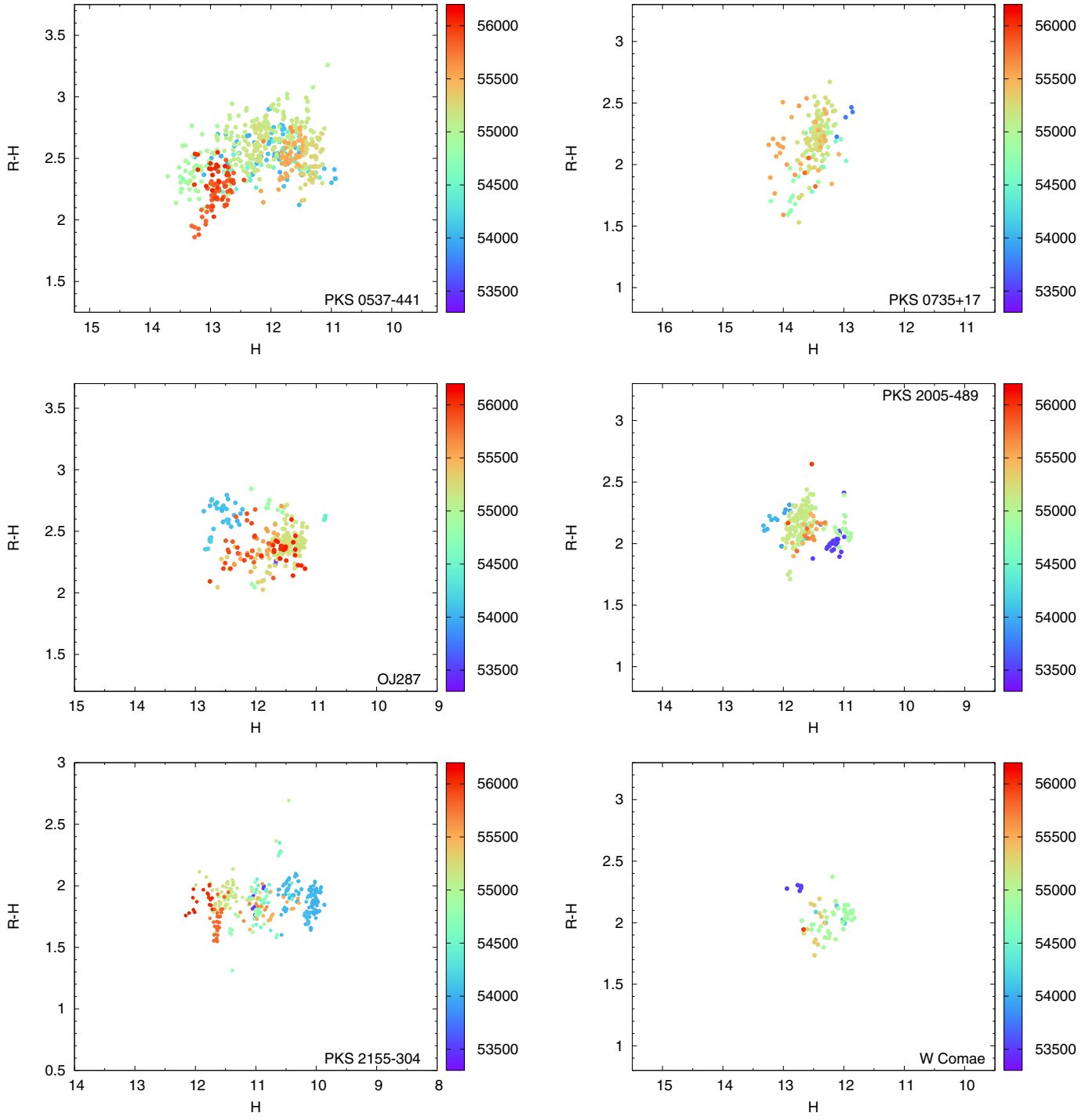

Fig. 6. Color-intensity diagrams for the BL Lacs. The color of each point is related to the epoch of detections of corresponding data, according to the bar on the right. Error bars are omitted for readability.

were performed within multiwavelength campaigns, where the optical and NIR monitoring was ancillary to X-ray or gamma ray (GeV, TeV) programs. In these cases the rate of monitoring could be typically once a day, or even once a week. The data suitable to search for variability on a time scale of hours are limited to a few epochs, while on much shorter time scales, the constraint is on the poor count statistics, owing to the diameter of the REM mirror. The threshold on the minimum flux detectable with a given integration time also depends on the mirror reflectance status, which has worsened after 2009, until a general maintenance intervention in 2012. When we were searching for rapid episodes, in addition to the visual control of each frame (Sect. 2), we chose to consider only those states over a minimum flux $f_{\rm min} \sim 3$ mJy in the optical bands, and $\simeq$1 mJy in the NIR bands. For fluxes $<f_{\rm min}$, no search of rapid variability events was performed. To identify potentially relevant variability events, we followed a procedure analogous to the one described by Montagni et al. (2006). We considered a series of N consecutive observations,

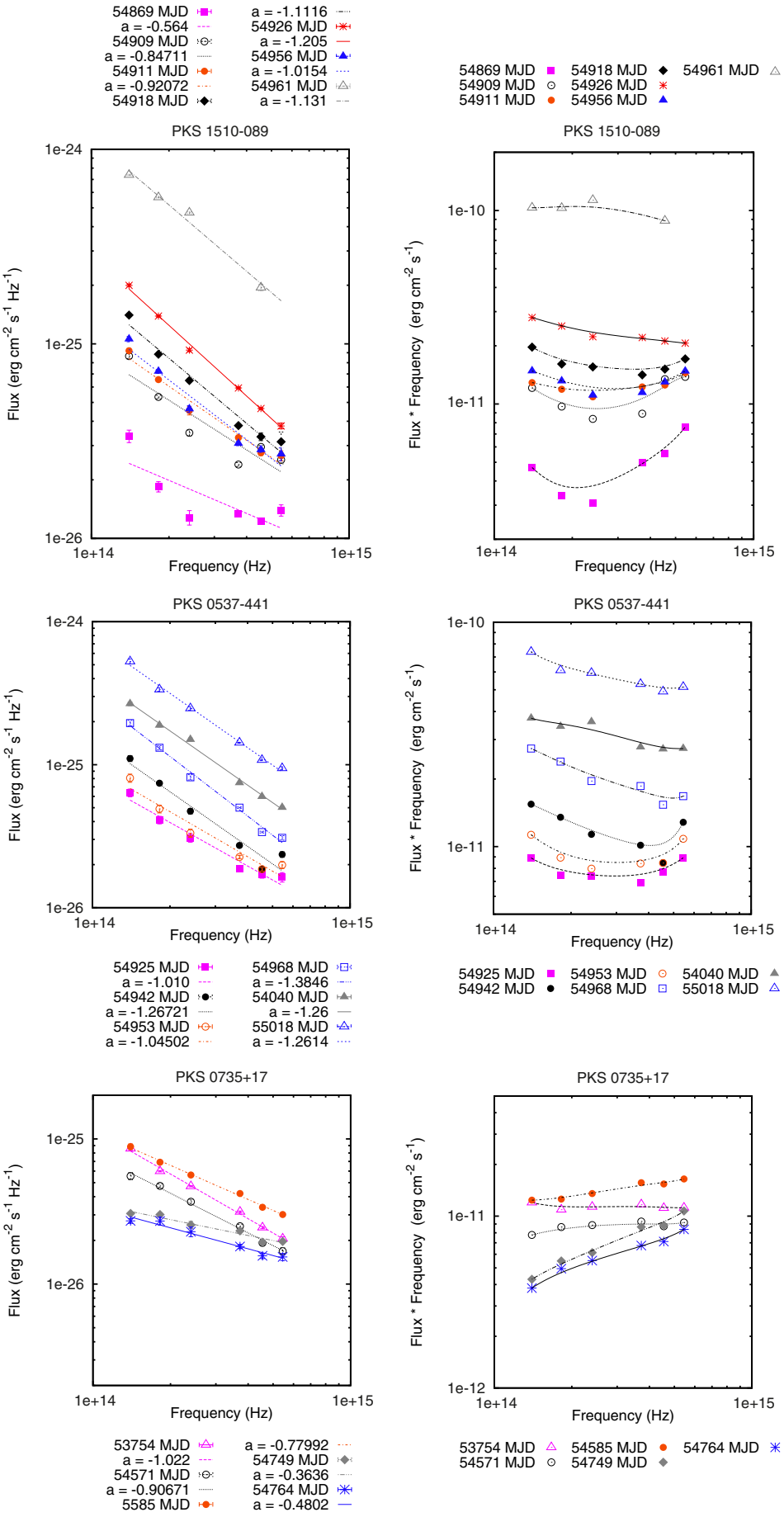

Fig. 7. Spectral flux distribution (*left panels*) and spectral energy distribution (*right panels*). The lines in the *left panels* are power-law fits and corresponding slopes *a* are reported. In the *right panels* the lines are a help for the eye.

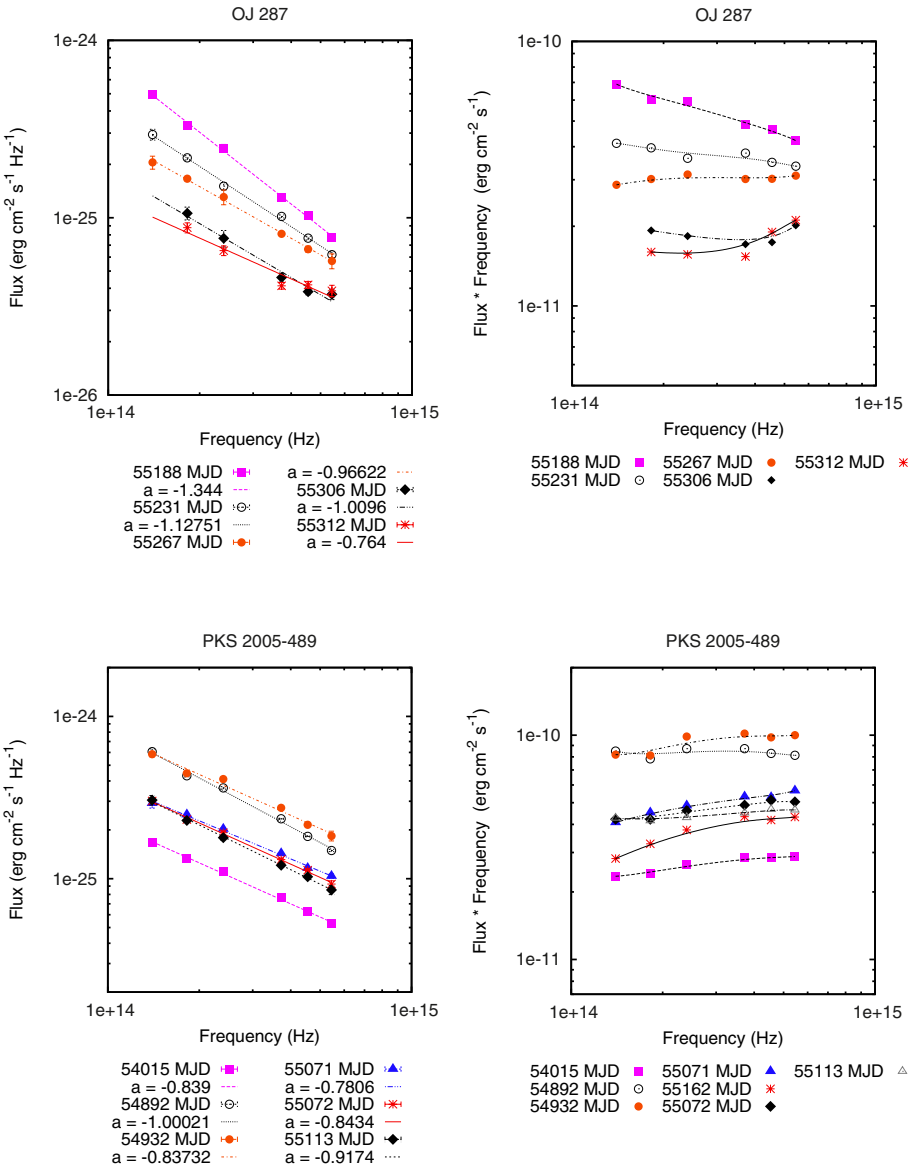

Fig. 7. continued.

for each of which the flux is measured. The flux-time dependence is best fitted with a linear relation, which yields a value of $\mathrm{d}f/\mathrm{d}t$. A time scale is defined as

$$\tau = \frac{\langle f \rangle}{\mathrm{d}f/\mathrm{d}t} \frac{1}{(1+z)} \tag{2}$$

where $\langle f \rangle$ is the average value of the flux and z the redshift. The search process for rapid events is fully automatized. An "event" is selected when τ is less than a given τ_0, and the uncertainty on τ is less than $\tau/2$. The event is discarded if the check star is significantly variable, and whenever τ is equal to or larger than $\xi^{-1}\tau_{\rm ck}$, where $\tau_{\rm ck}$ is the variability time scale of the check star, and ξ is a fixed value. All the images of an event are then visually examined, excluding the cases where the source or the reference stars are near the image borders or cases where spurious tracks or spots are apparent.

First we looked for relatively long and well documented events, considering $N \geqslant 30$ in the same night, with a value of $\tau < 12$ h and $\xi = 10$. We have retrieved two events of this type. The one referring to PKS 0537-441 (53 619 MJD) is reported in Fig. 8, see also Table 8. The linear time scale is ∼12 h.

Following the procedure suggested by Abdo et al. (2010) for Fermi gamma rays sources and adopted by Danforth et al. (2013) for UV photometry of the BL Lac object S5 0716+714, we also fitted the points in the night of the event with the function

$$f(t) = f_0 + a\left(\mathrm{e}^{(b-t)/\tau_{\rm r}} + \mathrm{e}^{(t-b)/\tau_{\rm d}}\right)^{-1} \tag{3}$$

where f_0 is a constant underlying flux level, a is a measure of the amplitude of the event, b roughly describes the time of the peak of the event, and τ parameters are the rise and decay time scales. The best fit is given in Fig. 8, and the relevant time scales are $\tau_{\rm r} \sim 1.5$ h and $\tau_{\rm d} \sim 12$ min (see Table 8). Unfortunately during the night of the event, only V photometry was collected. The event has some similarity with a variability episode of PKS 0537-441 deriving from the analysis of the REM archives, which is reported by Impiombato et al. (2011) and which was discussed in some detail by Zhang et al. (2013). However a careful analysis of the CCD images has shown the presence of a dark spot on the camera focal plane making the reliability of the event dubious, which therefore here is ignored.

The second event refers to PKS 2155-304 (53 678 MJD), see Fig. 8 and Table 8. The event was discovered with the automatic procedure in the V band, and has a very similar counterpart in

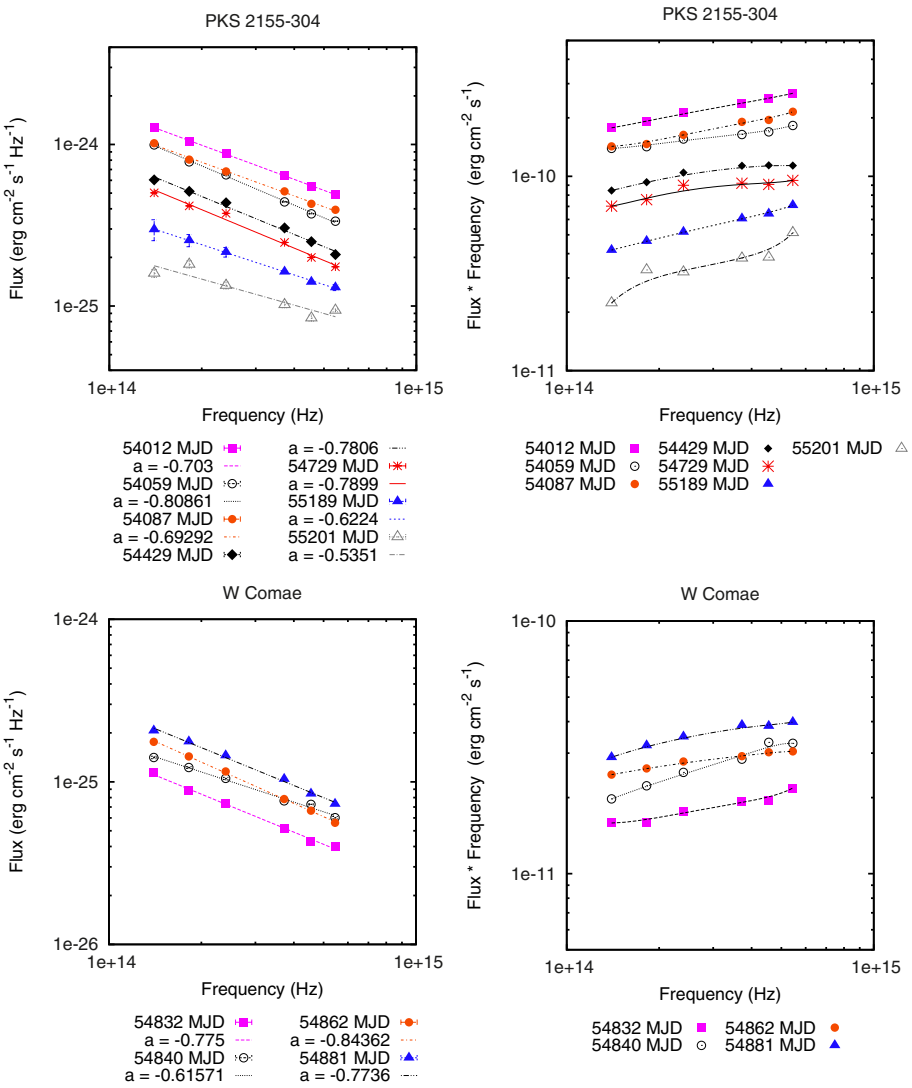

Fig. 7. continued.

Table 8. Rapid event time scales.

Source	Filter	MJD	N	Linear fitting		Exponential fitting		
				τ	τ_{ck}	τ_r	τ_d	reduced χ^2
PKS 0537-441	V	53 619	198	11h53min ± 16min	34d17h22min ± 1h56min	1h27min ± 6h48min	12min24s ± 8min13s	1.13
PKS 2155-304	H	55 837	10	2h15min ± 22min	1d7h3min ± 22h16min		22min ± 1h30min	4.60
	R	53 678	25	11h54min ± 25min	6d10h34min ± 1d23h48min		1h21min ± 39min	5.78
	V	53 678	31	12h00min ± 21min	7d16h28min ± 3d17h44min		1h39m ± 39min	1.16
	V	53 973	10	2h15min ± 14min	3d17h33min25s ±1d11h40min		3min14s ± 2min1s	1.79

Notes. The exponential fits refer to Eq. (3). For the episodes related to PKS 2155-304, in Eq. (3) τ_r is assumed equal to τ_d.

the R band. No rapid event was detected in NIR bands where coverage is poorer. The continuous lines in Fig. 8 are the fits with exponentials following Abdo et al. (2010).

We then looked for more rapid events. We have fixed a time scale $\tau_0 < 3h$, $\xi = 4$ and a number $N = 8$ of points. The only two events that we retrieved both refer to PKS 2155-304, see Fig. 9 and Table 8. The exponential time scales are now of the order of minutes. The event occurred on 53 973 MJD yields a time scale of three minutes and the reduced χ^2 indicates an acceptable fit with an exponential function. The case in 55 837 MJD is more complex. It seems that, superimposed on the exponential rise, there may be a spike that is, however, represented by a single point. We detect for both these episodes the very fast variability rate of 0.43 mag/h, comparable to the variability rate of 0.45 mag/h found by Danforth et al. (2013) for S5 0716+714.

6. Discussion

For the sources where the SED of the lower states are not well fitted by a power law (PKS 1510-089, PKS 0537-441, OJ 287, see Fig. 7), the indication is that the NIR bands yield a power-law index, which is unchanged with respect to the high states obtained by combining NIR and optical observations. In the lowest states a new component becomes apparent that shows up in the

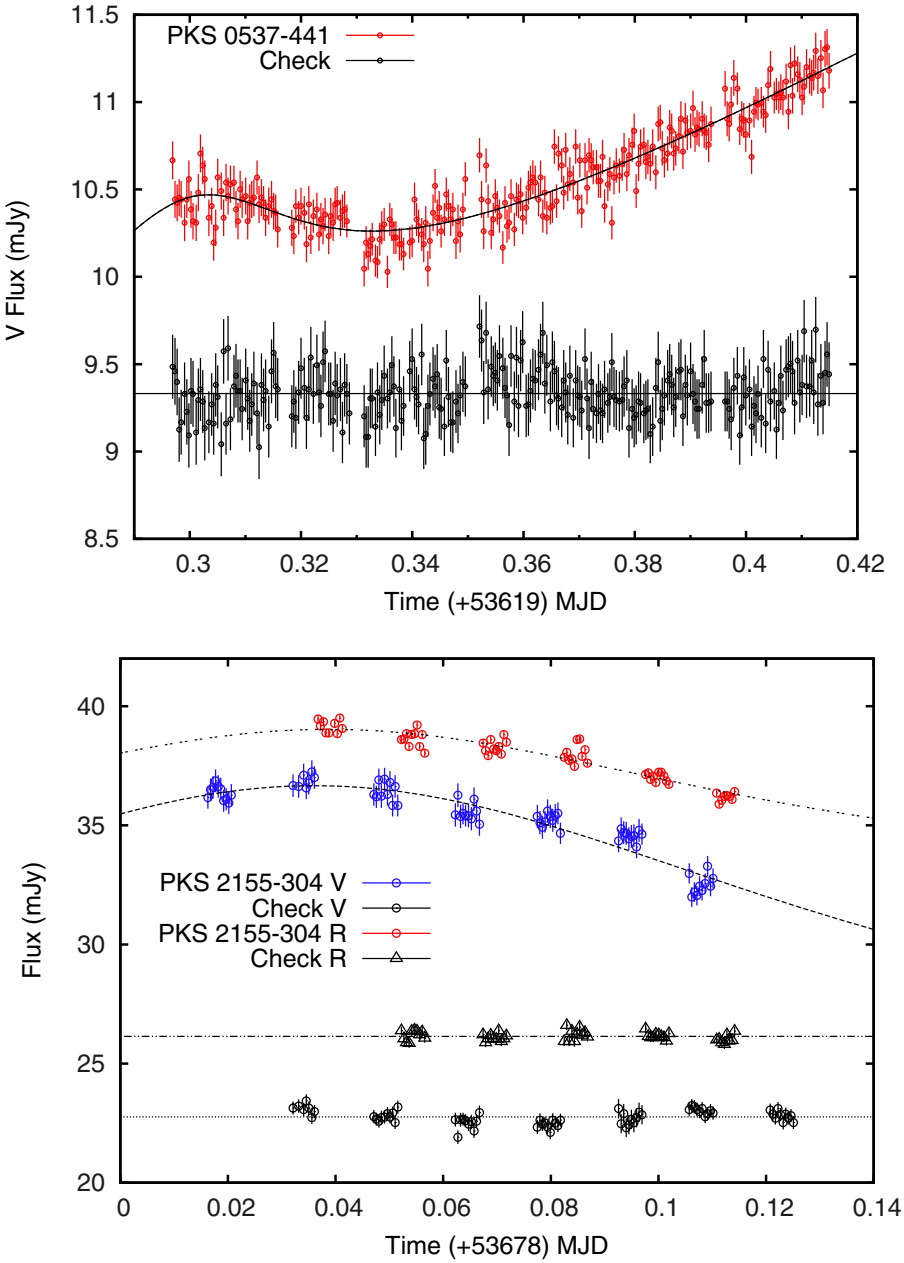

Fig. 8. Episodes of intra-night variability in PKS 0537-441and in PKS 2155-304. The check data has been multiplied ×3 for PKS 2155-304 and ×2 for PKS 0537-441.The lines are the best fits using Eq. (3).

optical. This component could be thermal, but this cannot be assessed, owing to the limited bandwidth covered by our six filters. In any case, the second component appears to be bluer than the power law. If the power law represents the variable part, this is consistent with the behavior of the variability index $\sigma^2_{\rm rms}$, which tends to be larger in the NIR with respect to the optical bands (see Table 6).

As shown in the previous section we have selected a number of episodes with time scales of hours or even shorter. Our selection criteria have been rather stringent. There is a comparable number of events, which may be real but do not satisfy one of our criteria. All the events derive from two sources that are very variable on time scales longer than one day, i.e. PKS 0537-441 and PKS 2155-304, and for which the total coverage is the largest, even with regard to the intra-night monitoring programs. For the other very variable source PKS 1510-089, we collected a number of a priori interesting events, but they corresponded to very low states of the source, and therefore are not considered here for the criterion given at the beginning of Sect. 5. Even when also taking the unconfirmed rapid events into account, one finds that hour time scales are rare. The ratio of their summed duration to the total exposure time is ~8/670 for PKS 0537-441 and ~20/730 for PKS 2155-304, where 670 h and 730 h are the overall observing times of the two sources. The discovery of these rapid events therefore requires very long monitoring campaigns. This inference cannot be applied to the case of S5 0716+714, where the one and only COS-HST observation found a rapid event.

The two most extreme events are those referring to PKS 2155-304 reported in Fig. 9, where the time scale events for a linear fit are on the order of hours, and those for the exponential fit are a few minutes. Similar short time scales have been found at $\lambda = 1400$ Å by Danforth et al. (2013) during the above-mentioned observation of S5 0716+714. In PKS 2155-304 sub-hour time scales have appeared in the TeV band during the famous active state on July 29−30, 2006 (Aharonian et al. 2007). The mass of the black hole in PKS 2155-304, is most probably $\sim 10^9\ M_\odot$ (Falomo et al. 1991; Kotilainen et al. 1998),

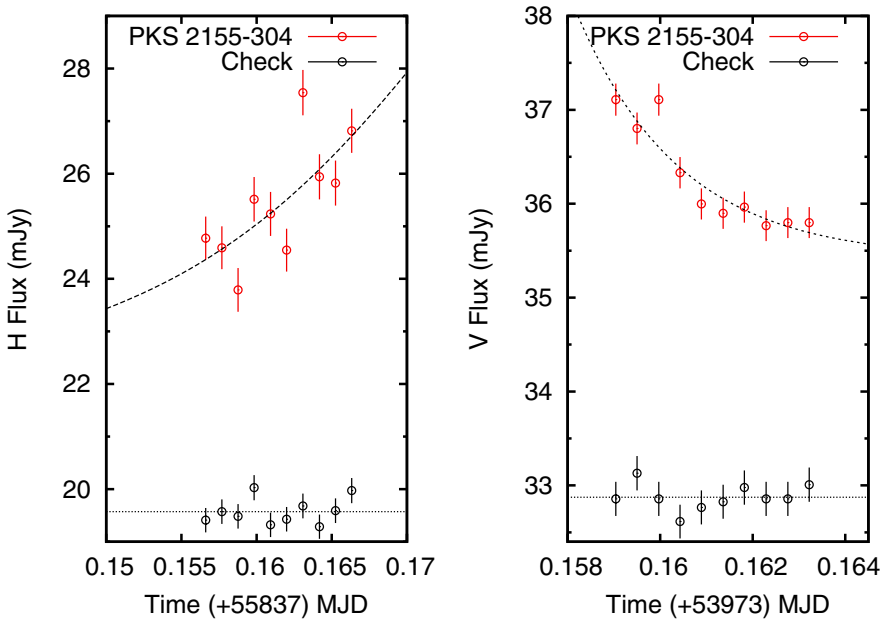

Fig. 9. Short variability events. In the *right panel* the check data has been divided by 2.5. In the *left panel* the check data has been multiplied × 1.4. The lines are the best fits using Eq. (3).

corresponding to a Schwarzschild radius $r_G \sim 2 \times 10^{14}$ cm. Assuming an emitting region of a few (say 5) r_G, the corresponding time scales are

$$\tau \sim \frac{R(1+z)}{c\delta} = \frac{4 \times 10^4 \text{ s}}{\delta} \quad (4)$$

where δ is the Doppler factor. A direct comparison with the reported time scales would require a specific model of the source, indicating in particular if the time scale to be considered is from the linear or exponential fit. In any case the reported rapid optical episodes indicate that the requirement of large Doppler factors is inevitable, in agreement with what is concluded for the variability at high energies.

Acknowledgements. We are grateful to the referee for a very positive and constructive report. We also thank Dino Fugazza for his efficient management of the REM observations and archive. This work has been supported by ASI grant I/004/11/0 and by PRIN-MIUR 2009 grants.

References

Abdo, A. A., Ackermann, M., Ajello, M., et al. 2010, ApJ, 722, 520
Aharonian, F., Akhperjanian, A. G., Bazer-Bachi, A. R., et al. 2007, ApJ, 664, L71
Blandford, R. D., & Rees, M. J. 1978, Phys. Scr., 17, 265
Bonning, E., Urry, C. M., Bailyn, C., et al. 2012, ApJ, 756, 13
Cardelli, J. A., Clayton, G. C., & Mathis, J. S. 1989, ApJ, 345, 245
Chatterjee, R., Fossati, G., Urry, C. M., et al. 2013, 2012 Fermi Symp. Proc., eConFC121028 [arXiv:1303.2095]
Ciprini, S., Takalo, L. O., Tosti, G., et al. 2007, A&A, 467, 465
Conconi, P., Cunniffe, R., D'Alessio, F., et al. 2004, Proc. SPIE, 5492, 1602
Covino, S., Stefanon, M., Sciuto, G., et al. 2004, Proc. SPIE, 5492, 1613
Covino, S., L., Treves, A., & Sbarufatti, B. 2010, 38th COSPAR Scientific Assembly, 38, 5
D'Ammando, F., Raiteri, C. M., Villata, M., et al. 2010a, 38th COSPAR Scientific Assembly, 38, 7
D'Ammando, F., Raiteri, C. M., Villata, M., et al. 2010b, in Accretion and Ejection in AGN: a Global View, eds. L. Maraschi, G., Ghisellini, & R. Della Ceca, ASP Conf. Ser., 427, 271
D'Ammando, F., Vercellone, S., Donnarumma, I., et al. 2010c, X-ray Astronomy 2009; Present Status, Multi-Wavelength Approach and Future Perspectives, AIP Conf. Ser., 1248, 415
D'Ammando, F., Bulgarelli, A., Chen, A. W., et al. 2011a, Adv. Space Res., 48, 76
D'Ammando, F., Vercellone, S., Donnarumma, I., et al. 2011b, J. Phys. Conf. Ser., 280, 012002
D'Ammando, F., Raiteri, C. M., Villata, M., et al. 2011c, A&A, 529, A145
D'Ammando, F., Antolini, E., Tosti, G., et al. 2013, MNRAS, 431, 2481
Danforth, C. W., Nalewajko, K., France, K., & Keeney, B. A. 2013, ApJ, 764, 57
Dolcini, A., Covino, S., Treves, A., et al. 2005, A&A, 443, L33
Dolcini, A., Farfanelli, F., Ciprini, S., et al. 2007, A&A, 469, 503
Edelson, R., Turner, T. J., Pounds, K., et al. 2002, ApJ, 568, 610
Edelson, R., Mushotzky, R., Vaughan, S., et al. 2013, ApJ, 766, 16
Falomo, R., Giraud, E., Melnick, J., et al. 1991, ApJ, 380, L67
Fiorucci, M., & Tosti, G. 1996, A&AS, 116, 403
Foschini, L., Treves, A., Tavecchio, F., et al. 2008, A&A, 484, L35
González-Pérez, J. N., Kidger, M. R., & Martín-Luis, F. 2001, AJ, 122, 2055
Hamuy, M., & Maza, J. 1989, AJ, 97, 720
Impiombato, D., Tosti, G., Treves, A., et al. 2008, in Proc. Blazar Variability across the Electromagnetic Spectrum, 43, available at http://pos.sissa.it
Impiombato, D., Covino, S., Treves, A., et al. 2011, ApJS, 192, 12
Kotilainen, J. K., Falomo, R., & Scarpa, R. 1998, A&A, 336, 479
Massaro, E., Giommi, P., Leto, C., et al. 2012, Multifrequency Catalogue of Blazars, 3rd edn. (Rome, Italy: ARACNE editrice)
Montagni, F., Maselli, A., Massaro, E., et al. 2006, A&A, 451, 435
Nandra, K., George, I. M., Mushotzky, R. F., Turner, T. J., & Yaqoob, T. 1997, ApJ, 476, 70
Pian, E., Romano, P., Treves, A., et al. 2007, ApJ, 664, 106
Pucella, G., D'Ammando, F., Romano, P., et al. 2010, A&A, 522, A109
Rector, T. A., & Perlman, E. S. 2003, AJ, 126, 47
Sasada, M., Uemura, M., Fukazawa, Y., et al. 2011, PASJ, 63, 489
Schlegel, D. J., Finkbeiner, D. P., & Davis, M. 1998, ApJ, 500, 525
Skrutskie, M. F., Cutri, R. M., Stiening, R., et al. 2006, AJ, 131, 1163
Tosti, G., Bagaglia, M., Campeggi, C., et al. 2004, Proc. SPIE, 5492, 689
Vaughan, S., Edelson, R., Warwick, R. S., & Uttley, P. 2003, MNRAS, 345, 1271
Zerbi, F. M., & Rem Team 2001, Astron. Gesellschaft Meeting Abstracts, 18, JD 0101
Zhang, B.-K., Wang, S., Zhao, X.-Y., Dai, B.-Z., & Zha, M. 2013, MNRAS, 428, 3630

Bibliography

Abdo, A. A., Ackermann, M., Ajello, M., et al. 2010, ApJ, 722, 520

Ahn C. P., et al., 2014, ApJS, 211, 17

Andreani P., Cristiani S., 1992, ApJ, 398, L13

Bahcall N. A., Chokshi A., 1991, ApJ, 380, L9

Barnes J. E., Hernquist L., 1996, ApJ, 471, 115

Becker, R. H., White, R. L., & Helfand, D. J. 1995, ApJ, 450, 559

Beckmann, V., Engels, D., Bade, N., & Wucknitz, O. 2003, A&A, 401, 927

Bennert N., Canalizo G., Jungwiert B., Stockton A., Schweizer F., Peng C. Y., Lacy M., 2008, ApJ, 677, 846

Bentz M. C., Peterson B. M., Netzer H., Pogge R. W., Vestergaard M., 2009, ApJ, 697, 160

Bentz M. C., et al., 2010, ApJ, 716, 993

Blandford R. D., McKee C. F., 1982, ApJ, 255, 419

Bonning E. W., Shields G. A., Salviander S., 2007, ApJ, 666, L13

Bonning, E., Urry, C. M., Bailyn, C., et al. 2012, ApJ, 756, 13

Boris N. V., Sodré L., Jr., Cypriano E. S., Santos W. A., de Oliveira C. M., West M., 2007, ApJ, 666, 747

Bruzual G., Charlot S., 2003, MNRAS, 344, 1000

Budavári T., et al., 2001, AJ, 122, 1163

Callegari S., Kazantzidis S., Mayer L., Colpi M., Bellovary J. M., Quinn T., Wadsley J., 2011, ApJ, 729, 85

Canalizo G., Stockton A., 2001, ApJ, 555, 719

Capak P., et al., 2007, ApJS, 172, 99

Cappellari M., et al., 2009, ApJ, 704, L34

Chakravarti, Laha, & Roy, 1967, Handbook of Methods of Applied Statistics, Vo. I, John Wiley and Sons, 392

Chu Y., Zhu X., 1988, A&A, 205, 1

Ciotti L., Ostriker J. P., 2007, ApJ, 665, 1038

Coil A. L., Hennawi J. F., Newman J. A., Cooper M. C., Davis M., 2007, ApJ, 654, 115

Coldwell G. V., Lambas D. G., 2006, MNRAS, 371, 786

Covino, S., Stefanon, M., Sciuto, G., et al. 2004, Proc. SPIE, 5492, 1613

Croom S. M., Shanks T., 1996, MNRAS, 281, 893

Croom S., et al., 2004, ASPC, 311, 457

Croom S. M., Smith R. J., Boyle B. J., Shanks T., Miller L., Outram P. J., Loaring N. S., 2004, MNRAS, 349, 1397

Croom S. M., et al., 2005, MNRAS, 356, 415

Croom S. M., et al., 2009, MNRAS, 399, 1755

Cumming A., Marcy G. W., Butler R. P., 1999, ApJ, 526, 890

Danforth, C. W., Nalewajko, K., France, K., & Keeney, B. A. 2013, ApJ, 764, 57

da Ângela J., et al., 2008, MNRAS, 383, 565

Danforth, C. W., Keeney, B. A., Stocke, J. T., Shull, J. M., & Yao, Y. 2010, ApJ, 720, 976

Decarli R., Falomo R., Treves A., Kotilainen J. K., Labita M., Scarpa R., 2010, MNRAS, 402, 2441

Decarli R., Falomo R., Kotilainen J. K., Hyvönen T., Uslenghi M., Treves A., 2012, AdAst, 2012,

Decarli R., Dotti M., Fumagalli M., Tsalmantza P., Montuori C., Lusso E., Hogg D. W., Prochaska J. X., 2013, MNRAS, 433, 1492

Denney K. D., et al., 2010, ApJ, 721, 715

De Rosa G., Decarli R., Walter F., Fan X., Jiang L., Kurk J., Pasquali A., Rix H. W., 2011, ApJ, 739, 56

Di Matteo T., Springel V., Hernquist L., 2005, Nature, 433, 604

Djorgovski S., 1991, ASPC, 21, 349

Djorgovski S. G., Odewahn S. C., Gal R. R., Brunner R. J., de Carvalho R. R., 1999, ASPC, 191, 179

Djorgovski S. G., Stern D., Mahabal A. A., Brunner R., 2003, ApJ, 596, 67

Djorgovski S. G., Courbin F., Meylan G., Sluse D., Thompson D., Mahabal A., Glikman E., 2007, ApJ, 662, L1

Dressler A., 1980, ApJ, 236, 351

Dunlop J. S., McLure R. J., Kukula M. J., Baum S. A., O'Dea C. P., Hughes D. H., 2003, MNRAS, 340, 1095

Ellingson, E., Yee, H. K. C., & Green, R. F. 1991, ApJ, 371, 49

Ellingson, E., Yee, H. K. C., & Green, R. F. 1991, ApJ, 371, 49

Fan J. H., Lin R. G., 1999, ApJS, 121, 131

Falomo, R., Treves, A., Kotilainen, J. K., Scarpa, R., & Uslenghi, M., 2008, ApJ, 673, 694

Falomo R., Bettoni D., Karhunen K., Kotilainen J. K., Uslenghi M., 2014, MNRAS, 440, 476

Farina E. P., Falomo R., Treves A., 2011, MNRAS, 415, 3163

Farina E. P., Montuori C., Decarli R., Fumagalli M., 2013, MNRAS, 431, 1019

Ferrarese L., Merritt D., 2000, ApJ, 539, L9

Ferrarese L., 2002, ApJ, 578, 90

Ferraz-Mello, S. 1981, AJ, 86, 619

Fisher, K. B., Bahcall, J. N., Kirhakos, S. & Schneider, D. P. 1996, ApJ, 468, 469

Foster, G. 1995, AJ, 109, 1889

Francis P. J., Drake C. L., Whiting M. T., Drinkwater M. J., Webster R. L., 2001, PASA, 18, 2

Fukugita M., Ichikawa T., Gunn J. E., Doi M., Shimasaku K., Schneider D. P., 1996, AJ, 111, 1748

Fukugita M., Nakamura O., Schneider D. P., Doi M., Kashikawa N., 2004, ApJ, 603, L65

Gavazzi G., Boselli A., Pedotti P., Gallazzi A., Carrasco L., 2002, A&A, 396, 449

Gebhardt K., et al., 2000, ApJ, 539, L13

Girardi M., Giuricin G., Mardirossian F., Mezzetti M., Boschin W., 1998, ApJ, 505, 74

González-Pérez, J. N., Kidger, M. R., & Martín-Luis, F. 2001, AJ, 122, 2055

Graham A. W., Erwin P., Caon N., Trujillo I., 2001, ApJ, 563, L11

Green P. J., Myers A. D., Barkhouse W. A., Mulchaey J. S., Bennert V. N., Cox T. J., Aldcroft T. L., 2010, ApJ, 710, 1578

Green P. J., Myers A. D., Barkhouse W. A., Aldcroft T. L., Trichas M., Richards G. T., Ruiz Á., Hopkins P. F., 2011, ApJ, 743, 81

Hashimoto Y., Henry J. P., Boehringer H., 2014, MNRAS, 440, 588

Heck A., Manfroid J., Mersch G., 1985, A&AS, 59, 63

Hennawi J. F., et al., 2006, AJ, 131, 1

Hennawi J. F., et al., 2010, ApJ, 719, 1672

Hernquist L., 1989, Natur, 340, 687

Hewett P. C., Wild V., 2010, MNRAS, 405, 2302

Hopkins P. F., Hernquist L., Cox T. J., Kereš D., 2008, ApJS, 175, 356

Horne J. H., Baliunas S. L., 1986, ApJ, 302, 757

Inada N., et al., 2010, AJ, 140, 403

Inada N., et al., 2012, AJ, 143, 119

Jurkevich, I. 1971, Ap&SS, 13, 154

Karhunen K., Kotilainen J. K., Falomo R., Bettoni D., 2014, MNRAS, 441, 1802

Kaspi S., Smith P. S., Netzer H., Maoz D., Jannuzi B. T., Giveon U., 2000, ApJ, 533, 631

Kaspi S., Maoz D., Netzer H., Peterson B. M., Vestergaard M., Jannuzi B. T., 2005, ApJ, 629, 61

Kayo I., Oguri M., 2012, MNRAS, 424, 1363

Kochanek C. S., Falco E. E., Muñoz J. A., 1999, ApJ, 510, 590

Kormendy J., Richstone D., 1995, ARA&A, 33, 581

Kormendy J., Gebhardt K., 2001, AIPC, 586, 363

Kormendy, J., Fisher, D. B., Cornell, M. E. & Bender, R. 2009, ApJS, 182, 216

Kotilainen, J. K., Falomo, R., Labita, M., Treves, A., & Uslenghi, M. 2007, ApJ, 660, 1039

Kotilainen J. K., Falomo R., Decarli R., Treves A., Uslenghi M., Scarpa R., 2009, ApJ, 703, 1663

Liu X., Shen Y., Strauss M. A., Greene J. E., 2010, ApJ, 708, 427

Liu X., Shen Y., Bian F., Loeb A., Tremaine S., 2014, ApJ, 789, 140

Lynden-Bell D., 1969, Natur, 223, 690

Loveday J., et al., 2012, MNRAS, 420, 1239

Mannucci F., Basile F., Poggianti B. M., Cimatti A., Daddi E., Pozzetti L., Vanzi L., 2001, MNRAS, 326, 745

Magorrian J., et al., 1998, AJ, 115, 2285

Marconi, A., & Hunt, L. K. 2003, ApJ, 589, L21

McIntosh D. H., Guo Y., Hertzberg J., Katz N., Mo H. J., van den Bosch F. C., Yang X., 2008, MNRAS, 388, 1537

McLure R. J., Kukula M. J., Dunlop J. S., Baum S. A., O'Dea C. P., Hughes D. H., 1999, MNRAS, 308, 377

McLure R. J., Dunlop J. S., 2001, MNRAS, 321, 515

McLure R. J., Jarvis M. J., 2002, MNRAS, 337, 109

Mo H. J., Fang L. Z., 1993, ApJ, 410, 493

Montero-Dorta A. D., Prada F., 2009, MNRAS, 399, 1106

Moore B., Lake G., Katz N., 1998, ApJ, 495, 139

Myers A. D., et al., 2006, ApJ, 638, 622

Myers A. D., Brunner R. J., Nichol R. C., Richards G. T., Schneider D. P., Bahcall N. A., 2007, ApJ, 658, 85

Myers A. D., Brunner R. J., Richards G. T., Nichol R. C., Schneider D. P., Bahcall N. A., 2007, ApJ, 658, 99

Myers A. D., Richards G. T., Brunner R. J., Schneider D. P., Strand N. E., Hall P. B., Blomquist J. A., York D. G., 2008, ApJ, 678, 635

Nakamura O., Fukugita M., Yasuda N., Loveday J., Brinkmann J., Schneider D. P., Shimasaku K., SubbaRao M., 2003, AJ, 125, 1682

Nolan L. A., Dunlop J. S., Kukula M. J., Hughes D. H., Boroson T., Jimenez R., 2001, MNRAS, 323, 308

Nolan, P. L., Abdo, A. A., Ackermann, M., et al. 2012, ApJS, 199, 31

Oguri M., et al., 2006, AJ, 132, 999

Oguri M., et al., 2012, AJ, 143, 120

Padmanabhan N., White M., Norberg P., Porciani C., 2009, MNRAS, 397, 1862

Pâris I., et al., 2012, A&A, 548, A66

Pâris I., et al., 2014, A&A, 563, A54

Peebles P. J. E., 1980, NYASA, 336, 161

Peebles P. J. E., 1980, lssu.book,

Peterson B. M., 1993, PASP, 105, 247

Peterson B. M., et al., 2004, ApJ, 613, 682

Plotkin, R. M., Anderson, S. F., Hall, P. B., et al. 2008, AJ, 135, 2453

Poggianti B. M., Smail I., Dressler A., Couch W. J., Barger A. J., Butcher H., Ellis R. S., Oemler A., Jr., 1999, ApJ, 518, 576

Popesso P., Biviano A., Böhringer H., Romaniello M., Voges W., 2005, A&A, 433, 431

Porciani C., Magliocchetti M., Norberg P., 2004, MNRAS, 355, 1010

Renzini A., 2006, ARA&A, 44, 141

Richards G. T., et al., 2001, AJ, 122, 1151

Richards G. T., Hall P. B., Vanden Berk D. E., Schneider D. P., Strauss M. A., Fan X., 2002, AAS, 34, #125.05

Richards G. T., et al., 2004, ApJS, 155, 257

Richards G. T., et al., 2009, ApJS, 180, 67

Roberts D. H., Odell S. L., Burbidge G. R., 1977, ApJ, 216, 227

Salpeter E. E., 1964, ApJ, 140, 796

Sanghvi J., Kotilainen J. K., Falomo R., Decarli R., Karhunen K., Uslenghi M., 2014, MNRAS, 445, 1261

Sandrinelli A., Treves A., Falomo R., Farina E. P., Foschini L., Landoni M., Sbarufatti B., 2013, AJ, 146, 163

Sandrinelli, A., Covino, S., & Treves, A. 2014, A&A, 562, A79

Sandrinelli A., Covino S., Treves A., 2014, ApJ, 793, L1

Sandrinelli A., Falomo R., Treves A., Farina E. P., Uslenghi M., 2014, MNRAS, 444, 1835

Scargle J. D., 1982, ApJ, 263, 835

Schechter P., 1976, ApJ, 203, 297

Schlafly E. F., Finkbeiner D. P., 2011, ApJ, 737, 103

Schlegel, D. J., Finkbeiner, D. P., & Davis, M. 1998, ApJ, 500, 525

M., 1963, Natur, 197, 1040

Schneider D. P., et al., 2003, AJ, 126, 2579

Schneider D. P., et al., 2010, AJ, 139, 2360

Serber W., Bahcall N., Ménard B., Richards G., 2006, ApJ, 643, 68

Sérsic, J. L. 1963, Boletin de la Asociacion Argentina de Astronomia La Plata Argentina, 6, 41

Shanks T., Boyle B. J., Peterson B. A., 1988, ASPC, 2, 244

Shaver P. A., 1984, A&A, 136, L9

Shen Y., et al., 2009, ApJ, 697, 1656

Shen Y., Loeb A., 2010, ApJ, 725, 249

Shen Y., et al., 2011, ApJS, 194, 45

Shen Y., 2013, BASI, 41, 61

Shen Y., et al., 2013, ApJ, 778, 98

Silk J., Wyse R. F. G., 1993, Phys. Rev., 231, 293

Skrutskie, M. F., Cutri, R. M., Stiening, R., et al. 2006, AJ, 131, 1163

Smith R. J., Boyle B. J., Maddox S. J., 2000, MNRAS, 313, 252

Smith K., et al., 2010, AAS, 42, #433.08

Stellingwerf R. F., 1978, ApJ, 224, 953

Stockton A., 1978, Natur, 274, 342

Strand N. E., Brunner R. J., Myers A. D., 2008, ApJ, 688, 180

Swingler D. N., 1989, AJ, 97, 280

Tytler D., Fan X.-M., 1992, ApJS, 79, 1

Urry, C. M., & Padovani, P. 1991, ApJ, 371, 60

Uslenghi M., Falomo R., 2008, in Modelling and Simula- tion in Science, ed. V. Di Gesu et al. (Hackensack, NJ: World Scientific), p. 313

Vanden Berk D. E., et al., 2001, AJ, 122, 549

van den Bosch R., de Zeeuw T., Gebhardt K., Noyola E., van de Ven G., 2006, ApJ, 641, 852

Veron-Cetty, M.-P., & Veron, P. 2000, A catalogue of quasars and active nuclei, 9th ed. Garching: European Southern Observatory (ESO), 2000, ESO Scientific Report no. 19

Vestergaard M., 2002, ApJ, 571, 733

Vestergaard M., Wilkes B. J., 2001, ApJS, 134, 1

Vestergaard M., Peterson B. M., 2006, ApJ, 641, 689

Vollmer B., Huchtmeier W., 2007, A&A, 462, 93

Wake D. A., et al., 2004, ApJ, 610, L85

White S. D. M., Rees M. J., 1978, MNRAS, 183, 341

Yee H. K. C., Green R. F., 1984, ASSL, 111, 583

Yee, H. K. C. & Green, R. F. 1987, ApJ, 319, 28

York D. G., et al., 2000, AJ, 120, 1579

Yu Q., Tremaine S., 2002, MNRAS, 335, 965

Zamfir S., Sulentic J. W., Marziani P., Dultzin D., 2010, MNRAS, 403, 1759

Zehavi I., et al., 2005, ApJ, 630, 1

Zel'dovich Y. B., 1964, SPhD, 9, 195

Zhang S., Wang T., Wang H., Zhou H., 2013, ApJ, 773, 175

Zhang, B.-K., Wang, S., Zhao, X.-Y., Dai, B.-Z., & Zha, M. 2013, MNRAS, 428, 3630

Zhang, B.-K., Zhao, X.-Y., Wang, C.-X., & Dai, B.-Z. 2014, Res. in Astronomy and Astrophysics, in press (arXiv:1405.6858)

Zhdanov V. I., Surdej J., 2001, A&A, 372, 1

Angela Sandrinelli